TECHNISCHE UNIVERSITÄT MÜNCHEN
Fakultät für Elektrotechnik und Informationstechnik
Lehrstuhl für Biologische Bildgebung

Multispectral methods for biological sensing and imaging. Theory and experiments.

Dipl.-Ing. Univ. Karin Radrich

Vollständiger Abdruck der von der Fakultät für Elektrotechnik und Informationstechnik der Technischen Universität München zur Erlangung des akademischen Grades eines

Doktor-Ingenieurs

genehmigten Dissertation.

Vorsitzender: Univ.-Prof. Dr.-Ing. Hans-Georg Herzog

Prüfer der Dissertation:

1. Univ.-Prof. Vasilis Ntziachristos, Ph.D.
2. Univ.-Prof. Dr.-Ing. habil. Gerhard Rigoll

Die Dissertation wurde am 10.09.2014 bei der Technischen Universität München eingereicht und durch die Fakultät für Elektrotechnik und Informationstechnik am 13.01.2015 angenommen.

Abstract

Multispectral imaging (MSI) acquires a collection of images at separate wavelengths bands lying within the ultraviolet to near infrared part of the electromagnetic spectrum. MSI capitalizes on the wavelength dependent properties of light when interacting with objects or tissues in order to reveal hidden objects, chemical compositions or processes that are otherwise invisible to the human eye. In biomedical context, MSI can be employed to detect the spectral signatures of molecules, therefore enabling their classification and distinction. It thereby exhibits the unique potential to simultaneously probe multiple molecules, a property that can contribute invaluably to the field of molecular imaging, and that yet remains to be explored.

This work investigates the potential of MSI to image multiple molecular components in living subjects. This endeavor is complicated by the fact that optical imaging is strongly affected by absorption and scattering of light in biological tissues, and their mixed contribution on the detected optical signal. Appropriate systems engineering and mathematical methods have to be developed and applied to such diffuse imaging regimes in order to obtain reasonable and quantitative read outs on physiological properties.

To meet this requirement, developments on the methodological and systems level were realized, spanning a wide range of potential application areas: from surface investigations of intrinsic tissue molecules to volumetric imaging of extrinsic molecular markers.

Presented theory and experiments encompass three different approaches. The first approach shows the development and optimization of a method for quantitative assessment of intrinsic tissue properties, i.e. tissue oxygenation, based on mathematical transformations of spectral curves. This enables the rejection of influences from non-hemoglobin absorption and tissue scattering on the computed oxygenation values. The second approach aims at translating multispectral methods for the distinction of multiple extrinsic molecular markers, i.e. fluorochromes, to *in-vivo* applications. For this purpose a novel multispectral fundus camera was developed that combines multi-wavelengths illumination with multi-wavelengths detection. This allows for a customized combination of excitation and emission for each fluorochrome, as well as the employment of multispectral unmixing

methods to *in-vivo* spectral acquisitions. The third approach finally tackles the methodological development for volumetric detection of multi-molecular data. In contrast to the first two problems, imaging of intrinsic and extrinsic contrast in planar geometries, this approach is based on the acquisition of tomographic data and reconstruction of images through the inversion of a light-tissue-interaction model. Due to the ill-posedness of the inversion problem, adequate regularization schemes had to be found and are presented herein.

Based on these three representative examples, this thesis shows the successful translation of multispectral concepts to *in-vivo* biomedical investigations. The assessment of multi-molecular information can drive biomedical research by improving the systems understanding of dynamic processes and interactions. This can ultimately affect the study of disease progression, treatment efficacy and drug development.

Acknowledgements

Many individuals have offered their guidance and support during the past years and have, by doing so, in one way or another left their marks on this thesis. This work would not have been possible without their valued help, encouragement, foresight and/or critique.
First and foremost I would like to thank my advisor Prof. Dr. Vasilis Ntziachristos for giving me the opportunity of pursuing a PhD in a field I am passionate about, and for the freedom he left me to explore different research paths. His insight and experience guided me through my professional development as well as the implementation of this thesis.

I am deeply indebted to Prof. Dr. Marius Ueffing, Dr. Stefanie Hauck and particularly to Dr. Alice Ly for their continuous support and astute scientific advice in many biological questions. I enjoyed very much working with Alice, who significantly contributed to the successful implementation of the retinal imaging project, both by scientific insight and her openness and sense of humor. Furthermore, I am grateful to Dr. Stylianos Michalakis who freely shared his insight and scientific effort by providing us with viral markers.

Special thanks go to Dr. Ralf Schulz and Dr. Angelique Ale who first introduced me to fluorescence molecular tomography and guided me through the first months of my graduate student years. The help of Pouyan Mohajerani, Maximilian Koch and Xiaopeng Ma on FMT related topics was essential and very much appreciated at later stages of my work. Several colleagues and collaborators from Klinikum Rechts der Isar have further contributed to the work presented in this thesis, whom I would like to sincerely thank. These were Dr. Ambros Beer, Dr. Johanna Bussemer and Sybille Reder, for work on combined FMT and PET imaging, and Dr. Moritz Wildgruber for other collaborative FMT projects.

I would like express my gratitude to Dr. Pilar Beatriz Garcia Allende and Panagiotis Symvoulidis for cooperation and advice in questions related to optical properties

quantification and multispectral imaging. I also thank iThera Medical for placing their gas analyzer at my disposal, which helped me with my work on oxygenation imaging.

I wish to thank Sarah Glasl, Uwe Klemm, Florian Jurgeleit and Dr. Karin Schaefer for animal handling and experimental support. I owe further thanks to Susanne Stern, Zsuzsanna Öszi, Silvia Weinzierl, Julia Niefnecker and Andreas Brandstädter for administrative support.
I thank all members of IBMI for discussions, advise, support and feedback, but also for nice times at skiing, Oktoberfest and Biergarten experiences.

Last but not least, my family and friends had essential impact on the success of this work. Their emotional support gave me strength during the past years and the writing process of this manuscript. I would particularly like to thank my parents for providing me with the education that brought me this far. Lastly, I thank Stephan Kellnberger who supported, advised, encouraged and comforted me and, most of all, displayed almost infinite patience during the thesis writing process.

Contents

List of Figures

List of Tables

List of abbreviations

AAV	adeno associated virus
BSS	blind source separation
CBR	cell-to-background ratio
CCD	charge coupled device
CD	cell density
CNR	contrast to noise ratio
CNS	central nervous system
cSLO	confocal scanning laser ophthalmoscope
CT	computed tomography
CW	continuous wave
DICOM	Digital Imaging and Communications in Medicine
DOT	diffuse optical tomography
EDTA	ethylenediaminetetraacetic acide
EMCCD	electron multiplying charge coupled device
FDG	2-fluoro-2-deoxy-glucose
FDM	finite difference method
FEM	finite element method
FITC	fluorescein
FMT	fluorescence molecular tomography
FOV	field of view
FWHM	full width half maximum
GFP	green fluorescent protein
Hb	hemoglobin
ICA	independent component analysis
ICG	indocyanine green
IDM	inverse distribution method
i.v.	intra-veneous
LSQR	least squares

LLC	Lewis lung carcinoma
ML	maximum likelihood
MFP	mean free path
MRI	magnetic resonance imaging
MRSI	magnetic resonance spectroscopy imaging
MSI	multispectral imaging
NIR	near infrared
NIRS	near infrared spectroscopy
NMDA	N-methyl-D-aspartate
NNLS	non negative least squares
OCT	optical coherence tomography
ON	optic nerve
PBS	phosphate buffered saline
PCA	principal component analysis
PDE	partial differential equation
pdf	probability density function
PET	positron emission tomography
RGB	red-green-blue (color space)
RGC	retinal ganglion cells
ROI	region of interest
RPE	retinal pigment epithelium
RTE	radiative transport equation
SPECT	single photon emission computed tomography
SPF	scattering phase function
SVD	singular value decomposition
SVM	support vector machine
TMFP	transport mean free path
US	ultrasound
VEGF	vascular endothelial growth factor
XCT	X-ray computed tomography
YFP	yellow fluorescent protein

1 Introduction

1.1 The role of engineering in biomedical sciences

Technological developments have driven progress in biological and medical research for centuries. The cellular composition of life and the existence of tiny creatures like bacteria, for instance, only became known with the invention of microscopy in the 17th century [66]. The optimization of grinding and polishing methods for lenses led Anton van Leeuwenhoek to be the first to observe and describe bacteria, yeast plants and the circulation of blood. With the first assembly of lenses into a compound microscope in 1665, Robert Hooke set the ball rolling for many biological discoveries and laid the foundations for the developments leading towards the intricate microscopy devices of today [66]. Indeed, modern biology and medicine would be unimaginable without the support of this optical device that is now one of the standard tools of investigation in areas like histopathology, cell and molecular biology.

The emergence of imaging technology constituted a further important achievement that had considerable impact on many aspects of healthcare delivery [46]. Imaging provided a means of preservation of snap-shots previously only projected onto and captured by the human eye. Furthermore, it lead to enhanced visualization and detection of the observed objects. Resuming the microscopy example, addition of optical detectors to microscopes enabled for instance the observation of previously undetectably weak signals (by adjusting exposure times) or of increased resolution (through the development of scanning technology). Physicians nowadays routinely rely on medical images for diagnostic purposes and treatment monitoring [46]. Not least because of this fact was imaging selected as one of the 20 greatest engineering achievements of the 20th century by the National Academy of Engineering (of America) [142].

Beyond microscopy, physicists and engineers have been the brains behind many

medical imaging developments that are now standard in clinical examinations, like ultrasonography, X-ray Computed Tomography (XCT), Magnetic Resonance Imaging (MRI) and Positron Emission Tomography (PET). The continuous demand for new imaging methods, ever faster devices, higher resolution, better contrast and the capability to handle larger data sets will most likely further increase the need of dedicated technology oriented research and developments.

1.2 Motivation and background

One of the key questions in current biomedical research calling for engineering and computational aid at different levels is the investigation of systems properties of whole organisms, i.e. the interaction of all (or at least several important) components making up one functional system. This concept is opposed to focusing on isolated parts of a system, which was (and partly still is) the accustomed paradigm in traditional biological research [23, 104].

Typically, biological methods for investigating a certain molecule of interest consist in extracting the desired cell or tissue sample from a living subject and further *in-vitro* processing. While such methods have contributed significantly to the comprehension of biological entities and processes and still constitute the backbone of biological research, they have the disadvantage of isolating the desired molecule from its most natural environment, the living organism. This may affect its behavior and ultimately falsify results. Experts agree that many biological reactions cannot sufficiently be explained by just summing up the knowledge on each single component that takes part in it, but that complex dynamic interactions and feed-back govern the final function of the complete system [104]. It is therefore crucial to investigate ways to track multiple molecular components simultaneously and over extended time periods *in-vivo*.

Imaging is an ideal technique for meeting the needs of modern biomedical research. Well established modalities like ultrasound or X-ray imaging have proved for decades their potential of non-invasively creating visual representations of the interior of the body. However, they predominantly visualize anatomical structures. With the advent of genomics, proteomics, and technological advances, modern targeted molecular imaging strategies are replacing the traditional anatomical or physiological approaches to the detection, evaluation, and monitoring of a variety of diseases and their treatment [46].

Molecular imaging attempts to non-invasivaly visualize, characterize and quantify biological processes at the cellular and subcellular level in living subjects [198]. It usually exploits targeted molecular markers as well as intrinsic tissue characteristics as the source of image contrast, and provides the potential for understanding of integrative biology [198].

Molecular probes designed to recognize disease-specific markers can be specifically developed to be employed in such diverse imaging modalities as Magnetic Resonance Imaging (MRI), X-ray Computed Tomography (XCT), nuclear imaging, optical imaging and Ultrasound (US) [193]. Hence, molecular readouts can be obtained based on different contrast mechanisms. In theory, an appropriate imaging modality can consequently be chosen based on the molecule, organ or disease under investigation. However, a limitation of most current molecular imaging approaches is their inability to simultaneously image more than one molecular target. While for instance one single target is used to diagnose and monitor cancer progression in nuclear imaging, this imaging modality cannot give representative feedback on the entire biochemical processes accompanying the disease. The entire process is however important in order to understand disease progression and to design efficient drugs addressing all key factors involved.

Following the demand for new *in-vivo* multi-molecular imaging concepts, this work presents research aiming at the development of new methods and systems for multi-molecular optical imaging in pre-clinical *in-vivo* settings. Pre-clinical studies are concerned with the investigation of disease progression, treatment efficacy and drug development for better understanding of molecular processes and efficient translation into human medicine. Such studies are typically conducted on animal models bearing diseases of particular interest to society that still lack sufficient understanding, like for instance cancer or diabetes. Apart from contributing to new biomedical insight, imaging methods and systems developed in pre-clinical settings can often be themselves translated to applications in human medicine.

Optical imaging typically refers to methods employing electromagnetic radiation in the visible (~400 nm - 700 nm) and near-infrared (~700 nm - 1400 nm) region. Figure 1.1 depicts the electromagnetic spectrum and allocates different imaging modalities to the radiation wavelength range that each one employs for imaging. In order to understand the choice of focussing on optical imaging methods for molecular imaging of multiple targets, we will first review the basic principle of operation and main characteristics of

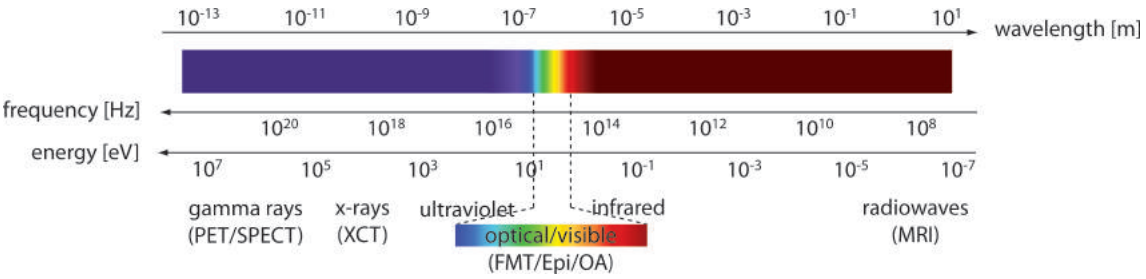

Figure 1.1: Electromagnetic spectrum and corresponding wavelength, frequency and energy ranges.

in-vivo imaging devices that are commonly disseminated to laboratories and clinics. The presented technologies are mainly approached with respect to their ability of molecular detection. Considered methods are: US, XCT, MRI, nuclear imaging and optical imaging, also including optoacoustics (OA). Key aspects like principle of operation, resolution, sensitivity etc. are visualized and summarized for every modality in a figure accompanying the respective modality description. Therein, the ability of simultaneously imaging multiple molecular targets is referred to as multiplexing. Data on the listed characteristics was assembled from References [46, 92, 115, 137, 195, 198].

Ultrasound: Ultrasound produces high resolution images based on reflected sound waves at boundaries between tissues of different acoustic impedance. A US transducer is placed in direct contact with the imaged object, where it sends sound frequencies between 1 and 20 MHz into the body. The same transducer detects the reflected waves and produces an image using time and direction of arrival of the reflected sound wave. The

	Principle of operation	Characteristics
Ultrasound	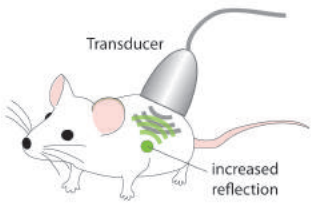	• spatial resolution: superficial: 10 - 100 µm; deep tissue (cm): 1 - 2 mm • penetration depth: cm • acquisition time: sec - min • sensitivity (with microbubbles): ~10^{-12} mol/l • multiplexing: no • molecular imaging agents: microbubbles • target: anatomical, physiological • cost: low - medium • safety: non-ionizing

Figure 1.2: Principle of operation and characteristics of ultrasound with respect to molecular imaging. Drawing adapted from [92]

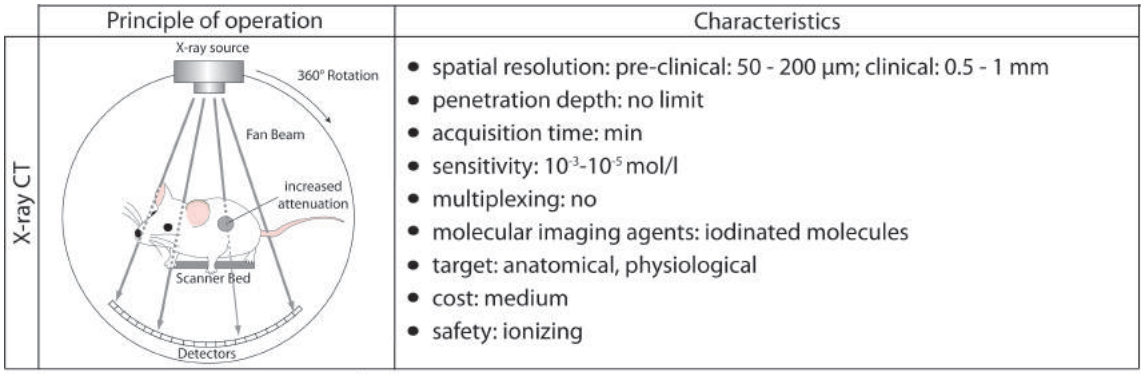

Figure 1.3: Principle of operation and characteristics of X-ray computed tomography with respect to molecular imaging. Drawing adapted from [92]

principle of operation of US is visualized in Figure 1.2, where the green dot represents a contrast agent, i.e. microbubbles in US, and its effect. The figure also summarized the characteristics of US, in particular with respect to molecular imaging.
Intrinsic tissue contrast only provides structural or functional (using the Doppler effect) information on the imaged object but gives no insight into molecular processes. Gas filled microbubbles have been used to improve image contrast by increasing the backscattered signal intensity at the tissue-microbubble boundary, for instance in imaging tumor vascularity in small animals [198]. Functionalization of these microbubbles with specific molecules including peptides or proteins has also enabled real-time, non-invasive molecular imaging of tissue targets expressed on vascular endothelial cells [198]. However, due to the comparatively large diameter of microbubbles, targeted molecular ultrasound is restricted to the intravascular compartment employing markers such as $\alpha_v\beta_3$ [49] or vascular endothelial growth factor [197]. Apart from this limitation, US is not capable of distinguishing reflections originating from different molecular markers.

X-ray Computed Tomography: XCT (Figure 1.3) measures the differential levels of attenuation of X-rays after having traversed a subject, i.e. source and detector are placed on opposite sides of the body. By rotating source and detector around the subject, XCT acquires projections at different angles. These are used to reconstruct a three dimensional map of the tissue density distribution. For instance, bones strongly absorb X-rays and are therefore imaged with high contrast compared to surrounding tissues.
Typically, XCT provides high resolution anatomical information at high penetration depth, but is limited by the lack of soft tissue contrast [198]. To increase soft tissue contrast, radiocontrast agents that strongly absorb X-rays are employed, like e.g. barium sulfate

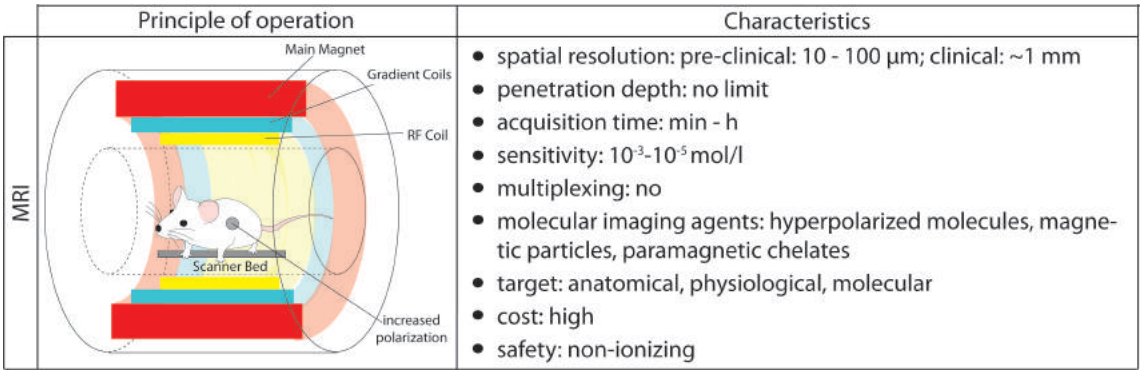

Figure 1.4: Principle of operation and characteristics of magnetic resonance imaging with respect to molecular imaging.

or iodine. The latter is commonly injected into the blood stream to enhance X-ray contrast for blood vessel imaging [156]. Attempts at labeling molecular probes with CT-compatible contrast agents have proved challenging [163]. Even successful implementations (e.g. [192]) suffer from the low detection sensitivity of the agents by XCT, which results in high agent concentration doses that would need to be administered to the imaged subject. Furthermore, even if better molecular probes should be available in future, there still remains the fact that ionizing radiation is employed, hence hampering the multiplexing potential of XCT. Multiplexed XCT requires the ability to separate photon energies [32, 95]. This is because X-ray attenuation in different tissues, or in contrast agent materials, varies depending on the employed X-ray energy. Individual energy dependent attenuation properties allow hence for the distinction of materials of different densities. However, detecting multiple energy levels means that the imaged subjects also have to be subjected to even higher radiation doses. This fact renders XCT inadequate for multi-molecular investigations. XCT is therefore hardly employed as a molecular imaging modality *per se*, but is usually rather combined to other molecular imaging modalities as complementary imaging device.

Magnetic Resonance Imaging: MRI (Figure 1.4) is a potent imaging modality that provides variable contrast to elucidate anatomical structures or pathologies based on magnetic properties of atomic nuclei within the body. Shortly, it relies on the alignment of magnetic moments of nuclei with an external magnetic field which leads to a steady-state magnetization of protons in tissue. In response to a specific resonance frequency, the magnetization changes orientation. The signal produced during the return (or relaxation) to the nuclei's initial position in alignment with the external magnetic field can be used to

produce an image representative of the proton density and tissue specific relaxation times. The MR signal is generated from the very small net difference in the number of nuclei that align parallel versus those that align anti-parallel with the magnetic field [92]. This effect, called polarization, depends on the magnetic field strength and is typically very low, resulting in poor sensitivity of MRI.
The versatility and uniqueness of MRI is derived from the fact that the nuclear magnetic resonance properties of a proton (most commonly used nucleus) are sensitive to its local physicochemical microenvironment. The MRI experiment can be tailored to exploit these properties to interrogate pathophysiology [198].
MRI provides both anatomical and functional information based on intrinsic contrast generation. Physiological and functional parameters can be furthermore monitored by specialized MRI techniques like dynamic contrast-enhanced MRI, where a paramagnetic contrast agent like gadolinium is employed to study for instance blood flow or perfusion [198], or by diffusion weighted MRI and blood oxygen level dependent MRI. (The detailed description of the general theory of MRI and its specialized techniques is beyond the scope of this thesis. Please refer to References [55,92] for more exhaustive reviews of this subject.)
Molecular imaging with MRI was attempted by development of various paramagnetic targeted agents reporting on cell death [208], tumor development [37] or angiogenesis [169], just to name a few. An alternative approach, magnetic resonance spectroscopy imaging (MRSI), measures the concentration of intrinsic tissue metabolites and has been used to probe metabolic pathways in cancer [55]. However, the intrinsically low detection sensitivity of MRSI, due to the low concentrations of tissue metabolites compared to water, results in very poor resolution and long acquisition times [92] and limits its utility for employment in molecular imaging.
Strategies of increasing the polarization of nuclear spins above the equilibrium polarization endowed by the field of the MRI magnet (i.e. creating hyperpolarization), are therefore currently among the top research topics in MRSI and have already shown great potential in imaging molecular targets [27]. Despite ongoing efforts, hyperpolarized MRSI is till in its early stages of development. The requirement of additional hardware for hyperpolarization and the short lifetime of hyperpolarized contrast agents (0.5-5 min) are just some of the current limitations of this technique.

Nuclear imaging: Two clinically employed imaging modalities are based on the measurement of the radioactive decay of intravenously injected, radiolabeled agents (Figure 1.5).

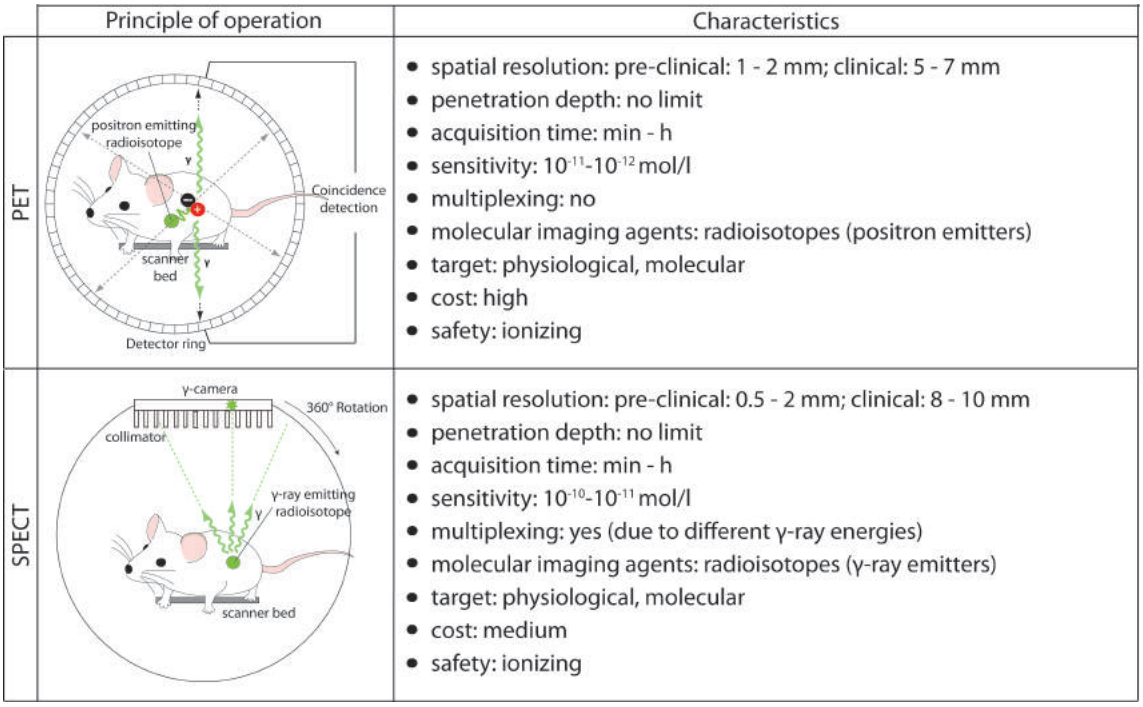

Figure 1.5: Principle of operation and characteristics of positron emission tomography and single photon emission computed tomography.

Positron Emission Tomotgraphy (PET) is a molecular imaging modality that determines the biodistribution of a radiolabeled agent using a ring of gamma ray detectors placed around the imaged subjects. PET takes advantage of the properties of radioisotopes which decay via positron emission. Positrons are ejected from the nucleus into surrounding tissue where they collide with electrons after a mean traveling distance of typically 1-2 mm, fundamentally limiting achievable resolution in PET. The positron-electron annihilation process leads to the production of two γ-ray photons, each with energy of 511 keV, traveling at opposite directions to one another [92]. Three dimensional images of the radioisotope's biodistribution are reconstructed based on directional information provided by the γ-ray trajectories. These trajectories are identified by coincidence detection of the two anti-parallel γ-rays (Figures 1.5).

The radioisotope is typically bound to a molecule of diagnostic interest, in nuclear imaging called a tracer. One of the most frequently employed PET tracers targets the body's metabolic activity by injecting a radiolabeled analog of glucose, ^{18}F-2-fluoro-2-deoxy-glucose (^{18}F-FDG). Since tumor cells often display increased metabolic demand compared to surrounding tissue, accumulation of FDG tracers can be used as indicator for cancer.

Single Photon Emission Computed Tomography (SPECT) employs tracers which decay via direct emission of single γ-rays. In order to obtain directional information for the reconstruction of 3D images from SPECT, a different setup has to be employed than in PET. Typically, SPECT scanners employ a gamma camera which is rotated around the subject to acquire tomographic data, similarly to XCT. Lead collimators are added to the camera that reject any photon whose trajectory is not normal to the camera plane, hence providing information on the photon's direction of emission.
Of all imaging modalities introduced so far, the two nuclear imaging techniques PET and SPECT are the only dedicated molecular imaging modalities, specifically developed for the purpose of imaging targeted molecules. Both PET and SPECT display in theory very high sensitivity to the imaged tracer. However, since the collimator in SPECT rejects many photons, SPECT sensitivity and resolution are significantly lower than for PET [92]. Because γ-ray energies in PET are always of 511 keV, different tracers cannot be employed simultaneously. Conversely, SPECT has some multiplexing capabilities due to the employment of different nuclides giving rise to gamma rays with differing energies [92]. Despite of some undeniable strengths of PET and SPECT in imaging molecular targets, nuclear imaging is clearly limited by its use of ionizing radiation, preventing frequent imaging of the same subject for instance for longitudinal monitoring.

Optical Imaging: Optical imaging is a generic term comprising a variety of modalities that employ light to produce imaging contrast. The best known technology in this field, microscopy, is traditionally employed for *ex-vivo* investigations. However, macroscopic imaging techniques enabling noninvasive, repetitive, whole body imaging (the latter only in small animals), have emerged during the past two decades [92].
Implementations of optical imaging devices for *in-vivo* applications comprise both tomographic (e.g. diffuse optical tomography, fluorescence molecular tomography) and surface imaging modalities (epi-illumination systems) (Figure 1.6). They typically measure the differential absorption of light in tissue.
First attempts at **deep-tissue volumetric imaging** using light resulted in the development of diffuse optical tomography (DOT). DOT is an imaging modality delivering NIR light, typically via fibers, to several locations (source locations) on the surface of the body part under investigation. Transmitted or reflected intensities are measured with an array of detectors [80]. For each source location each detector records the light reaching it, providing an image of the light transmission from that particular source. A model of the propagation physics is then used to infer the localized optical properties of the illuminated tissue [19].

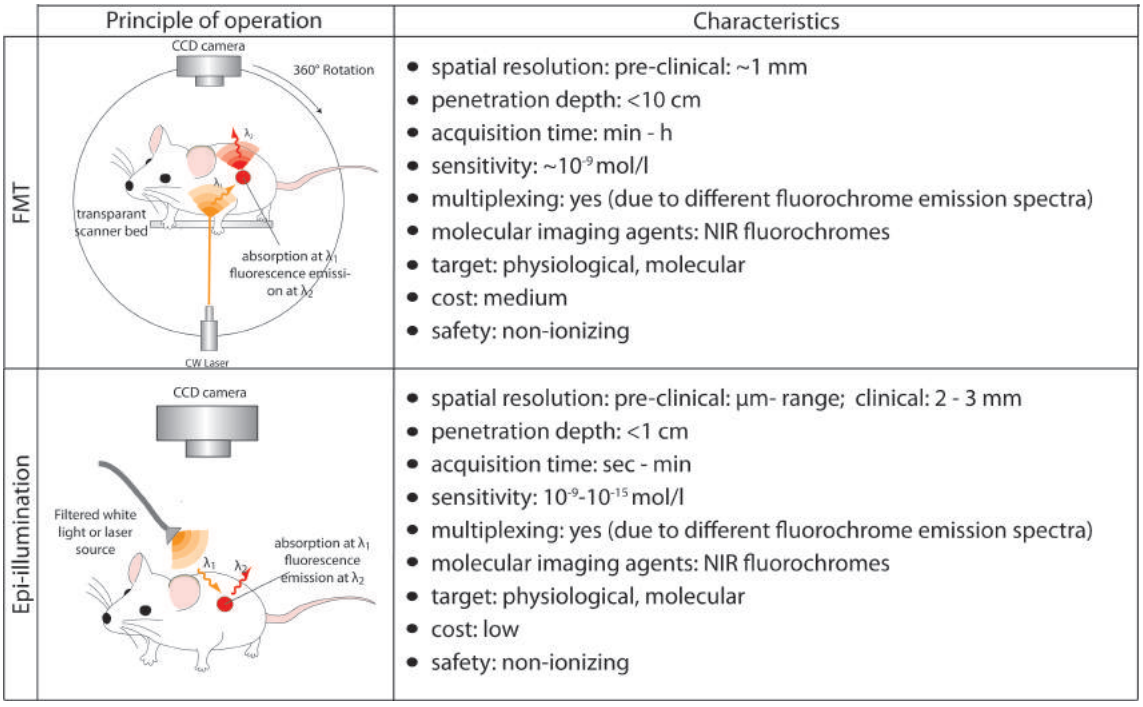

Figure 1.6: Principle of operation and characteristics of fluorescence molecular tomography and epi-illumination fluorescence imaging.

This model is parameterized in terms of the unknown scattering or absorption as a function of position in tissue [19]. Absorption in the NIR is primarily affected by oxygenated and deoxygenated hemoglobin. Typical DOT images therefore investigate effects related to hemodynamics and blood oxygenation, as for instance increased blood supply in tumors vs. normal tissue [135] or cerebral activity [48].

The diffusion approach was adapted to additionally measure concentrations of exogenous contrast agents [47], typically by employing some fluorescent dye. Such fluorescent dyes can be used as labels for molecular targets (analogously to PET/SPECT) to obtain molecular specificity. The technique based on this concepts is known as Fluorescence Molecular Tomography (FMT) and is typically employed in pre-clinical, small animal research [139]. State-of-the-art FMT systems typically scan focussed laser sources over the surface of the imaged subject for excitation of a fluorochrome, and employ CCD cameras and filters for emission detection on the opposite side of the subject. Source and detector can be mounted on rotation gantries in order to obtain projections at 360 degrees.

Epi-illumination (i.e. reflectance) systems for surface investigations of molecular processes probe the same contrast mechanisms as tomographic modalities, i.e. tissue chromophores or fluorescence. However, depth information is reduced and mainly planar

information of spatial distributions can be obtained. Current application areas of *in-vivo* molecular epi-illumination imaging are for instance fluorescence guided surgery, where tumor resection is aided by labeling tumors with fluorescent dyes [184], or in small animal imaging [111, 122].

One limitation of optical imaging approaches is the short penetration depth of light in the visible (µm - few mm) and near infrared (NIR) (mm - few cm) range. This has hampered the application of *in-vivo* diagnostic optical imaging methods to become standard clinical investigation tools. Exceptions exist, like for instance in fundus photography (for retinal diagnosis) or dermoscopy (for skin diagnosis). However, devices employed in these fields essentially acquire only simple reflectance images like any standard photographic camera would do, only adding some magnification optics. Otherwise, mainly prototypic devices have been employed in pilot studies in humans. Examples encompass fluorescence guided cancer surgery and diffuse optical tomography of breast or brain, as previously discussed. Furthermore, light in the visible and NIR region is strongly scattered leading to limited achievable resolution with increasing imaging depth.

Despite its diffusive character and low penetration depth, optical imaging has several advantages rendering it a particularly interesting concept for both small animal research and clinics. As already mentioned, optical imaging methods can image both intrinsic tissue contrast based on differential light absorption properties of tissue chromophores, and extrinsic tissue contrast like fluorescence. In comparison to the previously listed imaging modalities, optical methods have the unique capability of simultaneously assessing information on multiple molecules at once, employing non-ionizing radiation. This is due to the spectral properties of light and its interaction with biological tissues. Since every chromophore has an individual absorption spectrum, distinction of different chromophores can be done based on their light reflectance or transmittance characteristics. In simple terms, as in human vision, objects can be distinguished by their color. To enhance contrast and to enable the distinction of specific molecules, a variety of labeling strategies have been developed and still constitute a focus in molecular imaging research. Labeling cells and molecules with fluorochromes having different emission characteristics (i.e. colors) has already become a standard procedure to stain *ex-vivo* slices for fluorescence microscopy. Labeling concepts are currently modified to produce *in-vivo* compatible probes of high specificity, and image analysis methods can be adopted to analyze images from *in-vivo* experiments.

Not least, optical imaging was shown to provide very high sensitivity to molecular targets.

	Principle of operation	Characteristics
Optoacoustics	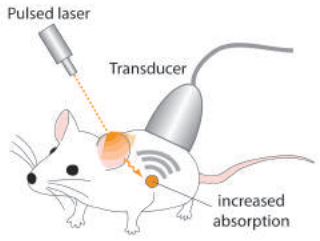	• spatial resolution: pre-clinical: 10 µm - 1 mm • penetration depth: ~ 5 cm • acquisition time: sec - min • sensitivity: 10^{-3}-10^{-6} mol/l • multiplexing: yes • molecular imaging agents: fluorochromes, nanoparticles • target: anatomical, physiological, molecular • cost: medium • safety: non-ionizing

Figure 1.7: Principle of operation and characteristics of optoacoustics with respect to molecular imaging.

Optoacoustic imaging: Strictly speaking, optoacoustic imaging belongs to the optical imaging field, given the definition of optical imaging used above as being a generic term for any modality using light to create imaging contrast. However, optoacoustic imaging combines the advantages of optical imaging with those of ultrasound by providing optical absorption contrast at ultrasound resolution. Shortly, the basic principle of operation of optoacoustics relies on the differential absorption of short laser pulses by tissue (Figure 1.7). The absorption process leads to thermal expansion of the illuminated tissue proportional to its absorption properties at the employed wavelength, resulting in the emission of broadband ultrasound waves. US waves are detected by arrays of US transducers and used to reconstruct images of the light absorption differences in the imaged tissue. This concept allows imaging at depths of several centimeters and provides higher resolution images than pure optical approaches. Furthermore, multispectral investigations are also possible since light at different wavelengths can be employed for tissue illumination, and molecular labeling approaches can be applied. There currently remain, however, some important limitations to optoacoustic imaging, restricting its applicability to multi-molecular studies. Most problematic is the issue of sensitivity to fluorescent targets, which is considerably lower than the sensitivity obtained with FMT. Although research to improve OA sensitivity is ongoing, current methods still require high contrast agent concentrations. A different complication arises from the fact that mainly direct-contact measurements can be obtained due to the low transmission of ultrasound through air (at least when high signal sensitivity is wanted). This hampers OA from being easily employed in areas like surgery where distance measurements are required.

Due to considerable research efforts, all presented *in-vivo* imaging modalities are on their way towards enabling molecular readings in clinical and/or pre-clinical settings. These efforts demonstrate the importance of molecular imaging in modern biological and medical research. However, most technologies are still limited by either low sensitivity (XCT, MRI, OA), restricted probe distribution (intravascular compartment in US), or by employment of high radiation doses (PET, SPECT, XCT). More importantly, however, is the fact that most technologies still fail at meeting the requirements set on modern molecular imaging as defined above, i.e. investigating multiple molecules at once. The only modalities potentially allowing for multi-molecular read outs are SPECT, OA and optical imaging. Of these three, optical imaging is the only candidate that can provide both high sensitivity and safety. Besides, a variety of optical imaging setups for *in-vivo* investigations can be conceived at relatively low cost, thus enabling the employment of similar multispectral methodology to a wide range of *in-vivo* applications, from epi-illumination imaging of surfaces to tomographic investigations of volumes.

1.3 Objectives and outline

The goal of this thesis was to investigate different methodological and hardware implementations enabling multispectral molecular readings *in-vivo*. The focus lay on the development of methods that could provide high molecular sensitivity, rather than particularly high resolution. Therefore, purely optical (i.e. employing optical methods in both illumination and detection path) approaches were considered herein. Purely optical methods allow a high degree of flexibility in terms of imaging setup, since contact-free strategies can be implemented leading to a high variety of potential application areas of such imaging setups.

The methods presented in the following chapters were developed for three different application areas and on three different levels which are all relevant to clinical and pre-clinical diagnosis and research. They all take advantage of the multispectral separation properties of light and aim at providing means for multi-molecular investigation of tissue to drive future biomedical advances.

The first method aims at the quantitative assessment of tissue oxygenation. Tissue oxygenation and vascular oxygen saturation are important indicators of physiology and the viability of human tissues and organs. Perturbation of oxygenation from physiological

values is a strong indication of systemic or local disease and has significant implications to the functioning of tissues and organs. Accurate assessment of tissue or vascular oxygenation is hence of great significance in the clinical environment. Oxygen transport to tissues is performed through the vascular system by red blood cells. These cells in turn contain hemoglobin, a molecule that has the ability to bind oxygen. Interestingly, the absorption spectrum of blood changes proportionally to the oxygen saturation of the hemoglobin present within. Oxygenated hemoglobin has a distinctively different spectrum than deoxygenated hemoglobin which can be even seen by the naked eye when in high concentration, for example via the bluish appearance of veins versus the redder color of arteries. This work capitalized on this property by developing a computational method using multispectral reflectance images from a custom made system that quantitatively computes tissue and vascular oxygenation independent of other tissue optical properties. The challenge consisted in finding a method that appropriately rejects the influence of other chromophores and more importantly of tissue scattering. This method was developed in an experimental approach on tissue mimicking phantoms and first pilot studies in tissues were performed.

While the first method was based on the detection of intrinsic tissue contrast, the second approach aimed at translating multispectral methods for fluorochrome separation, which have been established in *ex-vivo* microscopy, to *in-vivo* applications. For this purpose a novel multispectral fundus camera was developed that combines multi-wavelengths illumination with multi-wavelengths detection. This allows for a customized combination of excitation and emission for each fluorochrome, as well as the employment of multi-spectral unmixing methods to *in-vivo* spectral acquisitions. The mouse retina was chosen as a biological training set, as this tissue represents a highly ordered histological and cellular stratification. Furthermore, the retina is the only organ apart from skin that is non-invasively accessible in planar imaging geometry, due to the transparency of the pupil and lens. Since it is considered to be the outermost part of the brain it reflects on neuronal diseases and is furthermore affected by several systemic diseases as well as eye specific dysfunctions. Choosing this tissue as a test-case aimed at providing proof of successful technology development as well as generation of data sets suited for biomedical systems-level investigations.

The third approach finally tackled the methodological development for volumetric detection of multi-molecular data. In contrast to the first two problems, imaging of intrinsic and extrinsic contrast in planar geometries, this approach was based on the acquisition of tomographic data and reconstruction of images through the inversion of a light-tissue-interaction model. This project employed a Fluorescence Molecular Tomography system

in limited-projection-view configuration that recovers the biodistribution of fluorescence agents in the near-infrared regime in mice. The developed methodology improved upon the general reconstruction ability of this system by proposing a coregistration approach in order to incorporate anatomical information into the reconstruction of the molecular data. This allowed for the implementation of an adapted regularization method that affords independent reconstruction of multiple fluorochromes with improved accuracy.

The following chapters present theory, developed methods and instrumentation, as well as results obtained in pre-clinical experiments. Chapter 2 introduces to theory that is common and fundamental to all methods and systems presented in this work. It first presents and defines the term multispectral imaging and related data acquisition concepts. It further gives an overview on photon propagation in tissue, general optical properties of tissue and the basic principle of fluorescence and its use in biomedical research. This chapter also introduces standard modeling approaches describing light propagation in biological tissue. Theory that is specific to either surface or volumetric imaging will be covered in the respective chapters.
Chapter 3 describes the development of multispectral systems and methods for surface investigations. For that, a thorough introduction to the two considered imaging applications, oxygenation imaging and multi-fluorochrome imaging in the retina, is first given. The significance of oxygenation monitoring is outlined and previous work on oxygenation measurement devices and methods is reviewed. Equivalently, state-of-the art *in-vivo* multi-fluorochrome imaging in general and in particular in the retina, is discussed. Subsequently, two multispectral epi-illumination systems are introduced followed by mathematical and computational methods respectively applied to oxygenation and/or multi-fluorochrome imaging. First pilot studies on real tissues for oxygenation detection and on multi-fluorochrome imaging in the retina are shown.
Chapter 4 presents the developed methodology for volumetric multi-molecular investigations. First, the state-of-the-art in FMT imaging is examined, giving an overview over the historic development of optical tomography technology. Modeling and inversion schemes necessary for reconstructing tomographic fluorescence data is subsequently covered. The concept of hybrid imaging by introducing data from an anatomical imaging modality into the FMT reconstruction scheme is illustrated and its realization for limited-projection-angle FMT shown. The development of an adapted reconstruction method independently recovering different fluorescent probes is finally presented and the effects evaluated in *in-vivo* mouse experiments.
Chapter 5 offers a conclusion on the significance of the presented work.

2 Theoretical background for optical imaging of surfaces and volumes

The goal of this chapter is to introduce the reader to some of the basic concepts of optical imaging.
Section 2.1 defines the term multispectral and its meaning in the context of imaging employing visible and near-infrared light. Different acquisition methods for a full spatio-spectral data set are further introduced and application areas of multispectral imaging shortly discussed. Section 2.2 subsequently covers the theoretical background of light-tissue interactions. Here, basic optical properties of biological tissue are defined, as well as their description in tissue optics. These definitions are the foundation for the light propagation models presented in Section 2.3. Section 2.4 finally gives an overview of application areas of multispectral imaging versus light-transport modeling approaches.
Theory presented and notation used in this chapter are mainly based on two excellent textbooks by Wang [191] and Vo-Dinh [188].

2.1 Imaging spectroscopy

2.1.1 Combination of spectral and spatial information - the data cube

Spectroscopy is defined as the process of measuring the wavelength dependence of the interaction between matter and any portion of the electromagnetic spectrum, in the context of this thesis the interaction with light. Hence, imaging spectroscopy combines the detection abilities of two methods for the acquisition of light-matter interactions, namely wide-field (i.e. two dimensional or planar) epi-illumination imaging and spectroscopy.

The acquisition of scenes by some light-sensitive two dimensional detector is an intuitively comprehensible concept. Human vision and perception is based on the same concept, employing the retina as detection device and the brain for data processing. Similarly, standard photographic cameras attempt to reproduce the properties of human vision by capturing the interaction of light with physical objects through a combination of lenses and detectors (typically charge couples devices, CCD). Both, retina and standard photographic cameras, however, are limited in terms of spectral resolution and bandwidth.

In contrast to imaging, pure spectroscopy lacks spatial information but provides high resolution spectral information that can range from the ultraviolet to the infrared range of the electromagnetic spectrum. Light-tissue interaction, as will be discussed in Section 2.2, depends on the chemical composition of the respective biological material, which defines its absorption and scattering properties at each wavelength. The resulting reflectance spectrum can be a unique identifier, known as spectral signature, of a specific chemical compound like a molecule or, on a macroscopic level, of the physiological state of a biological entity (like tissue or organism).

The combination of spatial and spectral information leads to a three dimensional data set, a so called data cube, of increased descriptive potential compared to the individual data sets. In this case, two dimensions encode space, and each pixel within this spatial representation contains spectral information that is added as a third dimension to the data set. This concept is visualized in Figure 2.1 for random data elements, and Figure 2.2 gives an example of spectral reflectance acquisitions of a mouse retina. An example for the spectrum in one random pixel of the 2D image of the retina is presented above the images in Figure 2.2.

The information contained in a data cube can be employed to distinguish intrinsic tissue parameters like different tissue chromophores, or extrinsic contrast like fluorescence. Every pixel of the 2D spatial distribution can accordingly be assigned a spectral signature, therefore allowing for spacial mapping of spectral (and ultimately chemical) properties.
A forth dimension can be added to the imaging problem by introducing time, i.e. by sequentially acquiring a full data cube at different time points. Depending on the speed of the biological processes under investigation, dynamic imaging can impose hard requirements on the imaging hardware, as discussed in Section 2.1.2. Typically, spatial, spectral and temporal resolution are weighted against each other for every

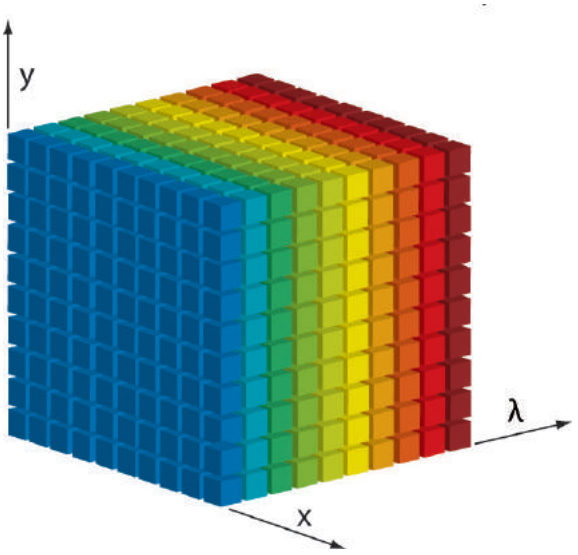

Figure 2.1: Spectral imaging data set consisting of two spacial and one spectral dimension. Adapted from [56].

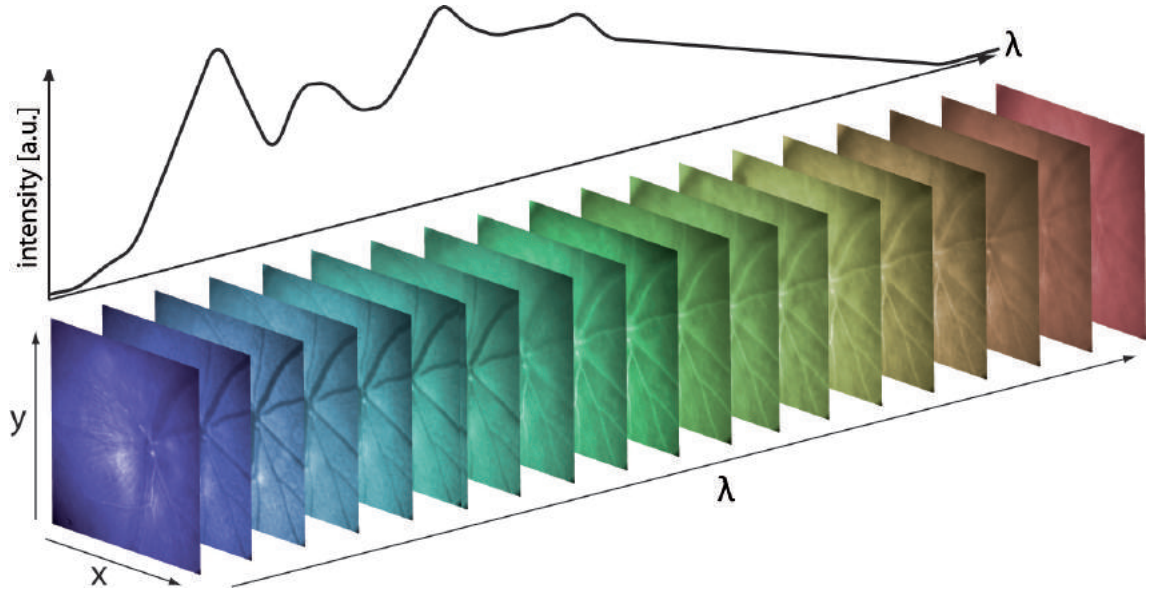

Figure 2.2: Reflectance images of a mouse retina acquired at different wavelength bands using spectral scanning.

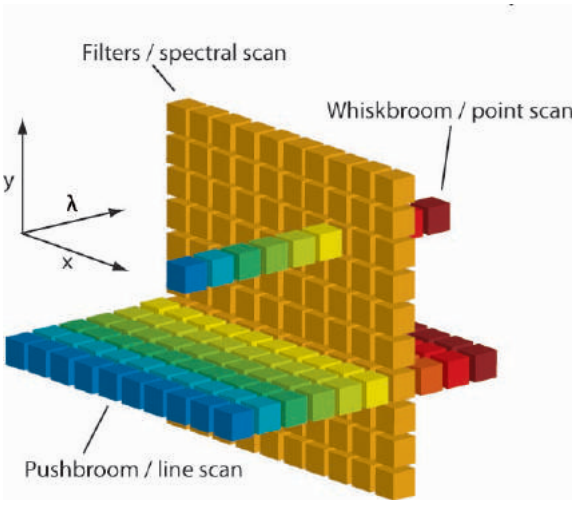

Figure 2.3: Methods for the acquisition of a spectral cube: whiskbroom or point scanning, pushbroom or line scanning and spectral scanning by employment of filters. Adapted from [188]

individual multi-spectral imaging application, resulting in a trade-off between the three parameters.

2.1.2 Data acquisition concepts

There are four major concepts to the acquisition of a full data set that fills the entire data cube.

The first two employ dispersive elements like prisms or gratings to separate light into its wavelength components (devices employing this concept are called spectrometers). The spectra are then collected simultaneously while scanning has to be performed along one or both spatial dimensions. The whiskbroom approach collects a full spectrum at one single point in space. Therefore, both spatial dimensions of the data cube have to be scanned to obtain an entire data cube. Pushbroom spectrometers acquire full spectra of all data points along one spatial dimension. Thus, the scanning process is reduced to the second spatial dimension.
The third concept is based on simultaneous acquisition of both special dimensions. Scanning is realized in the spectral domain by employing filters in front of a CCD camera and sequential acquisition of 2D images. The concepts of whiskbroom, pushbroom and spectral scanning are depicted in Figure 2.3.
The forth concept, finally, aims at acquiring all dimensions in a snap-shot. This can be

realized, for instance, by employing a two-dimensional computer-generated hologram grating to diffract light from a two-dimensional scene. The various diffraction orders are then distributed as a mosaic on a large two-dimensional CCD array and can be reconstructed to a data cube by adequate reconstruction algorithms [54, 54, 69].

Each of these four data acquisition concepts have advantages and disadvantages that have to be weighted against each other for every application area. Depending on the requirements on acquisition time, spatial resolution, spectral resolution and hardware considerations, the adequate choice for a certain experimental setup has to be done individually. Snapshot devices, for instance, are advantageous to image very fast biological processes that may otherwise be missed when employing more time consuming scanning technology. Although fast scanners exist, sensitivity limitations often impose longer acquisition times and make scanning mode time costly [54]. Large CCDs are however required to record both spatial and spectral information simultaneously, which usually results in a trade-off on spatial or spectral resolution, or both. Additionally, while the data acquisition process with snapshot technology can be very short, reconstruction of the data cube from dispersed images can be computationally intense.
When time considerations are less stringent, scanning technology may be a more adequate choice. High spectral resolution can be achieved by devices employing spectrometers as detection devices and scanning over space. In living specimens, however, such spatial scanning may be inadequate due to movement artifacts of the imaged subject. In such cases, and if spectral properties do not change fast, scanning the spectral domain and acquisition of the full two dimensional space at once may be more advantageous.
Hardware cost and other setup requirements may further influence the decision for one of the data acquisition concepts.

2.1.3 Processing multispectral images

Several approaches to process and analyze multispectral images have been developed in the past. Such approaches comprise for instance filtering for noise reduction or correction of uneven illumination. Coregistration of individual 2D images may be required when moving objects are investigated, or wavelength filters are employed that may not be perfectly aligned. While these concepts are part of the standard image processing toolbox, other methods aim at specifically analyzing spectral properties by computing the contributions of different chromophores or fluorochromes to the overall appearance of the de-

tected spectrum. Such approaches are generically termed as unmixing and will be subject of more detailed description in chapter 3.

2.1.4 Applications

Spectral imaging was initially developed for remote sensing of the earth, as well as planetary exploration. The latter, for instance, allowed for the identification of the nature of surfaces of extraterrestrial bodies [62]. Remote spectral imaging of terrestrial surfaces has found applications in agriculture and forestry for the remote distinction of soil types, crops, forest fires etc. Applications were extended to numerous areas like weld control, the evaluation of art and archeological findings, or water resource control [120].
More recently, imaging and analysis concepts developed for the before mentioned application areas were translated to life sciences to distinguish between multiple fluorescence labels in microscopy slices (e.g. [122]).
The adaptation of multispectral concepts to fluorescence microscopy are comparatively easy, since microscopy slices are very thin and can therefore be similarly treated as the reflectance images obtained from remote sensing of opaque surface. However, when considering thicker tissue samples as given in *in-vivo* applications, it becomes inevitable to first consider the interactions taking place between light and biological tissues and their influence on the detected images.

2.2 Light - tissue interaction

2.2.1 Photophysical processes of photon-matter interaction

The absorption of an incident photon by a molecule can give rise to a variety of secondary processes, which are best described by the Jablonski diagram in Figure 2.4. The diagram illustrates the quantized orbital energy levels of a molecule (S_0, S_1, S_2, etc.) and the transitions that can occur between them or their vibrational states (V_0, V_1, V_2, etc.) upon excitation and relaxation.

A photon is only absorbed if its energy matches the energy difference between two discrete energy levels in a molecule, otherwise the molecule will be transparent to that radiation. These energy levels define the absorption and the emission bands, i.e. the

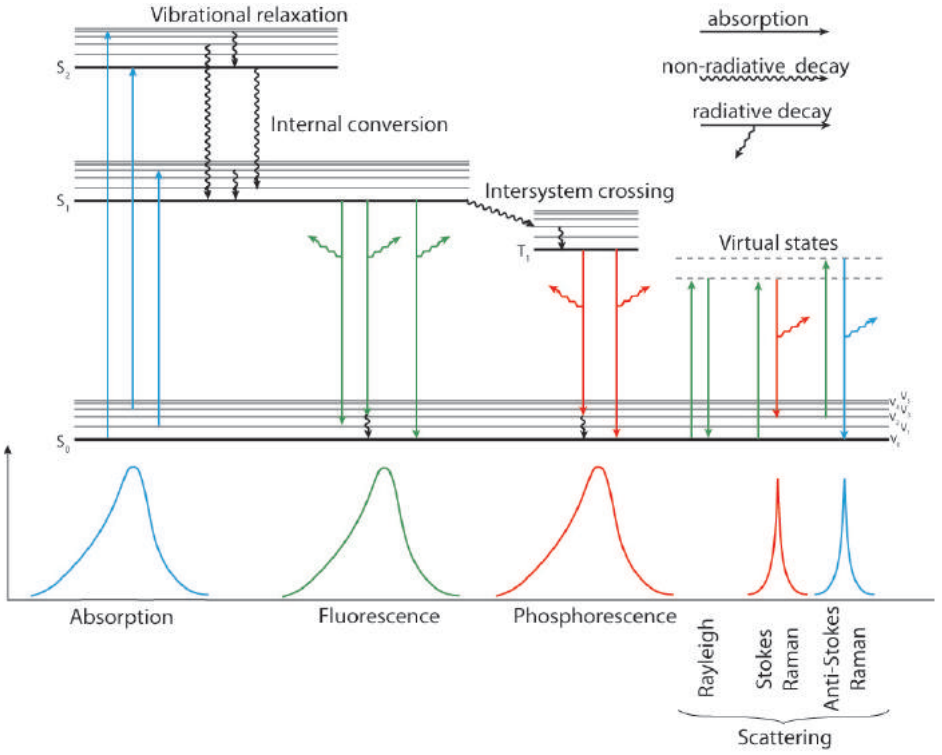

Figure 2.4: Jablonski diagram showing photon excitation and different relaxation mechanisms. Compiled from [110, 187, 191]

perceptible color, of the molecule [191]. The energy gained by a molecule causes the elevation of an electron to a higher energy level, i.e. from its ground state S_0 to an excited state S_n. Once elevated to an excited state, the electron can fall back into lower energy states by different, either radiative or non-radiative, processes.

Non-radiative energy dissipation, which means loss of energy in the absence of light emission, takes place by vibrational relaxation or internal conversion. Vibrational relaxation describes the transfer of energy to other vibrational modes as kinetic energy. If the excited electron transitions from one electronic state to another through vibrational relaxation, this process is referred to as internal conversion. Rarely, a third non-radiative phenomenon can occur which is called intersystem crossing. In this case an electron changes its spin multiplicity, i.e. it transitions to the lowest excited triplet state.

Radiative energy dissipation takes place through emission of a photon. The process of relaxation from the lowest excited singlet state (S_1) by light emission is known as fluorescence. The process of relaxation from triplet excited states after intersystem

crossing is known as phosphorescence.
All non-radiative and radiative processes take place on different time-scales, which is relevant for their probability to happen. The faster one transition, the more likely it is to occur. Absorption is the fastest process, followed by vibrational relaxation and internal conversion, fluorescence, intersystem crossing and finally phosphorescence [191].

A second type of photon-matter interaction is scattering, i.e. redirection of light. Scattering can happen without any energy exchange between photon and molecule, and is then known as elastic or Rayleigh scattering. This is the dominant scattering phenomenon in biological tissues [110]. Inelastic or Raman scattering in contrast describes a process that involves energy transfer, resulting in a scattered photon of either higher or lower energy compared to the incident photon. The energy of the emitted photon depends on the initial state of the hit molecule (being in ground state or a vibrational state) before interaction with the incident photon [191]. Compared to absorption, where an electron is raised to a real stationary state, scattering only raises the electron to a virtual, very short lived, energy state.

These basic photo-physical processes at a microscopic scale can be summarized into coefficients representing the average effects of microscopic interactions on macroscopic observations [110]. Relevant processes for the macroscopic optical description of tissue in the context of *in-vivo* diffuse optical imaging are absorption, scattering and fluorescence. The following sections therefore address the definition and description of these macroscopic optical parameters.

2.2.2 Absorption and scattering and their description in tissue optics

The two governing properties of tissue when it comes to interactions with light in the visible and near-infrared range of the electromagnetic spectrum are absorption and scattering. These properties are related to the generation of contrast for imaging.

The probability of an incident photon being absorbed after a unit path length of propagation in tissue is given by the tissue's absorption coefficient μ_a. The mean depth to which a photon can penetrate in a non-scattering medium is hence defined as $1/\mu_a$, and is called absorption mean free path. The attenuation of light in a non-scattering

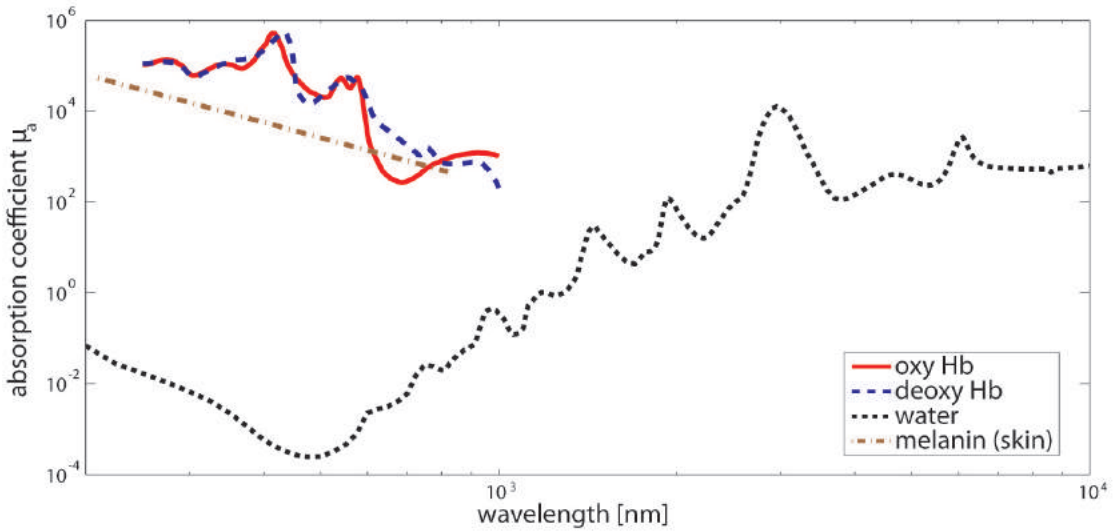

Figure 2.5: Absorption spectra of tissue chromophores. Data for figure extracted from [70, 147].

medium can be described by the Beer-Lambert law

$$I(x) = I_0 \, \mathrm{e}^{-\mu_a x} \tag{2.1}$$

where x denotes the propagation distance in the medium, I_0 the initial light intensity at $x = 0$ and I the light intensity at x.
Absorption results in the loss of the incident photon and energy transfer from the photon to the absorbing molecule. This energy can either be converted to another energy form like heat or can be partly re-emitted in form of fluorescence or phosphorescence [110].

Biological tissue is mainly composed of three absorbers: hemoglobin, melanin and water. Hemoglobin possesses two distinct forms having different absorption properties: oxygenated and deoxygenated hemoglobin. The apparent color of tissue hence depends on the combination of those absorbers. Absorption spectra for melanin, water, oxy and deoxy hemoglobin are depicted in Figure 2.5 for the ultra-violet to near-infrared wavelength range. Points of intersection between the two hemoglobin spectra are called isosbestic points. The spectral values in these points are insensitive to oxygenation changes of hemoglobin.

Equivalently to the attenuation coefficient, the scattering coefficient μ_s is defined as the probability of an incident photon being scattered after a unit path length of propagation in tissue. The non-scattered component $I(x)$ of light after traveling for a path

length x through a non-absorbing medium can also be described by the Beer-Lambert law [191]:

$$I(x) = I_0 \, \mathrm{e}^{-\mu_s x} \tag{2.2}$$

Scattering is defined as the redirection of the radiation of a photon [110] and mainly occurs when photons hit structures of similar dimension as the optical wavelength in presence of a refractive index mismatch between the structure and the surrounding medium. Light scattering in biological tissues therefore stems from its interaction with cells, cell membranes and subcellular structures [120].

The angular probability of a photon traveling along direction s being scattered into direction s' is given by the scattering phase function (SPF) which is a function of the cosine of the scattering angle $(\hat{s}, \hat{s}') = \cos\theta$, i.e.

$$p(\hat{s}, \hat{s}') = f(\cos\theta) \tag{2.3}$$

Since the SPF can be difficult to calculate, an approximation often used is the Henyey-Greenstein phase function [188]:

$$p(\cos\theta) = \frac{1}{2} \frac{1 - g^2}{(1 + g^2 - 2g\cos\theta)^{\frac{3}{2}}} \tag{2.4}$$

The Henyey-Greenstein function is a convenient approximation because it is parameterized by the anisotropy factor g, which is the average cosine of the scattering angle θ:

$$g = \int_{-1}^{1} \cos\theta \, p(\cos\theta) \, \mathrm{d}\cos\theta \tag{2.5}$$

Anisotropy is a measure of directionality retained after a single scattering event. It allows the description of highly forward scattering media ($g \cong 1$), highly backward scattering media ($g \cong -1$) and isotropic scattering ($g = 0$). Biological tissues are typically strongly forward scattering and have anisotropy values in the range between 0.8 and 0.99 [188].

The reduced scattering coefficient μ_s' is defined as

$$\mu_s' = \mu_s(1 - g) \tag{2.6}$$

and describes the equivalent isotropic scattering coefficient in a medium, i.e. the isotropic scattering in average as approximation by many anisotropic steps.

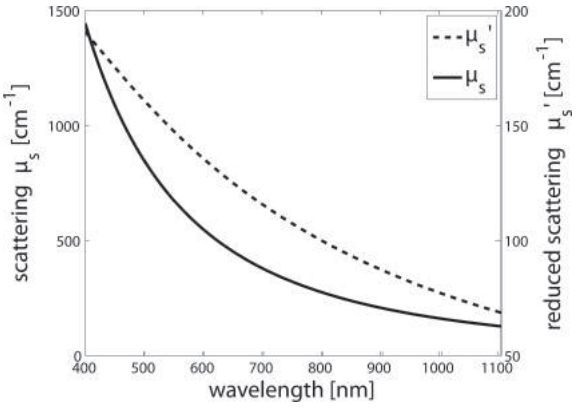

Figure 2.6: Scattering and reduced scattering coefficients of 10%-intralipid. Data for figure extracted from [185].

The average distance that a photon travels between consecutive scattering events is given by $1/\mu_s$ and is called the scattering mean free path. In contrast, $1/\mu_s'$ represents the distance traveled by a photon packet before it becomes effectively isotropic. This property can describe the diffusion of photons in a random walk of step size $1/\mu_s'$ and is called reduced scattering mean free path.

Tissue scattering properties are wavelength dependent. Typically, an exponential drop with increasing wavelength can be observed within the visible and near-infrared spectral range. This is shown in Figure 2.6 using the example of 10%-intralipid, an aqueous suspension of lipid droplets that is customarily employed to mimic tissue scattering in phantoms. Note that the shape of the scattering and reduced scattering coefficients represent the general wavelength dependence of scattering in tissue, but that absolute scattering strength is significantly lower in real tissue (by a factor of approximately 5 to 20).

The total attenuation coefficient for a medium exhibiting absorption and scattering is defined as

$$\mu_t = \mu_a + \mu_s \tag{2.7}$$

and the transport attenuation coefficient as

$$\mu_{tr} = \mu_a + \mu_s' \tag{2.8}$$

Tissue	Wavelength	Reduced scattering coefficient μ_s' [cm^{-1}]	Absorption coefficient μ_a' [cm^{-1}]
Skin	633 - 800 nm	30 - 6	0.96 - 0.024
Brain, Cortex	674 - 956 nm	10 - 8	0.25 - 0.1
Breast	630 - 800 nm	13 - 9	0.046 - 0.017
Lung	780 nm	20	0.02
Upper torso	750 nm	20	0.25
Lower torso	750 nm	15	0.5

Table 2.1: Exemplary values for typical optical properties of biological tissues. As indicated in the first three rows, scattering and absorption decrease with increasing wavelength. Extracted from References [110, 188].

Accordingly, the mean free path in an absorbing and scattering tissue is given by [134]

$$MFP = \frac{1}{\mu_t} \tag{2.9}$$

and the transport mean free path by

$$TMFP = \frac{1}{\mu_{tr}} \tag{2.10}$$

Scattering in most biological tissues dominates over absorption, i.e. $\mu_s \gg \mu_a$ and $\mu_s' \gg \mu_a$. Therefore, μ_t and μ_{tr} in 2.9 and 2.10 can be replaced by μ_s and μ_s', respectively. An equation describing the relation between MFP and $TMFP$ is then obtained:

$$MFP = TMFP(1-g) \tag{2.11}$$

An intuitive interpretation of 2.11 would be that for high values of g (i.e. forward scattering) light will have to travel longer before becoming diffuse [134].
Typical values for μ_a and μ_s' are given in 2.1.

Figures 2.5 and 2.6 together with Table 2.1 summarize the challenges optical imaging is subjected to due to light-tissue interactions. Penetration of light into tissues in the visible part of the spectrum is relatively low due high oxy and deoxy hemoglobin absorption. Penetration depth at wavelengths above 1300 nm in turn is limited by the absorption of water. The wavelength range between 600 nm and 1300 nm has become known as therapeutic window in which absorption is relatively weak and hence penetration depth up to several cm can be reached. However, within the therapeutic window scattering becomes dominant over absorption [188]. This results in light diffusion.

Although scattering also decreases in the near-infrared compared to the visible wavelength range, it still affects imaging in both regions considerably. Scattering leads to degradation of image resolution with increasing sample thickness due to the blurring effect of diffused light. Methods for rejecting scattered light have been developed for microscopic imaging and resulted in confocal and two-photon microscopy, which can image deeper and at higher resolution than traditional microscopy. However, these modalities are still limited to a penetration depth of several hundreds of micrometers. When it comes to deep tissue imaging, scattering plays a fundamental role on the appearance of the detected signals. The separation of effects originating from scattering and absorption becomes an ill-posed problem. Accurate light propagation models have been developed in order to extract useful information from such a diffusive imaging regime. Nevertheless, deep-tissue optical imaging usually comes at the expense of imaging resolution.

2.2.3 Fluorescence and its application for contrast generation in biomedical research

A fluorochrome is a molecule or chemical compound that emits photons in form of fluorescence upon excitation with light. The spectral characteristics of a fluorochrome are determined by its quantum properties. A wide range of transitions from various vibrational energy levels of the ground state to different vibrational levels of the excited states are typically allowed. These have different degrees of probability and ultimately combine to form the absorption spectrum of the fluorochrome. Similarly, transitions from the lowest excited state to different vibrational energy levels of the ground state are possible. This produces a wide range of photon energies and results in emission over a band of wavelengths rather than at one single wavelength. Most fluorochromes have distinct absorption and emission spectra, which may partly overlap. Examples of some widely employed fluorescent proteins and their characteristic absorption and emission spectra are shown in Figure 2.7.

Macroscopically, fluorescence processes can be characterized by their quantum yield, absorption coefficient (wavelength dependent) and fluorescence lifetime [110, 188]. The quantum yield η is defined as the ratio of the number of fluorescence photons

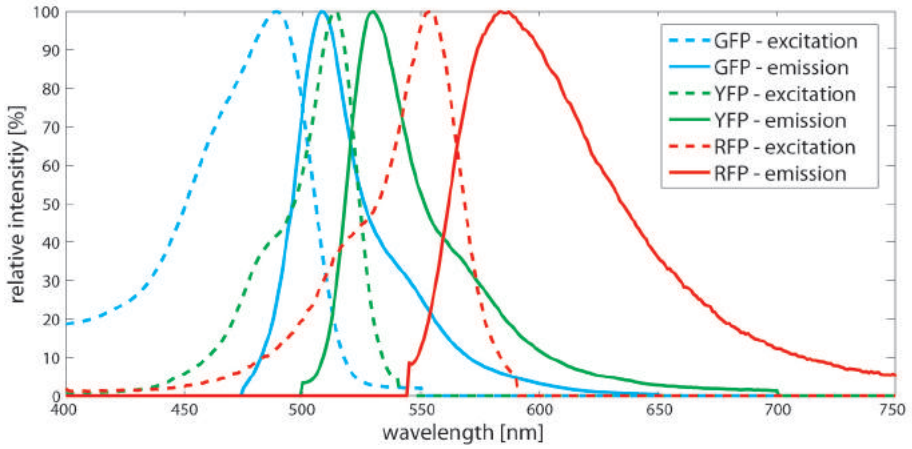

Figure 2.7: Excitation spectra of some of the most frequently used fluorescent proteins: GFP (green fluorescent protein), YFP (yellow fluorescent protein) and RFP (red fluorescent protein). Data for figure extracted from [116]

emitted $N_{emitted}$ to the number of photons absorbed $N_{absorbed}$, i.e.

$$\eta = \frac{N_{emitted}}{N_{absorbed}} \tag{2.12}$$

and gives the efficiency of the fluorescence process. A quantum yield of 1 would mean that photon absorption always leads to a photon emission.
The absorption coefficient $\mu_{a,fluo}$ at excitation wavelength λ_{ex} is given as

$$\mu_{a,fluo}(\lambda_{ex}) = \varepsilon \cdot \ln(10) \cdot C_{fluo} \tag{2.13}$$

where ε is the molar absorptivity of the fluorochrome and C_{fluo} is the fluorochrome concentration. The observable fluorescence emission intensity depends on the absorption coefficient at the excitation wavelength and the quantum efficiency of the fluorochrome.
The third important characteristic feature of fluorescence is its lifetime τ_{fluo}. It gives the decay of fluorescence after excitation with a short light pulse and depends on the time spent in the excited state, i.e.

$$\tau_{fluo} = \frac{1}{k_r + k_{rn}} \tag{2.14}$$

where k_r and k_{nr} are the rate constants of radiative and non-radiative transitions, respectively. For an excitation at time t_0 leading to an initial fluorescence intensity $I(t_0)$, the fluorescence intensity $I(t)$ at a later time t is given by [110, 187]:

$$I(t) = I(t_0) \cdot \frac{1}{\tau_{fluo}} \cdot \mathrm{e}^{-\frac{t-t_0}{\tau_{fluo}}} \tag{2.15}$$

Fluorescence lifetime is characteristic to the molecules and their chemical environment [156].

Fluorescence is particularly interesting to biomedical optical imaging research. That is because fluorescence dyes may be attached to specific molecules of interest to target molecular processes or visualize structural entities that are otherwise imperceptible.
If the observed property of a target of interest is not sufficiently different from that of the surrounding medium, extrinsic substances can be introduced into the body to artificially enhance or create contrast [156]. These so called contrast agents identify the location of specific molecules and report on their presence through their characteristic contrast mechanism. Different medical imaging fields employ contrast agents as a standard feature, as discussed in Chapter 1 in the context of molecular imaging. An example is the injection of iodine into the blood stream to detect blood vessels with X-ray imaging. Blood and surrounding soft tissue display similar X-rays absorption properties and can therefore not be distinguished in normal X-ray applications. Iodine, in contrast, is a strong X-ray absorber and its injection greatly enhances the differentiation capability between vasculature and soft tissue. In this case, the contrast mechanism is reporting on structural properties of the imaged object.
Molecular properties can be investigated by designing contrast agents that specifically bind to certain molecules. One prominent medical imaging modality capitalizing on this contrast mechanism is PET. For example, $[^{18}F]$-FDG is injected into a patient and is accumulated at sites of high metabolic activities. Because tumors often display increased metabolic activity compared to surrounding, non-diseased tissue, they have a higher demand for energy. $[^{18}F]$-FDG therefore accumulates in the tumor region and this accumulation can be detected with PET.

Similarly, biomedical optical imaging employs fluorescence to increase contrast on structural, functional or molecular level. There are two major fluorescence reporter strategies that are classified as direct and indirect methods [133].
Direct methods employ injectable fluorescent probes that can be used to selectively highlight internal organs, tumors or molecular processes [193]. The probes can be categorized into three subgroups. Figure 2.8 visualizes and compares the three labeling concepts (columns) for direct fluorescence imaging in terms of labeling mechanism (1st row), fluorochrome biodistribution (2nd row) and resulting contrast (3rd row).
The first group represents the majority of injectable probes and consists of non-targeted, i.e. non-specific, fluorescent agents. They distribute in different body compartments

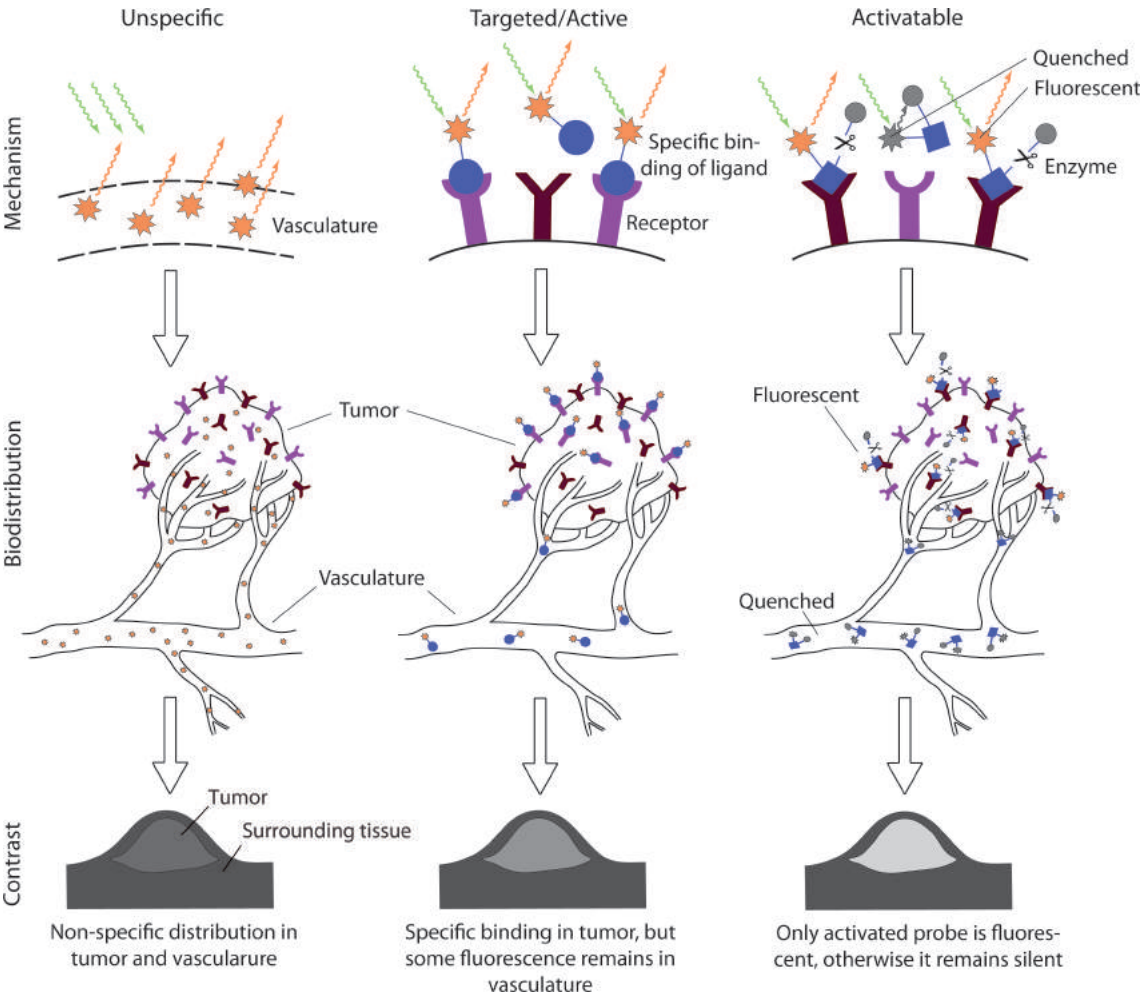

Figure 2.8: Comparison of different direct imaging fluorescent probe labeling concepts. Green arrows represent excitation light, orange arrows fuorescence emission. Partly adapted and modified from [130, 133, 193].

and report on physiological processes like blood flow and perfusion. Two of the best known non-targeted fluorescence probes are fluorescein (FITC) and indocyanine green (ICG). They are also two of the few fluorescence probes that are approved to be used in human medicine, where they are customarily employed in retinal angiography [10] or intraoperative imaging for tumor detection [184]. In animal studies, non-targeted probes may for example be employed for the detection of angiogenesis in tumors, or blood vessel leakage as a result of inflammation [103, 170].

The other two categories of fluorescence probes are designed to target specific antibodies, receptors or enzymes. Targeted probes are further divided into active and

activatable probes. Active probes consist of a fluorochrome that is attached to an affinity ligand specific for a certain target (therefore often called targeted probes) [133]. As their name implies, the characteristic of active probes is that they fluoresce even when they are not bound to the intended tissue target, i.e. they are always active. This may result in significant background signal from the unbound probe that is still present in the blood stream. Conversely, activatable probes carry quenched fluorochromes (i.e. their fluorescence is suppressed) that can only be activated in the presence of a specific enzyme of interest. These sensors increase signal-to-noise ratios because they remain dark in the absence of the tissue target, thus reducing background contributions to the detected signal. In contrast to the isotope tracers used in PET, fluorescent targeted probes are not yet applied to *in-vivo* human medicine but are still restricted to pre-clinical research. They have however found wide applications in small animal studies as imaging labels for the detection of tumors, inflammation, apoptosis and many other diseases (e.g. [5, 139]). One important aspect in fluorescent probe design for *in-vivo* imaging applications is the use of fluorochromes that absorb and emit light in the NIR, where light penetrates deepest [133].

Indirect fluorescence imaging visualizes gene expression and regularization by quantification of fluorescent protein presence. A reporter gene (transgene) is introduced into the cell and its transcription leads to the intrinsic production of a fluorescent protein by the cell [133]. Therefore, it indirectly reports on gene expression and regulation. Whole cells can be transfected to track their location or the transgene can be placed under a promoter for studying regulation. Furthermore, the fluorescence encoding gene can be fused to a gene of interest thus enabling the visualization of virtually every protein [133]. One of the most commonly used fluorescent proteins is green fluorescent protein (GFP) but several color shifted variants have become equally common during the past years. Efforts to produce fluorescence proteins in the NIR are ongoing and have shown continuous progress [166], but do still not belong to the standard toolbox for transgenic animal production. The use of transfected animals is therefore often restricted to *in-vitro* tissue investigations or to *in-vivo* experiments in very superficial tissue layers.

Figure 2.9 presents two different approaches to genetically encoded production of fluorescence. The first shown in Figures 2.9(a) illustrates the production of genetically modified animal lines by introduction of an indicator gene into the fertilized egg. The egg is then transplanted into a foster mouse resulting in offspring that have the gene randomly inserted into their genome [105]. Purely genetically modified mouse lines (F2) can be

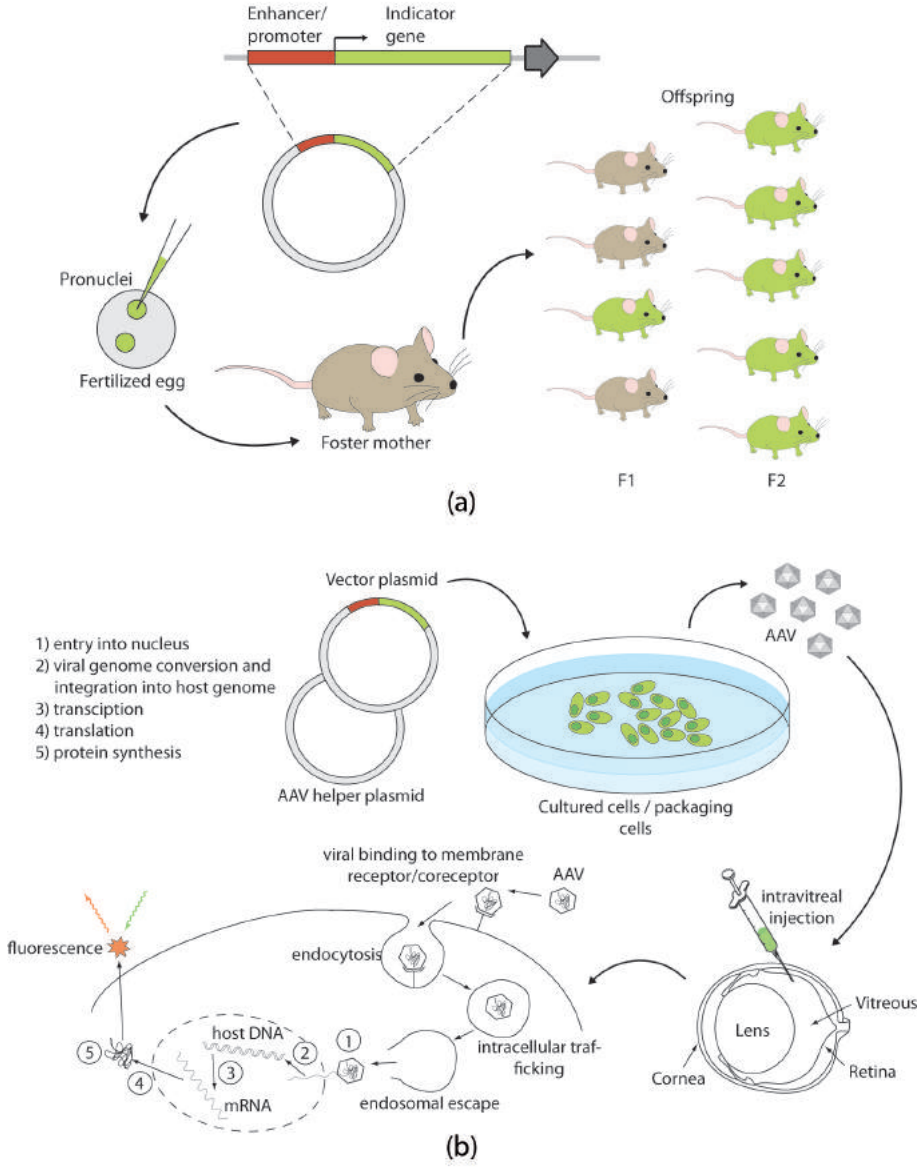

Figure 2.9: Fluorescence labeling approaches for indirect imaging. (a) Production of transgenenic mice by breeding. Adapted from [105]. (b) Transfection through local incorporation of viral vectors. Compiled and adapted from [105, 143, 190].

created by propagating the transgenic offspring from the first generation (F1). As a results of this approach, every cell or protein that is regulated by the respectively modified gene produces fluorescence in the transgenic mouse line. The second approach locally introduces a modified gene into an animal by viral vectors and hence only transfects cells in the injection area. The effect of transfection can be observed in the same animal days to weeks after transfection. Depending on the regulatory sequences included, the indicator

is expressed in specific cell classes [105]. The process of viral transfection is depicted in Figure 2.9(b) from culturing of adeno-associated viruses (AAV), over injection into a tissue of interest, here the eye, to the transfection of the cells in the respective tissue.

2.3 Models of light transport in tissue

This section introduces to two light-tissue interaction modeling concepts, based on the radiative transport equation. General aspects of the diffusion equation and Monte Carlo modeling are discussed. An implementation of the diffusion equation was used for the work presented in Chapter 4 and will be discussed in more detail there. Monte Carlo simulation was not used for this thesis, nevertheless the understanding of its concepts is fundamental for the discussions in Chapter 3.

2.3.1 Radiative transport theory

The most widely applied equation for describing photon transport in biological tissue is the radiative transport equation (RTE) [9]. It is based on a particle interpretation of light, therefore ignoring electromagnetic wave properties such as polarization and interference [9]. This is justified because multiple scattering events lead to decoherence effects in turbid media which in turn leads to the suppression of the wave nature of light [188]. Instead of tracking light waves, it suffices to track only the average energy they contain [188]. The RTE further only considers elastic scattering events, which means that the energy of non-absorbed photons always stays the same. In spite of these assumptions, RTE has proven to be sufficient to describe light - tissue interactions for many biomedical imaging applications.

The fundamental quantity in the radiative transfer model is the radiance $L(\vec{r},\hat{s},t)$ [$\mathrm{Wm^{-2}sr^{-1}}$], which can be defined by the following relationship:

$$dE = L(\vec{r},\hat{s},t)(\hat{s},\hat{n})\mathrm{d}A\mathrm{d}\Omega\mathrm{d}t \tag{2.16}$$

where $\mathrm{d}E$ is the amount of radiant energy at point $\vec{r}$ that is transported during differential time $\mathrm{d}t$ in the direction defined by the unit vector $\hat{s}$ across differential area element $\mathrm{d}A$ normal to $\hat{n}$ within differential solid angle element $\mathrm{d}\Omega$. (See Figure 2.10 for a

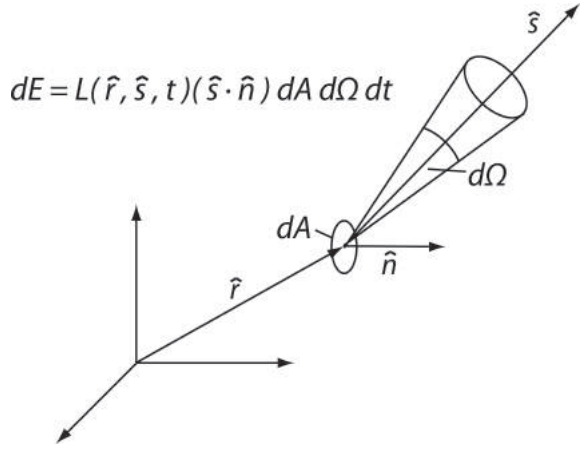

Figure 2.10: Radiant energy at point $\vec{r}$ that is transported in direction $\hat{s}$ across differential area element $\mathrm{d}A$ normal to $\hat{s}$ within differential solid angle element $\mathrm{d}\Omega$. Adapted from [188]

visualization of the energy flow and the involved variables.)

The RTE is derived from the principle of conservation of energy and describes the fundamental dynamics of the radiance $L(\vec{r},\hat{s},t)$ at time t and position $\vec{r}$ along propagation direction $\hat{s}$ [191]:

$$\frac{1}{c}\frac{\partial L(\vec{r},\hat{s},t)}{\partial t} = -\hat{s}\cdot\nabla L(\vec{r},\hat{s},t) - \mu_t L(\vec{r},\hat{s},t) + \mu_s \int_{4\pi} L(\vec{r},\hat{s}',t)p(\hat{s}',\hat{s})\mathrm{d}\Omega' + S(\vec{r},\hat{s},t) \quad (2.17)$$

μ_t $[\mathrm{cm}^-1]$ is the total attenuation coefficient and $p(\hat{s}',\hat{s})$ is the phase function, as respectively defined in Equations 2.7 and 2.3. As $p(\hat{s}',\hat{s})$ describes a probability density function we have $\int_{4\pi} p(\hat{s}',\hat{s})\mathrm{d}\Omega' = 1$. c is the speed of light and $S(\vec{r},\hat{s},t)$ represents radiance created by internal sources at position $\vec{r}$ along $\hat{s}$.

The rate of change of the photon radiance in Equation 2.17 (1^{st} term) is dependent on the energy diverging from point $\vec{r}$ (2^{nd} term), losses due to absorption and scattering (3^{rd} term) and gain due to photons scattered into $\mathrm{d}\Omega$ around $\hat{s}$-direction (4^{th} term) and local radiation sources at $\vec{r}$ (5^{th} term).

The RTE is mathematically difficult to solve. Simplified methods that still retain functionality have therefore been derived from the RTE. These are either based on stochastic or deterministic approaches. The most prominent examples will be introduced in the next sections.

2.3.2 The deterministic approach: Diffusion approximation

A simpler deterministic model that is derived from the RTE is the diffusion approximation. The diffusion approximation assumes both scattering and internal sources to be isotropic. It is obtained by expanding the radiance to a series of spherical harmonics and retaining only a limited number of terms. Only considering the first order spherical harmonics expansion results in the P1 approximation. The expansion of the radiance can then be written in terms of photon fluence rate $\Phi(\vec{r}t)$ and photon current density $\vec{J}(\vec{r},t)$

$$L(\vec{r},\hat{s},t) = \frac{1}{4\pi}\Phi(\vec{r},t) + \frac{3}{4\pi}\vec{J}(\vec{r},t)\cdot\hat{s} \tag{2.18}$$

with

$$\Phi(\vec{r},t) = \int_{4\pi} L(\vec{r},\hat{s},t)\mathrm{d}\Omega \tag{2.19}$$

and

$$\vec{J}(\vec{r},t) = \int_{4\pi} \hat{s}L(\vec{r},\hat{s},t)\mathrm{d}\Omega \tag{2.20}$$

Substituting Equation 2.18 into the RTE (Equation 2.17) and integrating over all 4π solid angles leads to

$$\frac{1}{c}\frac{\partial\Phi(\vec{r},t)}{\partial t} = -\nabla\vec{J}(\vec{r},t) - \mu_a\Phi(\vec{r},t) + S(\vec{r},t) \tag{2.21}$$

where $S(\vec{r},t)$ is the isotropic source. Substituting Equation 2.18 into the RTE (Equation 2.17) and multiplying with $\hat{s}$ prior to integration over all 4π solid angles leads to

$$\frac{1}{c}\frac{\partial\vec{J}(\vec{r},t)}{\partial t} + (\mu_a+\mu_s')\vec{J}(\vec{r},t) + \frac{1}{3}\nabla\Phi(\vec{r},t) = 0 \tag{2.22}$$

Assuming the fractional change in $\vec{J}(\vec{r},t)$ within the transport mean free path small, we can neglect the time-dependent term in Equation 2.22, which results in Fick's law of diffusion

$$\vec{J}(\vec{r},t) = -D\nabla\Phi(\vec{r},t) \tag{2.23}$$

where D is the diffusion coefficient, defined as

$$D = \frac{1}{3(\mu_a+\mu_s')} \tag{2.24}$$

Substituting Equation 2.23 in Equation 2.21 directly yields the inhomogeneous diffusion equation

$$\frac{1}{c}\frac{\partial\Phi(\vec{r},t)}{\partial t} - \nabla D\nabla\Phi(\vec{r},t) + \mu_a\Phi(\vec{r},t) = S(\vec{r},t) \tag{2.25}$$

which reduces in a time-independent state to

$$-\nabla D\nabla\Phi(\vec{r})+\mu_a\Phi(\vec{r})=S(\vec{r}) \tag{2.26}$$

Analytical solutions to the diffusion equation are scarce and have been obtained for only very simple cases [9]. Generally, solving a partial differential equation (PDE) which involves a source condition is done by the application of Green functions, which are a solution when the source is a delta function [9]. For instance, for the simple case of an infinitely short-pulsed point source $S(\vec{r}',t')=\delta(\vec{r}',t')$ in an infinite homogeneous scattering medium, the fluence rate $\Phi(\vec{r},t)$ at position $\vec{r}$ and time t is:

$$\Phi(\vec{r},t;\vec{r}',t')=\frac{c}{[4\pi Dc(t-t')]^{3/2}}\,\mathrm{e}^{\frac{-|\vec{r}-\vec{r}'|^2}{4Dct}-\mu_a c(t-t')} \tag{2.27}$$

For a time-independent state the analytical solution is given by:

$$\Phi(\vec{r};\vec{r}')=\frac{1}{4\pi Dc|\vec{r}-\vec{r}'|}\,\mathrm{e}^{-\sqrt{\frac{\mu_a}{D}}|\vec{r}-\vec{r}'|} \tag{2.28}$$

Due to the difficulty of finding analytical solutions for arbitrarily shaped geometries and inhomogeneous media, practical implementations employ numerical methods. The most common methods are finite difference (FDM) and finite element methods (FEM). Finite difference approaches are solved on cartesian meshes, which pose complications in the accurate representation of the tissue boundaries. For FDM the diffusion equation is simply discretized into three points for the x, y, z coordinates, and the fluence at each location calculated by a straight forward approximation of the derivative by a finite difference [91]. The FEM is more versatile in regard to complex geometries and for modeling boundary effects [9]. In contrast to FDM, elements have arbitrary shapes and are connected by nodes. FEM finds an approximate solution of the discretized general problem that lies in the vector space spanned by a finite number of basis functions. This reduces the forward problem to one of matrix algebra of finite size [9].

2.3.3 The stochastic approach: Monte Carlo Modeling

The Monte Carlo (MC) method for modeling of light propagation in tissue follows a stochastic approach that explicitly describes individual photon interactions. Photons are simulated as they undergo scattering and absorption events governed by local values of optical parameters [9]. Light is considered to travel in straight lines between different

scattering and absorption events. Random number generators are used to simulate the change of direction that occurs at each scattering event in accordance with the scattering phase function p [156]. Photons are injected into a medium and are traced until they get absorbed or escape the surface as reflection or transmission, thus contributing to a measurement [9]. The repetition of this tracking process for a large number of photon packages yields statistically relevant information on macroscopic photon distributions. The result is a set of different trajectories that are averaged to determine the reflectance or transmittance of the medium.

The MC method defines rules for photon propagation from the probability distribution of the angles of scattering and step sizes [191]. These are derived from macroscopic values of absorption and scattering coefficient, and the scattering phase function [58]. The sampling method repeatedly derives a variable χ lying within an interval (a,b) based on its probability density function $p(\chi)$ by generation of random numbers ξ uniformly distributed between 0 and 1. The approach, known as inverse distribution method (IDM) [191], samples χ by solving

$$P(\chi) = \int_a^{\chi} p(\chi)\mathrm{d}\chi = \xi \tag{2.29}$$

where $P(\chi)$ is the cumulative distribution function. Its inverse transformation is given by

$$\chi = P^{-1}(\xi) \tag{2.30}$$

Equation 2.30 correctly samples χ if $P(\chi)$ is uniformly sampled by ξ between 0 and 1. For better demonstration purposes Figure 2.11 offers a visual interpretation of the IDM. The arrows show the mapping from $p(\xi)$ (blue function and axes) to $p(\chi)$ (green function and axes) via $P(\xi)$ and $P(\chi)$.

The free path length of a photon between two interactions, the step size s, is calculated based on the probability density function

$$p_s = \mu_t \, \mathrm{e}^{-\mu_t s} \tag{2.31}$$

the cumulative probability of which is given by

$$\int_0^s \mu_t \mathrm{e}^{-\mu_t s'} \mathrm{d}s' = 1 - \mathrm{e}^{-\mu_t s} = \xi \tag{2.32}$$

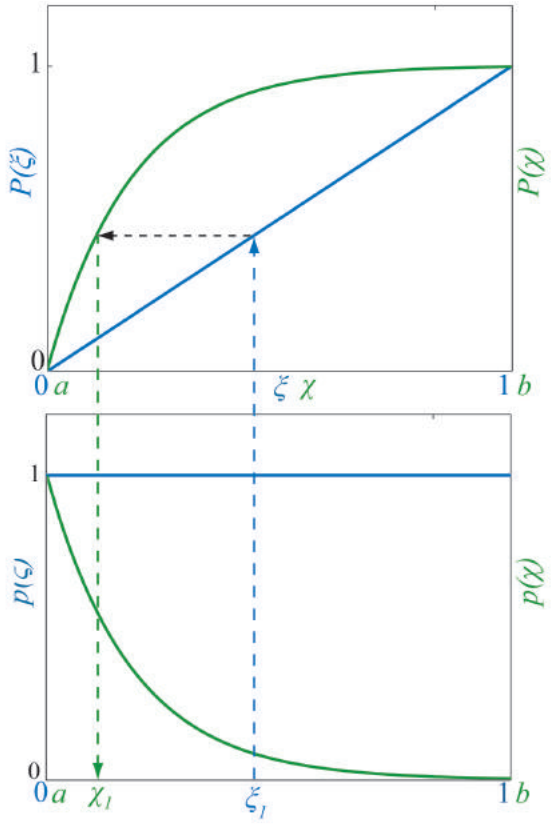

Figure 2.11: Inverse distribution method (IDM) for sampling of a random variable from a non-uniform distribution. Adapted from [191]

where $\xi \in [0...1]$ is a random number. Therefore, the step size can be randomly sampled as

$$s = -\frac{1}{\mu_t}\ln(1-\xi) = -\frac{\ln(\xi)}{\mu_t} \tag{2.33}$$

Once the step size is determined, the photon packet can be moved. When it reaches an interaction site, absorption and/or scattering can occur. Absorption is modeled by introducing a weighting scheme. A fraction $\triangle W$ of weight $W \in [0\ldots1]$ is absorbed at every interaction event according to

$$\triangle W = \frac{\mu_a}{\mu_t} W \tag{2.34}$$

W is updated after every such step, i.e. $W \leftarrow W - \triangle W$.

To model scattering, the polar angle $\theta[0 \leq \theta \leq \pi]$ and azimuthal angle $\phi[0 \leq \phi \leq 2\pi]$ are sampled relative to the previous direction of motion. The probability distribution of $\cos\theta$ is commonly given by the Henyey-Greenstein phase function (see Equation 2.4).

Monte Carlo simulation accordingly samples $\cos\theta \in [-1\ldots1]$ as follows:

$$\cos\theta = \begin{cases} \frac{1}{2g}\{1+g^2-(\frac{1-g^2}{1-g+2g\xi})^2\} & \text{if } g \neq 0 \\ 2\xi - 1 & \text{if } g = 0 \end{cases} \tag{2.35}$$

The azimuthal angle is sampled as

$$\phi = 2\pi\xi \tag{2.36}$$

As in Equation 2.29, $\xi \in [0\ldots1]$ represents a random number. The photon paths are finally terminated when either the weight becomes negligible or the photon leaves the boundary. In the latter case and if the photon hits the detector the photon weight is saved and contributes to the simulated diffuse signal [58].

Monte Carlo is based on the RTE and similarly considers only particle aspects of light and neglects wave phenomena. Compared to the diffusion approximation, MC simulations do not require that $\mu_s' \gg \mu_a$ and accurate results can be obtained close to sources and boundaries [84]. Other advantages of MC simulation include the ability to model transport processes in arbitrary geometries, in the presence of inhomogeneities and with complex boundary conditions. A major drawback is the long computational times required to obtain good statistics. This is especially true if the point of interest is located very far from incident light and absorption and scattering are high [201].

2.4 Application areas of imaging spectroscopy versus light transport models

Traditionally, the fields of imaging spectroscopy and diffuse optical imaging (including the appropriate modeling approach) were separate research areas.
Originating in remote sensing, imaging spectroscopy was previously mainly applied to reflectance imaging of surfaces which are not strongly influenced by subsurface interactions with light, like for instance in microscopy. Hence, typical application areas were in *ex-vivo* investigations.
Equivalently, diffuse optical modeling approaches were mainly applied to investigate one or few spectral regions, i.e. one fluorochrome, or 2 to 3 wavelengths for oxygen saturation detection. Hence, typical diffuse optical imaging implementations, although operating *in-vivo*, mainly investigated one single molecular marker.

Recently, combined approaches integrating light-tissue interaction modeling with multi-spectral data acquisition, and the development of appropriate computational methodologies were presented. Such approaches were for instance developed for surface investigations in skin. There, spectroscopic images were used combined with models of light propagation through different skin layers to extract disease specific parameters [98]. Alternatively, tomographic imaging of fluorescence distributions employing multi-spectral sources or detectors has been attempted. Multispectral data in tomography was in this case used for the correction of the influence of autofluorescence [43] or for quantification of probe binding [42]. However, all these approaches mainly aimed at improving the acquisition of one or few parameters *in-vivo* by employing multispectral methods. They did not aim at acquiring multiple readings of spectral properties originating in separate components.

Whether and how optical properties influence the accurate detection of multiple molecules in *in-vivo* applications of optical imaging always depends on the imaging context. Some surface imaging applications may not necessarily need to account for the influence of optical properties, like for instance retinal angiography. There, all relevant optical contrast is produced within 300 hundreds of micrometers from the surface. Hence, *in-vivo* multispectral imaging of shallow fluorescence signals can be treated similarly as *ex-vivo* multispectral cases. When it comes to deeper seated fluorescence signals or intrinsic tissue chromophores, influences of surrounding optical properties have to be considered either by modeling or development of alternative correction methods.

3 Multispectral methods for multi-molecular surface imaging

Chapter 2 introduced to the fundamental concepts of multispectral imaging and light-tissue interaction and modeling. In the light of these fundamental properties and the discussed considerations for surface versus volumetric imaging, implementations of multi-molecular imaging technology for *in-vivo* applications can take various forms. This it not surprising given the multitude of potential application areas (e.g. surface: skin, retina, surgical guidance etc.; volumetric/deep seated: cancer, inflammation, infections etc.). This thesis covers research conducted on three approaches for multispectral or multi-molecular imaging in living subjects. Two approaches investigated different concepts for epi-illumination imaging of surfaces and will be subject of this chapter. The third approach investigating volumetric imaging will be subsequently discussed in Chapter 4.

This chapter presents two practical implementations of systems for epi-illumination multispectral imaging, which were developed within the scope of this thesis. While both systems rely on the same spectral detection approach, i.e. filter based scanning, illumination concepts and acquisition optics differ due to the respectively intended application area. The overall goal was to develop systems and methods for (1) quantitative imaging of tissue oxygenation from arbitrary tissues based on multispectral images and (2) for imaging of multiple fluorochrome expression in the mouse retina. In the latter case, the retina was chosen to exemplify the translation of multispectral concepts to *in-vivo* research.
Section 3.1 introduces to the respective background for both application areas. Previous research and state of the art in oxygenation imaging, and multi-fluorochrome imaging in living subjects, with particular focus on retinal imaging, are discussed.
Subsequently, Section 3.2 presents the systems developed within the scope of this thesis and defines their respective characteristics. First, the non-contact multispectral system for

oxygenation imaging is introduced, followed by the multispectral mouse fundus camera. General commonalities of multispectral systems are outlined as well as the particular individual system requirements for specific application areas.
Multispectral image processing is addressed in Section 3.3. A linear mixing model is introduced that describes spectral images as a mixture of individual spectral contributions of each imaged component. Theoretical concepts for the recovery of original spectral components by linear unmixing, blind source separation (BSS) and pixel classification are subsequently presented. This section provides the fundamental background necessary for the comprehension of the image processing and analysis steps presented in the remaining of this chapter.
Sections 3.4 and 3.5 present the application of unmixing and/or classification methods to oxygenation and multi-fluorochrome detection scenarios, respectively. Section 3.4 in particular shows the development of a spectral transformation method correcting for the effects of optical properties on measured oxygenation spectra. This methods allows for quantitative oxygenation computation by linear unmixing of the transformed spectra. The imaging potential of the multi-spectral fundus camera is evaluated in Section 3.5. First, assessment of single fluorochromes and changes in their expression are illustrated. Then, BSS techniques and classification are evaluated as to their potential to separate overlapping fluorochrome spectra acquired *in-vivo* from the mouse retina.
The chapter closes with a summary of the presented concepts and an outlook on potential application of multispectral surface imaging in future.

The work presented in this chapter has resulted in two manuscripts, one in preparation and one submitted, to be published in peer-reviewed scientific journals (See list of publications, papers VI and VII.). Several figures and text passages were adopted from these manuscripts.

3.1 Introduction to multispectral imaging of intrinsic and extrinsic tissue contrast

3.1.1 Tissue oxygenation imaging

Tissue oxygenation and vascular oxygen saturation are important indicators of physiology and the viability of human tissues and organs [17, 25, 33, 77, 78, 98, 132]. Perturbation of

oxygenation from physiological values is a strong indication of systemic or local disease and has significant implications to the functioning of tissues and organs [77, 102, 176]. Accurate assessment of tissue or vascular oxygenation is therefore of great significance in the clinical environment.

Oxygen binds to hemoglobin molecules present in red blood cells and is by this means transported and delivered to the body. Oxygen saturation is a relative measure of the percentage of hemoglobin that has an oxygen molecule bound (oxygenated hemoglobin) compared to the total amount of hemoglobin (oxygenated + deoxygenated hemoglobin). Arterial blood has typical oxygen saturation values of 95 - 98 % and venous blood of 60 - 80 %. As previously shown in Chapter 2, oxygenated and deoxygenated hemoglobin are the two major absorbers of light in tissues [45]. Optical methods are therefore ideal candidates for characterizing oxygenation because oxy and deoxy hemoglobin detection can be performed without labels.
While arterial oxygenation is customarily measured in clinical settings using pulse oximetry [164], measurements of tissue oxygenation and the ability to image tissue oxygenation is more elusive. Optical imaging methods have been proposed for oxygenation measurements since the 70's. First attempts employed near infrared spectroscopy (NIRS) to measure cerebral oxygenation [31, 94, 186]. Extension of spectroscopy approaches to systems consisting of multiple illumination points and detectors in the 90's enabled NIR spectroscopic tomography. Tomographic NIRS systems have since been employed to resolve brain, muscle and tumor oxygenation [26, 79, 159, 202].

Chapter 2 discussed the challenge of quantifying oxy and deoxy hemoglobin in tissues due to photon scattering. Scattering increases the path length of photons traveling through tissue, thus resulting in increased attenuation and diffusion of transmitted or reflected light (see for instance [13, 45, 154, 171]). This hinders quantification of absorption properties in general and of oxygenation measurements in particular. Accurate knowledge of the reduced scattering coefficient is desirable to accurately quantify tissue absorption but can be difficult to obtain. Complications arise from mixed contributions of absorption and scattering on the detected signal, which generally make the recovery of scattering and its separation from absorption contributions an ill-posed problem.

Spectroscopic methods based on a source-detector pair, typically implemented with fibers that physically separate the illumination location from the detection location have shown promising results in resolving absorption from scattering tissue proper-

ties [20, 152, 211]. Correspondingly, imaging based on source-detector pairs has been considered to reveal the spatial distribution of oxygenation measurements [35, 136] but come with difficulties in interfacing multiple fiber pairs onto tissue. Imaging with non-contact source-detector pairs was also proposed for oxygenation imaging [28,36] but only showed the capability of measuring relative changes at comparatively low resolution.

A broad range of planar epi-illumination non-contact imaging methods based on photographic approaches using CCD cameras have been proposed for oxygenation imaging in diagnosis, monitoring and treatment [102, 176]. Images are obtained through optical filters and combine spatial and spectral information [98]. Planar epi-illumination wide-field camera measurements have been considered in imaging skin cancer [98], wound healing [99], retinal oxygenation in the context of diabetes [74], open surgery applications [60] and in endoscopic applications [16]. Besides the acquisition of images in non-contact mode, epi-illumination setup have the additional advantage of being able to acquire images in real time. Real-time oxygenation imaging can offer feedback on disease, abnormal physiology or organ viability as has for instance been studied in the context of laparoscopic renal donation [33] and heart surgery [132].

Different approaches have been proposed to derive functional tissue metrics using data obtained in planar epi-illumination by CCD cameras. Differences between the red and blue channels of an RGB camera have been shown to correlate to tissue oxygenation values [33], but only in a qualitative manner. Characterization of the effects of scattering changes would also be critical for better determining the accuracy of the method. For improving performance in resolving tissue oxygenation, the use of light propagation models has been considered. Such models may assume different skin layers [97, 204, 211] but make an assumption of constant scattering. Then they can solve for the tissue's absorption properties only [72, 97] but are prone to errors carried by the accuracy by which the scattering coefficient can be assumed known. Models that solve for both scattering and absorption have been also considered [204]. For example, continuous wave measurements at multiple wavelengths between 480 nm and 650 nm were inverted assuming a semi-empirical two-layer skin model predicting diffuse photon propagation [203, 204]. This approach accounted for melanin and hemoglobin absorption, scattering, layer thickness and internal reflections and found an estimate for these values by minimization of the error between prediction and simulated measurements. Errors of less than 5% were achieved in simulations assuming thin epidermal layers and low melanin concentrations. Errors increased with increasing layer thickness and melanin

concentration [205]. The method produced skin oxygenation measurements consistent with literature-based values but not yet in relation to the actual tissue imaged.

The use of spatially modulated light has been considered as an alternative method to improve on the ill-posed nature of solving for absorption and scattering using CW light. Structured illumination has been shown to extract tissue optical properties at a single wavelength [34], or measure oxygen saturation by using measurements at different wavelengths [60]. This approach has shown oxygenation measurement errors of less than 10% when measuring in a skin flap, bowel, and liver vascular occlusion experiments in pigs. For accurate operation, the method nevertheless requires calibration based on tissue mimicking phantoms and the generation of a lookup table.

An alternative approach for extracting tissue oxygenation is the use of isosbestic points that can compensate for scattering influences [17, 44, 73]. The advantage of this method over the structured illumination approach is that it can be applied without elaborate illumination and high computational requirements so it may be more appropriate for video-rate imaging.

An isosbestic point correction method was initially applied for measuring oxygen saturation in superficial arteries and veins, by retrieving the percentages of oxy and deoxy hemoglobin in whole blood [44]. The method assumed that oxy- and deoxy-hemoglobin in whole blood can be determined using only three measurements, two at isosbestic wavelengths and one at an oxygen sensitive wavelength. Corrections in two isosbestic points were assumed to be enough to account for the effects of scattering from the red blood cells and total hemoglobin concentration. Using a third isosbestic point, an alternative method was shown to additionally account for the influence of background tissue optical properties on the calculation of oxygen saturation, resulting in measurements of blood oxygenation *ex-vivo* [73].

Despite the demonstration on superficial blood-vessels or blood *ex-vivo*, the use of isosbestic methods for obtaining quantitative tissue saturation images *in-vivo* has not yet been demonstrated in other organs than the retina. Tissue measurements *in-vivo* present additional complexity compared to *ex-vivo* measurements or measurements of specific organs or structures. This is because tissue imaging comes with a wide variation of optical properties in the different organs and structures contained in the image. In addition, *in-vivo* tissue measurements are subject to more measurement errors, including

reduced signal-to-noise ratio compared to *ex-vivo* measurements which can be acquired with longer exposure (averaging) times, or measurement uncertainties due to tissue movement.

One of the aims set in this thesis was to identify a strategy for imaging tissue saturation *in-vivo*, using an isosbestic point method. A multispectral setup was developed and will be shown later, capable of acquiring up to 25 wavelength bands from any given surface. The investigation of different methods for a generalized approach for tissue saturation measurements *in-vivo*, employing data acquired with the multispectral setup, is then illustrated. The underlying hypothesis was that the employment of different isosbestic points and additional spectral transformations could increase the accuracy of the isosbestic method for imaging tissue saturation *in-vivo*. Therefore, the effect of introducing alternative isosbestic point combinations, distributed over a wider spectral range, additional transformations, and varying wavelength ranges for oxygenation computation is investigated. Finally, an optimized method that employs an ideal combination of isosbestic points, transformations and wavelengths is proposed.

3.1.2 Imaging of fluorescent labels

The detection of intrinsic tissue chromophores and fluorochromes (autofluorescence) is one application area of multispectral imaging. Such imaging strategies which do not employ labels to increase or create contrast are particularly adequate for clinical adaptation. Beyond their diagnostic potential, no contrast agent injection is required and related risks like allergy development against the contrast agent can be avoided. However, using only intrinsic tissue properties to investigate diseases or their therapy significantly limits the molecular targets that can be studied. Not all hallmarks of diseases display absorption characteristics that allow their nonambiguous identification and distinction from background. In such cases, introduction of additional contrast mechanisms is necessary in order to enable the observation of the desired target.

As introduced in chapter 1, molecular imaging modalities like PET work based on the injectable tracer principle. Similarly, fluorescence labels can be used in *in-vivo* optical imaging to visualize molecules, proteins, cells or organs (see Chapter 2). By capitalizing on the multispectral properties of light, multiple fluorescence labels can theoretically be employed simultaneously, providing multi-molecular read outs on molecular presence,

activation, expression, interaction etc. As can be expected, labeling with multiple fluorochromes is unfeasible in humans and falls into the domain of preclinical investigation. It nevertheless can be an important research tool for understanding disease progression and for the development of new, efficient and possibly personalized drugs.

A second topic in this chapter is therefore the development of hardware and methodology for *in-vivo* multispectral surface imaging of multiple fluorescent labels. In particular, the aim consisted in enabling the detection of a mix of molecular markers on a whole organ level *in-vivo* and at once. This approach contrasts other multispectral imaging approaches that have previously been applied to biological investigations which focus mainly on microscopic imaging of tissue slices [59, 118, 210] or macroscopic imaging of whole animals [82, 106, 111].

It was previously mentioned that the most common application of multispectral imaging in life sciences is in microscopy. Staining of biological samples with color or fluorescence dyes is a standard procedure in pathology. The development of multispectral illumination or detection systems in microscopy has moreover enabled simultaneous staining for multiple targets and appropriate unmixing methods have been developed to separate even overlapping spectra [131, 210]. The adaptation of multispectral imaging and unmixing to *ex-vivo* tissue samples is comparatively straight forward because labeling is easier than in *in-vivo* experiments. Influence of background tissue optical properties is significantly reduced and no movement artifacts have to be considered. While fluorescence microscopy is an essential tool in biological research, it can only provide static information on excised tissues, and more specifically only on microscopic parts of them. Macroscopic effects or interactions can hence easily be missed or are erroneously interpreted.

In-vivo multispectral imaging employing multiple labels has up till now mainly consisted in proof-of-principle studies imaging the fluorescence expression in whole mice. Levenson and Mansfield (2006) [112] for instance injected three unspecific fluorescent dyes with overlapping emission spectra subcutaneously into a mouse and imaged the fluorescence intensity employing a multispectral camera system. They succeeded in unmixing all three fluorochromes as well as two autofluorescence types (skin and food) and mapped them to their specific emission area on the mouse skin. In another study, the same authors used an antibody bound nanoparticle fluorescent probe to label subcutaneously injected cancer cells, and unmixed contributions of the nanoparticle

fluorescence from food and skin autofluorescence [122]. Their studies demonstrated the general potential of multispectral imaging of multiple fluorochromes for *in-vivo* studies. The unspecific distribution of fluorescent dyes in comparatively large areas however is not representative for real biological processes. Moreover, whole body imaging may not always provide sufficient resolution to depict specific processes of interest.

The approach herein instead focused on developing hardware and methods for imaging multiple fluorochrome distributions at whole organ level *in-vivo*. This approach not only allows to probe a whole functional entity at once, it also provides enough detail to visualize localized fluorescence of cells and molecules. The labeling strategy employed for this purpose consisted in ”smart” contrast generation that combines multiple fluorescence delivery mechanisms to the targeted cells or proteins in the organ of interest. This strategy allows to flexibly produce adapted fluorescence mouse models to investigate a disease or biological process of interest by selective labeling of relevant cells and proteins.

Advances in fluorescence labeling technology for *in-vivo* applications during the past decade have provided new means for targeting specific molecules in living organisms [83, 118, 130, 166, 193]. Besides the time consuming procedure of producing transgenic animals through breeding, alternative approaches for short term labeling are now available. Viral vectors can for instance be locally injected in adult mice to selectively transfect cells in one organ [39, 105, 189], resulting in fluorescence expression within weeks. Injectable probes in turn can provide targeted labeling within hours or days after injection [133, 138]. The strategy hence consisted in combining fluorescence expression from transgenic mice, which already had a fluorescent protein integrated into their genome, with fluorescence delivery by viral vectors and through injectable probes (see Section 2.2.3). Combining these three labeling methods provides a flexible and ”smart” way to produce multispectral animals that specifically express fluorescence in the molecules, cells or organs of interest.

The model organism considered in this study was the mouse retina. The retina is an approximately 300 µm thick, optically semi-transparent organ on the posterior part of the eye. It contains photoreceptor cells which transform light into electrical signals. Several nerve cell layers are subsequently responsible for transmitting those signal to the brain for processing. Therefore, the retina is the central organ responsible for vision in vertebrates. Figure 3.1 shows a cross section of the anatomy of the retina, and its location within the eye, for future reference.

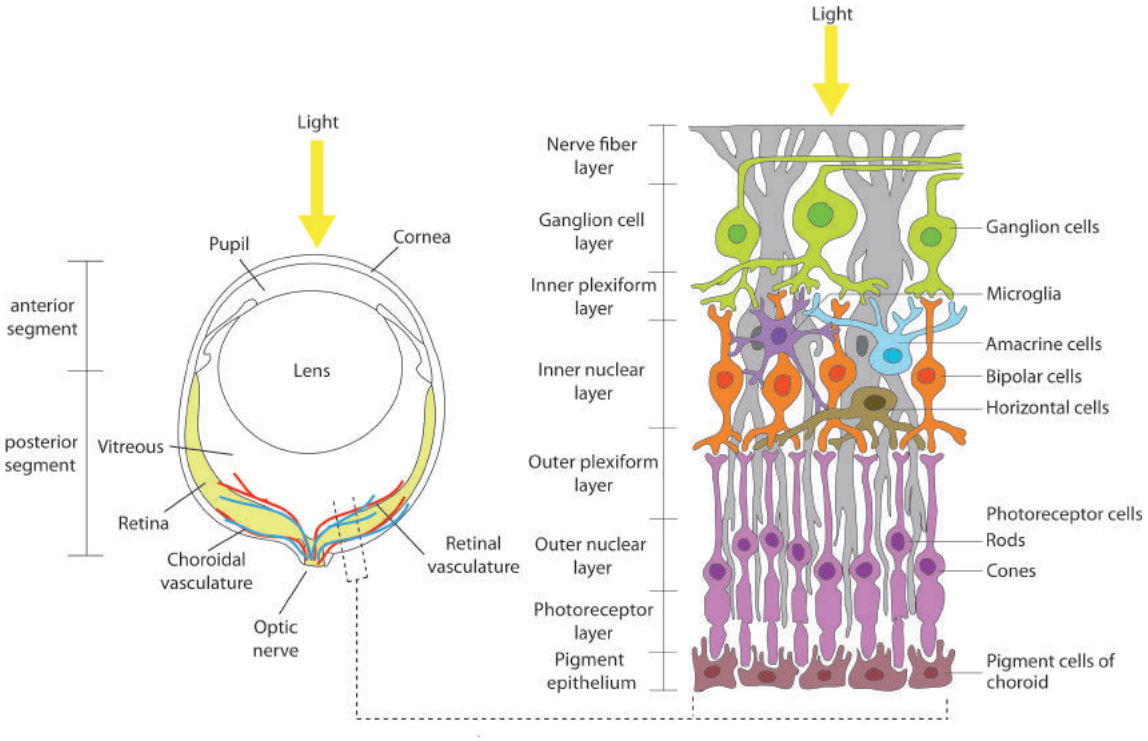

Figure 3.1: Cross section of the rodent eye (left) and the retina (right) with indication of retinal layers and cells. Adapted and modified from [7, 175, 190]

The retina was chosen because of its non-invasive accessibility and its diagnostic value not only for eye-specific pathologies but also systemic diseases. The posterior segment of the eye is easily accessible to *in-vivo* epi-illumination imaging due to the transparency of the lens. Therefore, surface imaging methods for visualizing the retina and the optic nerve can easily be applied. In fact, fundus imaging is already a standard diagnostic method employed in the clinics. Due to the retina's thin structure and semi-transparency to light, fluorescence stemming from any layer of the retina can be imaged in epi-illumination mode. Intravascular oxygen saturation, having diagnostic value in many diseases, can furthermore be assessed from the retinal vasculature. The retina hence constitutes an ideal model organism for the development of *in-vivo* multispectral imaging methods.

More important, however, than the accessibility of the retina for imaging is its diagnostic potential and high research interest. Generally, diseases affecting the retina can often result in significant disturbance or complete loss of vision. This affects life quality

of patients and their families considerably since vision is the central sense for perception of the environment for humans. Many important diseases manifest themselves in the retina. There are diseases that originate directly in the eye, like age related macular degeneration or glaucoma, which account for the most common causes of visual loss [1]. An additional interest in retinal research lies in its diagnostic significance for systemic diseases, i.e. originating in other parts of the body, like diabetes, hypertension or carotid artery occlusion [65, 100, 180]. Finally, the retina is considered to be the ”window to the brain” because it is anatomically and developmentally an extension of the central nervous system. It consists of retinal ganglion cells (see Figure 3.1), the axons of which form the optic nerve, whose fibers are, in effect, CNS axons. [119]. Several well-defined neurodegenerative conditions that affect the brain and spinal cord have manifestations in the eye, and ocular symptoms often precede conventional diagnosis of such CNS disorders. [119]

Clinical investigations of the posterior segment of the eye typically employ fundus cameras, confocal scanning laser ophthalmoscopes (cSLO) or optical coherence tomography (OCT) for diagnosis. A fundus camera essentially acquires a photograph of the retina which represents the amount of reflected quantity of light [1]. An external illumination is projected through the pupil into the eye and the reflected light is typically collected by a CCD camera. Illumination and detection paths are separated on the pupillary plane by optical apertures in order to avoid corneal and lenticular reflections which result in diminished image contrast [1]. Fundus cameras can be upgraded by integration of appropriate excitation and emission filters for angiography and autofluorescence imaging. More advanced technology is present in form of cSLO. cSLO employs a focussed laser beam that scans the retina at different depth. Reflected light originating from other layers than the focal plane of the laser is rejected by a confocal aperture in front of the optical detector. This results in higher resolution images than those obtained by fundus cameras and allows for an estimate of the 3D shape of the retina. Axial resolution is however low compared to the thickness of the retina [162], thus limiting the significance of the third dimension for diagnostic purposes.
When axial characteristics of the retina need to be investigated, OCT would be the modality of choice. OCT is an interferometric technique that computes the difference between a reference light beam and a second light beam backscattered from the retina, based on their cross-correlation. The depth of the occurrence of backscattering can hence be determined and an image of the differences of refractive indices of retinal structures is produced. In contrast to normal fundus photography or cSLO, OCT produces structural

images allowing for investigations of retinal layer structure [53] but is currently not employed to image molecular characteristics.
Recently, some prototypic implementations of optoacoustic systems for retinal imaging in rats were presented [93, 172]. However, only imaging of the vasculature was shown so far and cellular or molecular detection capabilities have yet to be realized. The most common systems currently employed in small animal retinal imaging for molecular imaging of fluorochromes are human fundus cameras and cSLO systems, adapted by integration of lenses to the size of the respective animal eye [51, 64, 81, 162]. They have successfully been employed for imaging molecular markers in mouse or rat retinae, but no study has yet investigated more than 2 fluorochromes at once (e.g. [148, 149]). To the best of the author's knowledge, no truly multispectral system has yet been implemented, capable of imaging multiple fluorochrome expressions in the retina of the same animal.

A further aim of this thesis was therefore to develop a multispectral fundus camera system for mice. Results from its application to a multispectral retina mouse model, created by smart labeling, is shown and unmixing and classification approaches previously developed for *ex-vivo* applications are evaluated *in-vivo*. The presented results show that the developed system is appropriate for imaging multiple fluorochromes, to separate fluorochromes having overlapping spectral bands, and to detect oxygenation. The system furthermore provides images that can be used for characterizing changes in morphology and fluorescence expression in the retina.
While some part of the hardware was specifically designed for imaging the retina, the applied image analysis methods could be generally applied to any surface-bound multi-fluorescence experiment, like for instance skin, given appropriate labeling is available.

3.2 Spectral imaging systems

Two multi-spectral imaging system setups were developed within the scope of this thesis. Both systems share the same image acquisition hardware but differ in employed image transmission optics and illumination. This difference arises from the individual requirements that each application area imposes on the imaging system.
The first multi-spectral setup was designed for acquiring wide-field epi-illumination images in contact-free applications. That is, both objective lens and illumination are placed away from the imaged surface, which is separated by air from the imaging system. This

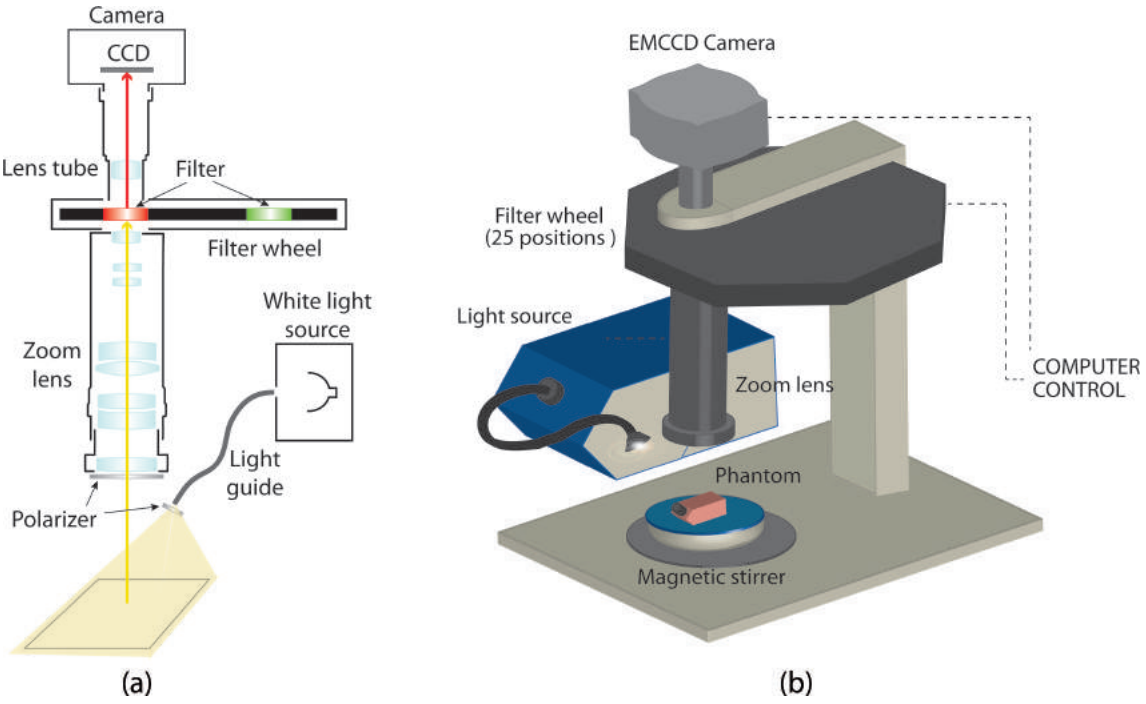

Figure 3.2: Non-contact multispectral imaging setup. (a) Schematic of the imaging optics employed. (b) 3D rendered image of the system as employed for imaging of tissue oxygenation phantoms.

is the most intuitive system design and can be employed to acquire reflectance images in many areas like, for instance, *ex-vivo* tissue slices as well as *in-vivo* images of skin or for surgical guidance. This system, which is described in Section 3.2.1, was used in this thesis for tissue oxygenation measurements and provided the data necessary for the development of an oxygenation quantification method.

The second multi-spectral setup was specifically designed for acquiring wide-field epi-illumination images of the mouse fundus. In contrast to the first system design, this setup is conceived to work when the objective lens is placed in direct contact with the mouse eye (using a coupling gel between cornea and imaging lens surface). Such a direct-contact design accounts for the additional boundary of the mouse eye lens and its abberation properties [144], which are otherwise not present in typical epi-illumination applications like the ones stated above. The multispectral fundus camera is described in Section 3.2.2.

3.2.1 Non-contact multispectral imaging setup

Figure 3.2(a) shows a schematics of the non-contact multi-spectral epi-illumination system, and Figure 3.2(b) a 3D representation of the setup. The detection part was

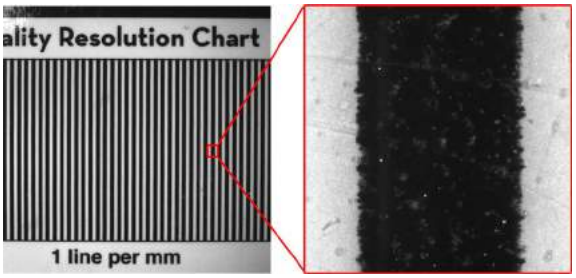

Figure 3.3: Maximal and minimal field of view of the multispectral non-contact imaging setup. A resolution chart was imaged where each line has a thickness of 1 mm.

composed of a 1 Megapixel EMCCD camera (LucaR, Andor Technology, UK), a custom made 25 position filter wheel (Cairn Research, UK) and an achromatic zoom system (Z16 APO, Leica Microsystems, Germany). The zoom system in the used configuration could provide magnifications between 0.36x and 11.5x. The filters (all Chroma Technology, USA) could be exchanged depending on the specific requirements of an experiment. Typically, narrow band filters of approximately 10 nm bandwidth were employed for acquisition of white light reflectance spectra in order to obtain sufficient spectral resolution.
The imaged objects were illuminated through a fiber optics light guide coming from a halogen cold light source (KL2500 LCD, Schott, Germany). Polarizers (Techspec, Edmund Optics, Barrington, NJ, USA) were positioned in front of the light guide and the detection lens in perpendicular arrangement in order to reject non-diffusively reflected light. The setup was connected to and acquisition was controlled by a personal computer.

For tissue oxygenation imaging, every sample was placed under the lens and illuminated by white light throughout the acquisition process. For every filter position one image was acquired and stored. One spectral acquisition could therefore consist of up to 25 images.
The system could also be employed for imaging fluorescence. An additional filter wheel was in this case placed in front of the light guide to select the appropriate excitation wavelength band. Alternatively, laser sources could be employed for excitation.

In the following, several properties of the system are characterized.

[1] **Field of view (FOV):** Figure 3.3 shows the maximal and minimal field of view that could be obtained with the multispectral system presented in Figure 3.2. A resolution chart (Edmund Optics) was imaged. The left image shows the maximal

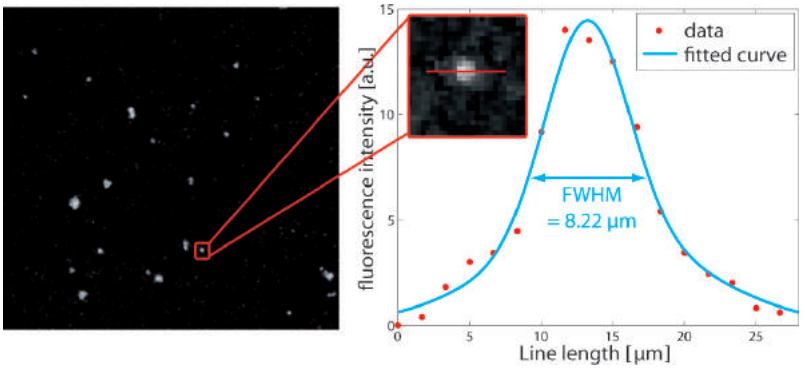

Figure 3.4: Resolution evaluation of the multispectral system by imaging of fluorescent microspheres. Left: Detail of the acquired microsphere image. Right: Intensity profile of a microsphere and fitted gaussian to the pixel intensities.

field of view and the right image a zoom in with the highest magnification resulting in the minimum field of view. One line on the resolution chart had a thickness of 1 mm.

[2] **Resolution:** The maximal resolution of the system was characterized using 4 µm fluorescent microspheres mounted on a slide (TetraSpeck, Life Technologies, Carlsbad, CA, USA) with excitation and emission properties of 488 nm and 509 nm respectively. Appropriate excitation and emission filters were placed in front of the light guide and into the emission filter wheel and an image was acquired with highest magnification. Figure 3.4 shows the resolution characterization. On the left a detail of the original image is shown and on the right is an intensity profile through one of the microspheres, after subtraction of the background intensity. The red dots indicate the pixel intensity at the respective location and the blue line is a gaussian fit to the discrete pixel data. The full with half maximum (FWHM) of the resulting curve is indicated in the graph. The resolution was computed as [191]

$$resolution = \sqrt{FWHM^2 - d^2} \tag{3.1}$$

where d is the finite microsphere diameter. This resulted in a resolution of 7.18 µm for the non-contact multispectral system.

[3] **Spectral sensitivity:** Each of the components of an imaging system has its specific spectral transmission (for optical lenses, filters and light sources) or detection (for CCD camera or other detectors) characteristics. I.e. the spectral sensitivity of the overall system is a result of the cumulative sensitivities/transmission characteristics of its single parts. Quantitative measurements have to take this system sensitiv-

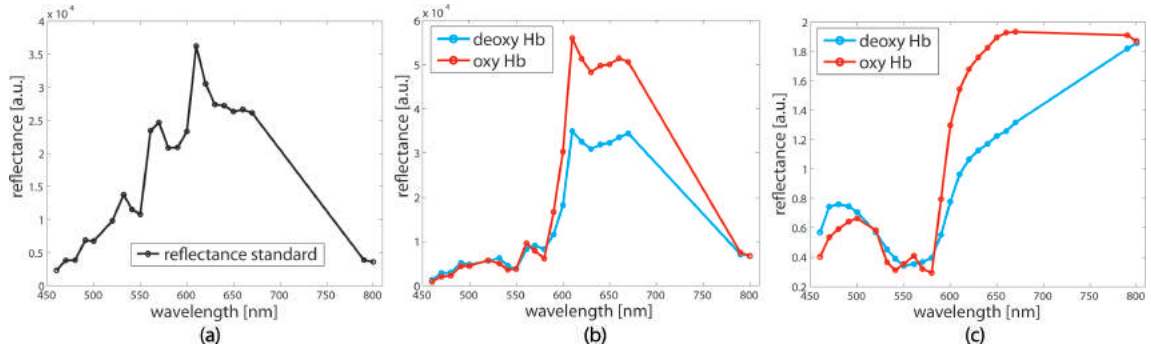

Figure 3.5: Multispectral system sensitivity characteristics. (a) Reflectance acquired from a white reflectance standard. (b) Raw reflectance data from fully oxygenated and fully deoxygenated tissue phantoms. (c) Corrected reflectance of oxy and deoxy phantoms with white reflectance standard curve.

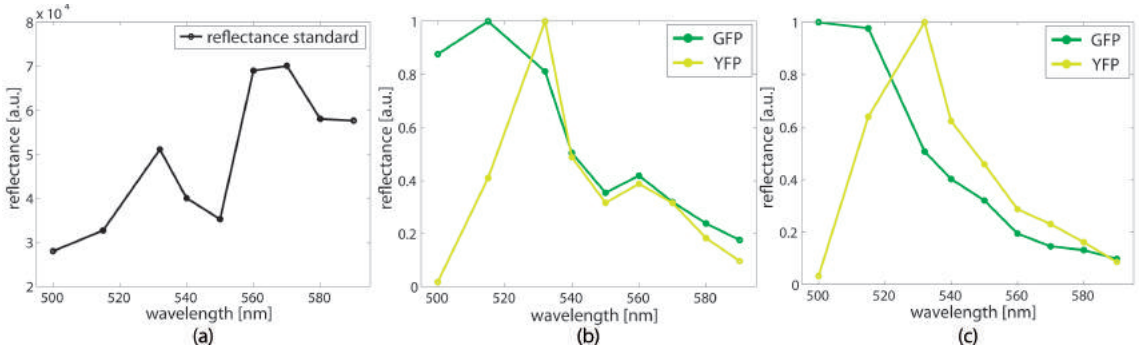

Figure 3.6: Correction of fluorescence spectra. (a) Reflectance acquired from a white reflectance standard. (b) Raw data from GFP and YFP imaging. (c) Corrected reflectance.

ity into account and correct the acquired spectra accordingly. Figure 3.5 shows the overall sensitivity and the correction of reflectance spectra using the sensitivity curve. Figure 3.5(a) depicts the detection gain at each spectral band considered for oxygenation imaging, as measured with a white reflectance standard (Ocean Optics, Dunedin, FL, USA). The dots represent the center wavelength of the employed 10 nm filters. Figure 3.5(b) gives two examples of raw oxy (red) and deoxy (blue) hemoglobin spectra acquired from a tissue mimicking phantom. Figure 3.5(c) shows the corrected oxy and deoxy spectra after division of the spectra in (b) by the spectral sensitivity curve in (a). It can be seen that the oxy and deoxy spectra display the expected shape only after correction with the spectrum of the reflectance standard (see Figure 2.5 for reference on the absorption spectra of hemoglobin).
Figure 3.6 shows the equivalent procedure for the correction of fluorescence spectra. Figure 3.6(a) shows the system sensitivity curve measured at nine spectral

bands between 500 nm and 590 nm (center wavelengths of filters represented by dots). Figure 3.6(b) depicts the raw fluorescence emission curves of GFP (green) and YFP (yellow) and Figure 3.6(c) the corrected spectra.

3.2.2 Multispectral fundus camera

Figure 3.7(a) shows a schematic of the multi-spectral mouse fundus camera, and Figure 3.7(b) a 3D representation of the setup. The detection part consisting of CCD camera and 25 position filter wheel were the same as used in the system presented in Section 3.2.1.
The optical system for projecting an image of the mouse retina onto the CCD was designed to account for the challenges imposed by the nature of the mouse eye and the dilation of its pupil. Typically, the pupil of a mouse eye can be dilated up to approximately 3-4 mm of diameter. This small opening hampers light coupling into the eye. Furthermore, corneal reflections can affect the contrast of the acquired image. Paques et al. [144] showed that the placement of an illuminating endoscope on the cornea allows counteracting corneal refractions by optical applanation and enables wide-field fundus imaging given that the diameter of the endoscope is equal or inferior to the diameter of the pupil.
Therefore, the centerpiece of the setup presented here consisted of an endoscope with 6 cm long otoscope (AA1218, Karl Storz, Germany) with parallel illumination and observation channels. This otoscope had an outer diameter of 3 mm and consisted of step index lenses, an angle of view of 0°, a field of view of 80° in air and a crescent-shaped illuminating tip. The small diameter of the endoscope allowed not only for wide-field image acquisition but also for efficient light coupling into the eye. The image of the retina was focused onto the CCD using a focussing adapter matched to the otoscope (20200043, Karl Storz, Germany). An additional zoom system with appropriately chosen achromatic lens pairs (Edmund Optics) was assembled and used for image relay and to allow for flexible magnification.
Illumination was introduced by an ”octopus-arm” light guide connected to the endoscope. This custom made light guide (SEDI-ATI Fibres Optiques, Courcouronnes, France) consisted of 36 single fibers, four of which were separated at one end of the light guide from the bundle as single fibers that were coupled to laser sources. The remaining 32 fibers were bundled to guide white light from a could light source (KL2500, Schott, Mainz, Germany). The 32-fibre bundle and the 4 separate fibers coming from the light sources were bundled into one single light guide that was coupled into the endoscope.

This enabled multi-spectral illumination, in addition to the multi-spectral detection part. In theory, any laser can be connected to the single fibers, making this system highly flexible and adaptable. The employed lasers for the experiments presented in this thesis had peak emission wavelengths at 488 nm (Obis, Coherent, Santa Clara, CA, USA), 594 nm (Excelsior, Spectra Physics, Santa Clara, CA, USA), 670 nm and 750 nm (both

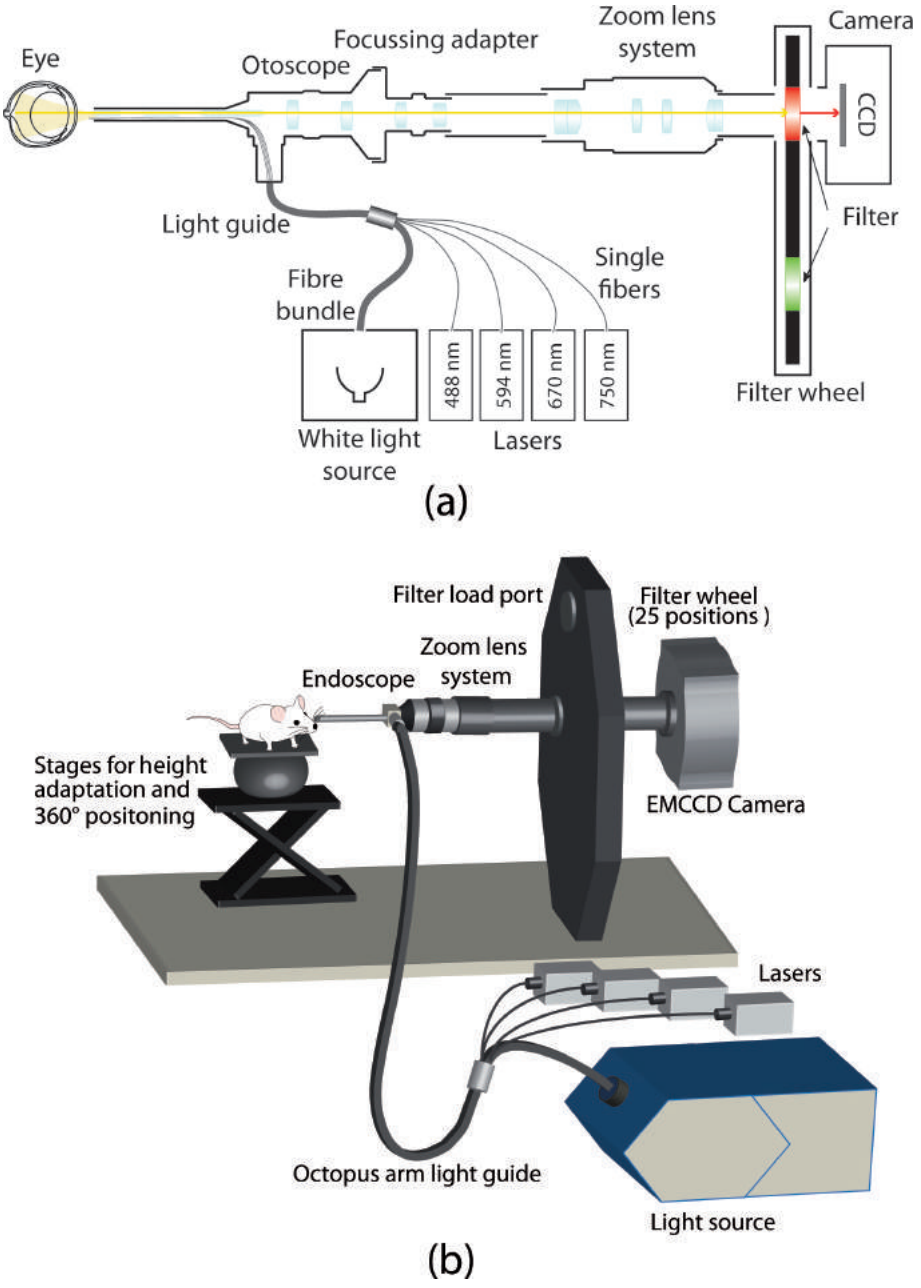

Figure 3.7: Multispectral fundus camera setup. (a) Schematic of the imaging optics employed. (b) 3D rendered image of the system as employed for imaging of the mouse retina.

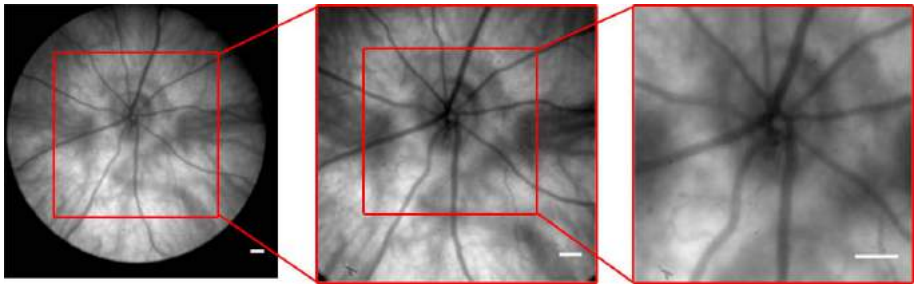

Figure 3.8: Maximal, intermediate and minimal field of view employed for retinal imaging.

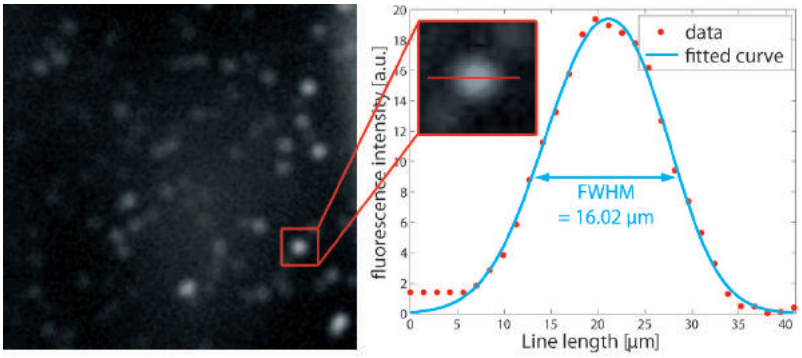

Figure 3.9: Evaluation of fundus camera resolution by imaging of fluorescent microspheres. Left: Detail of the acquired microsphere image. Right: Intensity profile of a microsphere and fitted gaussian to the pixel intensities.

BWF1, B&W Tek, Newark, DE, USA).

Field of view, resolution and spectral sensitivity were characterized equivalently as for the non-contact multispectral system presented in Section 3.2.1.

[1] **Field of view:** Figure 3.8 shows the maximum, intermediate and minimal FOV used in retinal imaging. The image was taken of an albino mouse and shows the fundus of its eye with the vasculature parting radially from the optic nerve head. The white scale bar in each of the three magnifications corresponds to 100 µm.

[2] **Resolution:** Figure 3.9 depicts the characterization of resolution of the fundus camera. The same microsphere slide as in Section 3.2.1 was employed. A detail of the acquired image is displayed on the left and the graph on the right shows the intensity profile through one of the microspheres. The resolution was computed using Equation 3.1 and resulted in 15.51 µm.

[3] **Spectral sensitivity:** The spectral sensitivity of the fundus camera was evaluated

by placing a white reflectance standard in front of the endoscope and acquiring images at every employed wavelength. Fluorescence and reflectance spectra could be hence corrected using the reflectance standard spectrum. Results corresponded to those previously shown in Figures 3.5 and 3.6, and are therefore omitted here.

3.3 Spectral mixing and unmixing

In this section we assume a data cube acquired with any of the approaches introduced in Section 2.1, or the systems presented in Section 3.2. A closer look at the actual interpretation of the data in the cube and its information content is required. Understanding the underlying principles that produce the measured spectra in every imaging pixel allows for the application of mathematical tools to extract "hidden" information on the (spectral) composition of the imaged scene.

3.3.1 Linear mixing model

We define a spectral image as a spatial-spectral distribution described by a function $f(\vec{r},\lambda)$ of position $\vec{r}$ and wavelength λ [156], where $\vec{r}$ can be 2D or 3D.[1]
In this chapter we exclusively deal with 2D reflectance images and add as a third dimension the wavelength, resulting in $f(\vec{r},\lambda) = f(x,y,\lambda)$. Such an interpretation of a spectral image was also shown in Figures 2.1 and 2.2. All examples and results shown in this chapter will therefore be implicitly from, or based on, spatial-spectral data from 2D spatial distributions. The 3D imaging case where wavelength is integrated as fourth dimension (and time could be the fifth, if considered) will be subject of Chapter 4.

The dependence of the spectral image $f(\vec{r},\lambda)$ on the position and the wavelength may take different forms [156]. Descriptive examples for three representative cases are given below and visualized in Figure 3.10.

[1] For the sake of completeness it has to be mentioned that all concepts introduced in this chapter would also apply to 1D spatial measurements. However, this would conflict with the interpretation of an "image" being a spatial distribution in two or three dimensions. The 3D case is included here, although the previous definition of a spectral cube only included 2D spatial images, since the presented methods could in theory be applied to any dimensional space.

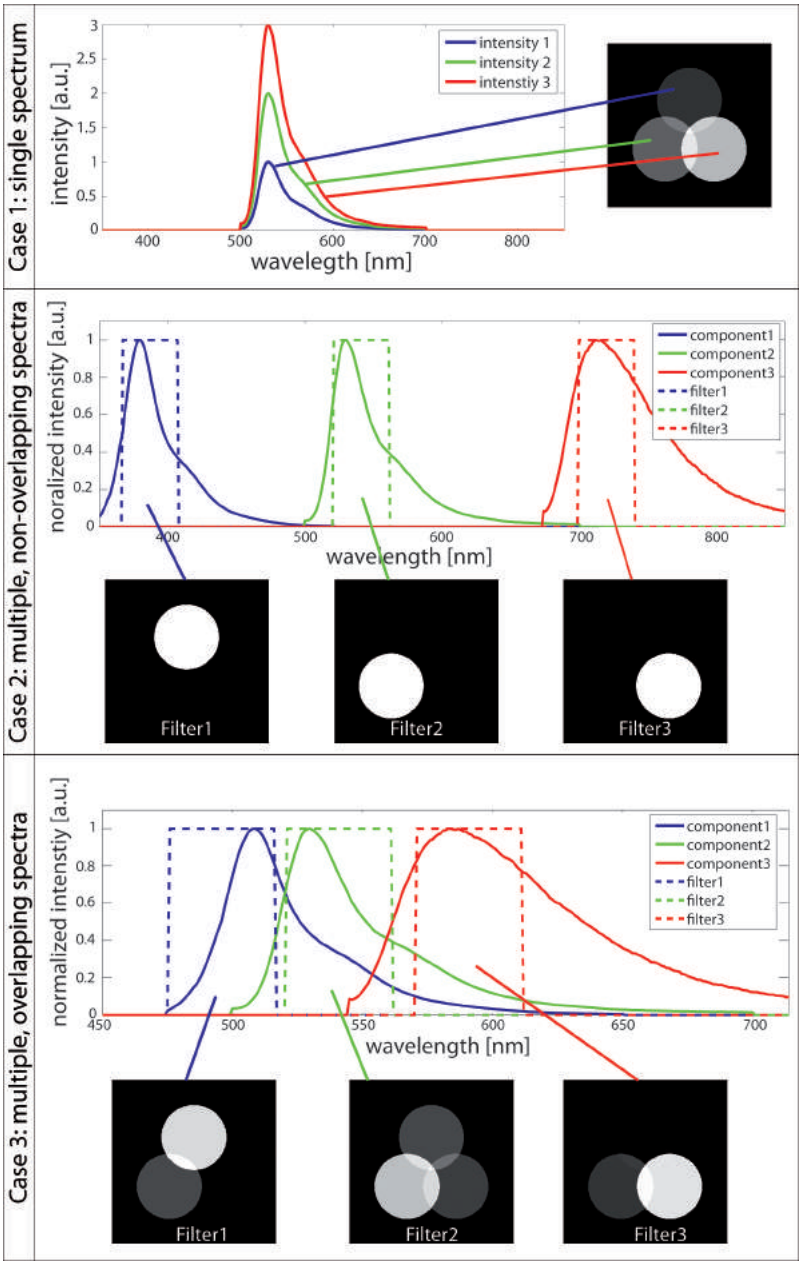

Figure 3.10: Linear mixing of three components having (a) the same spectrum but different intensities, (b) same intensities but different non-overlapping spectra, and (c) same intensities but different overlapping spectra. Ideal filters are represented as dashed lines. The resulting images employing the respective filter are depicted below the respective graph.

[1] **Single spectrum:** The first case assumes an object having the same spectral distribution in every point (i.e. only one substance makes up the whole object). Hence, all points differ only in intensity. This can be expressed by a separable function of

the form

$$f(\vec{r},\lambda) = a_0(\vec{r})s_0(\lambda) \tag{3.2}$$

where $f(\vec{r},\lambda)$ is the product of a function of position $a_0(\vec{r})$ and a function of wavelength $s_0(\vec{r})$. This is the simplest case of spectral imaging because the two processes of spatial imaging and spectral analysis are independent. Acquiring the spectrum in one single point would result in full spectral characterization of the object, and acquisition of an image at one single wavelength would suffice for complete characterization of the spatial distribution of the object within the imaged area.

[2] **Multiple, non-overlapping spectra:** The second case assumes that the imaged object contains N substances with spectral distributions $s_1(\lambda)$, $s_2(\lambda)$, ..., $s_N(\lambda)$, which are all non-overlapping. They have the according spatial distributions $a_1(\vec{r})$, $a_2(\vec{r})$, ..., $a_N(\vec{r})$, which are normalized such that $\sum_{i=1}^{N} a_i(\vec{r}) = 1$. The resulting spectral image is then given by

$$f(\vec{r},\lambda) = a_1(\vec{r})s_1(\lambda) + a_2(\vec{r})s_2(\lambda) + \ldots + a_N(\vec{r})s_N(\lambda) = \sum_{i=1}^{N} a_i(\vec{r})s_i(\lambda) \tag{3.3}$$

The different spectra $s_i(\lambda)$ of the N substances are called endmembers and their fractions $a_i(\vec{r})$ are called abundances. For non-overlapping spectra, employing N appropriate filters in front of the acquisition camera will allow for the identification of all $a_i(\vec{r})$.

[3] **Multiple, overlapping spectra:** The third case assumes that the imaged object contains N substances with spectral distributions $s_1(\lambda)$, $s_2(\lambda)$, ..., $s_N(\lambda)$, which are at least partly overlapping. This results in the same linear mixing model as presented in Equation 3.3 where all spectral contributions add up linearly. However, the employment of filters is not sufficient in this case to recover the original values of $a_1(\vec{r})$, $a_2(\vec{r})$, ..., $a_N(\vec{r})$, because each spatial image acquired with one filter contains mixed contributions of more than one substance, as shown in Figure 3.10. The process of estimating the abundances (and in some cases the endmembers as well) becomes more complicated and requires the employment of algebraic techniques. The generic term for this process is know as unmixing.

Generalizing and summarizing the insight from the previous examples, it can be said that spectral mixture data are interpreted as the weighted sum of the unknown component spectra [30]. A mixing model assumes that the measured spectra $f(\vec{r},\lambda)$ are a linear combination of N unknown pure substance spectra $s_1(\lambda)$, $s_2(\lambda)$, ..., $s_N(\lambda)$. The mixing

coefficients, or abundances, $a_1(\vec{r})$, $a_2(\vec{r})$, ..., $a_N(\vec{r})$, are proportional to the concentration of the respective pure substance in the mixture.
To represent a realistic experimental scenario, an additive noise term $w(\lambda)$ has to be integrated into Equation 3.3, yielding the final expression for the linear mixing model:

$$m(\vec{r},\lambda) = \sum_{i=1}^{N} a_i(\vec{r}) s_i(\lambda) + w(\lambda) \tag{3.4}$$

This noise term represents the measurement errors and model imperfections.

The main constraint in this mixing model is the non-negativity of both, the source signals (endmembers) and the mixing coefficients (abundances):

$$a_i(\vec{r}) \geq 0 \;\; \forall i, \vec{r} \text{ and } \; s_i(\lambda) \geq 0 \;\; \forall i, \lambda$$

To be physically realizable, the abundances should furthermore sum to one.

Equation 3.4 can be written in a discretized form to represent the digital imaging data acquired within this thesis. Using matrix notation, this results in

$$\mathbf{M} = \mathbf{AS} + \mathbf{W} \tag{3.5}$$

where $\mathbf{M}$ is the $(n \times m)$ multispectral measurement matrix, with n being the number of image pixels and m the number of spectral bands at which a 2D image is acquired. $\mathbf{A}$ is the $(n \times p)$ mixing matrix with its p column vectors representing the abundance of each pure spectrum. $\mathbf{S}$ is a $(p \times m)$ matrix containing the p pure spectra of the substances at the m measurement wavelengths. $\mathbf{W}$ is the $(n \times m)$ additive noise matrix.

Every pixel in a spectral image typically contains mixed contributions from different components having overlapping spectra, resulting in a situation as described in case 3.[2] Imaging non-overlapping spectra (case 2) can be a convenient approach to measuring multiple components because all component's contributions can directly be identified employing appropriate filters, without post processing of the data. Such an approach can be used for instance in fluorescence microscopy or fluorescence molecular tomography (see Chapter 4), where appropriate fluorescence dyes or probes can be chosen

[2] Imaging of single spectra (case 1) is not within the scope of this thesis, which is dedicated at investigating imaging of multiple components.

for labeling different molecules. Selection of separate emission bands is sometimes possible because emission spectra of fluorochromes are typically designed to be narrow. However, if more than two or three fluorescent labels are required, finding completely non-overlapping fluorochromes can already become challenging. Furthermore, intrinsic tissue chromophores and fluorochromes usually do not have narrow emission spectra but emit over broad ranges of the electromagnetic spectrum. An examples for this was given in Figure 2.5 for oxy and deoxy hemoglobin absorption. Consequently, the desire to extract from a spectrum the substances in the mixture as well as the proportions in which they appear, is important to many multispectral imaging applications [101].

Spectral unmixing is the procedure by which the measured spectra of mixed observations are decomposed into a collection of constituent spectra (endmembers) and a set of corresponding fractions (abundances) that indicate the proportion of each endmember present in the pixel [101].
Essentially, unmixing performs the inversion of Equation 3.5. Appropriate inversion algorithms are dominated by approaches that usually invoke some aspect of the method of least squares [101]. The next section will describe least squares methods for spectral fitting. Two blind source separation (and dimensionality reduction) methods, principle component analysis (PCA) and independent component analysis (ICA), will be subsequently treated.

3.3.2 Least squares methods

Assuming the absence of additive noise and that the spectra of the endmembers are known, the simples solution of the abundance estimation problem is obtained by an unconstrained linear least-squares problem formulation that has an explicit solution in terms of the pseudo inverse matrix [156]:

$$\mathbf{A}_{ULS} = (\mathbf{S}^T\mathbf{S})^{-1}\mathbf{S}^T\mathbf{M} = \mathbf{S}^+\mathbf{M} \tag{3.6}$$

where $\mathbf{A}_{ULS}$ is the matrix of unmixed abundances and $\mathbf{S}^+$ the pseudo inverse of $\mathbf{S}$. This unconstrained estimate for $\mathbf{A}$ minimizes $\|\mathbf{M} - \mathbf{S}\mathbf{A}_{ULS}\|_2^2$. $\mathbf{S}^+$ exists when there are more spectral bands than endmembers, and if $\mathbf{S}$ has full column rank, both requirements which are typically satisfied in multi-spectral imaging. Although Equation 3.6 provides an easy way to implement a solution of the problem in Equation 3.5, it enforces none of

the physical constraints on $\mathbf{A}_{ULS}$. This could result in negative values for the abundances or non-unity of their sum, both cases being without physical meaning.

The unconstrained solution can be refined by constraining it to fulfill the full additivity condition, i.e $\sum_{i=1}^{N} a_i = 1$ [101], but without imposing a positivity constraint, yet. The explicit solution is given by

$$\mathbf{A}_{STO} = \mathbf{A}_{ULS} + (1 - \mathbf{I}^T \mathbf{A}_{ULS}) \frac{(\mathbf{S}^T \mathbf{S})^{-1} \mathbf{I}}{\mathbf{I}^T (\mathbf{S}^T \mathbf{S})^{-1} \mathbf{M} \mathbf{I}} \tag{3.7}$$

where $\mathbf{I}$ is the identity matrix. The solution in Equation 3.7 consists of the unconstrained solution from Equation 3.6 with an additive correction term that depends on $\mathbf{S}$ and the error incurred by $\mathbf{A}_{ULS}$ in satisfying the full additivity constraint [101].

There is no closed form solution fulfilling the complementary constraint of nonnegativity [156]. Hence, to integrate the nonnegativity condition into the computation of the solution of the minimization problem, iterative approaches are commonly used. A well known algorithms including only the non-negativity constraint is for instance the nonnegative least squares algorithm (NNLS) [156]. Algorithms exist for transforming the fully constrained problem into an NNLS problem. Alternatively, the Trust-region reflective least squares algorithm [21, 24], which is implemented in MATLAB can be used for solving constrained linear least squares problems.

The methods presented above all require a priori knowledge on the endmember spectra present in the images. Their performance depends on the accuracy and completeness of these spectra and the absence of systematic errors in the data [61]. However, this kind of information is often not available. Alternative approaches to unmixing of multispectral imaging data that do not require a priori spectral information have to be consulted in such cases.

3.3.3 Blind source separation methods / dimensionality reduction

Blind source separation (BSS) methods aim at estimating the abundances only based on the measurement data without any information on the type of source signals (endmembers) or the mixing process. Two of the best known concepts are introduced here, principal component analysis and independent component analysis.

For this section we assume a measurement matrix $\mathbf{M}$ of zero mean. This can be easily obtained in any case by subtracting the mean of the measurements from $\mathbf{M}$ and re-adding it to the unmixed estimation of the endmembers.

3.3.3.1 Principal component analysis

Principal component analysis (PCA) is a simple non-parametric method of extracting estimations of endmember distribution and their spectra from mixed data sets. PCA furthermore provides a roadmap for reducing a complex data set to a lower dimension to reveal the hidden properties that underlie it [167]. The theory presented in this section is mainly based on an excellent educational paper by J. Shlens [167].

We assume two $(n \times m)$ matrices $\mathbf{M}$ and $\mathbf{R}_{PCA}$ related by a linear transformation $\mathbf{P}$ as follows:

$$\mathbf{R}_{PCA} = \mathbf{PM} \tag{3.8}$$

$\mathbf{M}$ can be interpreted as the original recorded multispectral data as presented in Equation 3.5. $\mathbf{R}_{PCA}$ is the re-representation of $\mathbf{M}$. PCA aims at finding matrix $\mathbf{P}$ that best re-expresses the data in $\mathbf{M}$ in order to dispose of the redundant information in $\mathbf{M}$. For that purpose, PCA makes several assumptions: (a) The source components / endmembers are statistically uncorrelated but the measurements in $\mathbf{M}$ are not [61]. (b) The probability distribution of the measurements is gaussian. (c) The principle components are orthogonal. (d) Large variances between measurements contain important components.

Given these assumptions are fulfilled, correlations between all possible measurements can be quantified using the covariance matrix of $\mathbf{M}$. Whereby the covariance matrix is given by

$$Cov(\mathbf{M}) = \frac{1}{m-1}\mathbf{M}\mathbf{M}^T \tag{3.9}$$

To reduce redundancy each variable should correlate as little as possible with other variables, i.e. covariance between different measurements should ideally be zero. Consequently, PCA tries to find the orthonormal matrix $\mathbf{P}$ that transforms the measurement matrix $\mathbf{M}$ such that the covariance matrix of $\mathbf{R}_{PCA}$ is diagonalized. The rows of $\mathbf{P}$ are then the principal components of $\mathbf{M}$. Projecting $\mathbf{M}$ along the new basis spanned by the principal components estimates the endmember distribution.

To calculate the principal components, $Cov(\mathbf{R}_{PCA})$ is first rewritten in terms of $\mathbf{P}$:

$$Cov(\mathbf{M}) = \frac{1}{m-1}\mathbf{PEP}^T \tag{3.10}$$

where $\mathbf{E} = \mathbf{MM}^T$ is a symmetric matrix. A symmetric matrix can be diagonalized by an orthogonal matrix of its eigenvectors, resulting in:

$$\mathbf{E} = \mathbf{UDU}^T \tag{3.11}$$

where $\mathbf{D}$ is a diagonal matrix containing the eigenvalues and $\mathbf{U}$ is a matrix of eigenvectors of $\mathbf{E}$, arranged as columns. A matrix $\mathbf{P}$ is selected so that each row of $\mathbf{P}$ is an eigenvector of $\mathbf{E}$, i.e. $\mathbf{P} = \mathbf{U}^T$. Substituting $\mathbf{U}^T$ by $\mathbf{P}$ in Equation 3.11 and subsequently substituting $\mathbf{E}$ in Equation 3.10 yields a new expression of the covariance matrix

$$Cov(\mathbf{R}_{PCA}) = \frac{1}{m-1}(\mathbf{PP}^{-1})\mathbf{D}(\mathbf{PP}^{-1}) = \frac{1}{m-1}\mathbf{D} \tag{3.12}$$

where $\mathbf{P}^T = \mathbf{P}^{-1}$ (because $\mathbf{P}$ is orthonormal). Since the choice of $\mathbf{P}$ diagonalizes $Cov(\mathbf{R}_{PCA})$, we can conclude that the eigenvectors of $\mathbf{MM}^T$ are the principle components of $\mathbf{M}$ and that the i^{th} diagonal value of $Cov(\mathbf{R}_{PCA})$ is the variance of $\mathbf{M}$ along the i^{th} row of $\mathbf{P}$. Hence, the unmixed components $\mathbf{R}_{PCA}$ are obtained by

$$\mathbf{R}_{PCA} = \mathbf{U}^T\mathbf{M} \tag{3.13}$$

Alternatively, a solution to finding the principle components can be obtained by singular value decomposition. Since such an implementation is typically computationally much more intensive than the covariance matrix approach and therefore less practical, it is only shortly presented here and can be reviewed in more depth elsewhere [167].
$\mathbf{M}$ can be decomposed by singular value decomposition (SVD) into an orthogonal matrix $\mathbf{U}$, a diagonal matrix Σ and another orthogonal matrix $\mathbf{V}^T$, i.e.

$$\mathbf{M} = \mathbf{U}\Sigma\mathbf{V}^T \tag{3.14}$$

Rewriting Equation 3.14 we obtain

$$\mathbf{U}^T\mathbf{M} = \Sigma\mathbf{V}^T = \mathbf{Z} \tag{3.15}$$

Equivalently to Equation 3.13, $\mathbf{U}^T$ in Equation 3.15 performs a change of basis from $\mathbf{M}$ to $\mathbf{Z}$. Therefore, SVD can be used to compute the principal components of $\mathbf{M}$.

One paradigm of PCA is to associate the largest variances with the most important principle components. The smallest variances and hence principle components are associated with noise and can therefore be removed from the data set. This reduces the dimensionality of the problem which can be beneficial in data sets containing much more spectral measurements than endmembers.

3.3.3.2 Independent component analysis

In some applications, the assumptions made for PCA are too stringent to apply to the measurement data. An alternative approach termed independent component analysis (ICA) aims at providing solutions using a less constrained set of problems. The formulation of the general problem is equivalent to the one defined for PCA [167]. I.e. a matrix $\mathbf{P}$ has to be found that diagonalized the covariance matrix of the measurements. However, the difference between the two methods is that PCA provides results where principal components are uncorrelated, while ICA finds endmembers that satisfy the more general and therefore stronger condition of statistical independence [61]. This condition accounts for projections that are not necessarily orthogonal. Furthermore, ICA assumes non-gaussian variables. While independence implies uncorrelatedness, uncorrelatedness vice versa does not always imply independence for non-gaussian variables [30].

Like in the previous section we assume two $(n \times m)$ matrices $\mathbf{M}$ and $\mathbf{R}_{ICA}$ related by a linear transformation $\mathbf{P}$ as follows:

$$\mathbf{R}_{ICA} = \mathbf{P}_{ICA}\mathbf{M} \tag{3.16}$$

Because of the assumption of independence, ICA finds a basis such that the joint probability distribution of the columns $\mathbf{p}_i$ of $\mathbf{P}$ can be factorized for all i and j, $i \neq j$ [167]:

$$p(\mathbf{p}_i, \mathbf{p}_j) = p(\mathbf{p}_i)p(\mathbf{p}_j) \tag{3.17}$$

Approaches to finding such a basis are based on the Central Limit Theorem, which tells that the sum of independent random variables tends toward a gaussian distribution, while the original variables are non-gaussian. Thus, a sum of two independent random variables usually has a distribution that is closer to gaussian than any of the two original random variables [89]. Consequently, the ICA problem can be solved by finding a matrix $\mathbf{P}$ which

maximizes the non-gaussianity of $\mathbf{PM}$ and provides the independent components in $\mathbf{R}_{ICA}$.

In order to use non-gaussianity for ICA estimation, a measure for non-gaussianity has to be found. Such measures are, for instance, based on kurtosis or approximation of negentropy [89, 177]. Alternatively, maximum likelihood methods use the degree of mutual independence as specified by the joint probability density function to find an unmixing matrix $\mathbf{P}$ [178]. Having such measures permits to use standard optimization methods to iteratively update the unmixing matrix in order to maximize this measure of non-gaussianity or similarity [178]. In order to find all independent components the search needs to be furthermore constrained to a space that iteratively gives estimates of the basis vectors of $\mathbf{P}$ which are uncorrelated with the previous ones.

Kurtosis (or the fourth-order cumulant) is a classical measure of non-gaussianity and is defined for a random variable y as

$$kurt(y) = E\{y^4\} - 3(E\{y^2\})^2 \tag{3.18}$$

Since the fourth moment of a gaussian variable y equals $3(E\{y^2\})^2$, kurtosis is zero for a gaussian random variable, and for most non-gaussian variables non-zero [88]. An algorithm estimating the independent components would start with some estimation of matrix $\mathbf{P}$ and compute the direction in which the kurtosis of $\mathbf{R}_{ICA} = \mathbf{PM}$ is growing or decreasing most strongly (depending on the sign of the kurtosis) based on the available mixed measurements in $\mathbf{M}$. Using some gradient method a new matrix $\mathbf{P}$ can be found iteratively.

Another measure for non-gaussianity can be derived from the differential entropy of a random variable y, which can be interpreted as the degree of information that the observation of the variable gives. Differential entropy of a vector $\mathbf{y}$ with density $p(\mathbf{y})$ is defined as:

$$H(\mathbf{y}) = -\int p(\mathbf{y}) \log p(\mathbf{y}) p(\mathbf{y}) \mathrm{d}\mathbf{y} \tag{3.19}$$

According to information theory, a gaussian variable has the largest entropy among all random variables of equal variance. Non-gaussian variables have hence small entropy. A measure of non-gaussianity that is zero for a gaussian variable and always nonnegative is given by an alternative expression known as negentropy J:

$$J(\mathbf{y}) = H(\mathbf{y}_{gauss}) - H(\mathbf{y}) \tag{3.20}$$

where $\mathbf{y}_{gauss}$ is a gaussian random vector of the same covariance matrix as $\mathbf{y}$.
An approximation of negentropy using non-quadratic functions was shown to provide a more robust estimator [88] than the original negentropy approach. The approximation for a random variable y is given by

$$J(y) \propto [E\{G(y)\} - E\{G(\nu)\}]^2 \tag{3.21}$$

where G is a non-quadratic function that has to be carefully chosen, and ν is a gaussian variable of zero mean. For $G(y) = y^4$ one obtains a kurtosis based approximation.

Finally, we shortly discuss the maximum likelihood (ML) estimation method, which is a popular approach for estimating the ICA model. The ML ideas can be used in the context of ICA by formulating the mixing problem as one where the observation data is modeled to have specified probability density function that is parameterized by the mixing matrix $\mathbf{A}$ (Equation 3.5) or its inverse $\mathbf{W} = \mathbf{A}^{-1}$ [12]. We reinterpret Equation 3.5 (ignoring the error term) in terms of column vectors, given by

$$\begin{bmatrix} \uparrow & \uparrow & & \uparrow \\ \mathbf{m}_1 & \mathbf{m}_2 & \dots & \mathbf{m}_m \\ \downarrow & \downarrow & \downarrow & \downarrow \end{bmatrix} = \mathbf{A} \begin{bmatrix} \uparrow & \uparrow & & \uparrow \\ \mathbf{s}_1 & \mathbf{s}_2 & \dots & \mathbf{s}_m \\ \downarrow & \downarrow & \downarrow & \downarrow \end{bmatrix} \tag{3.22}$$

This method models the relationship between the likelihood $p_{\mathbf{m}_i}(\mathbf{m}_i|\mathbf{W})$ of the signal mixtures $\mathbf{m}_i$ given $\mathbf{W}$ and the assumed source signal joint probability density function $p_{\mathbf{s}_i}(\mathbf{s}_i) = p_{\mathbf{s}_i}(\mathbf{W}\mathbf{m}_i)$ to be

$$p_{\mathbf{m}_i}(\mathbf{m}_i|\mathbf{W}) = p_{\mathbf{s}_i}(\mathbf{W}\mathbf{m}_i)|\mathbf{W}| \tag{3.23}$$

where $|\mathbf{W}|$ denotes the absolute value of the determinant of the Jacobian matrix $|\frac{\partial \mathbf{R}_{ICA}}{\partial \mathbf{m}_i}|$ [178]. Equation 3.23 defines a likelihood function $L(\mathbf{W})$ which is parameterized by $\mathbf{W}$. If the m source signals are mutually independent, so that the joint pdf $p_{\mathbf{s}_i}$ is the product of its m marginal pdfs, then Equation 3.23 can be written as:

$$\log L(\mathbf{W}) = \sum_{k=1}^{m} \sum_{i=1}^{n} \log p_{\mathbf{s}_i}(\mathbf{w}_i^T \mathbf{m}_k) + n \log |\mathbf{W}| \tag{3.24}$$

where $\mathbf{w}_i$ is the i^{th} row of $\mathbf{W}$. The task of an ICA algorithm now consists in finding a $\mathbf{W}$ that maximizes the function in Equation 3.23 to find the maximum likelihood estimate.

The algorithm used within this thesis for ICA computations was FastICA [88]. FastICA

finds the independent sources by using a fixed-point iteration scheme in order to maximize non-gaussianity, as measured by approximated negentropy as presented in Equation 3.21. (This algorithm can however also integrate kurtosis by appropriately choosing the non-quadratic function G in Equation 3.21). FastICA can furthermore be considered as a fixed-point algorithm for maximum likelihood estimation of the ICA data model [89].

An important difference between ICA and PCA, beyond the different assumptions made on the source component properties, is that ICA does not determine the order, i.e. the importance, of the independent components. As a consequence, an evaluation of the information content of each independent component has to be made by the user. Such evaluation could be biased, and moreover impractical for large data sets. Glatz et al. [61] proposed a method for combining PCA and ICA to first reduce the dimensionality of the problem using PCA and then presenting ICA with a better conditioned problem.

3.3.4 Classification

Pattern classification is the process of identifying a pattern as a member of one of a set of categories, or classes, of known properties [156]. Several nonparametric classification methods have been widely applied to biomedical spectral image processing [120]. Examples include support vector machines (SVM), artificial neural networks (ANN), spectral information divergence (SID) and spectral angle mapper (SAM). In this section we shortly introduce the underlying concepts of support vector machines, being one of the preferred classification methods in the spectral imaging field [120]. This type of classification was applied within this thesis as alternative approach to the BSS methods previously described. The aim was to compare BSS approaches and classification as to their efficiency in identifying endmembers from overlapping fluorescence emission spectra in *in-vivo* applications. Since classification approaches assign every image pixel to one type of class, in contrast to BSS approaches that allow for mixed pixels, the comparison of unmixing with one single classification type seemed appropriate for a general conclusion on the applicability of unmixing versus classification methods.
The following theoretical introduction is mainly based on References [18, 120, 123].

SVM is a kernel based machine learning technique that classifies data by finding the best hyperplane that separates all data points of one class from the data points of another class. Such a hyperplane should ideally have the largest possible distance from

any training data point in order to allow for good classification results. The equation of a hyperplane for any set of points $\mathbf{x}$ can be written given as

$$\mathbf{w} \cdot \mathbf{x} + b = 0 \tag{3.25}$$

where $\mathbf{w}$ is the normal vector to the hyperplane and b is a real constant.
We assume a training data set $\mathbf{x}_i$, $i = [1, \ldots, M]$, containing data points belonging each to one of two classes $y_i = \pm 1$. If the training data set is linearly separable then there exists at least one choice of the parameters $\mathbf{w}$ and b such that $y_i(\mathbf{w} \cdot \mathbf{x}_i + b) > 0$ for all training points. In this case, SVM finds a hyperplane that has the largest margin, i.e. the largest distance, to the closest point $\mathbf{x}_i$ from the data set. The maximum margin solution is found by solving

$$\arg\max_{\mathbf{w},b} \left(\frac{1}{\|\mathbf{w}\|} \min_i (y_i(\mathbf{w}^T \mathbf{x}_i + b)) \right) \tag{3.26}$$

Direct solution of this optimization problem would be very complex. It can however be converted into an equivalent problem that is easier to solve. The reformulated problem consists in finding $\mathbf{w}$ and b that minimize $\|\mathbf{w}\|^2$ for all $(\mathbf{x}_i, y_i)$, i.e.

$$\arg\min_{\mathbf{w},b} \frac{1}{2} \|\mathbf{w}\|^2 \tag{3.27}$$

such that

$$y_i(\mathbf{w} \cdot \mathbf{x}_i + b) \geq 1 \tag{3.28}$$

In order to solve this constrained problem, Lagrange multipliers α_i are introduced, resulting in :

$$L(\mathbf{w}, b, \alpha) = \arg\min_{\mathbf{w},b} \max_{\alpha_i \geq 0} \left(\frac{1}{2} \|\mathbf{w}\|^2 - \sum_{i=1}^{M} \alpha_i (y_i(\mathbf{w} \cdot \mathbf{x}_i + b) - 1) \right) \tag{3.29}$$

Since we look for a stationary point of $L(\mathbf{w}, b, \alpha)$ we can set its gradient with respect to $\mathbf{w}$ and b to 0, resulting in

$$\mathbf{w} = \sum_i \alpha_i y_i \mathbf{x}_i \tag{3.30}$$

$$0 = \sum_i \alpha_i y_i \tag{3.31}$$

Substitution of 3.30 and 3.31 into Equation 3.29 results in the dual representation of the maximum margin problem

$$\tilde{L}(\alpha) = \sum_{i=1}^{M} \alpha_i - \frac{1}{2} \sum_{i,j} \alpha_i \alpha_j y_i y_j k(\mathbf{x}_i, \mathbf{x}_j) \tag{3.32}$$

where $k(\mathbf{x}_i, \mathbf{x}) = \mathbf{x}_i^T \cdot \mathbf{x}_j$ is defined as the kernel function. $\tilde{L}(\alpha)$ is maximized over α_i, such that

$$\alpha_i \geq 0 \tag{3.33}$$

$$\sum_{i=1}^{n} \alpha_i y_i = 0 \tag{3.34}$$

Equation 3.32 takes the form of a quadratic programming problem that can be solved for α. The value of b can the be determined as

$$b = \frac{1}{M_S} \sum_{i \in S} \left(y_i - \sum_{j \in S} \alpha_j y_j k(\mathbf{x}_i, \mathbf{x}_j) \right) \tag{3.35}$$

where M_S is the total number of support vectors.

For non separable data the concept of soft margins is employed. That is, a plane is searched that separates the data sets as cleanly as possible, while allowing misclassification. Points lying on the wrong side of the boundary are however softly penalized. The optimization problem is then expressed as

$$\min_{w,,b,s} \left(\frac{1}{2} \|\mathbf{w}\|^2 + C \sum_i s_i \right) \tag{3.36}$$

such that

$$y_i(\mathbf{w} \cdot \mathbf{x}_i + b) \geq 1 - s_i \tag{3.37}$$

$$s_i \geq 0 \tag{3.38}$$

where s_i are are non-negative slack variables which measure the degree of misclassification of the data $\mathbf{x}_i$. The objective function from 3.36 is hence penalized by non-zero s_i. C is a regularization parameter that controls the trade of between slack variable penalty and the margin.
Using Lagrange multipliers μ_i as done above the problem is re-expressed as

$$L(\mathbf{w}, b, \alpha) = \arg\min_{\mathbf{w},s,b} \max_{\alpha,\mu} \left(\frac{1}{2} \|\mathbf{w}\|^2 - \sum_{i=1}^{M} \alpha_i (y_i(\mathbf{w} \cdot \mathbf{x}_i + b) - 1 + s_i) + C \sum_{i=1}^{M} s_i - \sum_{i=1}^{M} \mu_i s_i \right) \tag{3.39}$$

Assuming a stationary point and setting the gradient of $L(\mathbf{w}, b, \alpha)$ with respect to $\mathbf{w}$, b and s_i to zeros results in

$$\mathbf{w} = \sum_i \alpha_i y_i \mathbf{x}_i \tag{3.40}$$

$$0 = \sum_i \alpha_i y_i \tag{3.41}$$

$$\alpha_i = C - \mu_i \tag{3.42}$$

Substitution of Equations 3.40, 3.41 and 3.42 into 3.39 gives the dual Lagrangian form

$$\tilde{L}(\alpha) = \sum_{i=1}^{M} \alpha_i - \frac{1}{2} \sum_i \sum_j \alpha_i \alpha_j y_i y_j \mathbf{x}_i^T \mathbf{x}_j \tag{3.43}$$

such that

$$0 \leq \alpha_i \leq C \tag{3.44}$$

$$\sum_{i=1}^{n} \alpha_i y_i = 0 \tag{3.45}$$

The solution for b is then given by

$$b = \frac{1}{M_{\mathcal{M}}} \sum_{i \in \mathcal{M}} \left(y_i - \sum_{j \in \mathcal{S}} \alpha_j y_j k(\mathbf{x}_i, \mathbf{x}_j) \right) \tag{3.46}$$

where $\mathcal{M}$ denotes the set of indices of data points having $0 < \alpha_i < C$.
After solving Equation 3.43, or respectively Equation 3.32, a new point $\mathbf{x}$ can be classified by the decision function

$$\operatorname{sgn}(\mathbf{w} \cdot \mathbf{x} + b) = \operatorname{sgn} \left(\sum_{i=1}^{M} y_i \alpha_i k(\mathbf{x}_i, \mathbf{x}) + b \right) \tag{3.47}$$

In non-linear classification problems, the kernel takes different forms and can belong to a variety of function classes, like polynomial functions or gaussian radial basis functions.

3.4 Multispectral image analysis I: Oxygenation computation

Section 3.3 illustrated how the data contained in a data cube can be interpreted and analyzed in order to extract possibly hidden information. Before applying such methods to multispectral images, however, the nature of the imaged subject and the contrast generating molecule have to be considered. As discussed in Section 3.1.1, optical properties may influence considerably the acquired data and mask the properties of the molecule that is

under investigation. This is particularly problematic when quantitative read outs are desired, as in the case of tissue oxygenation detection. This section therefore describes the development of a method that attempts at correcting the influences of optical properties on the measured tissue oxygenation spectra. Spectral unmixing can only extract meaningful oxygen saturation information from spectra after such correction methods have been applied.

3.4.1 Spectral transformations for correction of the effect of optical properties on oxygenation spectra

The method considered herein assumes measurements obtained from a multi-spectral epi-illumination imaging system (as presented in Section 3.2.1), i.e. images of an identical field of view at different spectral bands. Calculation of oxygen saturation is based on a spectral measurement data set $M(\lambda)$ assumed normalized for the exposure time and detection gains at each spectral band considered. Two reference spectra $R_{100}(\lambda)$ and $R_0(\lambda)$ are representing the reflectance of oxygenated and deoxygenated hemoglobin, whereby the subscripts 100 and 0 represent percent oxygen saturation. The spectra $R_{100}(\lambda)$ and $R_0(\lambda)$ are further assumed of spectral step of 1 nm. Likewise, $M(\lambda)$ is linearly interpolated to a spectral step of 1 nm. Interpolation is necessary to determine the location of the isosbestic points for the employed discrete measurement wavelengths.

Three isosbestic points $I(\lambda_{min})$, $I(\lambda_{mid})$, $I(\lambda_{max})$ lying within the measured wavelength range are further assumed. $I(\lambda_x)$ represents an isosbestic point at wavelength λ_x, whereby x takes the values *min*, *mid* and *max* indicating the isosbestic points located at the lowest, middle and highest wavelength value, respectively.

Differences in tissue scattering and the presence of tissue absorbers other than hemoglobin influence the shape of the measurement spectrum $M(\lambda)$ for a given oxygenation value. Tissue optical properties that are not due to oxy or deoxy hemoglobin are considered herein as background tissue optical properties. Consequently, accurate quantification of tissue oxygenation would require that $M(\lambda)$ is insensitive to (or corrected for the influence of) background tissue optical property variations.

The methods considered herein apply transformations to $M(\lambda)$ in order to reduce its sensitivity to the background optical properties of tissue. The starting point of the

methods investigated herein is the method proposed in Reference [73], which performs two transformation steps. The first step assumes two linear functions $m(\lambda)$ and $r(\lambda)$ which pass through isosbestic points $I(\lambda_{min})$ and $I(\lambda_{max})$ of $M(\lambda)$ and $R_{100}(\lambda)$, respectively, so that $m(\lambda_{min}) = M(\lambda_{min})$, $m(\lambda_{max}) = M(\lambda_{max})$, $r(\lambda_{min}) = R_{100}(\lambda_{min})$ and $r(\lambda_{max}) = R_{100}(\lambda_{max})$.

A first transformation $M'(\lambda)$ of the measurement spectrum $M(\lambda)$ can be then written as

$$M'(\lambda) = M(\lambda) + r(\lambda) - m(\lambda) \tag{3.48}$$

where $M'(\lambda)$ is a new spectrum that passes through $R_{100}(\lambda_{min})$ and $R_{100}(\lambda_{max})$, i.e. $M'(\lambda_{min}) = R_{100}(\lambda_{min})$ and $M'(\lambda_{max}) = R_{100}(\lambda_{max})$. This first correction step reduces influences of scattering and non-hemoglobin absorption on $M(\lambda)$. In other words, $M'(\lambda)$ represents spectral variations only due to absorption by hemoglobin.

The second transformation resulting in $M''(\lambda)$ further stretches or compresses $M'(\lambda)$ in order to force $M''(\lambda)$ to pass through the third isosbestic point $I(\lambda_{mid})$:

$$M''(\lambda) = (M'(\lambda) - r(\lambda)) \cdot \frac{R_{100}(\lambda_{mid}) - r(\lambda_{mid})}{M'(\lambda_{mid}) - r(\lambda_{mid})} + r(\lambda) \tag{3.49}$$

This step compensates for experimental setup influences as for instance changes in illumination. $M''(\lambda)$ represents the corrected measurement spectrum and constitutes the basis for all following computations.

The method in Reference [73] computes $M''(\lambda)$ using a fixed set of three isosbestic points, i.e. $I(\lambda_{min}) = 522nm$, $I(\lambda_{mid}) = 569nm$ and $I(\lambda_{max}) = 586nm$ and evaluates the oxygen saturation based on a single additional measurement at 560 nm, which is an oxygen sensitive wavelength. Alternatively, this thesis investigates whether the accuracy of isosbestic methods can be improved by using different isosbetic points, an extended range of oxygen sensitive wavelengths and/or additional transformations beyond the ones applied in Equations 3.48 and 3.49.

The work herein researched methods that could improve the performance of isosbestic methods, a development that was geared towards achieving absolute tissue oxygenation measurements *in-vivo*, using multi-spectral epi-illumination images. One particular aim was to identify a robust method which would account for the increased

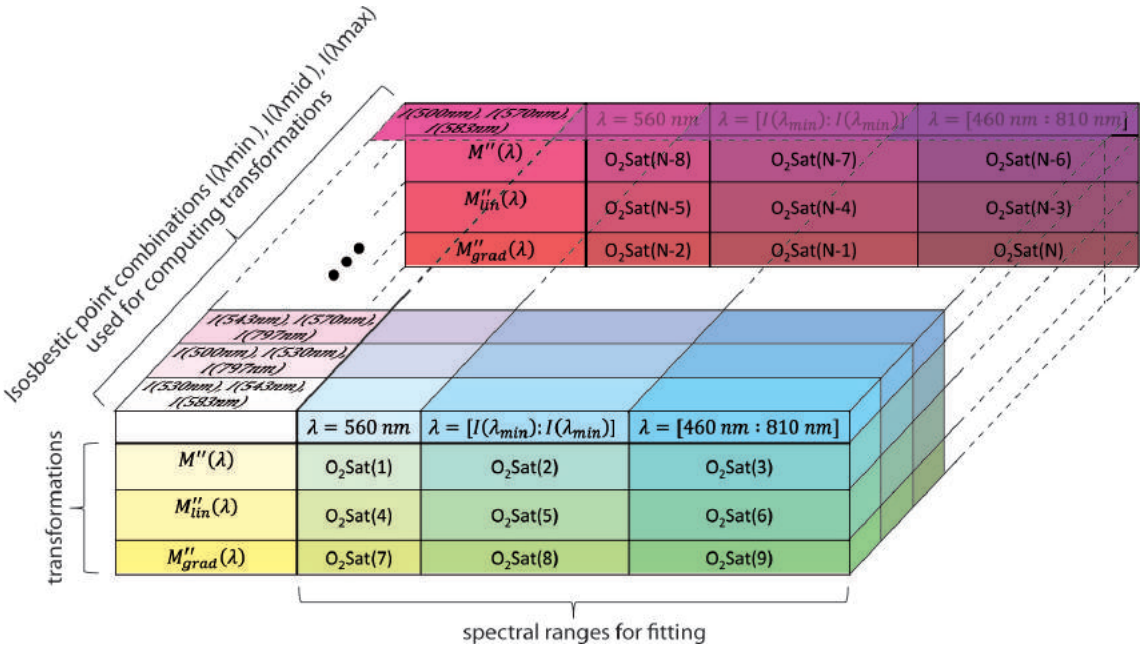

Figure 3.11: Matrix containing N alternative oxygenation values, each computed by employing different transformations (rows), spectral ranges (columns) and isosbestic point combinations (depth).

complexity of *in-vivo* oxygenation detection in arbitrary organs. Increased complexity may arise from (A) increased noise, e.g. due to movement artifacts or shorter exposure times, over *ex-vivo* measurements. Additionally, whole tissue imaging has to handle (B) possibly widely varying scattering and non-hemoglobin absorption compared to measuring single targets such as blood or a blood vessel. Another remedy attempted in the research herein was to improve upon the (C) possibly insufficient measurement sensitivity in the visible range between 500 nm and 590 nm due to the small absolute difference between oxy and deoxy spectral curves, compared to the difference in the red and near-infrared range between 590 nm and 800 nm.

The idea behind this work was that the introduction of alternative isosbestic point combinations and additional spectral transformations could improve the saturation computation accuracy. To examine this hypothesis, a comparison of the effects of including different isosbestic points, different transformations and different spectral ranges on the results of oxygenation computation is conducted herein. Figure 3.11 summarizes the general concept of this approach, which will be outlined in more detail below. Figure 3.11 shows a $(3 \times 3 \times J)$-dimensional matrix where the rows represent three different transformations, $M''(\lambda)$, $M''_{lin}(\lambda)$ and $M''_{grad}(\lambda)$. $M''_{lin}(\lambda)$ and $M''_{grad}(\lambda)$

N° isosbestic point	1	2	3	4	5	6
Wavelength [nm]	500	530	544	570	583	797

Table 3.1: Wavelengths and numbering of isosbestic points considered within this thesis.

are additional transformations applied on $M''(\lambda)$, which will be defined later in this section. The columns represent three different spectral ranges that were used to compute oxygenation. The depth of the matrix represents the different combinations of isosbestic points considered for the computation of Equations 3.48 and 3.49. This third dimension of the matrix (i.e. its depth) can have as many elements as there are isosbestic point combinations for a given wavelength range. For simplicity, only some examples of isosbestic point combinations are given in the matrix. Generally, for a wavelength range containing K isosbestic points and where 3 out of these K points are used, this results in J possible combinations, whereby J is computed by

$$J = \binom{K}{3} = \frac{K!}{(K-3)!3!}$$

The combination of all three transformations with all three spectral ranges and all J isosbestic point combinations provides N alternative ways to compute the oxygenation value of a sample, where $N = 3 \cdot 3 \cdot J$. The N O_2Sat values (i.e. [O_2Sat(1), ..., O_2Sat(N)]) populate the matrix in Figure 3.11. These N values can be evaluated as to the best accuracy by assessing the error between the computed and the real oxygenation value in all N cases. The computed value showing the smallest error defines the ideal method for oxygenation computation. The following paragraphs explain step by step how these N alternatives are computed.

In this study, all possible combinations of 3 isosbestic points lying within the wavelength range between 460 nm and 810 nm were used for the computation of $M''(\lambda)$. In this wavelength range there are 6 isosbestic points and therefore $J = 20$. Table 3.1 lists all isosbestic point wavelengths considered. This approach hence provided 20 alternative versions of $M''(\lambda)$ that could all be used for oxygenation computation and compared to each other as to their ability to accurately provide quantitative oxygenation readings. (Note that the employment of more than 3 isosbestic points would lead to nonlinear distortion of the original spectrum given non-ideal, i.e. noisy, data. This would negate the linear aspect of the applied transformations. For confirmation, the employment of 4 or more isosbestic points was also tested in this study and resulted in completely distorted spectra. These results are however not subject of this thesis.)

Two additional transformations applied to $M''(\lambda)$ are introduced, resulting in two new spectral curves $M''_{lin}(\lambda)$ and $M''_{grad}(\lambda)$. These additional transformations account for points (B) and (C) mentioned above, i.e. widely varying optical properties and insufficient sensitivity.

The first additional transformation subtracts from $M''(\lambda)$ a piecewise linear function $r_{lin}(\lambda)$ that connects all isosbestic points. Given K isosbestc points , $r_{lin}(\lambda)$ can be mathematically written as

$$r_{lin}(\lambda) = \sum_{a=1}^{K-1} r_{a,a+1}([\lambda_a : \lambda_{a+1}]) \tag{3.50}$$

Where λ_a is the wavelength of the a$^{\text{th}}$ isosbestic point, $r_{a,a+1}(\lambda)$ is a linear function going through $M''(\lambda_a)$ and $M''(\lambda_{a+1})$, and $[\lambda_a : \lambda_{a+1}]$ gives the wavelength interval where $r_{a,a+1}(\lambda)$ is defined as non-zero. The function $r_{lin}(\lambda)$ essentially computes a straight line between two neighboring isosbestic points in $M''(\lambda)$.

$M''_{lin}(\lambda)$ is obtained by subtracting $r_{lin}(\lambda)$ from $M''(\lambda)$, i.e.

$$M''_{lin}(\lambda) = M''(\lambda) - r_{lin}(\lambda) \tag{3.51}$$

Accordingly, $R_{lin,100}(\lambda)$ and $R_{lin,0}(\lambda)$ represent the equivalently transformed spectra of $R_{100}(\lambda)$ and $R_0(\lambda)$:

$$R_{lin,100}(\lambda) = R_{100}(\lambda) - r_{lin}(\lambda) \tag{3.52}$$

$$R_{lin,0}(\lambda) = R_0(\lambda) - r_{lin}(\lambda) \tag{3.53}$$

The second additional transformation consists in computing the gradient $M''_{grad}(\lambda)$ of $M''(\lambda)$, i.e.

$$M''_{grad}(\lambda) = \frac{d}{d\lambda} M''(\lambda) \tag{3.54}$$

$$R_{grad,100}(\lambda) = \frac{d}{d\lambda} R_{100}(\lambda) \tag{3.55}$$

$$R_{grad,0}(\lambda) = \frac{d}{d\lambda} R_0(\lambda) \tag{3.56}$$

whereby $R_{grad,100}(\lambda)$ and $R_{grad,0}(\lambda)$ analogously represent the gradients of $R_{100}(\lambda)$ and $R_0(\lambda)$.

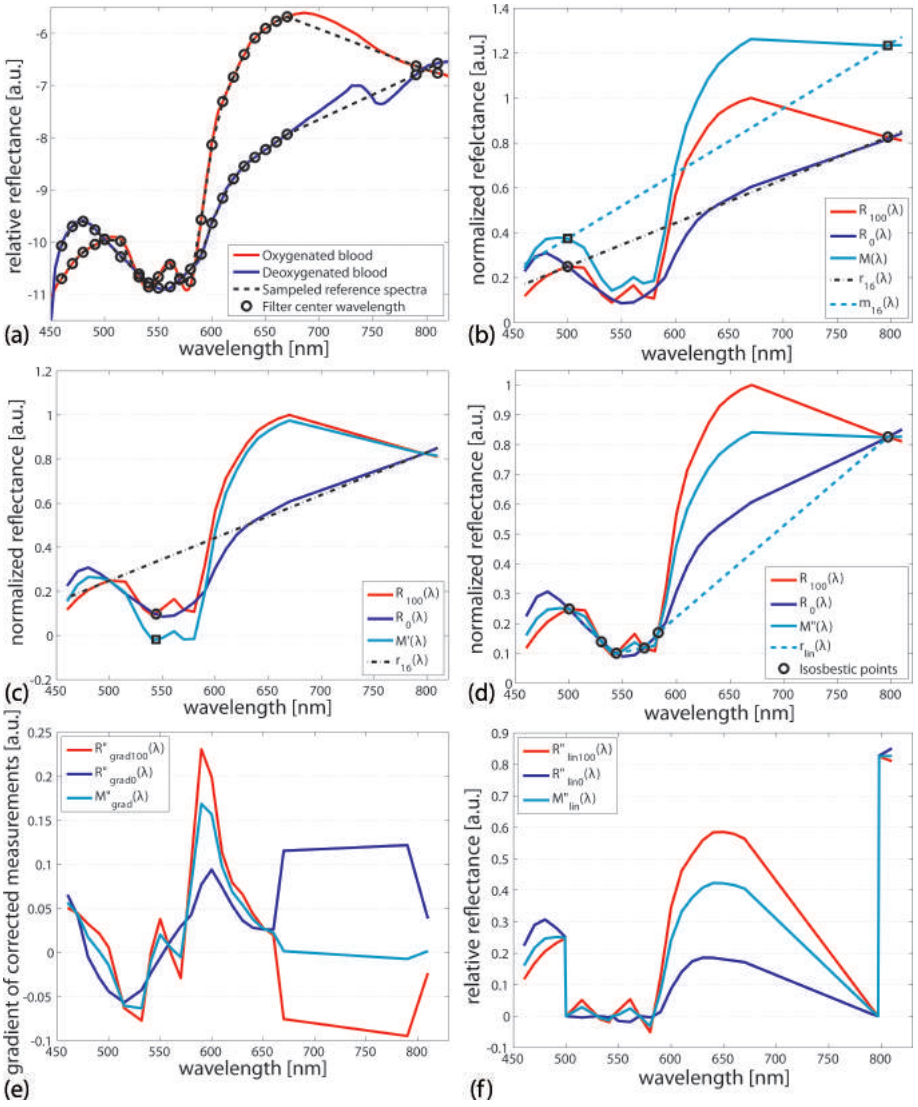

Figure 3.12: Isosbestic point correction method employing isosbestic points at 500 nm, 544 nm and 797 nm.

$M''_{grad}(\lambda)$ emphasizes on the spectral variations in $M''(\lambda)$ and may therefore be more sensitive to small oxygenation changes than $M''(\lambda)$. It is computed to better bring out the variability of $M''(\lambda)$ in the visible range where absolute differences between oxy and deoxy hemoglobin are small. $M''_{grad}(\lambda)$ is employed to investigate whether the increased sensitivity in the visible is advantageous for accurate oxygenation detection.

Figure 3.12 exemplifies the transformations performed in Equations 3.48 to 3.56 for an assumed measurement $M(\lambda)$ of 60% oxygenation, employing isosbestic points $I(\lambda_{min}) = 500nm$, $I(\lambda_{mid}) = 544nm$ and $I(\lambda_{max}) = 797nm$. Since these were the 1st, 3rd and 6th isosbestic points according to their location in the used wavelength range, they

are identified in the following as (1,3,6). Other isosbestic point combinations will be named accordingly.

Figure 3.12(a) depicts the quasi continuous reflectance spectra of oxy and deoxy hemoglobin as well as the sampling points, i.e. the center wavelength of the used filters (circles). The discrete reference spectra $R_{100}(\lambda)$ and $R_0(\lambda)$ resulting from these sampling points are presented as dashed lines. Figure 3.12(b) contains $M(\lambda)$ (cyan), $R_{100}(\lambda)$ (red) and $R_0(\lambda)$ (dark blue), as well as the respective lines connecting $I(\lambda_{min})$ and $I(\lambda_{max})$, i.e. $m(\lambda)$ and $r(\lambda)$. Figure 3.12(c) depicts the transformed spectrum after the first transformation step as computed in Equation 3.48, i.e. $M'(\lambda)$. The isosbestic points that were used in the second transformation for scaling of $M'(\lambda)$ are marked by a circle on $R_{100}(\lambda)$ and a square on $M'(\lambda)$. Figure 3.12(d) shows the transformed spectrum $M''(\lambda)$ as computed by Equation 3.49. Note that although only isosbestic points 1, 3 and 6 were used, the curves overlap in all six isosbestic points (circles) for this ideal case. Figure 3.12(e) shows $M''_{lin}(\lambda)$, $R_{lin,100}(\lambda)$ and $R_{lin,0}(\lambda)$ (Equations 3.51 - 3.53) which are all zero at the locations of the isosbestic points and only show the oxygen sensitive curves between two neighboring isosbestic points. Figure 3.12(f) finally shows $M''_{grad}(\lambda)$, $R_{grad,100}(\lambda)$ and $R_{grad,0}(\lambda)$ (Equations 3.54 - 3.56). It can be observed that the variability of the spectrum between 500 nm and 590 nm is better brought out by $M''_{grad}(\lambda)$ compared to $M''(\lambda)$, therefore increasing the sensitivity to oxygenation changes in this wavelength range.

$M''_{lin}(\lambda)$ and $M''_{grad}(\lambda)$ were computed for all $J = 20$ versions of $M''(\lambda)$, resulting now in $J \cdot 3 = 60$ alternative ways of computing oxygenation (i.e. filling the rows and depth of the matrix in Figure 3.11).

Relative oxygenation was finally computed by spectral fitting to different wavelength ranges using a constrained linear least-squares solver (see Section 3.3.2):

$$\hat{\mathbf{x}}_{oxy} = \min_{\mathbf{x}} \frac{1}{2} \|\mathbf{R} \cdot \mathbf{x}_{oxy} - \mathbf{M}\|_2^2 \text{ such that } 0 \leq \mathbf{x} \leq 1 \tag{3.57}$$

where $\mathbf{M}$ is a matrix or vector taking the spectra $M''(\lambda)$, $M''_{grad}(\lambda)$ or $M''_{lin}(\lambda)$ and $\mathbf{R}$ is a matrix taking the respective reference spectra $[\ R_{100}(\lambda)\ \ R_0(\lambda)\ ]$, $[\ R_{grad,100}(\lambda)\ \ R_{grad,0}(\lambda)\ ]$ or $[\ R_{lin,100}(\lambda)\ \ R_{lin,0}(\lambda)\ ]$. $\mathbf{x}_{oxy}$ represents the original (and usually unknown) oxygen saturation and $\hat{\mathbf{x}}_{oxy}$ contains the estimated relative oxygenation value.

The influence of the employed spectral range on the accuracy of computed oxygenation values was further investigated by introducing varying fitting wavelength ranges (columns in 3.11). Using an extended wavelength range could reduce the influence of noise and measurement inaccuracies in some wavelength. The first considered option computes oxygenation based on only one single value at 560 nm (as in Ref. [73]), the second uses all measurements lying within the wavelength range of the respectively employed isosbestic points, i.e. between $I(\lambda_{min})$ and $I(\lambda_{max})$. The third uses the entire available wavelength range, i.e. 460 nm to 810 nm.

Summarized, the oxygenation was computed using each of the transformations $M''(\lambda)$, $M''_{lin}(\lambda)$ and $M''_{grad}(\lambda)$ according to Equation 3.57, whereby fitting was performed using three different wavelength ranges, $\lambda = 560\,\text{nm}$, $\lambda = [I_{min}(\lambda) : I_{max}(\lambda)]$ and $\lambda = [\lambda_{min} : \lambda_{max}]$. Given $J = 20$ isosbestic point combinations, 3 transformed curves and 3 wavelength ranges for computation of the oxygenation values, this resulted in $J \cdot 3 \cdot 3 = 180$ different ways of computing oxygenation (as presented in Figure 3.11).

The last step in computing absolute oxygenation values based on the relative values provided by Equation 3.57 consisted in finding a mapping curve that maps the relative values to absolute values. We employed a training subset of $M(\lambda)$ with real oxygenation given by $\mathbf{x}_{train}$ and computed $\hat{\mathbf{x}}_{train}$, which is equivalent to $\hat{\mathbf{x}}_{oxy}$ for the training set. The relationship between $\hat{\mathbf{x}}_{train}$ and $\mathbf{x}_{train}$ was determined by finding a polynomial curve $p_{fit}(\hat{\mathbf{x}}_{train})$ through least squares fitting that best maps $\hat{\mathbf{x}}_{train}$ to $\mathbf{x}_{train}$. This step was only performed once for each spectrum in the training set to obtain a general mapping curve $p_{fit}(\hat{\mathbf{x}}_{oxy})$. $p_{fit}(\hat{\mathbf{x}}_{oxy})$ was then saved and directly used for all further computations to map all $\hat{\mathbf{x}}_{oxy}$ values for all measurements presented later in this section and determine the absolute oxygen saturation O_2Sat, i.e.

$$O_2Sat = p_{fit}(\hat{\mathbf{x}}_{oxy}) \tag{3.58}$$

p_{fit} basically represents the relationship between real and computed oxygenation values that may be non-linear due to system specific parameters.

The mean error between the computed O_2Sat and real oxygenation values, i.e. $\mathbf{x}_{oxy}$, were assessed and compared for all curve types $M''(\lambda)$, $M''_{grad}(\lambda)$ and $M''_{lin}(\lambda)$, using all isosbestic point combinations and all wavelength ranges, as were corresponding standard

deviations and maximum errors. The combination of transformed curve, isosbestic points and spectral range showing the smallest mean error was then proposed to be employed in an optimal oxygenation computation method.
Isosbestic point combination $I(530nm)$, $I(570nm)$ and $I(583nm)$ and the oxygen sensitive wavelength 560 nm are included in this analysis, because they are close to the values used in a previous publication for vascular oxygen saturation detection [73]. This allows for the comparison with previously published results.

3.4.2 Evaluation based on tissue mimicking phantom data

The proposed method was evaluated based on measurements acquired from tissue mimicking phantoms. This provided a controlled and reproducible experimental environment with measurements that could be validated.
Phantoms were composed of varying quantities of absorbing and scattering materials in order to obtain different optical properties. Most phantoms were composed of rabbit blood (treated with Ethylenediaminetetraacetic acid (EDTA) against coagulation), intralipid for introducing tissue-like scattering, and sodium chloride (NaCl) solution. Blood volume varied between 2% and 6% of the total phantom volume. Intralipid varied between 0.4% and 2%. This resulted in absorption and scattering properties at 650 nm of $0.04\text{cm}^{-1} < \mu_a < 1.2\text{cm}^{-1}$ and $5.0\text{cm}^{-1} < \mu_s' < 25.0\text{cm}^{-1}$. Different amounts of sodium hydrosulfite (Sigma-Aldrich, USA) were added to the phantoms to obtain different oxygen saturations. The quantities were extracted from [22] and adapted to account for the blood-NaCl mixture. This resulted in a concentration of approximately 0.1 mg sodium hydrosulfite per gramm phantom to fully deoxygenize a phantom. The actual oxygen saturation value $\mathbf{x}_{oxy}$ for intralipid phantoms was measured with a gas analyzer (Combiline, Eschweiler, Germany) right before and again right after the imaging experiment in order to ensure the stability of the oxygen saturation value throughout the experiment, as well as for validation of the computational results obtained from Equation 3.58.
Some additional phantoms were composed of the same components listed above, only replacing intralipid by titanium dioxide (TiO_2). The purpose of this second group was to validate the accuracy of the proposed method in the presence of a different scatterer. This also explored scattering properties lying at the limits of the physiological range in order to assess the continuous accuracy of the proposed method in presence of strong scattering. TiO_2 concentrations were between 2.5 g/L and 5 g/L, resulting in scattering

properties at 690 nm of $20\text{cm}^{-1} < \mu_s' < 40.0\text{cm}^{-1}$ according to [125]. Due to the powdery texture of TiO_2, the phantoms containing this scatterer could not be measured in the gas analyzer. Therefore, only fully oxygenated and fully deoxygenated TiO_2 phantoms were considered.

The liquid phantom mixtures were filled to the brim into flasks (Falcon 353107, Becton Dickinson and Company, USA) containing a magnetic stir bar that was air-tightly closed to avoid oxygen exchange of the phantom with air. The phantom was then placed in the imaging setup on a magnetic stirrer that kept stirring throughout the acquisition process. This prevented the blood and intralipid or TiO_2 to separate and deposit during the experiment. The stirrer was covered by black absorbing tape.
Images were acquired at 23 spectral bands and corrected for exposure times and spectral sensitivity. Mean pixel values lying within a region of interest selected from the images were input as $M(\lambda)$ into the computational process described above.

Figure 3.13 shows spectra of all imaged phantoms before and after isosbestic point correction, for two representative combinations of isosbestic points, (1,3,6) and (2,4,5). Figure 3.13(a) depicts $R_{100}(\lambda)$ and $R_0(\lambda)$ in red and blue, respectively. The two used isosbestic point combinations are numbered and indicated by arrows. Figure 3.13(b) presents all acquired phantom spectra $M(\lambda)$ in light gray in the background. The colored, highlighted spectra represent an example of the influence of different optical properties on the appearance of $M(\lambda)$, given similar oxygen saturation values. The highlighted curves all had oxygenation values of 97%-99%. The same curves are tracked throughout Figures 3.13(b-h) in order to show the changes introduces by the different transformations. The phantom composition for the highlighted curves is given in the legend, where e.g. i1.2/b4 indicates that the respective phantom was composed of 1.2% intralipid and 4% blood. $M''(\lambda)$, $M''_{lin}(\lambda)$ and $M''_{grad}(\lambda)$ using combination 1 are shown in Figures 3.13(c), (e) and (g) and $M''(\lambda)$, $M''_{lin}(\lambda)$ and $M''_{grad}(\lambda)$ using combination 2 are shown in Figures 3.13(d), (f) and (h). The inlays in Figures 3.13(c)-(d) and (f)-(h) each show a zoom into the green/orange part of the spectrum. It can be noticed that corrections using actual measurements did not result in perfect overlay of all $M''(\lambda)$ in the isosbestic points that were not used for transformation. This can be seen for instance in the inlay in Figure 3.13(c) at 570 nm (isosbestic point 4), as well as in Figure 3(d) at 544 nm (isosbestic point 3) and much more strikingly at 797 nm (isosbestic point 6). Therefore, Figures 3.13(e) and (f) show transformed spectra after subtraction of the offset between isosbestic points, i.e. $M''_{lin}(\lambda)$. The differences in $M''(\lambda)$ compared to

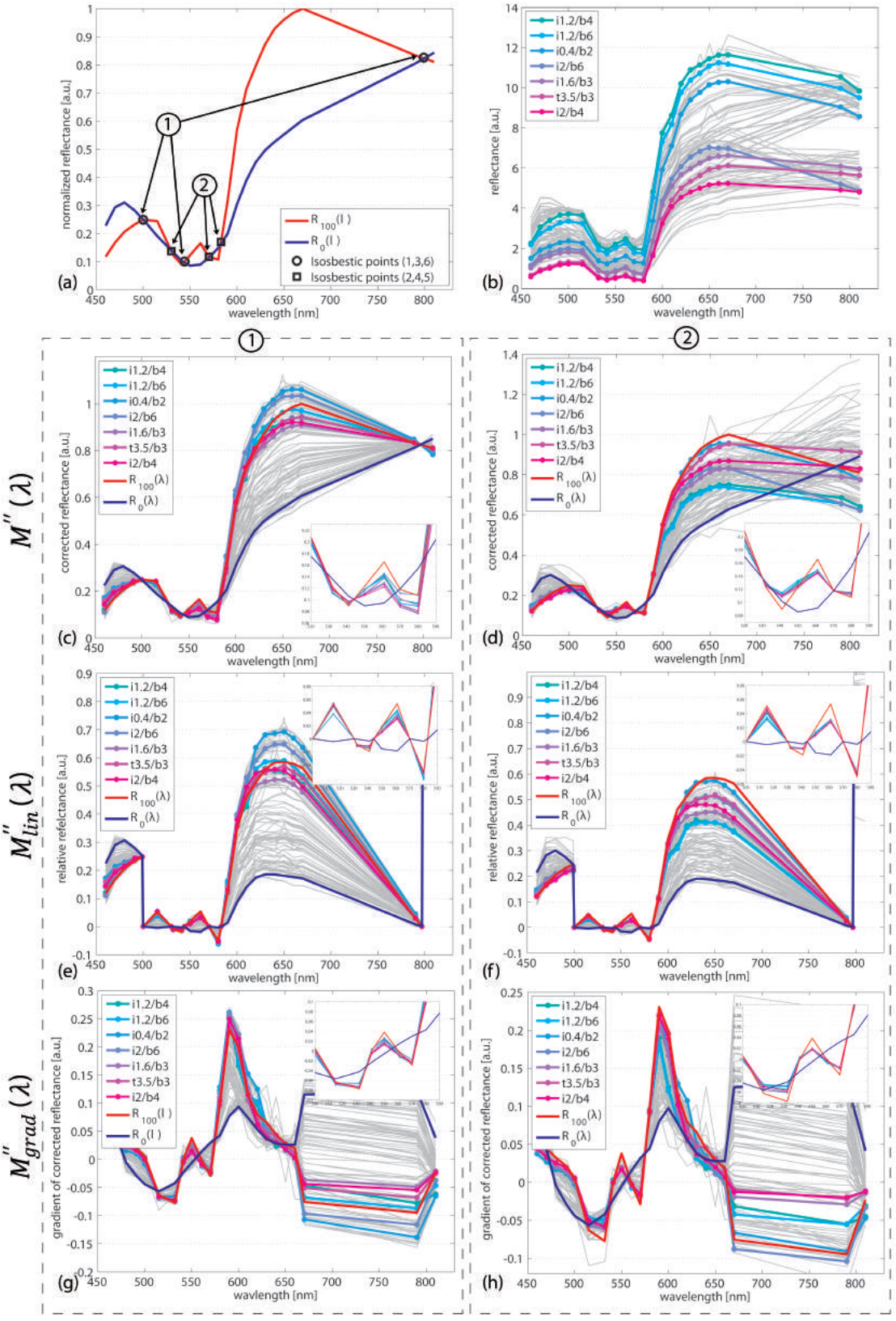

Figure 3.13: Effect of different transformations employing two different isosbestic point combinations on $M(\lambda)$. See text for detailed description of (a) - (h).

$R_{100}(\lambda)$ and $R_0(\lambda)$ due to the isosbestic points used, affect $M''_{lin}(\lambda)$ as can for instance be observed in the relative location of the highlighted curves. For these curves, isosbestic point combination 1 (Figure 3.13(e)) produced transformed spectra which were closer to the reference $R_{lin,100}(\lambda)$ than isosbestic point combination 2 (Figure 3.13(f)). An almost perfect overlap of all highlighted curves among themselves and compared to $R_{grad,100}(\lambda)$ in the range between 500 nm and 590 nm was achieved when using $M''_{grad}(\lambda)$ and isosbestic point combination 1, as finally shown in Figure 3.13(g). Isosbestic point combination 2, shown in Figure 3.13(h), yielded less agreement among the transformed curves.

Figure 3.14 depicts examples for $\hat{\mathbf{x}}_{oxy}$ and O_2Sat computed from the phantom measurements for some representative isosbestic point combinations (indicated above each sub-figure). Figure 3.14(a) depicts as squares the computed $\hat{\mathbf{x}}_{train}$ values obtained from a training subset of phantoms versus the validation measurements $\mathbf{x}_{train}$, as measured with the gas analyzer. These values were obtained using $M''_{grad}(\lambda)$ transformed by isosbestic point combination (1,4,6), and fitting to the entire spectrum, i.e. 460 nm - 810 nm. A polynomial fit to these values is presented as dashed line. The polynomial fit seemed to match data very well, but the computed values underestimated the real oxygenation. Hence, one of the phantoms having fully oxygenated blood was used to calibrate all other phantoms of the training set. The adjusted values resulted in the final O_2Sat for the training set and are depicted as circles. The general mapping line $p_{fit}(\hat{\mathbf{x}}_{oxy})$ that was subsequently used for all phantoms is shown as continuous black line. Figures 3.14(b) to 3.14(e) show O_2Sat versus $\mathbf{x}_{oxy}$ for all phantoms as circles, as well as $p_{fit}(\hat{\mathbf{x}}_{oxy})$ as a continuous line. Figure 3.14(b) shows O_2Sat computed using $M''_{grad}(\lambda)$ transformed by isosbestic point combinations (1,4,6) and fitting to the entire spectrum. Figure 3.14(c) shows O_2Sat computed using the same transformation and isosbestic points like in 3.14(b), but only using the value at 560 nm for oxygenation computation. Figures 3.14(d) and 3.14(e) show the equivalently computed O_2Sat values as in 3.14(b) and 3.14(c), respectively, when using isosbestic points (2,4,5). It can be observed that O_2Sat values do not fall along $p_{fit}(\hat{\mathbf{x}}_{oxy})$ in Figures 3.14(c) and (e), i.e. when using only the wavelength 560 nm for O_2Sat computation. Individual polynomial fitting curves adapted to these two data sets are represented as dashed lines. The mean errors, as well as the standard deviation achieved with these isosbestic point combinations and fitting ranges are written in the corner of each graph, e_g being the error obtained with $p_{fit}(\hat{\mathbf{x}}_{oxy})$, and e_i being the error obtained using the individual fitting lines for mapping. It can be observed that all error values increase when using isosbestic combination (2,4,5)

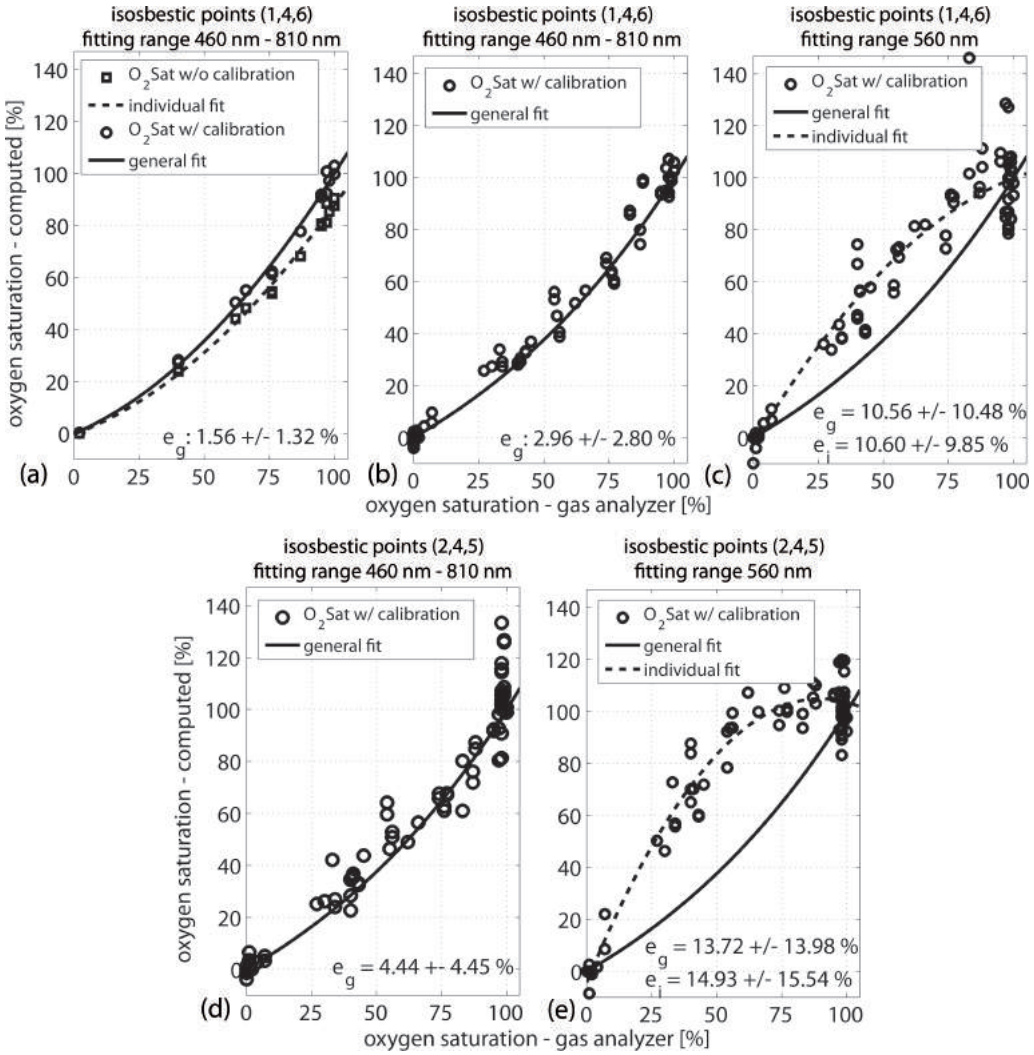

Figure 3.14: Fitting line p_{fit} and evaluation of oxygen saturation computation errors for two representative isosbestic point combinations. See text for detailed description of (a) - (e).

compared to (1,4,6). Using an individual fit that is better adapted to the computed O_2Sat values instead of using $p_{fit}(\hat{\mathbf{x}}_{oxy})$, also did not improve on the mean error.

Figure 3.15 depicts the errors obtained using $M''(\lambda)$, $M''_{lin}(\lambda)$ and $M''_{grad}(\lambda)$ for all isosbestic point combinations and fitting wavelength ranges. Figures 3.15(a)-(c) show the mean errors between $\mathbf{x}_{oxy}$ and O_2Sat and standard deviations in percent oxygenation computed for $M''(\lambda)$ (blue), $M''_{lin}(\lambda)$ (red) and $M''_{grad}(\lambda)$ (black) using each isosbestic point combination (x-axis). The circles indicate the maximum error that was achieved with the respective isosbestic point combination and curve type. Figure 3.15(a) shows the errors using the entire spectrum for fitting, Figure 3.15(b) using only the respective

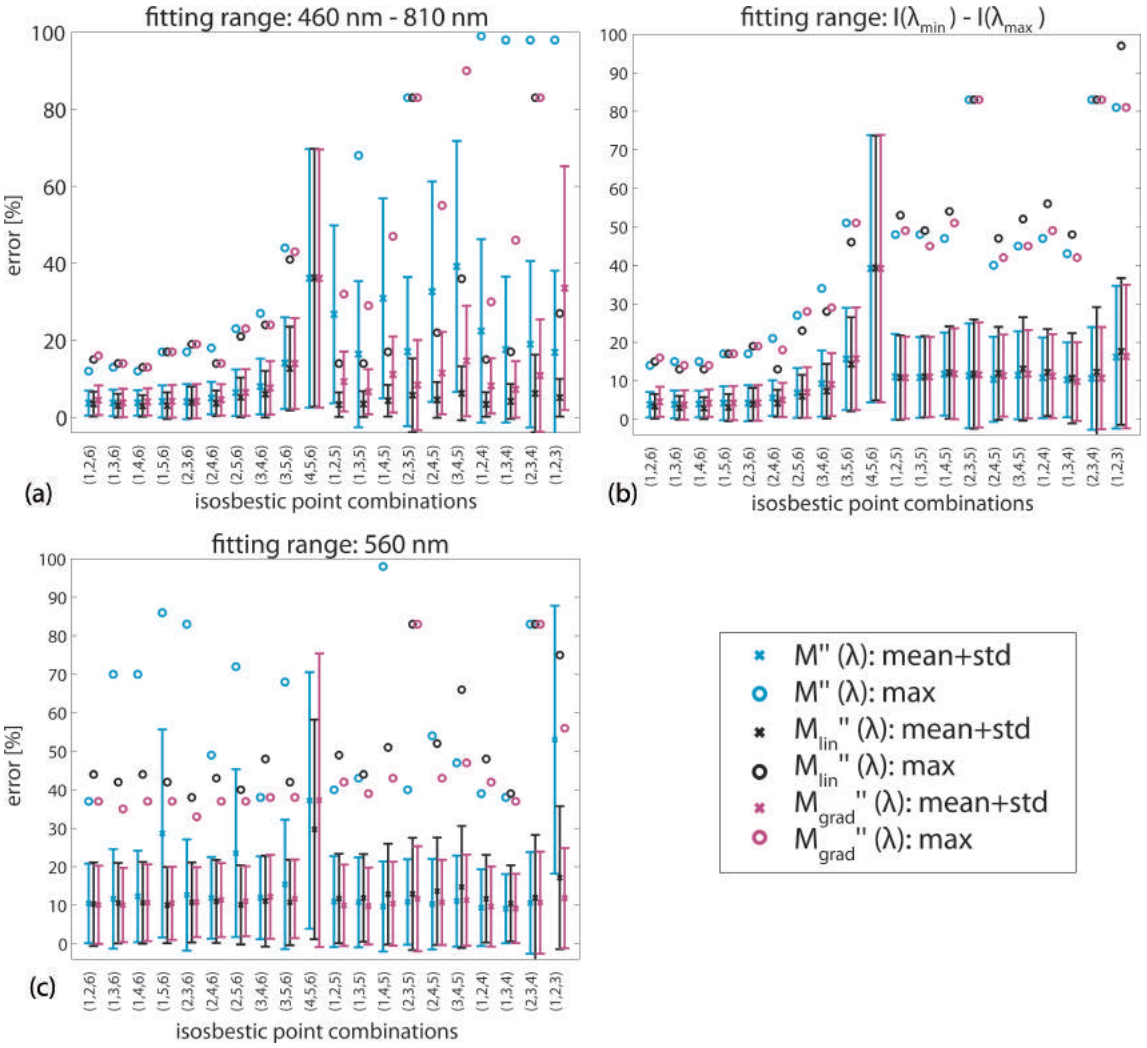

Figure 3.15: Evaluation of oxygen saturation computation errors for all isosbestic point combinations (x-axis), all spectral fitting ranges (a-c) and all spectral transformations (cyan, black, magenta, see legend).

spectrum between $I(\lambda_{min})$ and $I(\lambda_{max})$ and Figure 3.15(c) exclusively using the value at 560 nm . Note that the employment of isosbestic points (2,4,5) would result in a similar procedure as used by Hammer et al. [73]. The exclusive use of the value at 560 nm after transformation with (2,4,5) would hence reproduce as closely as possible their method, of course still considering that there is difference in the measurement setup and imaged tissue.

Employing the entire spectrum for O_2Sat computation resulted in smallest errors when the distance between $I(\lambda_{min})$ and $I(\lambda_{max})$ was high and isosbestic point 6 in the NIR at 797 nm was one of the three isosbestic points used. In this case $M''(\lambda)$, $M''_{lin}(\lambda)$ and

$M''_{grad}(\lambda)$ all showed similarly good results, the smallest error being of 2.96 +/- 2.80 % using (1,4,6) and $M''_{grad}(\lambda)$. The approach where only isosbestic points in the visible spectrum were used also displays smallest errors when employing $M''_{grad}(\lambda)$. Note for instance the error for (1,2,5) being 3.25 +/- 3.04 %, which is similarly small as the errors using combinations including isosbestic point 6.
Reducing the fitting wavelength range to the wavelengths between $I(\lambda_{min})$ and $I(\lambda_{max})$ (Figure 3.15(b)) did not significantly affect the errors for those combinations including isosbestic point 6. The smallest error of 2.90 +/- 2.82 % was still achieved using (1,4,6) and $M''_{grad}(\lambda)$. Isosbestic point combinations that did not include the NIR region now, however, had a significantly reduced wavelength range for fitting of at most 500 nm - 583 nm. The errors for these combinations increased for $M''_{grad}(\lambda)$, but were partly smaller when using $M''(\lambda)$ and $M''_{lin}(\lambda)$. The error at (1,2,5) using $M''_{grad}(\lambda)$ also increased to 11.00 +/- 11.02 % now that only a reduced spectrum was available for fitting.
Using one single wavelength for O_2Sat computation finally resulted in similarly high errors for almost all isosbestic point combinations.

It is noticeable that the combination (4,5,6) resulted in the worst errors in all cases. High errors are due to the fact that $r(\lambda)$ (see Equation 3.48) between the 4th and 6th isosbestic point already almost passes through isosbestic point 5. This affects the second transformation step drastically since the denominator in Equation 3.49 can become close to zero or negative, thus either producing infinitely high results or changing the sign of the problem. It is clear that such a setting cannot be used with our correction method. It was however included for completeness.

Different conclusions can be drawn from the analysis of the errors presented in Figure 3.15: Using the entire available measurement spectrum for data fitting, best results were always obtained with $M''_{grad}(\lambda)$. Figure 3.12(f) already indicated that curve variations could be detected with higher sensitivity in the wavelength range between 500 nm and 580 nm when using $M''_{grad}(\lambda)$. This was confirmed by the results presented in Figure 3.13, where almost perfect overlap of $M''_{grad}(\lambda)$ and $R_{grad,100}(\lambda)$ could be obtained in Figure 3.13(g). Furthermore, smallest error values of less than 3% were obtained for isosbestic combinations where $I(\lambda_{min})$ and $I(\lambda_{max})$ lay the furthest apart, i.e. (1,4,6) or (1,3,6), as shown in Figure 3.15. Some of the combinations that did not employ isosbestic point 6 also reached relatively low error values, as for instance (1,2,5), when using the whole spectrum for fitting. The results from these combinations still relied on the NIR spectrum since the values in the NIR also influenced the fitting result.

When employing only the part of the spectrum lying between the respective $I(\lambda_{min})$ and $I(\lambda_{max})$ used for transformation, isosbestic point combinations like (1,4,6) or (1,3,6) still performed best and error values stayed almost unchanged. This was expectable, since in this case the range between isosbestic points covers most of the available wavelengths range, i.e. 500 nm - 797 nm. I.e. the available fitting data was not strongly reduced. The combinations without NIR isosbestic points that performed well when employing the entire wavelength range for fitting, like (1,2,5), however, resulted in an increased error when their fitting data range was reduced. This suggests that even if the appearance of the transformed spectra in the NIR seemed disordered when omitting the use of isosbestic point 6 for correction (Figure 3.13(d)), the curve shape in the NIR region was still indicative for oxygen saturation and added important input to its computation.
Finally, the errors when employing only the oxygen sensitive wavelength 560 nm were all similarly high lying around 10%, while in some cases errors were particularly high like for (1,5,6).

Combing all findings from the three curve types $M''(\lambda)$, $M''_{lin}(\lambda)$ and $M''_{grad}(\lambda)$ leads to the suggestion, that best results can always be obtained employing $M''_{grad}(\lambda)$ and using isosbestic point combinations that include both wavelengths in the NIR and visible range. Using only data in the visible increases the error significantly. However, reducing the influence of the blue and green spectrum to its minimum by choosing three of the highest isosbestic points for correction resulted in increased errors as well. This suggests that only having information from the red part of the spectrum is also not sufficient. The combination of the variability of the spectra in the visible, where oxy and deoxy hemoglobin rise and fall alternatingly, and the different slope of the curves in the red and NIR region is important to obtain accurate and quantitative oxygenation readings.
Figure 3.16 summarizes the concepts of the approach developed herein, from the method proposed by Hammer et al. [73] (a), to the alternative oxygenation computation approaches investigated herein (b), to the finally proposed optimal computation method (c). All steps run through are numbered in order, where same numbers in different processes (i.e. Figure 3.16 (a), (b) or (c)) indicate equivalent steps. The adopted computational concepts from other publications are highlighted in red.

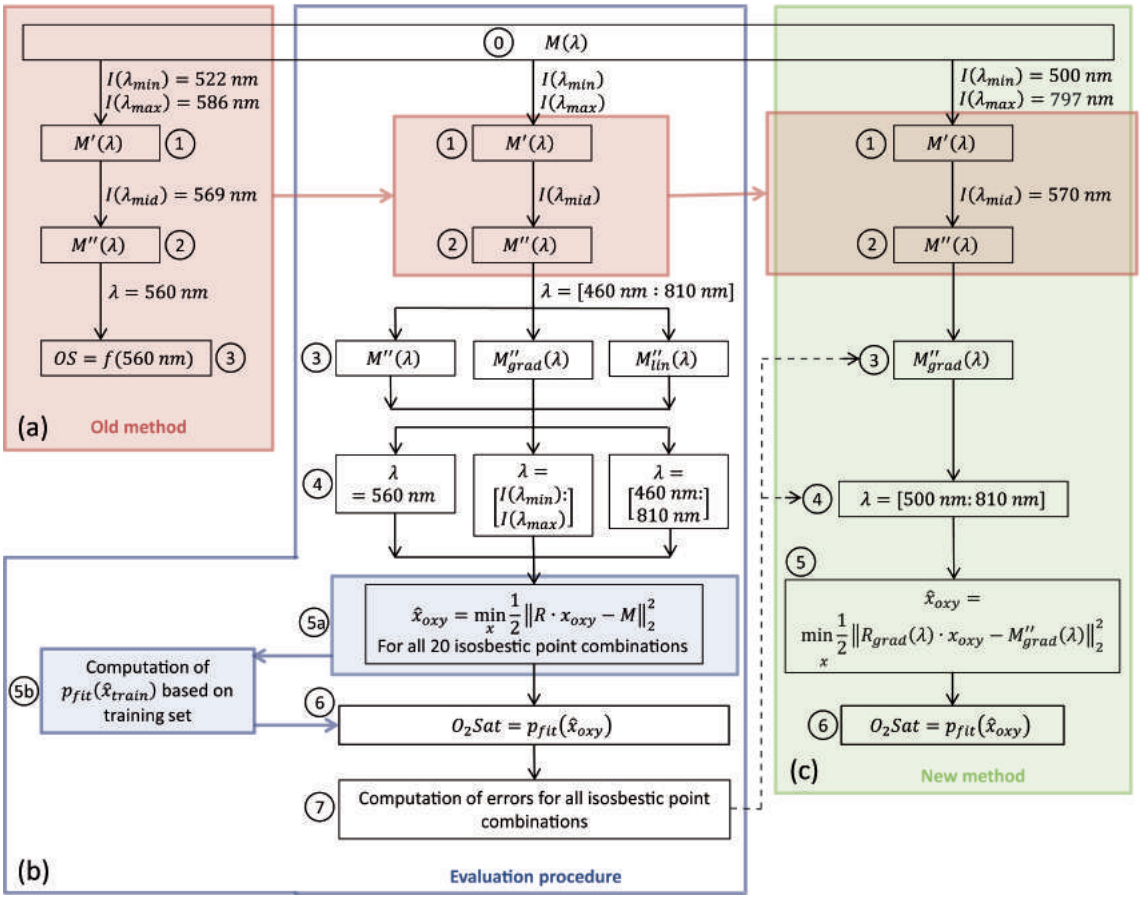

Figure 3.16: Schematic of oxygen saturation computation methods. (a) Method as proposed by [73]. (b) Methodology for finding optimal oxygen computation method. (c) Proposed optimal solution.

3.4.3 Translation to *in-vivo* applications

Finally, the findings from the phantom study were applied to three pilot experiments in real tissues. I.e. O_2Sat was computed using $M''_{grad}(\lambda)$ and employing the best identified isosbestic point combination for correction, i.e. (1,4,6).

The method proposed in Figure 3.16(c) was tested for the detection of changes in three different real tissue scenarios: in a finger subjected to vascular occlusion, in vascular imaging in a mouse ear and in an intraoperative context by imaging different exposed organs. Due to movements of the experimental subjects semi-automatic coregistration of the images was performed prior to image analysis. For the computation of oxygen saturation, regions of interest were then chosen in the tissues and mean values of the

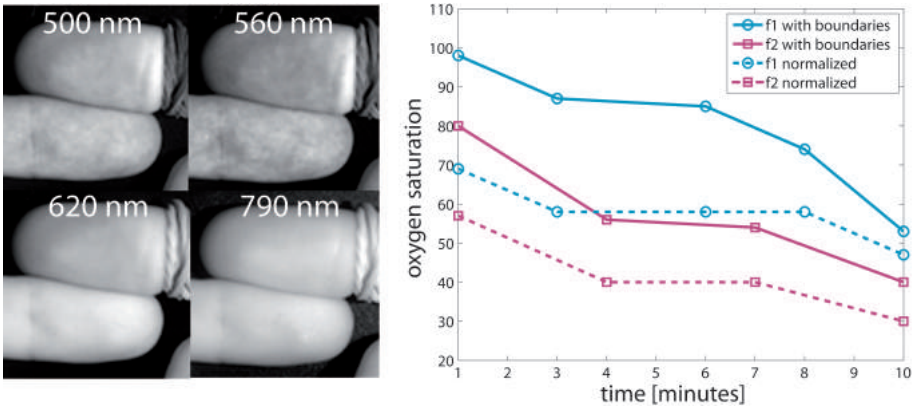

Figure 3.17: Decrease of oxygen saturation over time in fingers subjected to vascular occlusion.

contained pixels were further used as spectra $M(\lambda)$ in Equation 3.48.

Vascular occlusion was achieved by placing an elastic strap around the index finger of one hand of a volunteer. The occluded index was placed together with the second, normally perfused index finger under the lens of the imaging system directly after fitting of the elastic strap. A complete set of multispectral images was acquired every 2-4 minutes for 10 minutes in total.
Figure 3.17 depicts in the graph the computed decrease in O_2Sat in occluded fingers over the time period of 10 minutes in two volunteers. Two different curves are shown per finger, one displaying the O_2Sat values as computed by Equation 3.58 (continuous lines), the other using the non-occluded finger for normalization (equivalent to the calibration used for the phantoms). The images on the left give an example of the relative change of absorption appearance at different wavelengths.

For the measurement of superficial arterial and venous oxygen saturation, nude mice were anesthetized using i.p. injection of Ketamine-Xylacine and placed under the lens of the imaging system so that one ear lay in the field of view of the camera. A catheter was introduced into the tail vein in order to euthanize the mice during the imaging process without changing their position. Complete sets of multispectral images were acquired *in-vivo*, directly after the administration of a lethal dose of Ketamine-Xylacine and 20 minutes after death.
For the computation of oxygen saturation in ear vasculature optical density spectra were used. Optical density spectra were obtained by dividing pixel values in the vessels by pixel values of surrounding tissue close to the vessels [44, 78].

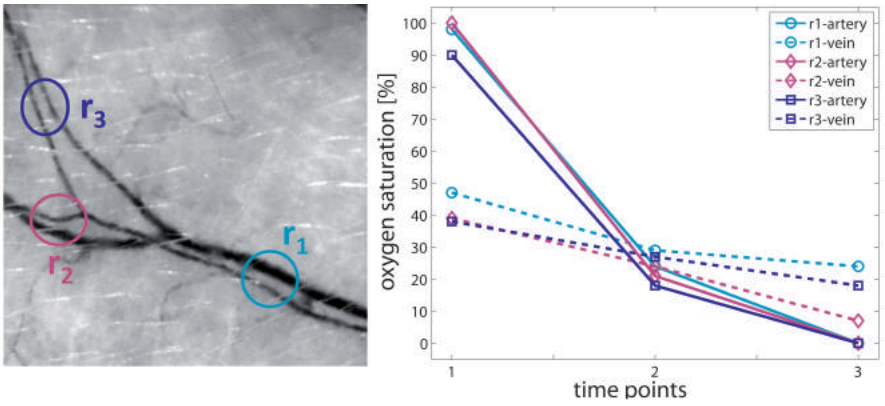

Figure 3.18: Arterial and venous oxygen saturation in a mouse ear *in-vivo* (1), after death (2) and *ex-vivo* (3).

Figure 3.18 depicts the results of the computation of O_2Sat in arteries and veins in a mouse ear. O_2Sat values are shown in the graph over three time points - *in-vivo*, right after euthanasia, and 20 minutes after death. The three sampled regions are shown in the image on the left.

For organ oxygenation measurements in intraoperative imaging, CD1 mice were anesthetized and their abdomen opened to expose different organs. Analogously to the ear experiment, the organs were imaged *in-vivo* and post mortem after euthanasia via a catheter. During the *in-vivo* acquisitions, mice were subjected to a respiratory change from normal air to 100% O_2. After approximately 8-10 minutes of baseline measurements with normal air, 100% O_2 was turned on for approximately 15 minutes. After this period O_2 was turned off and mice returned to breathing of normal air. The mice were euthanized another 12 minutes later and were imaged *ex-vivo* for 15 minutes. Complete sets of multispectral images were acquired every 2-4 minutes.
Figure 3.19 presents the change of O_2Sat in five different organs measured in two mice: pancreas, kidney, spleen, stomach and intestine. The five regions are indicated in the image at the top left. The absorption appearance at a second wavelength is equally displayed. The graphs for the five organs each show O_2Sat over time. The time points for switching on and off of O_2 are indicated by vertical lines, as well as the time of euthanasia. A clear increase in oxygen saturation can be observed in intestine and spleen for both mice after turn on of O_2 and a significant drop after euthanasia. Kidney and stomach show some fluctuations when breathing normal air and O_2 but an increase is nevertheless perceptible, as well as the drop after euthanasia. In the pancreas area, increase of O_2 seemed to affect O_2Sat the least, but euthanasia again is clearly visible in the curves.

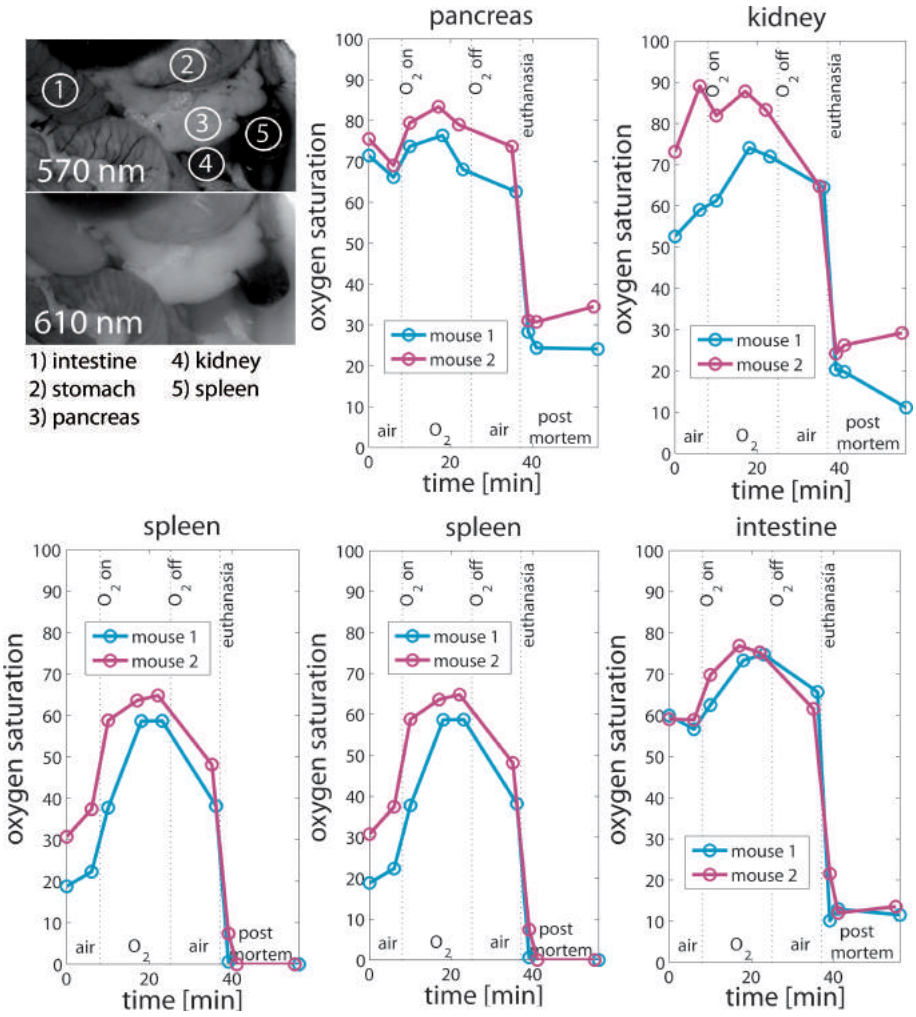

Figure 3.19: Oxygen saturation of different organs of mice breathing room air, 100% O_2 and after euthanasia.

To conclude, in all three experimental cases oxygenation changes over time were observed. Dynamical O_2Sat changes corresponded to the expectations. O_2Sat dropped the longer the fingers stayed occluded. A difference in arterial and venous oxygen saturation in a mouse ear was computed *in-vivo* and both values dropped after death. And organ oxygenation values mainly increased when mice breathed 100% O2 in comparison with normal air, and a steep drop was observed after death.

3.4.4 Discussion and conclusion: Oxygenation computation

The aim of this study was the development of a robust tissue oxygenation detection method that is independent of the influence of any tissue optical properties other than absorption by hemoglobin. This was achieved by spectral transformations based on isosbestic points which enabled corrections purely based on experimental data. This data-driven approach overcomes the need for elaborate modeling of tissue structure and properties on a per-tissue basis. Particularly, the aim consisted in applying such a method to multispectral imaging data, providing both spatial and spectral information, without significantly compromising acquisition time. Since the proposed approach is predominantly little affected by tissue properties and the specific imaging setup, it could be applicable to many biological and medical areas, like in superficial detection of skin abnormalities, for intraoperative applications to monitor tissue well-being during surgery, or in retinal imaging. The study adapted and optimized a reflectance spectrum correction method, which was initially developed for the detection of whole blood oxygen saturation in superficial vasculature [73]. The investigations presented herein allow the extension of this concept to general tissue oxygenation detection problems in epi-illumination imaging setups. The found optimal oxygenation computation method employs isosbestic points at 500 nm, 544 nm and 797 nm for the first two transformation steps (Equations 3.48 and 3.49). Oxygenation is then computed using the gradient curve $M''_{grad}(\lambda)$ and the spectrum between 500 nm and 797 nm. This conclusion was reached by an iterative process employing different combinations of isosbestic points, transformations and spectral ranges. All possible isosbestic point combinations and the resulting transformed spectral curves $M''(\lambda)$ were investigated and compared. Furthermore, two additional transformations were introduced, namely $M''_{grad}(\lambda)$ and $M''_{lin}(\lambda)$, in order to evaluate which curve bares the most accurate oxygenation information. For each of the combinations and curves, the relative oxygen saturation values $\hat{\mathbf{x}}_{oxy}$ were computed by spectral fitting to reference spectra of oxygenated and deoxygenated hemoglobin. The best mapping relationship $p_{fit}(\hat{\mathbf{x}}_{oxy})$ between computed and real oxygenation was found based on a training subset of the phantom measurements. $p_{fit}(\hat{\mathbf{x}}_{oxy})$ was used for mapping of all values resulting in the absolute oxygenation O_2Sat. Errors between O_2Sat and $\mathbf{x}_{oxy}$ were determined to assess the performance and conclude on an optimal isosbestic point combination and transformation method.

Compared to the observations by Hammer et al. [73], the proposed approach found that the use of an isosbestic point in the near-infrared and fitting for a larger wavelength

range improves the accuracy and is better suited for retrieving oxygen saturation measurements from tissue. Hammer et al. obtained errors of less than 3% when only investigating vascular oxygen saturation. Equivalently, their approach was reproduced herein employing similar isosbestic points, i.e. isosbestic point combination (2,4,5), and computing tissue oxygenation based on the value of $M''(\lambda)$ at 560 nm. The error obtained with this combination for the tissue phantoms was around 10%, while the alternative approach using the NIR isosbestic point resulted in an error of less than 3%. This suggests that the approach using the NIR isosbestic point is more robust and can be applied more widely to general tissue imaging.

The work presented in this study can be extended in various directions. The validation of the proposed method in different tissues and body regions remains the most important task for future investigation. The pilot tissue experiments presented herein were performed to give an indication as to possible applications of the developed isosbestic point method. While the results presented show that relative changes can be well assessed in such different tissues as finger, ear and organs, these results have not yet been validated as to their quantitative accuracy. In all three cases, an independent validation of the real oxygenation through different modalities would be appropriate. This however lies beyond the scope of the current study, where the focus lay in methodological development and evaluation, and should be subject of future studies.
Further work should also focus on optimizing the used wavelengths and hence filters in order to obtain a minimal filter set that still provides all necessary curve points, but reduces data acquisition as much as possible. One first reduction was already shown in this study, where all measurements below the first isosbestic point at 500 nm could be discarded, as shown by the error comparison in Figures 3.15(a) and (b). Such wavelength reduction would accelerate the acquisition process, which can be crucial in some applications like for instance intraoperative imaging. Not only would changes be detected faster, but movement artifacts would also be smaller and easier to handle. The combination of the isosbestic point method with good, fast and, according to the application, real time coregistration methods and motion flow algorithms would enable a pixel wise oxygenation computation. This would result in real-time, dynamic oxygen saturation maps of entire imaged tissue regions.

Several limitations are present in this study that may restrict the translation of the quantification ability from phantoms to real tissue. While the phantoms employed herein were homogeneous, real tissue hardly ever is. It is well known for instance that skin is

composed of different layers having different absorption and scattering properties [204], or that kidneys have different tissue oxygenation in the cortex and the medulla [25]. The proposed method computes the general oxygenation of the sum of all layers, assuming that they would react similarly when subjected to changes in oxygen supply. It remains to be validated if this assumption is sufficient by more thorough experimental tissue studies . Furthermore, light of different wavelength penetrates to different depth, especially when comparing the visible and NIR region. If oxygenation values in different tissue layers change differently, this may affect the computed oxygen saturation values when using isosbestic points in both the visible and NIR. While this should not affect relative O_2Sat change measurements, it may influence the quantification in certain either very thin or very heterogonous tissues. Thus, this may limit the applicability of the method to certain areas or require calibration measurements prior to the actual experiment.

To conclude, this section showed the optimization and evaluation of a method for quantitative oxygenation measurements independent of non-hemoglobin tissue optical properties, which is purely data based and does not rely on any modeling or assumptions about the tissue. Such a method enables the application of the same kind of imaging setup and methodology to many different medical areas, and reduces the need for dedicated hardware and algorithmic development for each single application case. Tissue oxygenation is an important indicator for many abnormalities in the human body and reliable and accurate measurements are of highest importance. The proposed method can help laying the foundation for quantitative oxygen measurements in many diagnostic medical fields.

3.5 Multispectral image analysis II: Detection of multiple fluorescent labels

This section shows the results obtained from employing the multispectral fundus camera introduced in Section 3.2.2 to mice expressing multiple fluorochromes. First, imaging of single fluorochrome expression is shown *in-vivo* and *ex-vivo* in order to evaluate whether the developed system provides sufficient spatial resolution and spectral sensitivity to resolve varying spatial distributions and different fluorescence intensities. Then, the application of BSS and SVM classification, as introduced in Section 3.3, is shown. Their respective efficiency in separating overlapping spectra acquired *in-vivo* is evaluated. The

multi-spectral capabilities of the fundus camera are furthermore evaluated by imaging and quantifying intravascular oxygenation in the mouse fundus, employing the isosbestic point methods previously described in Section 3.4. Finally, after having evaluated the system capabilities on single or double fluorochrome mice, first results from multispectral mice simultaneously expressing five different fluorochromes *in-vivo* are shown.

3.5.1 Experimental animals and procedures

Two transgenic mouse models were employed in this study. The first mouse line expresses YFP in the ganglion cells under the $Thy1$ promoter (B6.Cg-Tg(Thy1-YFP)16Jrs/J, The Jackson Laboratory, Bar Harbor, ME, USA) [50]. The second mouse line expresses GFP in the microglia due to the replacement of the CX3XR1 gene by a GFP reporter gene (B6.129P(Cg)-Ptprc^{a}Cx3cr1^{tm1Litt}/LittJ, The Jackson Laboratory) [96]. Please refer to Figure 3.1 for an overview of retinal anatomy and cell types.

Additional fluorescent markers were delivered to the retina by adeno-associated viral (AAV) vectors (provided by Dr. Stelianos Michalakis, Department of Pharmacy, Faculty of Chemistry and Pharmacy, Ludwig-Maximilians-Universität, Munich, Germany). pAAV-hSyn-Cheta-mCherry is an AAV-vector driving localized expression of mCherry fluorochrome on the plasma membrane of different types of neurons under the control of human Synapsin. Peak excitation of mCherry is at 587 nm and peak emission at 610 nm. pAAV2.1-sc-EF1a-eGFP is an AAV-vector driving expression of eGFP in a variety of cells in the retinal pigment epithelium and inner nuclear layer under the promoter $EF1a$ (elongation factor 1a) [107]. For viral transfection, 1 µL of the respectively employed vector was injected intravitreally into the mouse eye. Imaging of viral vectors was performed between 1 and 3 month after injection.

A targeted probe (scVEGF/Cy, SibTech Inc., Brookfield, CT, USA) was used for investigating vascular endothelial growth factor (VEGF) expression. VEGF is a signal protein which stimulates blood vessel formation. Overexpression of VEGF can result in a variety of retinal diseases and was for instance associated with glaucoma [2]. scVEGF/Cy is derivatized with Cy5.5 fluorescent dye and was originally intended for imaging mouse tumor neovasculature. Its labeling potential in retinal tissue has, to the best of the author's knowledge, not yet been explored. 1 µL of 150 µg/mL scVEGF/Cy was injected intravitreally 24 hours prior to imaging.

Vasculature was labeled with either indocyanine green (ICG, Pulsion Medical Systems, Munich, Germany) or fluorescein (FITC, Sigma, Saint Louis, MO, USA), both injected via catheter into the tail vein (100 nmol of ICG and 5.3 nmol of FITC in 100 µL, respectively). ICG has peak excitation at around 800 nm and peak emission at around 830 nm. FITC has similar excitation and emission characteristics as GFP. Both ICG and FITC are frequently employed as contrast agents in angiography, also in human medicine.
In total, this provided five different fluorescence emission bands induced by different labeling mechanisms: GFP/FITC, YFP, mCherry, Cy5.5 and ICG.

For *in-vivo* imaging mice were anesthetized with Isoflurane (Isoflurane 2%, O_2 0.9 L/min). The pupils were dilated by applying a drop of 0.5% Tropicamide (Mydriaticum Stulln UD, Pharma Stulln GmbH, Stulln, Germany) on the cornea. Transparent eye gel (Vidisic, Bausch & Lomb, Madison, NJ, USA) was subsequently applied on the eye to avoid drying out of the cornea. This gel also served as coupling medium between the tip of the fundus camera and the mouse eye. The mice were then placed in front of the fundus camera, one eye being in contact with the endoscope. Multispectral images were acquired employing the respectively appropriate light sources and emission filters.

After *in-vivo* imaging, mice were euthanized and the retinae excised for *ex-vivo* validation. The retinae where mounted on slides either as flat mounts or as cross sections and imaged either with a fluorescence microscope or with the non-contact multispectral system described in Section 3.2.1.

3.5.2 Imaging of single fluorochrome expression

For evaluation of the spectral sensitivity and resolution of the fundus camera, each of the fluorochromes was separately imaged in individual mice. This allowed for the observation of pure emission patterns without crosstalk between fluorochromes.

Figure 3.20 shows in the top row *in-vivo* images of five single fluorochrome expression patterns and in the bottom row microscopy images of the respective *ex-vivo* flat mounts. It can be observed that the multispectral fundus camera provides sufficient resolution for capturing very different expression patterns, as for instance shown in the two transgenic mice. *In-vivo* microglia images show localized GFP expression while

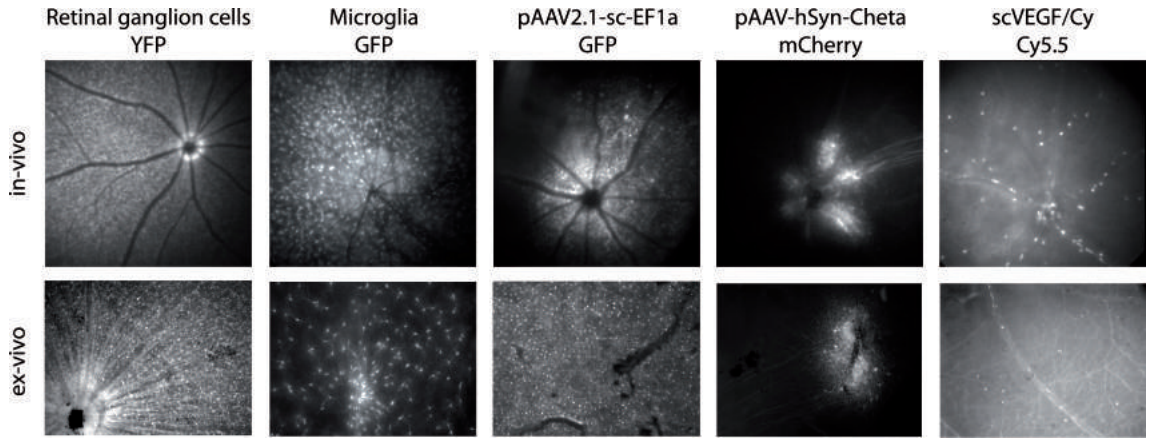

Figure 3.20: *In-vivo* and *ex-vivo* fluorescence emission patterns of five different fluorochromes / fluorescent proteins in the mouse retina.

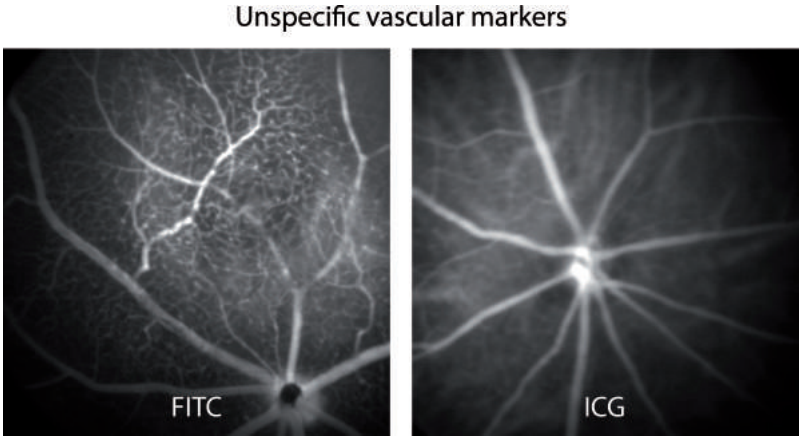

Figure 3.21: Fluorescence angiography in the mouse retina employing two different fluorescent dyes.

RGCs seem to cover almost the entire retina, resulting in uniform YFP expression . *Ex-vivo* images confirm these expression patterns.

The two employed AAVs were expected to transfected different cells of the retina and indeed showed very different distribution patterns *in-vivo*. This distribution pattern was confirmed *ex-vivo*, which also allowed the identification of the labeled cell types. While the GFP-AAV seemed to be expressed on the whole retina by bipolar cells, the mCherry-AAV selectively labeled the membranes of a subtype of ganglion cells.

In-vivo images of the targeted VEGFR-2 probe finally showed labeling of the retinal vasculature, as well as increased signal intensity in several localized spots along the blood vessels. *Ex-vivo* imaging confirmed this observation.

Figure 3.21 depicts the fluorescence intensity acquired in the retinae of two pig-

mented mice after i.v. injection of different vascular markers. Comparing ICG and FITC in the vasculature leads to the conclusion that FITC can be imaged with higher resolution than ICG. This is because light penetrates less deep in the green than in the NIR spectral range. Therefore, FITC images display less contribution of fluorescence originating in choroidal vasculature and hence less diffusion than ICG images. Since the vascular probes FITC and ICG are nonspecific dyes and do not bind to a target molecule, they are washed out by the blood stream and are therefore not present *ex-vivo*.

Figures 3.20 and 3.21 show that beyond different expression patterns, also different fluorescence intensities can be captured by the fundus camera. GFP expression in CX3CR1-GFP mice for instance was very weak in comparison to YFP expression in Thy1-YFP mice, or to FITC emission intensity. Significantly higher exposure times were necessary to image CX3CR1-GFP given the same illumination intensity. Appropriate acquisition time and filtering however allowed for the detection of even weak signals.

3.5.3 Assessment of changes

A next step in evaluating the *in-vivo* imaging capabilities of the multispectral fundus camera consisted in investigating whether changes in fluorescence intensity, fluorescence distribution patterns and cell shapes can be captured and quantified. For this, fluorescence expression changes in Thy1-YFP and CX3CR1-GFP mice was assessed in eyes affected by glaucoma. Diseased and non diseased eyes were imaged, analyzed and compared.
Glaucomas are a group of progressive optic neuropathies that are characterized by a slow and progressive degeneration of retinal ganglion cells (RGCs) and their axons, resulting in optic nerve degeneration and ultimately in vision loss [108, 207]. Experimental glaucoma was induced by intravitreal injection of N-methyl-D-aspartate (NMDA). NMDA-induced excitotoxicity is a well-known model to induce RGC injury [129]. This kind of injury has been implicated in the pathogenesis of glaucoma and is widely used as a glaucoma model. One mouse eye was injected with 2 µL of 20 nmol of NMDA and the second with the same amount of phosphate buffered saline (PBS) solution. The PBS-injected eye served as control. The control was used to ensure that the induced RGC injury did occur due to NMDA administration and not due to increased intraocular pressure, which can be a side effect of intravitreal injections. Intraocular pressure changes could also lead to cell death or changes, however without selectivity to RGCs. Thy1-YFP mice were imaged 1 day and CX3CR1-GFP mice 5 days after glaucoma induction.

The images of both NMDA-injected and PBS-injected eyes were post-processed to allow the quantification of differences between the diseased (NMDA) and healthy (PBS) eye. Images were first filtered to (at least partly) correct for uneven illumination. Cells were subsequently segmented by thresholding the images. Only signals lying above a threshold T were defined as originating form targeted fluorescence expression in cells (in contrast to background autofluorescence emission). T was computed by:

$$T = \mu(I) + 2 \cdot \sigma(I) \tag{3.59}$$

where I represents the respective image, μ is the mean and σ the standard deviation of all pixel intensities in I.

Changes affecting retinal ganglion cells were quantified by computing the difference of the cell-to-background-intensity ratio in NMDA and PBS eyes, and by assessment of the cell density. Cell-to-background-ratio (CBR) was computed by

$$CBR = \frac{\mu(I \geq T)}{\mu(I < T)} \tag{3.60}$$

The enumerator in Equation 3.60 represents the mean value of all pixels of image I having intensities above T and the denominator the mean value of all pixels of I of lower intensity value than T. A low value of CBR indicates little contrast between regions identified as fluorescent cells and background tissue, and hence rather uniform fluorescence distribution. A high value of CBR indicates strong contrast between regions identified as fluorescent cells and background tissue, respectively.
Cell density (CD) was quantified by computing the ratio between the number of pixels being classified as fluorescent cells and the number of pixels belonging to the background. CD for an image with N pixels was computed by

$$CD = \frac{\sum_{i=1}^{N}(I_i \geq T)}{\sum_{i=1}^{N}(I_i < T)} \tag{3.61}$$

The enumerator in Equation 3.61 represents a count of all pixels having an intensity value above T and the denominator, equivalently, of all background pixels.
Figure 3.22 shows the changes observed in RGCs of the Thy1-YFP mouse 1 day after injection of NMDA and PBS. Fluorescence images of NMDA and PBS eyes are depicted in Figure 3.22(a). The yellow box indicates the region of interest (ROI) in the images

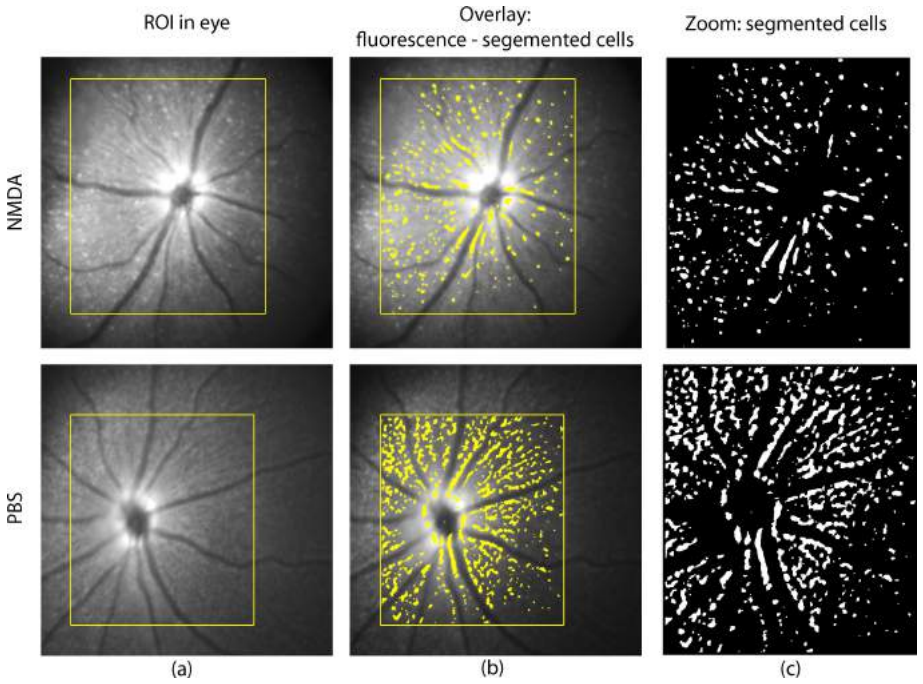

Figure 3.22: Segmentation of retinal ganglion cells in a diseased (top) and healthy (bottom) eye. (a) Fluorescence image and ROI used. (b) Segmentation within ROI. (c) Binary image of segmented cells in ROI.

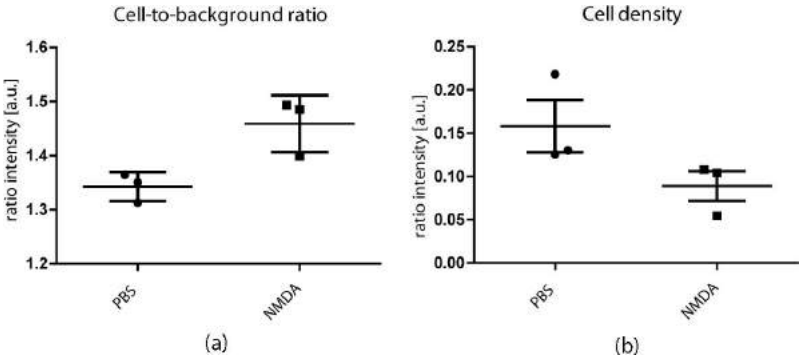

Figure 3.23: YFP expression changes induced by NMDA injection. (a) Difference in cell-to-background intensity ratio in PBS and NMDA eyes. (b) Difference in cell density in PBS and NMDA eyes.

that was selected for analysis. Hence this region goes as I into Equations 3.60 and 3.61. Segmented fluorescence is highlighted as yellow overlay in Figure 3.22(b). Figure 3.22(c) depicts the binary image of the respectively segmented cells. Figure 3.23 shows the quantification of changes based on data acquired from three mice. Figure 3.23(a) depicts CBR values for both PBS and NMDA eyes and Figure 3.23(b) the respective cell densities. The values for each individual mouse are depicted as dots for PBS eyes and squares for NMDA eyes. The mean value computed from the three mice plus/minus the

standard deviation are shown as bars.
CBR was higher in all three NMDA eyes compared to the PBS eyes. In contrast, cell density was reduced in the diseased eyes. This suggests that NMDA induced cell death, leading to a reduction in RGC density and hence higher perceptible contrast of the remaining ganglion cells.

Microglia cell changes were quantified by assessing the fluorescence intensity change at the optic nerve (ON) head and by measuring the morphological changes of microglia cell shape. That is because microglia, as the main immune defense cells in the retina, migrate towards the diseased region. Therefore, the shape of migrating microglia is expected to be elongated, in contrast to static microglia. Preliminary studies furthermore showed that migration goes towards the optic nerve. This results in increased cell accumulation in this region several days after disease induction.
Microglia cells were segmented equivalently to YFP cells using Equation 3.59 for threshold computation. Fluorescence intensity at the optic nerve was quantified by computing the ratio between the mean fluorescence intensity within an ROI at the optic nerve and the rest of the image (henceforth denoted as nerve to retina ratio - NRR). NRR is given by

$$NRR = \frac{\mu(I(ON))}{\mu(I(\overline{ON}))} \tag{3.62}$$

where $I(ON)$ are all pixels of I lying within the ROI chosen around the optic nerve, and $I(\overline{ON})$ are all pixels that are not part of the optic nerve ROI.
Morphological changes were quantified by fitting ellipses to all segmented cells and quantifying (1) the maximal axis length of the ellipses and (2) the ratio between the mean maximal axis length l_{min} of all cells and the mean minimal axis length l_{min} of all cells. Option (2) resulted in the axis-length-ratio (ALR) computed by

$$ALR = \frac{\mu(l_{max})}{\mu(l_{min})} \tag{3.63}$$

Figure 3.24 shows the changes observed in a CX3CR1-GFP mouse 5 days after injection of NMDA and PBS. Figure 3.24(a) depicts the fluorescence images where the ROIs give the regions that go as I into Equations 3.62 and 3.63. The segmented fluorescence is overlayed in yellow on the images in Figure 3.24(b). Figure 3.24(c)) depicts the binary images of cell segmentations and shows the different appearance of cellular structures in diseased and healthy eyes. Figure 3.24(d) exemplifies how the cell shape was measured and gives a definition of the ellipse axes used for computation of the axis length ratio.

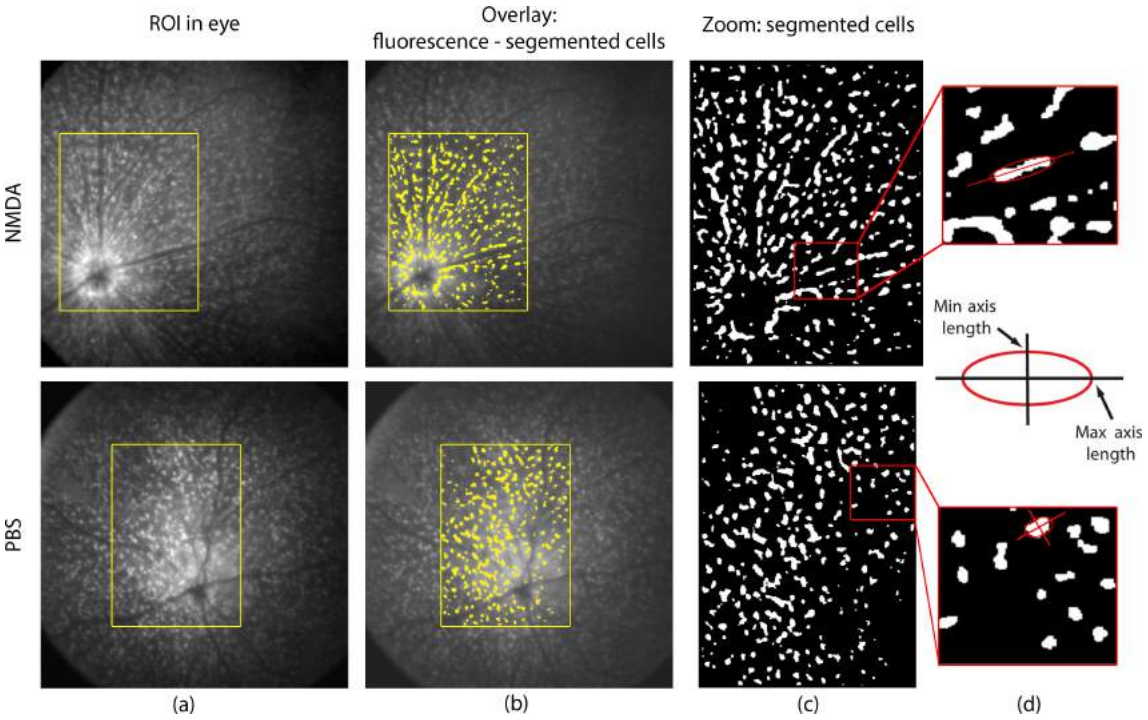

Figure 3.24: Segmentation of microglia cells in diseased (top) and healthy (bottom) eye and cell shape quantification example. (a) Fluorescence image and ROI used. (b) Segmentation within ROI. (c) Binary image of segmented cells in ROI. (d) Zoom into segmentation images and example for fitted ellipse to cell shape.

Figure 3.25 finally shows the quantification of differences between PBS and NMDA eyes from data of 3 imaged mice. The NRR was higher for all 3 observed mice (Figure 3.25(a)), as was the maximal cell length (3.25(b)) and the ALR (3.25(c)).

RGC and microglia results show that both fluorescence intensity and morphological changes could be quantified from *in-vivo* images. The changes induced by NMDA on the two cell types showed very different effects which could both be characterized employing images acquired with the multispectral fundus camera. This suggests that the imaging system and analysis approach are generally capable of assessing a variety cellular changes *in-vivo*, beyond the two shown examples. The presented fundus camera is therefore not only capable of imaging different fluorochrome distributions but can detect subtle changes that can be analyzed to diagnose and monitor disease progression and eventually treatment, or to investigate multiple molecules of interest and their role in diseases of interest.

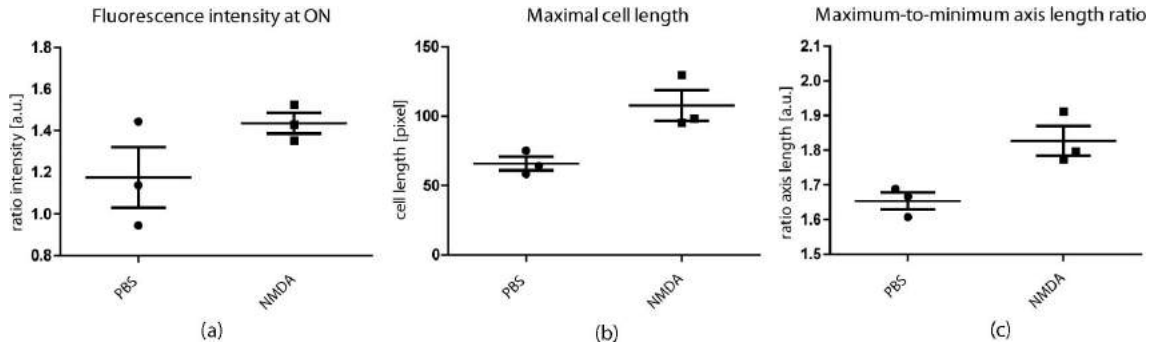

Figure 3.25: GFP expression changes induced by NMDA injection. (a) Difference in optic-nerve-to-retina ratio in PBS and NMDA eyes. (b) Maximal cell axis length in PBS and NMDA eyes. (c) Difference in mean axis length ratio in PBS and NMDA eyes.

3.5.4 Separation of mixed fluorescence

The final goal of the developed multispectral fundus camera was to enable imaging of multiple fluorochromes. The probability that the emission spectra of the employed fluorochromes overlap increases with increasing number of fluorochromes. This is because emission spectra of typical fluorochormes are rather broad (20-40 nm), and because many of the most frequently employed fluorochromes emit in similar wavelength ranges (for instance GFP and YFP). An appropriate multispectral imaging system therefore needs to provide sufficient spectral resolution to separate overlapping spectra in order to compute the unmixed spatial distribution of the original fluorochromes.

A next step in the evaluation of the multi-spectral fundus camera and in the development of an adequate image analysis methodology for *in-vivo* imaging consisted in investigating different methods for endmember identification from *in-vivo* mixed signal images of the retina.

For this purpose a dual-fluorochrome mouse line was created by crossing the two single fluorochrome transgenic mouse lines. Hence a mouse line was obtained that simultaneously expressed both GFP and YFP in microglia and RGCs, respectively.

The challenge in this unmixing approach was twofold: First, movement artifacts had to be eliminated by coregistration of the spectral images. Second, the contributions of two fluorochromes with very different fluorescence intensities had to be separated. I.e. Thy1-YFP expression dominated almost all spectral images due to its higher fluorescence intensity (as evaluated in Section 3.5.2). This fact motivated the employment of a narrow band laser that allows the measurement of CX3CR1-GFP at an emission wavelength band

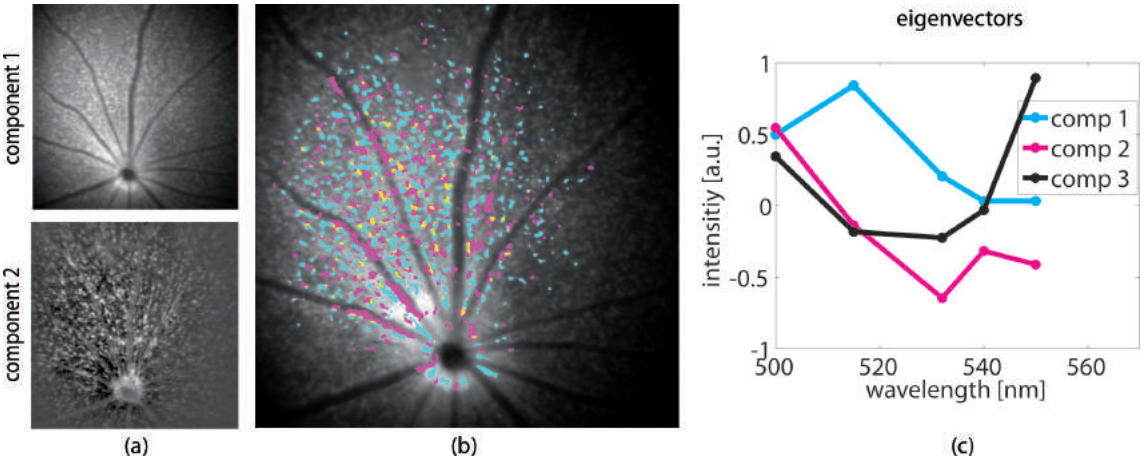

Figure 3.26: First two components computed by PCA using 5 spectral bands for unmixing. (a) Components. (b) Segmented cells from components 1 (cyan) and 2 (magenta). Yellow labeled pixels indicate overlap of both components. (c) Eigenvectors of first 3 PCA components.

at which Thy1-YFP hardly shows any expression, i.e. at 500 nm (see Figure 3.6 for a reminder of the spectrum of both fluorochromes). This was the only emission wavelength that provided higher contribution of GFP than YFP signals, while all other images (i.e. images acquired at wavelength above 510 nm) where dominated by YFP expression and often already saturated before sufficient GFP signals could be collected.

Three different unmixing approaches were investigated, as described in Section 3.3. Retinal images were unmixed with PCA and ICA, using different numbers of spectral bands, respectively. Then, a combined PCA-ICA approach was employed where the most important components identified by PCA were used for computation of ICA. The results of these three unmixing strategies were compared to each other and evaluated based on the available knowledge of the true fluorescence distribution from the single fluorochrome mouse experiments. Furthermore, the distinction of GFP and YFP cells was attempted through classification of each image pixel as belonging to one of the two cell classes. This was realized using an SVM classifier as described in Section 3.3.4.

Figure 3.26 shows the results after unmixing of mixed GFP and YFP signals using PCA. For this particular example, PCA was computed using 5 spectral bands between 500 nm and 550 nm. The two main components identified are shown on the left. The cells in these two images were segmented by computing the threshold as given by Equation 3.59. The image in the center depicts this segmentation as overlay on a fluorescence reflectance image, where cyan represents the first PCA component and magenta the

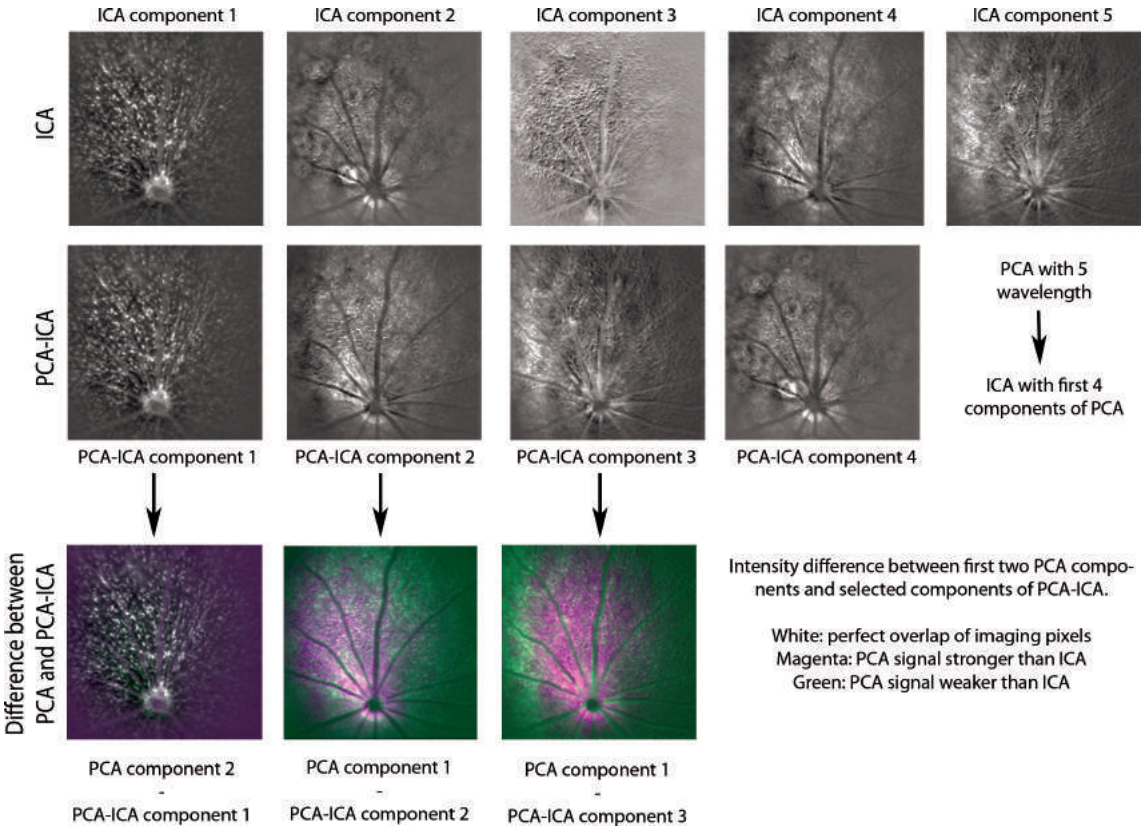

Figure 3.27: Unmixing using ICA and ICA-PCA, and comparison to PCA unmixing results. Top row: ICA results using 5 spectral bands for unmixing. Central row: ICA-PCA results after dimensionality reduction. Bottom row: Comparison of ICA-PCA and PCA.

second. Pixels where the components overlap spatially are shown in yellow. The graph on the right shows the computed eigenvectors (i.e. the spectra of the endmembers) for the first three components. The spectrum of component 1 thereby resembles the emission spectrum of YFP and the spectrum of component 2 the one of GFP. The third component may represent autofluorescence or image noise.

Figure 3.27 shows the results from ICA using 5 spectral bands (first row), and from PCA-ICA where the first 4 component from PCA were used for ICA computation (second row). A comparison between components computed by ICA-PCA and standalone PCA (as shown in Figure 3.26) is also shown (third row).
Since ICA provides no measure of component significance, the order of the shown components is random. It can be seen that the component shown in the first column for both ICA and PCA-ICA is the only one resembling one of the components previously

computed by PCA (component 2) while the others don't show cellular structures but rather seem to represent noise. The last row of Figure 3.27 displays the difference between the first two PCA component (the respectively used component is indicated below the images) and the images computed by PCA-ICA as indicated by arrows. White indicates that the compared images are identical in the respective pixels. Magenta indicates that the signal intensity in those pixels was higher in the PCA component than in the ICA component. Green indicates that the signal intensity in the respective pixels was lower in the PCA component than in the ICA component. It is obvious that PCA component 2 and PCA-ICA component 1 are similar, only slightly differing in the peripheral regions of the image, probably due to the uneven illumination. PCA component 1 however differs significantly from PCA-ICA components 2 and 3.

PCA did not only provide images that corresponded to the expected fluorochrome distributions as previously observed in single fluorochrome mice. It computed corresponding spectra that resemble well the spectra of GFP and YFP. ICA and PCA-ICA in contrast only recovered one of the original fluorochromes consistently, namely GFP, and failed at providing an accurate image of YFP distribution. It can be therefore concluded that PCA is an adequate method for endmember detection from multispectral retinal images.

Appendix A shows the complete evaluation of PCA, ICA and PCA-ICA employing 2 to 7 spectral bands. The images shown in this section are a representative selection of the obtained results.

After evaluation of the potential of PCA and ICA for accurate endmember computation, a classification method was applied and adapted to the data, and results compared to PCA unmixing results. Figure 3.28 depicts the training and classification process. Figure 3.28(a) shows two images that were used for classification. The top image was acquired at 500 nm, which is a wavelength band that should be more sensitive to GFP expression, and the bottom image at 560 nm, which should be more sensitive to YFP expression. A support vector machine was trained by selecting pixels from the two images and assigning them to one of two classes: class 1 - GFP and class 2 - YFP. The training is illustrated in Figure 3.28(b), where the computed support vectors are also indicated by circles. Figure 3.28(c) shows the classification of all pixels lying within the region of interest indicated in (a). The continuous line corresponds to the separation line computed by the SVM classification. The dashed, dotted-dashed and dotted lines at

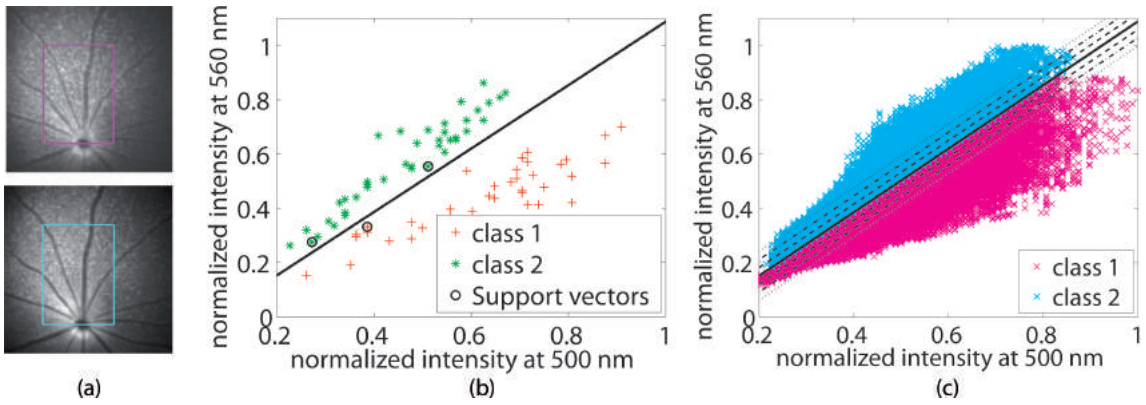

Figure 3.28: Support vector machine training and classification. (a) Images used for training and classification. Top: GFP sensitive image. Botton: YFP sensitive image. Employed ROIs are indicated in each image. (b) Training using manually selected pixels from images in (a). (c) Classification of all pixels lying within indicated ROI.

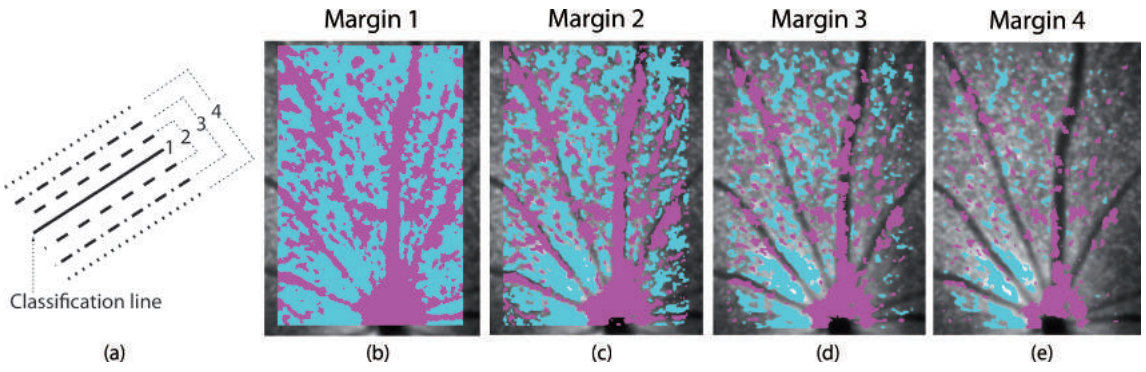

Figure 3.29: Effects of rejecting classified pixels based on the margin around the classification line. (a) Employed margins. (b)-(e) Pixel classification using respective margin.

both sides of the classification line indicate equidistantly increasing margins from the classification line.

Figure 3.29 shows results obtained from using the SVM classification for separating GFP and YFP signals. Classification of the pixels lying within the shown region of interest in Figure 3.28(a) and using all pixels as classified in Figure 3.28(c) results in the representation shown in 3.29(b). Magenta represents GFP-classified, cyan YFP-classified pixels. It can be observed that with such a classification method every pixel is assigned to one class and no background tissue is considered. Margins around the classification line were therefore introduced, shown in Figures 3.28(c) and 3.29(a). Classified pixels lying within the respective margin were defined as belonging to the background and not assigned neither to GFP nor to YFP classes. Four different margin widths were

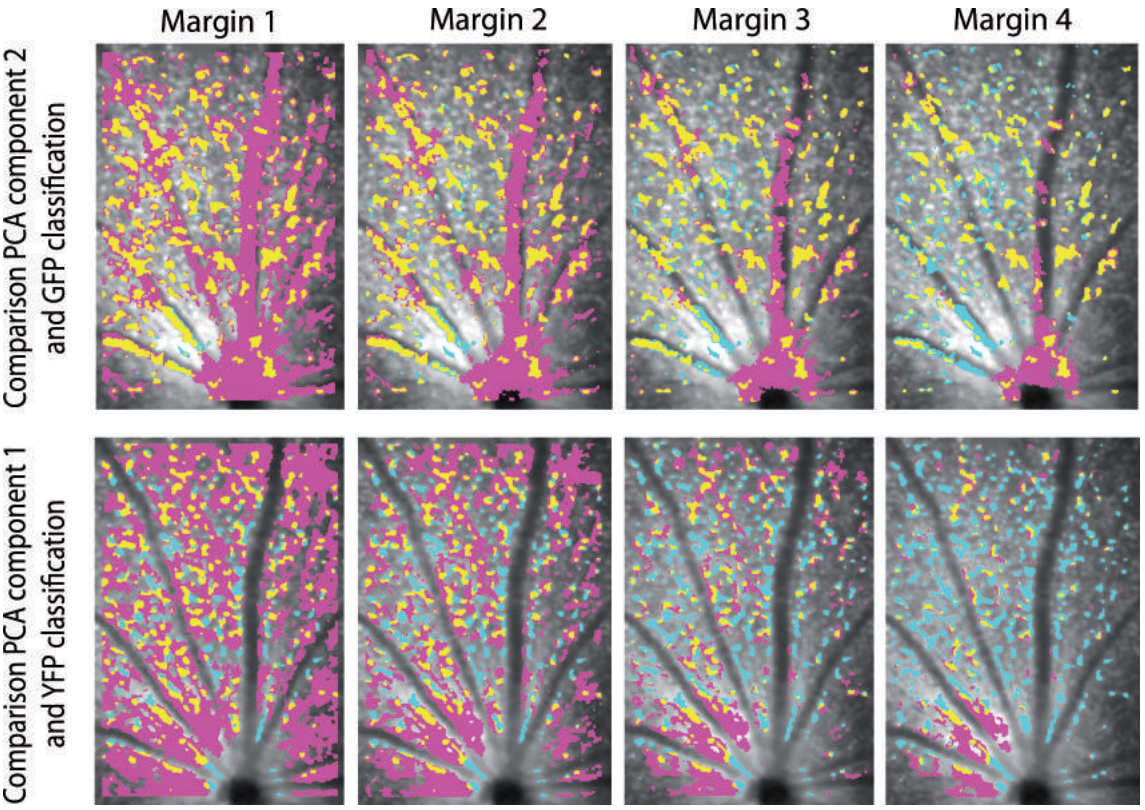

Figure 3.30: Comparison of PCA unmixing results with pixel classification using different classification margins, as presented in Figure 3.29.

considered as indicated in Figure 3.29(a), whereby the first margin with equaled to zero. The corresponding classification images are shown in Figures 3.29 (b) to (e), whereby margin width increases with increasing numerical order. With increasing margin width, less pixels were assigned to the classes resulting in a representation that better corresponds to the single fluorochrome images as shown for instance in Figure 3.20.

In order to evaluate the classification results, SVM classification was compared to PCA unmixing results of the same mouse. The results of this comparison are shown in Figure 3.30. The columns of the image matrix shown correspond to the 4 margin regions considered in Figure 3.29. The first row compares the classification of GFP to the 2nd component of PCA, the second row compares the classification of YFP to the 1st component of PCA. Cyan indicates in all images the PCA result for the respective fluorochrome, magenta the respective SVM classification results. Yellow indicates where PCA and SVM classification overlap, i.e. for which pixel classification and PCA unmixing agree.

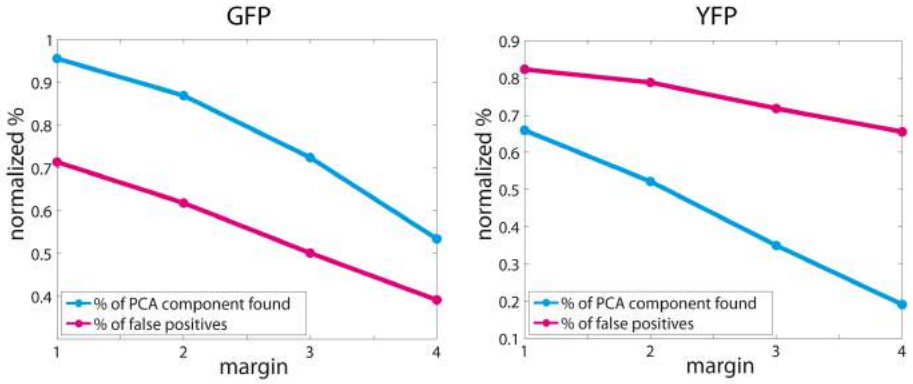

Figure 3.31: Evaluation of SVM classification as a function of employed margin for GFP emission detection (left) and YFP emission detection (right).

The graphs in Figure 3.31 (a) and (b) quantify this agreement, or rather disagreement. The cyan curve shows the percentage of the PCA signal that was found by SVM classification for increasing margin width. The magenta curve shows the percentage of pixels that were classified as being YFP or GFP respectively, but that did not correspond to PCA results, i.e. they were false positives. The graphs basically show the effect of choosing different boundaries for pixel classification. Using the classification line directly (i.e. margin 1) resulted in the complete fragmentation of the image in two classes, hence also including areas that might not have been of one of the two cell types, like the vasculature. Increasing the margin did affect GFP classification significantly. While false positive classifications were reduced, i.e. there were less pixels wrongly classified as being GFP pixels, this also resulted in less overlap with PCA results. YFP classification was for all chosen margin widths even less accurate than GFP classification. Low agreement with PCA results was obtained and false positive results were high for all margins widths.

The results obtained in this section lead to the conclusion, that PCA most reliably computes the original spectral components from the mixed GFP-YFP spectral images. ICA only detected one of the components, GFP, and seemed to only recover noise in all remaining components. Classification also performed worse than PCA, resulting in either too many or insufficient pixel classifications.

3.5.5 Imaging of intravascular oxygenation

In addition to imaging multiple fluorescent labels, the potential of the multispectral fundus camera in imaging intrinsic tissue chromophores was evaluated. The method

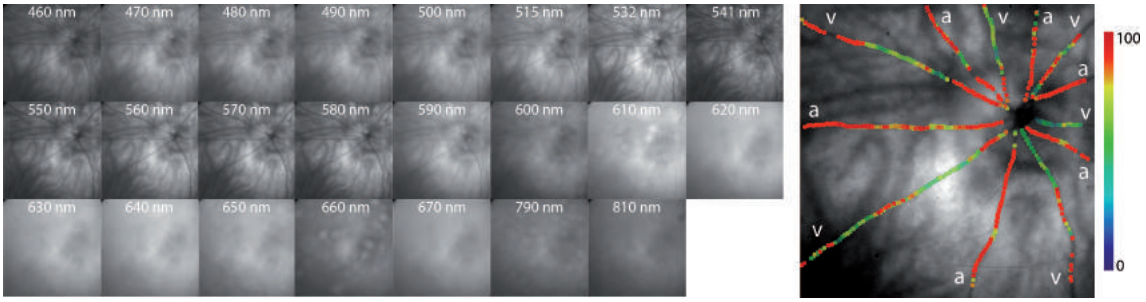

Figure 3.32: Intravascular oxygenation imaged in an albino mouse.

developed in Section 3.4 for oxygen saturation quantification was applied to retinal imaging to show its potential in assessing intravascular oxygenation in the mouse fundus. Imaging retinal oxygenation provides the possibility of extracting information on oxygen transport changes in diseases in addition to the molecular readings obtained from targeted fluorochrome expression.

Oxygenation was imaged in both single fluorochomre transgenic mice, the one being on albino background, the other being on pigmented background. This was done in order to show that oxygenation can be assessed independent of the background optical properties, which significantly change the intrinsic spectral reflectance images acquired.

Figure 3.32 shows the computed intravascular oxygenation in the albino mouse. The image matrix on the left shows the reflectance images at every wavelength band employed. Note the change in contrast between vasculature and surrounding tissue in the green/orange spectrum compared to the red and NIR part of the spectrum. The image on the right depicts the intravascular oxygen saturation computed employing the reflectance images shown on the left. Based on the obtained oxygenation values veins and arteries could be identified (labeled by v for veins and a for arteries).

Figure 3.33 presents the computed intravascular oxygenation in a pigmented mouse. The left images show the reflectance acquired from the pigmented mouse. Contrast differs now significantly from the albino mouse, as can be in particular seen in the red part of the spectrum, where vasculature now appears bright compared to the background tissue. Nevertheless, oxygen saturation could also be computed and is shown on the right. Arteries and veins can again be distinguished and are labeled in the image.

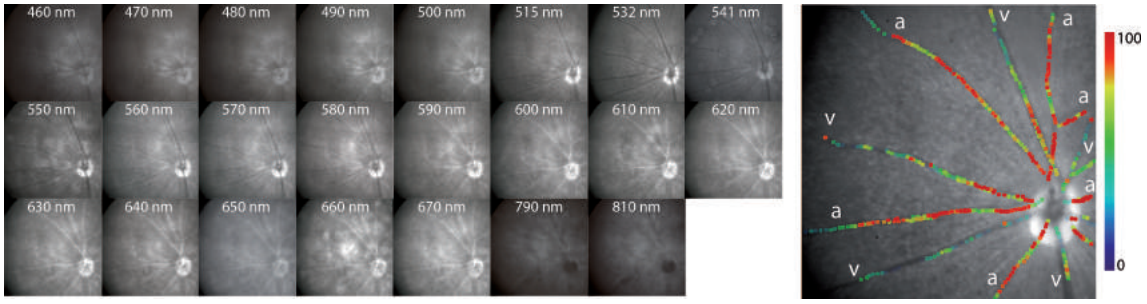

Figure 3.33: Intravascular oxygenation imaged in a pigmented mouse.

3.5.6 Multispectral imaging of multi-fluorochrome retinae

Finally, multispectral mice were produced by combining GFY, YFP, mCherry, Cy5.5 and ICG expression in the same mouse. For this purpose Thy1-YFP mice were injected with both vectors (expressing GFP and mCherry respectively), the VEGF receptor probe and the vascular marker ICG. Multispectral mice were imaged using narrow band filters of 10 nm bandwidth in the wavelength region between 500 nm and 590 nm in order to allow the separation of GFP and YFP signals. The other three fluorochromes were imaged with one filter each sice their emission spectra were sufficiently apart to allow their non-overlapping detection. Figure 3.34 is a representative depiction of the images and cell segmentations obtained from imaging of these multispectral mice. Examples for the original acquired images at different wavelength are given at the top and on the left (top left and center: mixed GFP and YFP emission, top right: scVEGF/Cy, left center: mCherry, left bottom: ICG). The center wavelength of the filter used for acquisition of the respective image is indicated in every image. After application of PCA to unmix GFP and YFP contributions and segmentation of every fluorochrome emission pattern, the individual contributions were overlayed in one image, shown on the bottom right of Figure 3.34. This overlay provides a multispectral representation of the different fluorochrome patterns present in the retina and allows the visualization of different cell types, receptors or vascular perfusion.

3.5.7 Discussion and conclusion: multi-fluorochrome imaging

The aim of this study was to provide the methods and system for multispectral detection of multiple molecular markers *in-vivo*. The experimental model considered was the mouse retina, which defined the requirements on some parts of the hardware implementation. Subsequently investigated image analysis methods, although applied to the retina

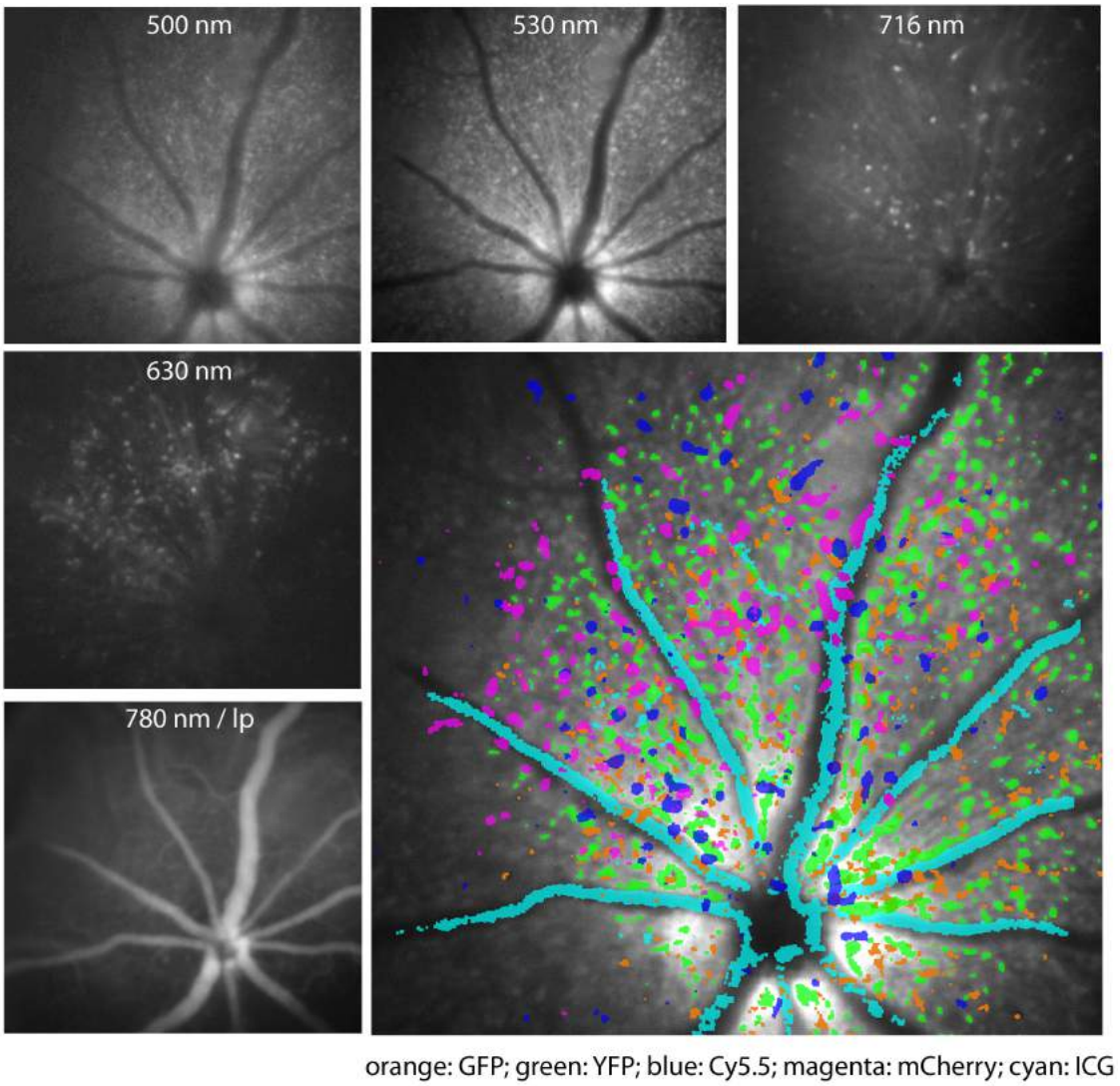

Figure 3.34: Multispectral images of a multi-fluorochrome mouse retina. Acquired raw images employing different filters are shown on the top and left. The resulting fluorochrome segmentation is presented on the bottom right.

in this case, could be, however, translated to multi-fluorochrome investigations in other superficial tissues.

A multispectral fundus camera was developed for this purpose. The fundus camera employed adaptable illumination by multiple lasers or white light sources and enabled the measurement of 25 spectral bands of reflected or emitted light from the retina. This allowed for individual, fluorochrome specific adaptation of illumination and detection for an ideal separation of fluorescence emission bands. The multispectral imaging

potential of the system was first investigated by imaging of single fluorochrome emission. Blind source separation methods, as well as SVM classification were afterwards studied in order to asses the fluorochrome separation potential when observing overlapping multispectral signals *in-vivo*. Best unmixing results were obtained employing PCA, which not only recovered endmember distributions corresponding to previously observed single fluorochrome expression patterns, but also provided realistic spectra of the endmembers. Furthermore, the ability to track changes in fluorochrome expression patterns was investigated, an important ability when imaging disease progression or therapy. Morphological changes in cell shape, as well as changes in cell density or regional fluorescence intensity could be observed and quantified by the means of fluorochrome emission pattern segmentation and fluorescence ratio computation. The capabilities of the multispectral fundus camera were shown to reach beyond the detection of extrinsic contrast agents. Intrinsic properties, like intra-vascular oxygen saturation, could be detected in both albino and pigmented mice, due to spectral imaging of reflected white light and the employment of appropriate computational methodology (as introduced in Section 3.4.1). Finally, first experiments in mice expressing simultaneously five different fluorochromes confirmed the capability to image multi-molecular expression. This proves promising for future investigations in disease models of multispectral mice.

The work on multispectral retinal imaging could be extended in various directions. While the focus in this work lay on multi-molecular detection, future work should concentrate on improving detectable resolution. Adaptation of multispectral excitation and emission to cSLO systems and the implementation of adaptive optics technology could be appropriate steps in this direction. Adaptive optics is a technology employing deformable mirrors in order to reduce the effect of wavefront distortion caused by the eye lens and cornea. It has already found successful application mainly in human fundus imaging [124, 155] where photoreceptor cells could be resolved. Recently, adaptive optics has also been employed in mouse fundus imaging systems providing impressive resolution. Images, however, still suffer from low signal to noise ratios, therefore requiring the acquisition and averaging of many image frames [57]. Nevertheless, future implementations will certainly improve on this shortcoming and integration of multispectral and high-resolution technology should soon become realizable. Further work should also be dedicated to the application and evaluation of the proposed methodology to different mouse models, in terms of both fluorchromes employed and diseases studied. This is to confirm the potential of the multispectral imaging approach in a larger variety of experimental cases. At the time of writing of this thesis, such a study employing

multispectral mice is in fact ongoing, performed by the author and collaborators. Finally, the development of more labels (both probes and vectors) for the retina that specifically target molecules of interest also remains one topic of future research, although not from a technical engineering perspective.

To conclude, this section showed the capabilities of a multi-molecular imaging system for investigating the mouse retina and introduced methodology for image analysis. Imaging of multiple molecular markers in the retina bears great potential to research a variety of systemic and retinal pathologies. The proposed methodology can be translated to a variety of other applications, enabling multi-fluorochrome detection in superficial tissues. This approach can help advancing integrative multi-molecular research, by providing the means to simultaneously track many key parameters of disease.

3.6 Conclusion and recommendations for future work

This chapter introduced concepts, systems and methods for multispectral imaging in surface tissue investigations. Approaches targeted the detection of both intrinsic as well as extrinsic tissue contrast. The proposed methods concentrated on some specific parameters, like tissue oxygenation and fluorescence emission, mainly observed separately from each other. The integration of imaging hardware and methodology for simultaneous investigation of both intrinsic and extrinsic contrast was suggested in the case of retinal imaging, but needs further development to be practically applicable to any kind of superficial tissue investigation. Besides the suggestions for future work previously made, further recommendations addressing some common aspects of the multispectral imaging concepts introduced shall be mentioned here.

One aspect when further enhancing such multispectral imaging approaches should focus on reducing total acquisition time for the acquisition of a data cube. Detectors of higher sensitivity would be one solution, the introduction of alternative wavelength scanning devices another possibility. Wavelength bands in tunable filters (liquid crystal or acousto-optic type) can for instance be switched at high speed and provide high spectral resolution. Besides, they have the advantage of providing perfectly overlapping images acquired at different spectral bands, while separate filters often result in small x-y shifts. Disadvantages, however, lie in the inflexible hardware, i.e. the spectral rage is determined by the range of the tunable filter. Filters in filter wheels, in contrast, can be changed

easily and the spectral range therefore adapted to specific needs. Another limitation is the transmission of tunable filters, which is often below the one of separate filters. However, it should be only a question of time until this limitation is overcome.
Further hardware implementations could split the image path by beam splitters and add a second detector for simultaneous detection of two wavelength bands. This would for instance allow the continuous detection of very fast processes with one detector, while the second could be used for wavelength scanning of slower processes. Examples where such an approach would be interesting is in calcium signalling imaging, a process typically occurring on a millisecond time scale. The realization of such a two-detector modification of the fundus camera presented herein was performed during the time of this thesis and general feasibility of simultaneous imaging confirmed. However, due to the lack of appropriate test cases that would actually require such a setup, all experiments presented in this work only used the one detector implementation.

Multi-spectral imaging devices for multi-molecular imaging should in future combine the properties presented here for intrinsic and extrinsic detection. Image analysis methodology should furthermore be enhanced to include the detection of other intrinsic tissue chromophores and autofluorescence. Absolute quantification of fluorescence emission would also be desirable. This, however, would have to involve fluorochrome specific calibration and correction algorithms taking into account the influence of optical properties on the detected fluorescence signals. This is a non-trivial endeavor and currently under investigation at the Institute of Biological and Medical Imaging by colleagues.

Such further research and improvements would result in truly multi-molecule surface imaging devices and methods, allowing for investigations of high descriptive value. This would provide a powerful tool for molecular imaging.

4 Multispectral methods for multi-molecular volumetric imaging

The overall goal of the work presented in this chapter was to develop a methodological framework that enables unbiased volumetric imaging of multiple molecules for *in-vivo* investigations. It presents the theory, methods, experiments and results obtained to meet this goal.

Section 4.1 introduces the used molecular imaging modality - Fluorescence Molecular Tomography (FMT). The basic principle of operation of this diffuse optical imaging device is briefly outlined, followed by an overview of the evolution of FMT from stand-alone devices to hybrid implementations that combine molecular data with anatomical data obtained from, e.g., XCT or MRI. The section closes with a discussion on considerations and requirements for multi-molecular investigations using hybrid FMT. The concept of coregistering limited-projection-angle FMT with XCT is introduced, as well as the gaol of automatized incorporation of anatomical priors into the reconstruction process.

Section 4.2 presents theoretical background on light transport modeling and image reconstruction in the context of stand-alone FMT, followed by regularization aspects introducing anatomical prior information into the inversion process for hybrid FMT schemes. The incorporation of so called regularization factors into the regularization matrix for segment wise regularization is discussed.

The imaging systems employed in this work, i.e. limited-projection-angle FMT and preclinical X-ray CT, are described in Section 4.3. Data acquisition by FMT and segmentation of XCT images are further subjects of this section. This part is fundamental for understanding the coregistration strategy developed for combining FMT and XCT data sets, presented in Section 4.4.

First reconstruction results obtained by hybrid limited-projection-angle FMT-XCT are reported in Section 4.5. These are compared and evaluated against stand-alone FMT reconstructions of the same imaged homogenous and heterogenous tissues. This section concentrates on a proof-of-principle, showing the potential improvements that can be

obtained by hybrid limited-projection-angle FMT, and therefore employs manually selected regularization factors. Section 4.6 goes one step further, showing the development of a data-driven scheme for automatically estimating regularization factors from hybrid limited-projection-angle FMT-XCT data, leading towards user independent FMT-XCT reconstructions. This method enables independent and unbiased reconstruction of multiple molecules in the same experimental animal.
Section 4.7 expands the approach of multi-molecular imaging by showing the coregistration of an additional molecular imaging modality, PET, into the multi-molecular imaging framework. This section aims to give an outlook on the potential of hybrid limited-projection-angle FMT for multi-molecular investigations.
The chapter closes with a discussion of the results and some recommendations for future work in Section 4.8.

The work presented in this chapter has resulted in two peer-reviewed journal papers that have meanwhile been published by the author and colleagues [150, 151]. Several figures and text passages were adopted from these publications.

4.1 Introduction to fluorescence molecular tomography

4.1.1 Background

Fluorescence Molecular Tomography (FMT) is a method that images tissue biomarkers by resolving the bio-distribution of fluorescently labeled agents and reporters that enable non-invasive *in-vivo* imaging of cells and cellular moieties in small animals or other tissues [138, 165, 174, 193, 195]. Similarly to other *in-vivo* molecular imaging modalities like PET and SPECT, FMT utilizes agents that target functional and molecular tissue parameters. Due to this basic ability, FMT can study disease progression or monitor therapy non-invasively, which enables highly diverse applications such as cancer, cardiac, inflammation or neurodegenerative imaging [14, 71, 121, 127, 196]. One of the strengths of FMT over nuclear imaging devices is the use of non-ionizing energy, typically in the near-infrared range of the optical spectrum. An additional advantage is the ability to resolve many tracers simultaneously by using fluorescent labels at different wavelengths. Therefore, different contrast mechanisms can be concurrently studied, for example the relative expression of different receptors or the relative concentrations of different types

of cells. Conversely, the most important limitation is the diffusive character of near infrared photons that propagate in tissues, which complicates image formation and quantification and limits the size (depth) of the object that can be imaged, typically to a few cm [134, 194].

The basic principle of operation of FMT relies on the injection of a near-infrared fluorescent probe into the blood stream of a small animal, and the detection and reconstruction of its accumulation in specific diseased sites. Tissue is illuminated by a laser source at the fluorochrome's excitation wavelength and gets absorbed by the fluorescent probe. The emitted fluorescence exits in diffuse light patterns on the tissue boundary, which are collected by some kind of photon detector. These boundary measurements can be combined in a tomographic scheme and used in a mathematical model describing the photon propagation in tissue (like for instance the diffusion equation discussed in Chapter 2) to reconstruct the unknown volumetric distribution of the fluorescence source [133, 138]. In contrast to surface imaging methods like those discussed earlier (Chapter 3), FMT operates in trans-illumination mode, meaning that illumination and detection occur on opposite sides of the imaged subject. Although signals detected in epi- and trans-illumination mode exhibit similar nonlinear dependencies to depth and tissue optical properties, the latter provides more information on the imaged subject. This is due to the different volumes sampled with each of the two imaging geometries. In trans-illumination mode, light propagates through the whole volume and therefore samples it entirely. In epi-illumination on the contrary, exact sampling depth is unknown [133]. Additionally, trans-illumination data can further be normalized by dividing the image acquired at the emission wavelength by the image acquired at the excitation wavelength, thus correcting for influences like heterogeneous illumination or background tissue optical properties [4].

The diffusive character of photon propagation in the visible and near-infrared range generally makes the recovery of fluorescence biodistribution an ill-posed problem and limits achievable resolution of FMT to an order of magnitude of millimeters. Significant improvements on employed hardware, setup geometries and reconstruction approaches since the first appearance of FMT, however, have resulted in current systems that allow for reconstructions with sub-millimeter accuracy [160]. These improvements mainly focused on developments on data collection schemes for stand-alone FMT, but also on the combination of optical tomography with other tomographic imaging modalities into hybrid systems that offer complementary data on anatomy to guide FMT reconstruction.

These improvements represent the basis for the methodological developments presented in this chapter. The next two sections are therefore dedicated to review the evolution of FMT and hybrid FMT, before introducing to the concept of imaging multiple molecules with hybrid FMT.

4.1.2 Evolution of stand-alone FMT geometries

Original stand-alone FMT setups employed light guiding fibers to couple light into and from the tissue. Such arrangements have several disadvantages. Fiber placement, for instance, can be very cumbersome on irregular tissue surfaces. This difficulty was in some approaches overcome by the employment of an imaging chamber with fixed geometry. Experimental objects were placed in this chamber, which was then filled with a diffuse fluid matching the animal's mean optical properties. This approach simplified the imaging geometry to a manageable cylinder or slab shape and improved fiber coupling. On the downside, it also introduced additional tissue boundaries and inhomogeneities in the sampled volume. One of the most important drawbacks of fiber-based systems, however, is the restricted number of fibers that can practically be employed due to spatial constrains of the imaging setup. Therefore, achievable resolution in such setups is limited to a few millimeters.

Alternatively, non-contact setups have been proposed that, first, resolve the issues of fiber coupling, or of additional scattering and absorption introduced by matching fluids. Second, they enable higher resolution imaging by increasing the detector readings. In these setups, detection fibers are replaced by CCD cameras and excitation is realized by scanning a focused laser spot over the tissue surface.
Information on the imaged geometry can be obtained by two approaches: The first employs imaging cassettes that determine the object's geometry. They consist of transparent plates between which the object is slightly squeezed to avoid movements during data acquisition. These cassettes also create a predefined geometrical shape that can be used to guide the reconstruction process. With this concept, only limited angular projections perpendicular to the plate surface can be acquired by the camera.
The second approach extracts arbitrary three dimensional shapes with surface capture optical methods (like for instance photogrammetry). Since no imaging cassette is obstructing the view on the object, this concepts allows for full-projection-angle acquisitions. For acquiring projections at all angles, either the imaged subject is rotated and the

hardware is kept in a fixed position, or the hardware can be mounted on a rotating gantry and the subject remains fixed.
In addition to experimental simplicity compared to fiber-based methods, full-projection-angle non-contact data collection schemes offer information rich data sets, due to both large angular and spatial sampling.

Most non-contact fluorescence tomography systems that have been disseminated to the laboratory operate as limited-projection-angle systems, i.e. more specifically acquiring optical projections from a bounded slab geometry [29, 63, 127, 157, 168, 206]. Compared to full-projection-angle systems, the slab geometry is technically easier to implement and comes with several operational advantages including easy animal placement, shorter experimentation times and offers systems of reduced cost. This geometry also offers the possibility to develop rigid animal holders that can be translated between different modalities for obtaining hybrid data [128]. Full-projection-angle systems, in contrast, often need dedicated hardware development and integration in order to afford hybrid data acquisitions. Conversely, the slab geometry attains imaging performance limitations because it offers limited resolution along the axis of the projections [63, 200]. In addition, surface artifacts are more pronounced as the number of available projections decreases [109].

4.1.3 Evolution of hybrid FMT

Although most optical tomography implementations reported so far operate as stand-alone systems, several studies have shown that the combination of optical tomography approaches with other modalities, in particular modalities yielding anatomical information such as MRI [140, 146] or XCT [160] can further improve image reconstruction performance. Improvements can be delivered by utilizing the anatomical information as prior information to limit the uncertainty of the tomographic problem [15, 41, 68, 113, 117, 199]. Typically, knowledge about the internal structures of an animal, i.e. the segmentation of different tissue types like bones, lung, heart, brain etc., allows the assignment of different optical properties to each of these tissues and consequently more appropriate modeling of photon propagation inside each tissue type. A similar practice is employed in PET whereby information on density differences from XCT scans is used for attenuation correction resulting in superior PET reconstructions [183]. Yet it is even more crucial in FMT inversions due to the stronger dependence of near-infrared photons on the tissue

optical properties [153]. In addition, the anatomical information can be used to define functionals that can be employed in the reconstruction process to restrict the ill-posed nature of the inverse problem and stabilize the performance of the method [15, 41].

The use of priors from an anatomical modality in optical tomography of tissues has been demonstrated in the past. As early as 1995 Barbour et al. [15] examined theoretically the potential utility of incorporating MR-derived anatomical image data to enhance the quality of tomographic optical imaging in order get over the hurdle imposed by the diffusive character of light propagation in tissue. Their approach consisted in simulating measurements for segmented 3D MRI data sets of breast tissue in which different tissue types were assigned different optical properties. Consequently, the dependence of image quality on different properties, also related to the reconstruction algorithms, could be investigated. At that time, optical tomography - with or without priors - was still in its infancy. Nevertheless, the simulations presented in this early work showed promise to the feasibility of recovering relevant information form optical measurements and lead on the right track for further hardware and software developments.

Additional methodological approaches incorporating priors in optical tomography [90, 114, 145, 146] and implementations that combined DOT or FMT with MRI [67], ultrasound [209] or XCT [85, 117] were since proposed. Pogue and Paulsen [145], and Pogue et al. [146], for instance, examined a reconstruction algorithm that would take advantage of the data available from a composite MRI-NIRS system for imaging the rat cranium. They tested its ability to obtain high-spatial-resolution images of the near-infrared optical absorption coefficient in simulations and were able to distinguish even local perturbations located inside one tissue type. Intes et al. [90] used a different approach to incorporate prior information. Their algorithm was based on a Bayesian framework with a spatially varying *a priori* probability density function extracted from MRI anatomical maps and the additional incorporation of physiological priors. Furthermore, X-Ray mammography was the anatomical modality of choice with Li et al. [114] which was included by a modified Tikhonov regularization method in the diffuse optical tomography reconstruction. They explored the usage of two different types of priors that combined the L-curve approach for finding one parameter with a signal-to-noise ratio type of maximization for the second. Their simulations showed promising results for contrast-to-noise ratio and resolution improvement. On the instrumentation front, Gulsen et al. [67] presented a combined DOT and MRI system for small animal imaging, whereby a similar approach was also considered in clinical studies [141]. Ultrasound and

optical tomography was combined in a handheld device by Zhu et al. [209].

The combination of FMT with anatomical devices has also been investigated. Davis et al. [40], for instance, incorporated a fluorescence imaging system directly into a clinical MRI to improve detection of brain tumors in mice. The regularization was based on segmented MR images and a Laplacian-type regularization matrix that had been introduced in [41]. The potential gain from integrating MRI and FMT has been realized by several groups and is currently one major focus of hybrid FMT research [179]. FMT has also been recently combined with X-ray CT (XCT) in a hybrid animal imaging system based on free-space CCD camera photon collection [160]. This approach enabled the collection of high spatial-sampling data at 360 degree projections. The integration of the optical hardware onto the gantry of a micro-CT device allowed accurate coregistration of FMT and XCT images. Similar approaches fixed the acquisition system and rotated the animal instead [38, 200]. Different reconstruction schemes incorporating XCT anatomical data were investigated both for the forward problem [87] and for the inverse part [4, 85, 86, 160]. Ale et al. [4], for instance, compared different regularization methods based on Tikhonov, Laplace and different weighting of segments and concluded from simulations and *ex-vivo* experiments that the latter approach was the most promising. Hyde et al. [86] used a similar approach employing different weighting but additionally focused on the development of data driven regularization and investigated the influence of subdivision of anatomical segments on the reconstruction outcome.
Hybrid implementations are scarce when it comes to limited-projection-angle FMT geometries. While the translation possibility of the imaging cartridge has been used to compare FMT and anatomical images [128], no investigation so far has examined the improvements offered when incorporating anatomical information into data acquired from animal models of disease *in-vivo*.

4.1.4 Imaging of multiple molecules with FMT

The improvements in reconstruction quality obtained by free-space FMT implementations and the incorporation of anatomical data into the reconstruction of FMT data are undeniable. These engineering and algorithmic achievements have afforded distinguished biological studies [3, 5, 42] that can result in better understanding of biological processes, therapy design and drug development.
A next important step in the progress of hybrid FMT approaches is the development

of multi-spectral schemes that capitalize on the unique ability of the hybrid optical method to simultaneously image several targeted agents at higher imaging accuracy than stand-alone FMT systems. Complementing traditional molecular biology methods with the non-invasive acquisition of multi-molecular information is highly desirable as a unique method that can offer insight into dynamic processes in unperturbed biological tissues. Correspondingly, hybrid FMT reconstructions implemented using automatically computed priors have the potential to deliver better accuracy in volumetric multi-wavelength imaging, complementing multi-wavelength (multispectral) imaging strategies considered in two-dimensional surface weighted epi-illumination mode, as discussed in Chapter 3.

Dual-wavelength concepts based on the combination of one targeted and one untargeted probe have been introduced for 360 degree (i.e. full-projection-angle) FMT systems [42, 181]. These concentrated on the correction and normalization of the targeted probe by using the untargeted probe as internal control. Conversely, independent assessment of different targeted probes that simultaneously report on different molecular events is desirable and adequate data acquisition and reconstruction methods have to be developed for this purpose. The work presented in this chapter is dedicated to report on considerations and methodological developments conducted towards the goal of enabling independent multi-molecular investigations with hybrid FMT, and to show the obtained results.

Before moving on to the presentation of the conducted work, some considerations regarding the requirements for multi-molecular FMT imaging are necessary. The three following points mainly guided the choice of imaging setups and methodological developments presented in the following sections:

[1] **Short acquisition time:** One important aspect in *in-vivo* investigations is the experimental time. An experimental animal cannot be subjected to stress, like imaging, over extended time periods. Acquisition of N fluorochromes, however, results in an increase of FMT acquisition time by a factor of N compared to single fluorochrome acquisitions. Therefore, fast acquisition methods had to be favored and, if necessary, a trade off against data sampling density had to be considered.

[2] **Multi-modality:** The minimum requirement towards multi-modality was the incorporation of data from an anatomical imaging device, due to the conclusions made in Section 4.1.3. For a truly multi-molecular approach, however, the possibility

to integrate different imaging modalities into the FMT framework would be even more beneficial. Beyond the realization of hybrid reconstructions by incorporation of anatomical data from XCT or MRI, additional molecular imaging data like PET or SPECT could be added to the multi-molecular data set. An information rich data set of molecular distribution could hence be created.

[3] **Hardware availability:** The developed methods aim at providing an improved molecular investigation scheme to a broad range of medical and biological researchers. Cumbersome and dedicated hardware developments were therefore avoided. Instead, methods that can be applied to commercially available imaging systems were favored.

Based on the defined requirements, a hybrid FMT scheme for independent assessment of multiple molecules was conceived and implemented. For this purpose, a limited-projection-angle FMT setup was employed and hybrid data was incorporated by coregistration to micro X-ray CT data (both imaging modalities are described in Section 4.1.3). As stated in the requirements, acquisition of multiple molecules imposes time restriction on each wavelength in order to keep animal stress on an acceptable level. While 360 degree systems offer higher information density, they are also time costly and the measurement of multiple molecules results in long experimental procedures leading to long anesthesia times for the experimental animal, that may not be survived. Limited projection FMT offers implementation simplicity, as it does not require rotating gantries but offers a sub-set of the information available to 360 degree systems. This subset may not provide the same reconstruction accuracy as 360 degree acquisitions in stand-alone FMT systems. The combination with anatomical data, however, can improve the accuracy of limited-projection-angle FMT, and the development of adapted reconstruction and regularization schemes can subsequently lead to an imaging system capable of reconstructing many molecular markers after acquisition in comparatively short time. The employment of limited-projection-angle FMT further enables the utilization of an imaging cartridge that can be employed to translate the imaged animal to other imaging modalities beyond XCT, like PET. This results in additional molecular readouts and increases the diagnostic potential of hybrid FMT.

The improvements achieved in the imaging performance of limited-projection-angle (slab geometry) FMT systems when incorporating hybrid anatomical information *in-vivo*, had to be investigated first. This was preceded by the implementation of an adequate co-registration approach, which was achieved by means of an animal cartridge that can

offer rigid animal translation between a stand-alone FMT scanner and a XCT animal micro-scanner. Based on obtained results, a method for automatic and independent estimation of regularization factors for the incorporation of priors was derived. All methodological developments were first evaluated on tissue mimicking phantoms. Their universality was then confirmed on more realistic, heterogeneous tissues, i.e. in mouse models of cancer.
By improving the overall reconstruction performance and enabling automatic, data-driven regularization, this work provides a methodological framework for multi-molecular *in-vivo* investigations. The developed method was tested in dual-wavelength, or respectively dual-molecular-marker, experiments. The obvious extension of this work by employing a larger number of fluorescent agents at different spectral bands and the possibility of co-registration with a larger number of imaging modalities is also discussed.

4.2 Forward and inverse models

This section presents theory for modeling light propagation in FMT and for the inversion of diffuse imaging data. The incorporation of anatomical prior information into the regularization matrix, as well as schemes for automatic regularization factor estimation are also introduced.

4.2.1 Forward model

Modeling of photon propagation in tissues is based on the time-independent diffusion equation (Equation 2.26). In order to incorporate fluorescence into the modeling process, two coupled equations describing photon densities at the excitation and emission wavelengths are used. The propagation of excitation light into tissue from a source S at position $\vec{r}_s$ and at excitation wavelength λ_x is given by

$$-\nabla D_x \nabla \Phi_x(\vec{r}) + \mu_{ax}\Phi_x(\vec{r}) + \varepsilon c(\vec{r}) = S\delta(\vec{r}-\vec{r}_s) \tag{4.1}$$

and the propagation of the emitted light after excitation by S is given by

$$-\nabla D_m \nabla \Phi_m(\vec{r}) + \mu_{am}\Phi_m(\vec{r}) = -\eta\varepsilon c(\vec{r})\Phi_x(\vec{r}) \tag{4.2}$$

where the subscripts x and m indicate the wavelength dependence of the variables on λ_x and λ_m, respectively. ε is the Molar extinction coefficient, $c(\vec{r})$ is the fluorochrome concentration at $\vec{r}$ and η is its quantum yield. Assuming the wavelength difference between λ_x and λ_m small, absorption and diffusion coefficients can be approximated as being equal at both wavelengths, i.e. $D = D_x = D_m$ and $\mu_a = \mu_{ax} = \mu_{am}$.

The first order Born approximation can be used for describing the fluorescence measurement at detector position $\vec{r}_d$ from a fluorescence source at $\vec{r}$, within a volume Ω, yielding

$$\Phi_m(\vec{r}_d, \vec{r}_s) = \Theta_s \int_{\vec{r}\in\Omega} G(\vec{r}_d, \vec{r}) n(\vec{r}) \Phi_x(\vec{r}, \vec{r}_s) d\vec{r} \tag{4.3}$$

where $G(\vec{r}_d, \vec{r})$ is the Green's function solution (see Equation 2.28) to the diffusion equation, $n(\vec{r})$ is the unknown fluorochrome distribution and Θ_s is the power of the excitation point source. As fluorescence photon densities are much smaller than photon densities caused by the excitation laser source, we further approximate $\Phi_x(\vec{r}, \vec{r}_s) \approx \Theta_s G(\vec{r}, \vec{r}_s)$.

The normalized Born approximation gives the ratio of photon densities at emission and excitation wavelengths created by a point source at $\vec{r}_s$ on the boundary and detected by a detector at $\vec{r}_d$ on the boundary

$$\frac{\Phi_m(\vec{r}_d, \vec{r}_s)}{\Phi_x(\vec{r}_d, \vec{r}_s)} = \int_\Omega \frac{G(\vec{r}_d, \vec{r}) n(\vec{r}) G(\vec{r}, \vec{r}_s)}{G(\vec{r}_d, \vec{r}_s)} d\vec{r} \tag{4.4}$$

This normalization eliminates system related effects like source intensity variations and reduces the sensitivity of the reconstruction for errors in the optical properties that are used for forward model calculation [6, 173].

As discussed in Chapter 2, the analytical formulation of the Green's functions is only valid under certain idealized conditions, which are not fulfilled in our case. Therefore, in this thesis, Green's functions are calculated numerically using a finite element system implemented using a proprietary MATLAB-interface to the Deal II framework [160]. The necessary FEM mesh is generated from the XCT volume, using the outer surface of the imaged object as boundary.

Discretization of the volume into small volume elements finally leads to a linear formulation of the forward problem, which can be expressed for a source-detector-pair

as

$$\frac{\Phi_m(\vec{r}_d,\vec{r}_s)}{\Phi_x(\vec{r}_d,\vec{r}_s)} = \sum_{\Omega} \frac{G(\vec{r}_d,\vec{r})n(\vec{r})G(\vec{r},\vec{r}_s)}{G(\vec{r}_d,\vec{r}_s)} \triangle V \tag{4.5}$$

where $\triangle V$ represents the size of a voxel.

4.2.2 Inversion

For all source detector pairs, Equation 4.5 can be written in a simplified form as a linear matrix system, i.e.

$$\mathbf{y} = \mathbf{W}\mathbf{x} \tag{4.6}$$

where $\mathbf{W}$ is a $N_{measurements} \times N_{voxels}$ matrix containing the weights (sensitivities) for every volume element (voxel) and each source-detector pair assumed, and $\mathbf{y}$ and $\mathbf{x}$ are vectors containing the normalized measurements and the unknown fluorescence distribution, respectively.

Equation 4.6 can be inverted to recover the unknown fluorescence distribution in the volume. However, reconstruction requires uniqueness of the inverse problem, which is not given in the case of the time-independent diffusion equation [8]. Noisy measurements further complicate the already ill-posed problem.

Meaningful solutions can nevertheless be found by minimizing the error between measurements and forward model, and employing regularization methods that stabilize the solution [76] by imposing e.g. continuity or smoothness. This results in the following expression:

$$\mathbf{X} = \arg\min(\|\mathbf{W}\mathbf{x} - \mathbf{y}\|_2^2 + \lambda^2 \|\mathbf{L}\mathbf{x}\|_2^2) \tag{4.7}$$

whereby $\mathbf{L}$ is called the regularization matrix and λ the regularization parameter which determines the order of influence of the penalty term $\|\mathbf{L}\mathbf{x}\|$ on the minimization problem relative to the residual. $\mathbf{X}$ is the result of the reconstructed fluorescence distribution.
The choice of an appropriate regularization parameter λ can be difficult. To determine the respective λ value for each reconstruction in this work, the minimization of Equation 4.7 is solved for 200 different values of λ. Those values are chosen to be logarithmically spaced between $10^{-6} \cdot \|\mathbf{W}\|$ and $10^{1} \cdot \|\mathbf{W}\|$. An optimal λ value is typically selected by L-curve analysis [75] by plotting the solution norm versus the residual norm and then choosing the λ value at the first corner of the resulting L-curve. In Section 4.6

an alternative choice of λ for the computation of regularization factors will be introduced.

The regularization of the residual norm is often realized by a Tikhonov type regularization matrix [9, 71, 182], i.e. $\mathbf{L}$ equals the identity matrix $\mathbf{I}$. This is the case when no prior information is implemented. $\mathbf{L} = \mathbf{I}$ means that all voxels are equally regularized. Conversely, prior information can be implemented by using an $\mathbf{L}$ matrix that contains different values for different tissue segments in its diagonal [4, 86], henceforth denoted as regularization factors.[1] These factors are employed to offer a different degree of regularization to different tissue structures (segments). It was previously shown that this kind of varying regularization can improve the reconstruction of $\mathbf{x}$ in the context of hybrid FMT-XCT [3, 4] (see also Section 4.1.3 for other hybrid approaches). One challenge related to the employment of regularization factors, however, consists in their determination. Manual selection of regularization factors can only be admissible when the fluorescence biodistribution in the imaged object is very well know. Since this is rarely the case in diagnostic imaging scenarios, objective, data-driven methods for regularization factor computation should be employed. The next section addresses this subject in more depth.

4.2.3 Varying regularization

The integration of anatomical data into the FMT reconstruction enables mapping of optical measurements to the surface of an accurate geometrical shape. Internal structures can furthermore be segmented from the anatomical data set, as will be described in Section 4.3, and used to implement functional priors in the forward model and structural priors in the inversion of (limited-projection-angle) FMT.

A data-driven two-step inversion method was previously proposed in the context of 360 degree degree systems [4, 86] for automatically estimating spatially varying regularization factors in the $\mathbf{L}$-matrix , employed to establish priors in Equation 4.7. The two-step inversion method consists of a first inversion step, performed by using anatomical information as prior information in the forward model and employing Equation 4.7 with $\mathbf{L} = \mathbf{I}$ to derive relative fluorescence strengths per segment. Regularization factors for each segment are then estimated from reconstructed intensity values in the

[1] Other publications use the terminology "weights" to denote the different entries in $\mathbf{L}$. This is omitted here in order to avoid confusion with the weights contained in the weight matrix $\mathbf{W}$.

different tissue segments, typically proportionally to the calculated mean signal intensity per segment. Assuming a tissue containing N different segments and a matrix $\mathbf{I}_0$ of size $1 \times N$ containing the average reconstructed intensity in each segment after the first inversion, the segment specific regularization factors f_{seg} are obtained as

$$f_{seg} = \sqrt{\frac{(1+\beta)\max(\mathbf{I}_0)}{\mathbf{I}_0(seg_i) + \beta \max(\mathbf{I}_0)}} \tag{4.8}$$

Where seg_i is the segment containing the voxel i and β is set to 0.066 [86, 126]. This constrains f_{seg} to be in the range $f_{seg} \in [1, \sqrt{1+1/\beta}]$. The second inversion step incorporates these segment specific regularization factors into the diagonal of the $\mathbf{L}$-matrix in order to achieve spatially varying regularization in combination with an adequate regularization parameter λ. Depending on the regularization factor, each segment is stronger (large regularization factor) or weaker (small regularization factor) regularized. I.e. reconstructed intensities appear smoother as the regularization factor increases. The advantage of the two-step data-driven approach is that it is free of user-based assumptions or heuristic selection of regularization factors.

An adaptation of this approach is introduced later in this chapter (Section 4.6.1) for the development of an automatic computational scheme for regularization factor estimation in hybrid limited-projection-angle FMT applications. The basic feasibility of hybrid reconstructions with limited-projection-angle FMT and its evaluation, however, was first investigated with manually set regularization factors, in order to simplify the problem (Section 4.5).

4.3 Imaging setup and data acquisition

4.3.1 FMT setup and data acquisition

For fluorescence tomography a limited-projection-angle trans-illumination tomography system (FMT 2500, VisEn Medical, Woburn, MA) was used. This system consisted of two continuous wave laser sources for excitation at 680 nm and 750 nm. The laser light was guided from the laser through light guiding fibers to a x-y–translational stage. The stage was used to scan a focused laser spot over a region of interest on the surface of the experimental object. Images were acquired by a CCD camera placed on the opposite

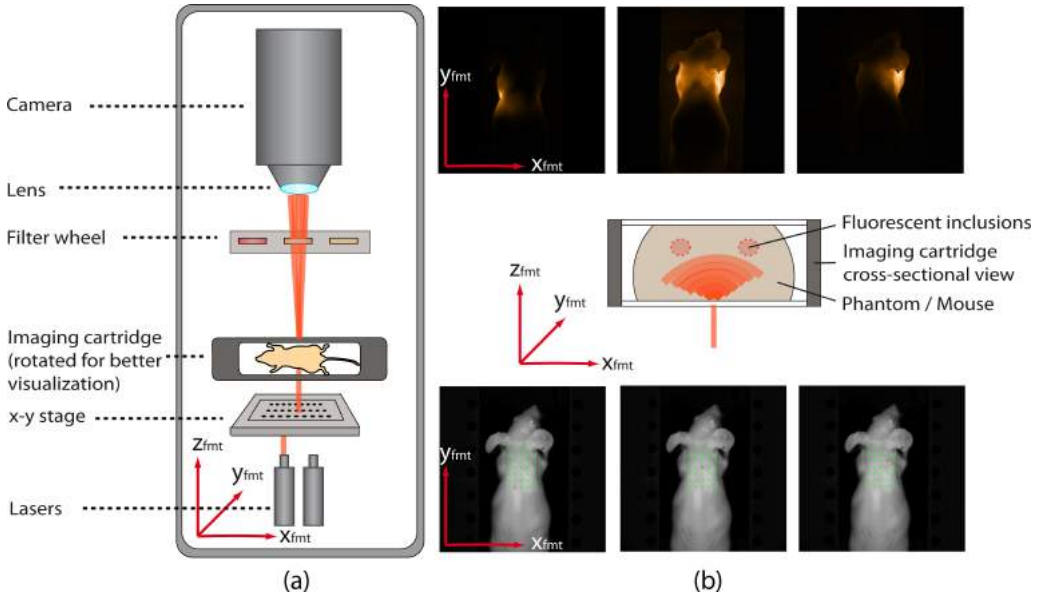

Figure 4.1: Schematic of a limited-projection-angle FMT system (not in right scale) and example for acquired images. (a) FMT setup including lasers, x-y stage for scanning, a filter wheel and a camera. (b) The laser is scanned along the x and y axis (bottom row) and a camera is acquiring the trans-illumination images for each scan (top row). The center shows a cross section of the cartrige containing a phantom with two fluorescent inclusions.

side of the imaged object from the laser sources. A filter wheel in front of the camera was used for filter selection for the respective emission wavelength. Figure 4.1 depicts a schematic of the setup arrangement (not true to scale) and representative images of the scanning process and the respectively acquired diffuse images.

The imaged object was placed in an imaging cartridge consisting of transparent plates, perpendicular to the angle of projection and parallel to the detection plane of the CCD camera. The transparent plates were made of glass-reinforced extruded nylon and covered with an anti-reflection coating for the NIR. The object was inserted between the two transparent plates which apply mild compression to the phantom or mouse body. In this manner the object stayed immobile in the same position while sequentially imaged by FMT, XCT or PET. Figure 4.1(b) shows the cross-section of such a cartridge containing a tissue mimicking phantom with two fluorescence tube insertions (red circles).

The cartridge was always inserted in the same horizontal position in the FMT system, by means of rigid rails. It contained fiduciary markers consisting of small cavities in the frame which were visible in the X-ray CT images. The fiduciary markers are manufactured to mark a plane that is parallel to the detection plane of the CCD camera and were employed to track the position of the cartridge when inserted into the XCT bore

Figure 4.2: FMT imaging cartridge containing (a) a phantom and (b) a mouse. Small holes in the non-transparent margin of the cartridge serve as fiduciary markers (arrows).

so that FMT and XCT data could be accurately coregistered. Figure 4.2 depicts such an imaging cartridge containing a phantom (a) and a mouse (b). The position of the fiduciary markers are highlighted by red arrows.
Typical scan patterns assumed spacings of 2 - 3 mm on a regular grid, depending on the size of the region of interest. On average an area of around 30 mm x 15 mm was scanned, leading to approximately 66 - 128 source points. For each point scanned, transillumination images were collected at the emission and the excitation wavelengths. White light mouse photographs were also collected and served as the basis for coregistration. Exposure times and laser power information were recorded and employed to scale the intensities in the fluorescence and intrinsic images. The scaled images and information on respective source positions served as input to the hybrid FMT reconstruction method presented in Section 4.2.1.

For comparison of hybrid and stand-alone FMT reconstructions, the reconstructed fluorescence signal distribution computed by the stand-alone FMT device with an isotropic resolution of 1 mm was also exported in DICOM (Digital Imaging and Communications in Medicine) format. It was overlaid to the XCT volume by fiducial mapping using the software package AMIRA (Visage Imaging GmbH, Berlin, Germany). This post-reconstruction overlay was used to compare and validate the results attained with the pre-reconstruction overlay.

4.3.2 X-Ray CT data acquisition and segmentation

For anatomical imaging a small animal X-ray CT (Inveon, Siemens Preclinical Solutions, Knoxville, TN, USA) was used. The imaging protocol for the experiments conducted in this study was set to acquire a 3D data set at an effective resolution of 104 µm after fourfold binning. The CT x-ray source operated at 80 kV and 500 µA with an exposure

time of 200 ms for each of the 360 acquired projections. The three dimensional CT data was post-processed to account for beam hardening and exported in DICOM format for further processing.

Segmentation of the XCT data was performed to single out different anatomical structures. When imaging the upper mouse thorax 4 organs were typically segmented, i.e. the lung, bone, heart and remaining tissue. The segmentation was performed (semi-)automatically using thresholding, seed growing and signal detection algorithms as previously reported by Freyer et al. [52].
Summarized, because of the high contrast, bone segmentation could be performed using an automatically derived threshold. From this first segmentation the ribcage was obtained and used for localization of the lung, which was finally segmented using a seed growing algorithm. The seed points were automatically determined from an intensity histogram of voxels lying inside the region of interest determined by the ribcage. For the segmentation of the heart a shape model was used that was iteratively adjusted based on the ribcage and lung segmentations. In contrast to the method described by Freyer et al. the initial position of the heart was not determined automatically but through user input, since in the present case the typical thorax shape was deformed by squeezing in the imaging cartridge.
For subcutaneous tumor mice, an additional segmentation of the tumor area was performed. This area was selected manually based on the XCT images.
For phantom studies, only the tubes and the background medium were segmented from the complete volume, since no other distinguishable structures were present (see Figure 4.1(b) for phantom shape and tube location). For segmentation purposes, the tube walls were employed as boundary indicators since they are visible with high contrast on the XCT images due to their different X-ray absorption characteristics compared to the phantom background medium. The tube boundaries were manually selected in two transversal slices of the XCT reconstruction, each at one end of the phantom, and this input was used for automatic extraction of the rest of the tubes throughout the volume. All voxels lying inside the extracted tube walls were consequently assigned to the tube segments.

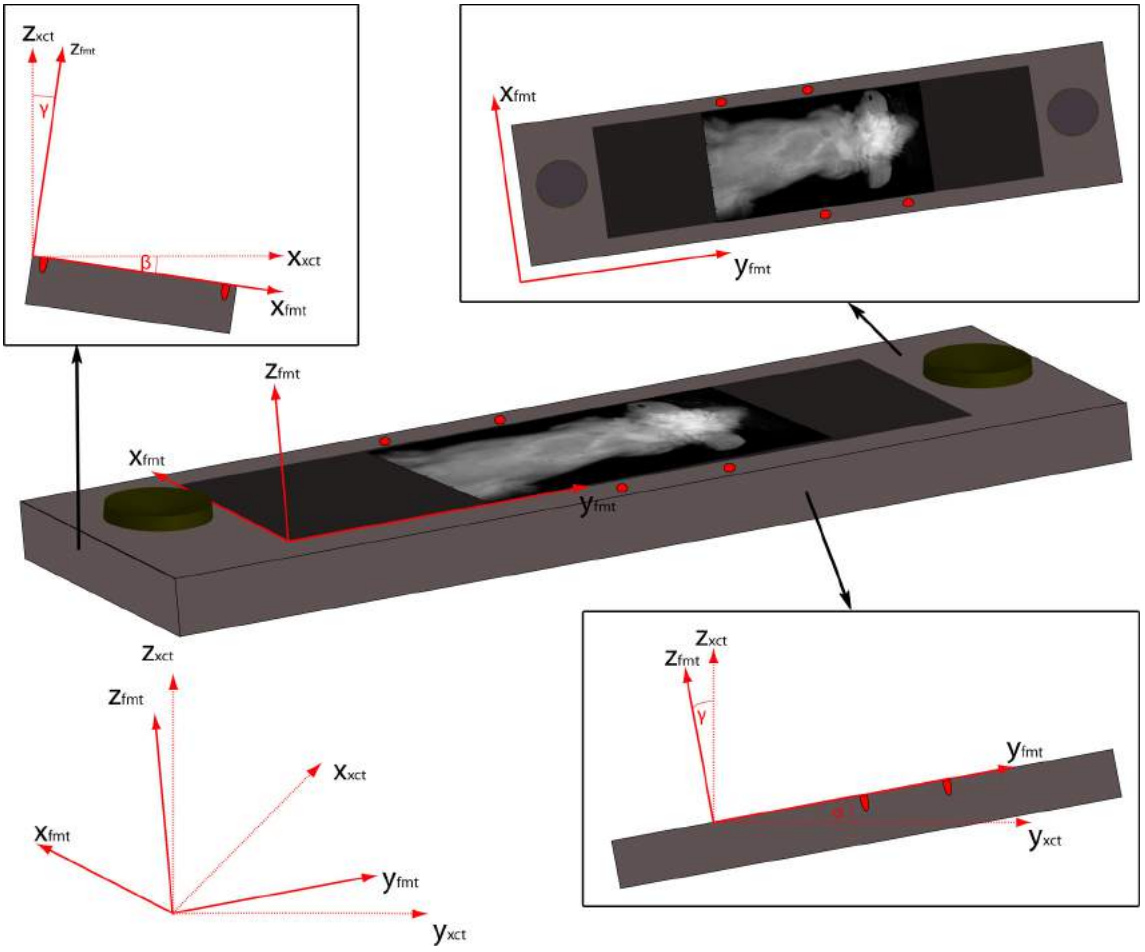

Figure 4.3: Coregistration concept for alignment of FMT and XCT data sets. The coordinate systems of XCT and FMT respectively are mapped to each other through rotation and translation.

4.4 Coregistration of FMT and XCT data

The first step towards the incorporation of priors into the reconstruction of limited-projection FMT data consisted of integrating XCT data into the FMT framework. This was achieved by coregistration of the respective data sets.

For registration purposes, information from the fiduciary markers on the imaging cartridge was combined with boundary information of the animal, as seen on XCT images and the animal photographs obtained by the FMT system. These guided the translation and rotation of the reconstructed 3D XCT volume to fit in a common coordinate system with the FMT data. A schematic of this concept can be seen in Figure 4.3. The white light image taken in the FMT device defined the coordinate system to which the XCT volume

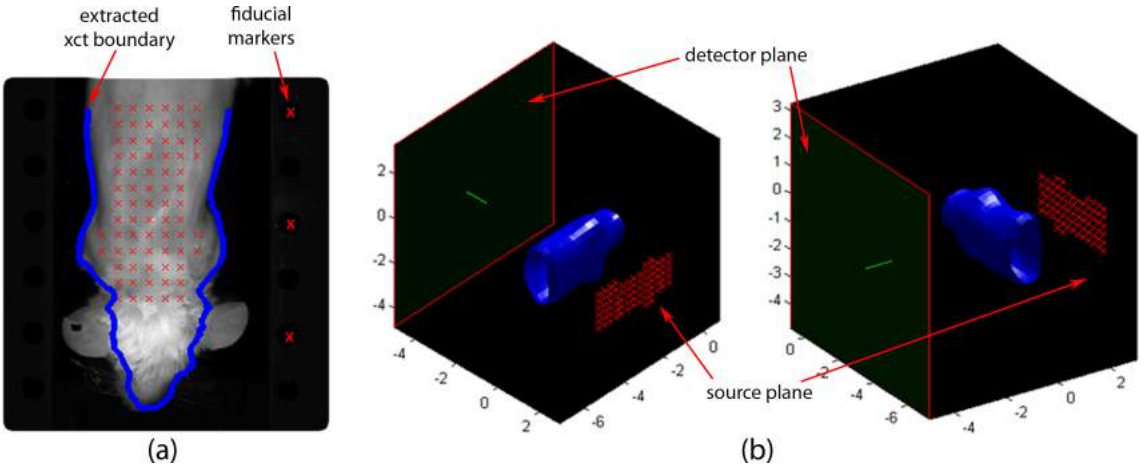

Figure 4.4: Example for coregistered FMT-XCT data set. (a) Fiduciary markers and boundary mapping were used for the fusion of the FMT and XCT data sets. (b) The source and detector information from the FMT device were projected on the boundary computed from the XCT.

had to be coregistered. Since, however, the XCT information is three-dimensional whereby the photograph is two-dimensional, it was not possible to directly extract information on possible rotation of the cartridge in the XCT system, but the plane defined by the fiduciary markers was considered as the horizontal plane corresponding to the photograph. The fiduciary markers were then employed to measure and correct for the rotation angle between the x, y and z axis in XCT and FMT.

After rotation, x- y translation was applied to align the XCT images and FMT data to a common coordinate system. More specifically, the orientation of the cartridge (transversal, sagittal plane) was extracted from the reconstructed XCT images based on the cartridge plates and fiduciary markers. According to Figure 4.3, the angles denoted by α, β, γ between the XCT planes (x_{xct}, y_{xct}, z_{xct}) and the (x_{fmt}, y_{fmt}, z_{fmt}) plane of the photograph from the FMT device were computed by projecting the FMT photograph to the x_{xct}- y_{xct} ($z_{xct} = 0$) plane and computing the angles between this plane and the ones defined by the fiduciary markers along the transversal and sagittal slices. Then the 3D XCT image was rotated so that it could be aligned with the (x_{fmt}, y_{fmt}, z_{fmt}) plane. Having consequently produced two parallel data sets a translation step was then performed to map the boundary and fiduciary information from the XCT to the mouse photograph. To achieve this, the animal boundary from the XCT was produced by projecting the XCT slices along the z axis on one single plane that corresponded to the FMT photographic plane (i.e. a maximum intensity projection and subsequent boundary extraction by thresholding). This step is visualized in Figure 4.4. Figure

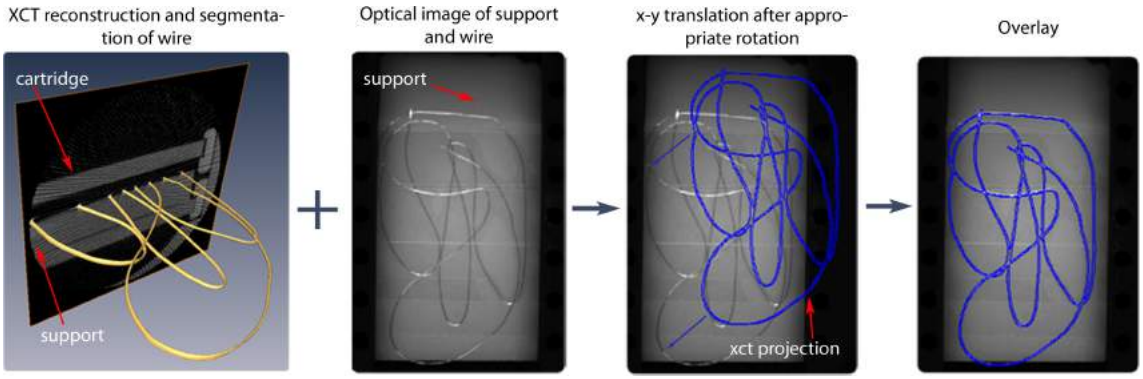

Figure 4.5: Evaluation of FMT-XCT coregistration accuracy by imaging of a thin wire phantom. The XCT image (1st panel from left) and optical image (2nd panel from left) were coregistered and overlayed (3rd and 4th panel).

4.4(a) depicts a black and white image of a mouse acquired with the FMT camera and the overlaid boundary extracted from the XCT image, shown in blue. The laser source positions and the location of the fiduciary markers are projected onto the overlay in red. This projection is enabled by the integration of both modalities into one geometrical framework. The acquired fluorescence images could then accordingly be projected onto the same geometrical scheme.
Summing up, in contrast to other coregistration approaches previously used for FMT-XCT post-reconstruction coregistration using a cartridge [128] this approach is not mapping two 3D data sets to each other using fiduciary markers but performs pre-reconstruction 2D to 3D mapping and employs additionally the sample boundary for more accurate coregistration results. The width dimension (z) of the animal was obtained from the XCT and confirmed both by the internal measurement system in the FMT device, which measures the cartridge width using two ultrasound transducers, and the display on the cassette.

The accuracy of the co-registration method was examined using a 230 µm copper wire placed in random directions in the cartridge and imaged by XCT and FMT (only reflectance image). Figure 4.5 illustrates the results obtained from the validation study examining the coregistration of FMT and XCT data. It shows an XCT image (1st panel from left) and a photograph (2nd panel from left) of the wire phantom as well as the overlay of both data sets after rotation, scaling and translation. The wire shape extracted from XCT data and projected in one plane could be perfectly aligned with the FMT reflectance image without any apparent non overlapping regions. The coregistration accuracy was measured as the distance between the wires as seen by the optical and the

XCT image on the overlay of Figure 4.5, 4th panel. This difference was found to be 1 pixel (worst case), i.e. max. 154 µm, i.e. much smaller than the resolution achieved by FMT.

4.5 Hybrid reconstruction of limited-projection-angle FMT

This section evaluates the general feasibility of hybrid reconstructions of limited-projection-angle FMT data. It presents the results obtained after integration of anatomical data into the reconstruction of limited-projection-angle FMT. Two scenarios were considered to compare and evaluate the improvements; the first employing homogeneous tissue in form of a tissue mimicking phantom, and the second employing heterogeneous tissue in form of an *in-vivo* mouse experiment.
Because previously well characterized homogeneous and heterogeneous tissues were employed, manually selected regularization factors could be used for this proof-of-principle study. For inversions shown in this section, we assigned the smallest regularization factor ($f_{seg} = 1$) to the region(s) that were expected to have highest fluorescence signals. The other regions were assigned a high regularization factor ($f_{seg} = 4$). These regularization factors were lying within the admissible range defined above (Equation 4.8). This allocation of $\mathbf{L}$-matrix regularization factors is therefore a variation of the method presented by Hyde et al. [86].
Note that manual selection of weights is only appropriate when using phantoms or specific mouse models where the appearance of disease or fluorescence distribution is known before-hand [4, 85]. This approach was only used herein for demonstration purposes with limited-projection-angle schemes, using known phantoms and animal models. However, data-driven regularization factor allocation is instead recommended for more general cases where the appearance of disease or the fluorochrome bio-distribution is not known before-hand [3] and will be subject of Section 4.6.

4.5.1 Evaluation on homogeneous tissues

First implementation and evaluation of hybrid reconstruction of limited-projection-angle FMT-XCT was performed on a homogenous tissue mimicking phantom representing

a mouse thorax in shape and size. The full potential of hybrid versus stand-alone reconstructions was subsequently confirmed in mouse experiments which constitute more realistic test cases due to heterogeneous tissue properties.
Cylindrical, tissue mimicking phantoms with inclusions containing a NIR fluorescence dye with peak excitation at 679 nm and peak emission at 702 nm (Alexa Fluor 680, Life Technologies Ltd, Paisley, UK) were imaged in both modalities. The phantoms were composed of a mixture of an adequate ratio of intralipid, ink, agar and water in order to attain tissue properties of $\mu_s' = 12\,\mathrm{cm}^{-1}$ and $\mu_a = 0.2\,\mathrm{cm}^{-1}$ and were shaped to semi-cylinders resembling the shape of a mouse torso. The phantom measured approximately 36 mm in length and had a diameter of 30 mm at the widest point, the two inclusions had a diameter of approximately 3 mm. The tubes were positioned in the upper curved part of the semi-cylinder as depicted in Figure 4.1(b) by the red dotted circles, and filled with the NIR fluorescent dye diluted in liquid with the same optical properties as the phantom, resulting in a fluorochrome concentration of 100 nmol .

Three ways of integrating anatomical data into the reconstruction of optical signals were considered and compared in this study: The first did not use any information from the XCT but was based on boundary detection through the FMT camera and further assumed slab geometry due to the imposed shape of the imaging cartridge. Reconstructions based on this method were automatically provided from the used FMT imaging system. The second used the exact boundary detected by the XCT scan but no further anatomical information. The third fully integrated all available information from the XCT data, i.e. boundary and other segmented internal tissues (tubes for the phantom, organs for the mouse experiments). Consequently, depending on the different level of available anatomical information, different inversion schemes had to be implemented.

The first two approaches used a regularization matrix $\mathbf{L} = \mathbf{I}$ in the inversion, since no knowledge on the internal structures was available, and hence only differed in the assumed tissue geometry. The third approach employed a regularization matrix with varying regularization factors in the diagonal. Figure 4.6 depicts the respective geometries used for reconstruction and regularization, as well as the corresponding regularization matrixes. Figure 4.6(a) shows one transverse slice of the slightly compresses phantom between the two transparent plates. The location of the fluorescence tubes can be seen due to the different X-ray attenuation properties of the tube walls compared to the phantom attenuation. Figure 4.6(b) presents the tissue geometry that the stand-alone FMT systems assumes based on the white light reflection image in transparent blue overlay on the XCT

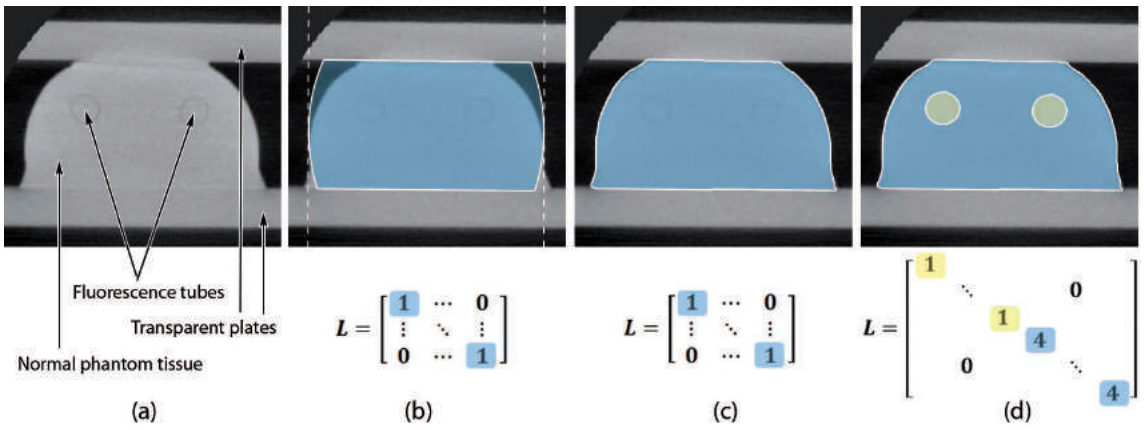

Figure 4.6: XCT cross section of the tissue mimicking phantom showing the different geometries employed for FMT reconstruction. (a) XCT slice. (b) Geometry employed in stand-alone FMT reconstructions. (c) Geometry employed when using the boundary extracted from the XCT data. (d) Geometry employed when XCT data segmentation is considered.

slice. Only the boundaries of the object are visible on the optical image acquired by the CCD. They are used to approximate the shape of the object by projecting the boundary along the z-axis (marked by dashed white lines) and fitting a flattened elliptic shape to the whole width. The regularization matrix is uniform for the whole blue marked area. When the exact shape of the object is known, a much more accurate volume can be chosen for reconstruction, as indicated in Figure 4.6(c). The regularization matrix however stays the same in absence of internal segmentation. Figure 4.6(d) finally shows the segmented tubes in yellow. The regularization matrix now contains different regularization factors in its diagonal, corresponding to each voxel's affiliation to one of the tissue segments.

Figure 4.7 shows the reconstruction of the fluorescence signal assuming the phantom being an infinite homogeneous slab and without the use of priors (stand-alone reconstruction). Figure 4.7(a) depicts in gray three-dimensional X-ray CT images of the cassette and phantom inside the XCT scanner. Reconstructed fluorescence signals are co-registered on the images in dark red color. Figure 4.7(b) shows transverse (axial) slices at different locations along the y axis (as referred to in Figure 4.1). The slices are showing the localization of the reconstructed fluorescence signal inside the phantom. The location of the tubes can be seen on the XCT images and are highlighted in the first slice with red circles. It can be observed in the upper image of the 3D representation and in all transversal slices of Figure 4.7 that fluorescence distribution seen on stand-alone FMT reconstructions is partially located outside the real volume (highlighted by red arrows)

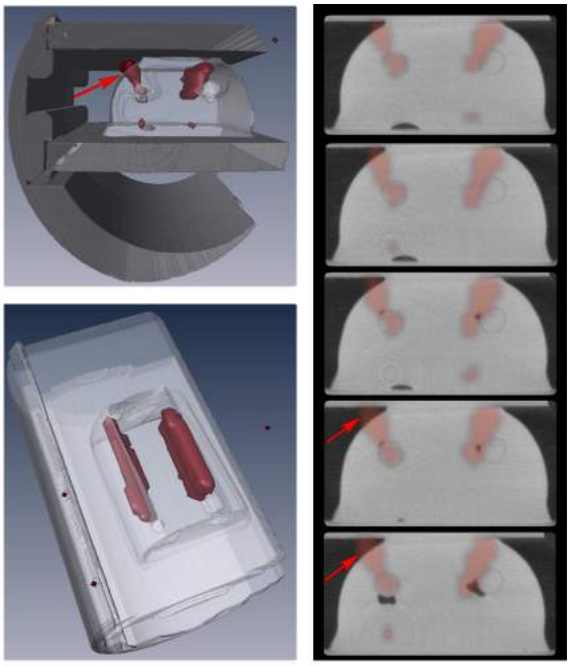

Figure 4.7: Phantom experiment showing reconstructions from stand-alone FMT. (a) Three dimensional representation of the phantom with cartridge and adapter, showing the entire reconstruction provided by stand-alone FMT. In the lower image the fiduciary markers can be seen as red dots. (b) Exemplary slices through the reconstructed volume.

and only partially coincides with the fluorescent inclusions.
Figure 4.8 shows the corresponding reconstructions without priors, but using the actual phantom shape as boundary into the inverse code. The upper image in Figure 4.8(a) shows the location of the five slices inside the phantom. The use of the boundary overall improves imaging performance, over stand-alone reconstructions in particular along the horizontal axis (Figure 4.8(b)). On the vertical axis, both reconstructions reconstruct an elongated shape rather than a circle. The stand-alone reconstruction shows a displacement of the center of the ellipse toward the phantom boundary. Conversely, the use of the actual boundary better estimated the center of the fluorescence activity.
Figure 4.9 finally depicts the reconstruction using the actual phantom boundary and anatomical priors. Here, additionally to the improved horizontal alignment one can observe improved vertical alignment and confinement of the main fluorescence signal to the tubes.

The difference in reconstruction accuracy for the three reconstruction methods applied to phantom imaging was evaluated. For that, the localization of the reconstructed

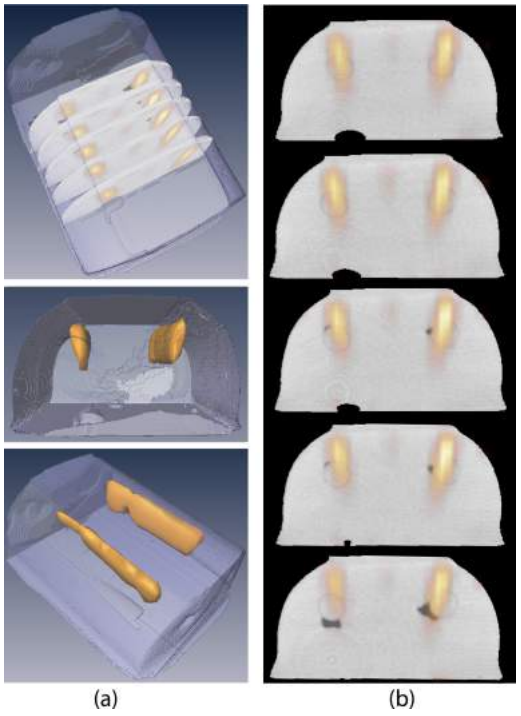

Figure 4.8: Phantom experiment showing reconstructions from hybrid FMT-XCT using the outer XCT boundary for reconstruction. (a) Three dimensional view of the reconstructed fluorescence distribution using Tikhonov regularization. The top image shows the position of the five slices that are shown in (b). (b) Slices through the reconstructed volume.

fluorescence in the phantom was determined by defining concentric circles with increasing radius around the tubes and calculating the percentage of the total reconstructed signal per slice that was located inside the circles depending on the distance from the tube. Figure 4.10 (a) shows one exemplary slice with the concentric circles at distances of 0 mm to 5 mm from the tube depicted in red. The innermost circle is at 0 mm distance from the tube which means that it represents exactly the tube boundary. Each of the other circles has a distance of 1 mm from the other circles. The graph in Figure 4.10 (b) shows the percentage of the recovered signal as a function of the distance from the tube for the stand-alone FMT (blue), FMT-XCT using only the boundary of the phantom (yellow) and FMT-XCT using priors (red). Stand-alone FMT thus only localized 19% of the reconstructed signal inside the tube and even in a distance of 5 mm around the tube not more than 68% of the signal could be found. The reconstruction using the accurate mouse boundary and Tikhonov reconstruction recovered 33% of the signal inside the tubes and went up to 91% in a distance of 5 mm. The hybrid reconstruction using priors finally started with a localization of 77% inside the tubes and already reached 100% in a distance of 2 mm around the tubes.

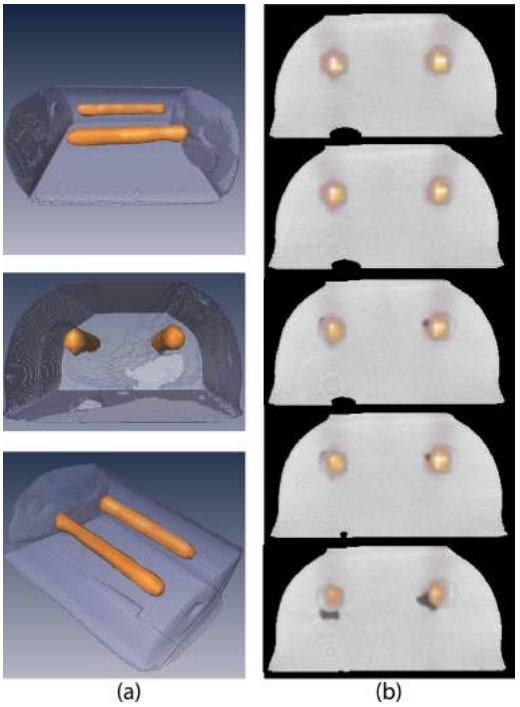

Figure 4.9: Phantom experiment showing reconstructions from hybrid FMT-XCT using the segmented XCT volume for reconstruction. (a) Three dimensional view of the reconstructed fluorescence distribution using differently weighted segments for regularization. (b) Slices through the reconstructed volume.

The results from the phantom study suggest that the use of prior information can reduce the ill-posed nature of the limited-projection-angle FMT inverse problem and improve the imaging performance, as previously seen for 360 degree projection FMT [3].

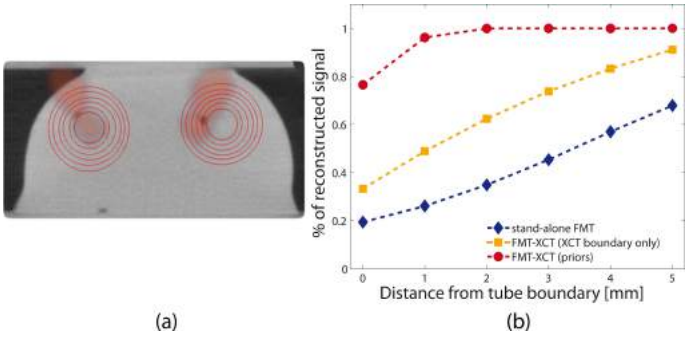

Figure 4.10: Comparison of reconstruction accuracy using the three different reconstruction approaches in the phantom study. (a) Delineation of concentric circles around fluorescent tubes considered for localization evaluation. (b) Plot of the percentage of reconstructed signal located inside a certain radius (x-axis) around the actual tube.

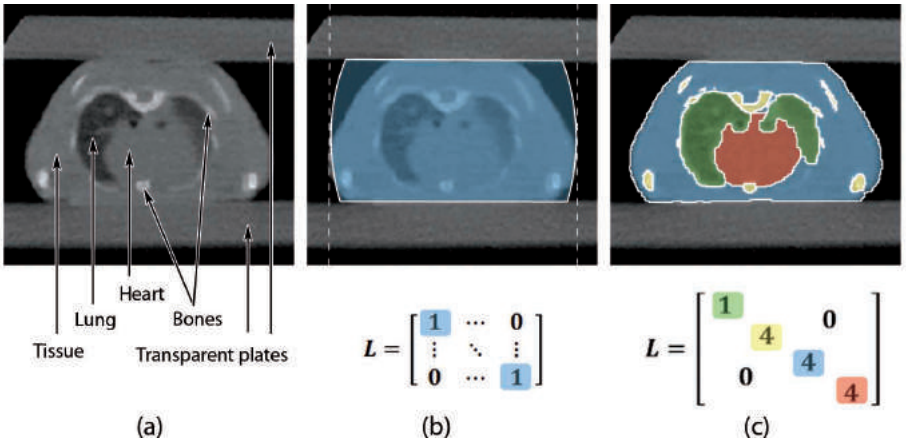

Figure 4.11: XCT cross section of a mouse thorax showing different geometries employed for FMT reconstruction. (a) XCT slice. (b) Geometry employed in stand-alone FMT reconstructions. (c) Geometry employed when XCT data segmentation is considered.

It is even more essential for limited-projection-angle FMT, since reducing the information contained in the data collected increases the ill-posed nature of the reconstruction problem. The experimental findings from the phantom measurements show that the image performance improves when using the actual boundary in the inversion, as compared to assuming the phantom being an infinite slab, a convenient theoretical approximation of early diffuse optical tomography approaches [63]. Naturally, the most accurate performance is found when anatomical priors of internal structures were also employed (Figure 4.9).

4.5.2 Evaluation on heterogenous tissues

Tissue phantoms are convenient approximations to real tissue scenarios and adequate for pilot experiments and proof-of-principle studies. To fully investigate the potential of hybrid limited-projection-angle FMT reconstruction, however, real tissue displaying multiple boundaries and heterogeneous tissue optical properties were required.
Similarly to the phantom study, different reconstruction geometries were assumed for stand-alone and hybrid reconstructions, also resulting in different regularization matrixes. Figure 4.11(a) shows a transversal XCT slice of a mouse thorax, where the bones and the lung can clearly be distinguished from the other tissues. Stand-alone FMT again only uses the boundaries of the mouse and therefore reconstructs fluorescence biodistribution using the same geometrical shape as already seen for the phantom (Figure 4.11(b)). Using the

XCT information on the other hand provides information on the exact mouse shape and a segmentation of some internal organs, as shown in Figure 4.11(c). Regularization factors are now individually assigned to all segments. Assuming a mouse with lung tumors into which a fluorescent probe targeting these tumors is injected, highest fluorescence is expected from the lungs. Therefore, this segment receives the lowest regularization factor (marked green in the regularization matrix in Figure 4.11(c)). The other segments, i.e. bones (yellow), heart (red) and mixed tissue (blue) are all assigned a high regularization factor, because little fluorescence is expected in these regions.
Segmentation is not only useful for the inversion process. For the mouse study, different optical properties were assigned in the forward model to each of the segmented organs to take into account their varying level of scattering and absorption. Optical properties values were extracted from [3]. The difference in XCT and FMT resolution was taken into account by proportionally assigning each FMT voxel to its higher resolved anatomical segments as previously described in [4, 85, 86].

A well-known lung tumor mouse model (Kras [R49]) was used for the evaluation of hybrid limited-projection-angle FMT reconstructions in heterogeneous tissues. A targeted fluorescence agent comprising an integrin $\alpha_v\beta_3$ antagonist and a NIR fluorochrome with peak excitation at 675 nm and peak emission at 693 nm (IntegriSense 680, PerkinElmer, Waltham, MA, USA) was administered. Integrins are a group of transmembrane receptor proteins. Changes in their expression are associated with tumor growth, which generally makes them an interesting target in molecular imaging.
At the beginning of the imaging session the mice were anesthetized and placed in the previously described multi-modal imaging cartridge that held the mouse during the entire acquisition period in both FMT and XCT in a fixed position.
In contrast to the phantom experiments, the exact fluorochrome distribution was unknown. In order to evaluate the reconstruction outcome, *in-vivo* reconstructions had to be compared to *ex-vivo* validation slices of the same mouse. Following *in-vivo* imaging the mice were therefore euthanized and frozen while still in the imaging cartridge in order to keep their slightly squeezed shape for validation. The mice were sliced in a cryotome (CM 1950, Leica Microsystems) and each slice was imaged using an epi-fluorescence system at the according excitation/emission wavelength of 680 nm/700 nm [158]. In the following, images of *ex-vivo* slices showing the true fluorescence distribution will be compared to the corresponding reconstructed slices from the *in-vivo* measurements as to their accordance in signal localization and relative signal intensity.

Figure 4.12 depicts results from the *in-vivo* studies. It compares stand-alone reconstruction using slab geometry and hybrid reconstruction using priors with *ex-vivo* fluorescence images of the corresponding *in-vivo* slices. The extraction of boundary information and its incorporation into such optical imaging problems was previously already shown using other means like e.g. imaging with photogrammetric 3D cameras [161] or volume carving based on silhouette images [43]. The phantom study additionally showed best results when using priors. This *in-vivo* study therefore concentrated on the methodology and improvements specific to the hybrid FMT-XCT approach, namely through incorporation of priors due to organ segmentation.

Figure 4.12(a) shows stand-alone FMT reconstruction as it is output by the FMT 2500. In Figure 4.12(b) the reconstruction using varying regularization factors is presented. Finally, Figure 4.12(c) contains *ex-vivo* slices indicating the actual fluorescence intensity and distribution. The corresponding position in the mouse body can be seen in Figure 4.12(top). All slices in one row but belonging to different columns correspond to each other.

The *ex-vivo* validation images (Figure 4.12(c)) show several areas with increased fluorescence intensity compared to surrounding lung tissue. Some examples are highlighted by red arrows. While in some slices only single outstanding points can be observed (e.g. slice 2) others show more than one above-average fluorescent signal source (e.g. slice 4). The hybrid reconstruction using priors (Figure 4.12(b)) resolves the single fluorescence sources very well (e.g. arrows in slices 1 and 2) but seems not to be able to distinguish between three proximate but distinct spots (like in slice 4). Those are reconstructed as one single fluorescence source centered between the three source points.

The stand-alone method (Figure 4.12(a)) in turn allocates most of the reconstructed signal outside the lung tissue. Most of this distribution is moreover not in the expected region but above and below the lung.

As *in-vivo* optical imaging achieves less resolution than the *ex-vivo* validation method, reconstructed distributions can ”irradiate” into adjacent tissue slices and appear there with less intensity. This can for example be observed in the third and fourth slice of the hybrid reconstruction (Figure 4.12(b)). The fluorescence signal in the middle of both (beneath the spine) only appears in the fourth *ex-vivo* slice and is quasi anticipated in the third slice of the hybrid reconstruction.

Note that due to the process of freezing and small displacements of the animal during this time, small shifts between *ex-vivo* and *in-vivo* images are expected and no utterly identical representation can be achieved.

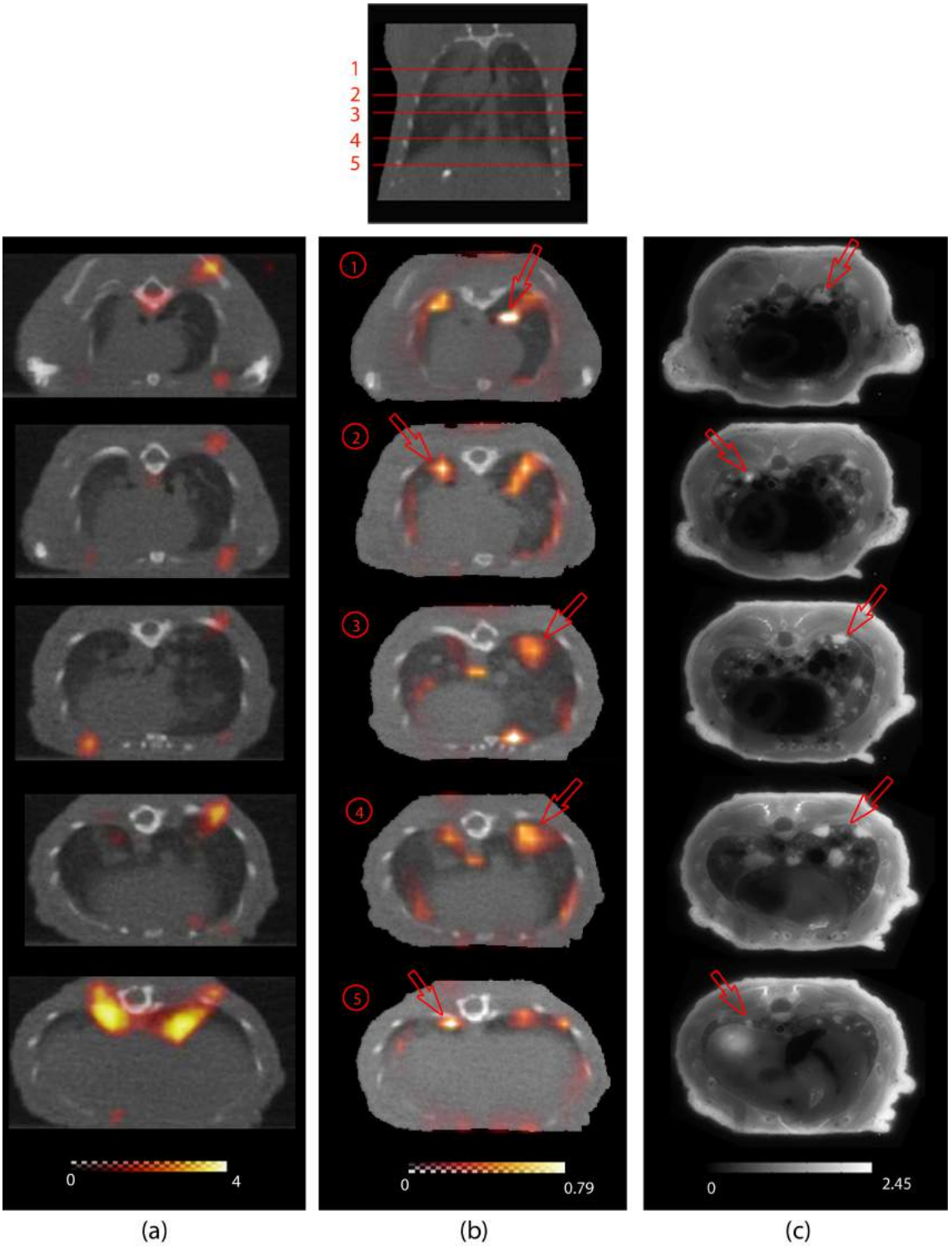

Figure 4.12: Comparison of FMT reconstructions computed using (a) stand-alone FMT without boundary or prior information and (b) hybrid FMT-XCT and the segmentation information derived from the XCT. (c) Corresponding *ex-vivo* slices. All slices in one row are the same. The positions of the slices in each column are depicted in the top image.

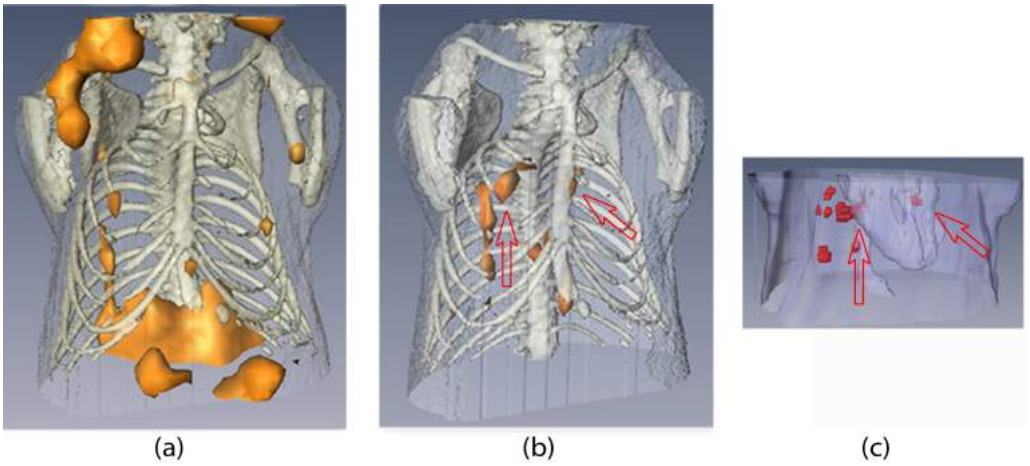

Figure 4.13: Three dimensional representations of (a) stand-alone reconstruction and (b) hybrid reconstruction using priors visualize the probe distribution and the fluorescent hot spots. (c) The 3D representation acquired from the *ex-vivo* slices shows signals in the same spots as the hybrid reconstruction in (b).

Figure 4.13 finally shows 3D views of the fluorescence distribution as to the stand-alone (Figure 4.13(a)) and hybrid (Figure 4.13(b)) reconstructions, as well as the *ex-vivo* distribution (Figure 4.13(c)). Here it becomes even more obvious where the main fluorescence signals in the stand-alone reconstruction are allocated to. A threshold to both *in-vivo* 3D representations was applied in order to receive similar sized fluorescence signals in the lung. In the stand-alone case (Figure 4.13(a)) this leads to proportionally higher signal intensities in those regions that were determined by the reconstruction to be the main fluorescence hot spots - around the shoulder and below the lung. For the hybrid reconstruction basically all areas are located inside the chest. This corresponds well to the *ex-vivo* 3D image, which was assembled form cryoslices obtained every 250 µm, where the chest region around the heart (transparent structure inside the chest in Figure 4.13(c)) is displayed. The most intense fluorescence spots are shown in red and arrows highlight the associated regions in Figures 4.13(b) and 4.13(c).

A comparison of all *ex-vivo* and *in-vivo* measurements was done by defining in the cryosections a region around each tumor where a reconstructed signal would be admissible. Since the FMT reconstruction signal is more diffuse than the real signal, this region was chosen up to 2 mm around the actual tumor. The ratios of maximum fluorescence intensity in the tumor over maximum intensity in the muscle and in the lung were calculated for the cryosections. The same ratios were calculated for the *in-vivo* data in the corresponding regions as determined from the cryosections.

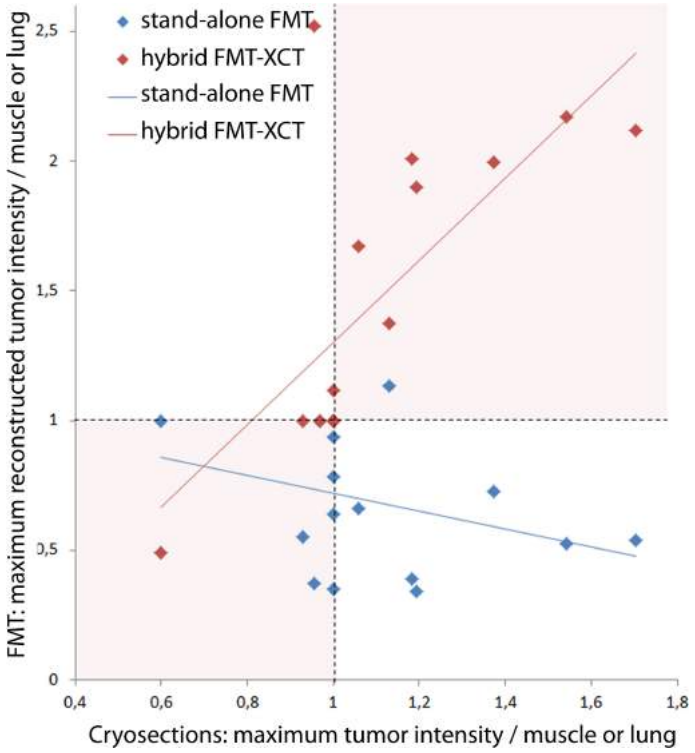

Figure 4.14: Comparison of reconstruction accuracy using the different reconstruction approaches in the *in-vivo* mouse study. Plot of tumor/muscle and tumor/lung ratios in the *ex-vivo* cryoslices vs. *in-vivo* stand-alone (blue) and hybrid (red) reconstructions.

Ratios of tumor/muscle and tumor/lung in the cryoslices versus the ratios of the same regions in the FMT reconstruction are shown in Figure 4.14. Generally, if the FMT reconstruction corresponds well to the *ex-vivo* slices the tumor/lung or tumor/muscle ratios should ideally linearly increase or decrease with increasing or decreasing cryoslice ratios. Therefore, acceptable data pairs would lie in the two quadrants highlighted in light red. It can be seen that almost all data pairs (92%) from the reconstruction using priors fulfilled this requirement and the general trend of the data showed a linear increase (red dots and line). The reconstructions from the stand-alone FMT in contrast only plotted half of the data pairs inside the red quadrants (50%) and the trend line shows that the FMT signal was decreasing with increasing cryoslices signal (blue dots and line).

In conclusion, the *in-vivo* measurements corroborated the findings from the phantom experiment. It was found that reconstructed fluorescence signals were misplaced or erroneously allocated to areas outside the tissue volume, leading to imaging artifacts, when the inversion was performed with software that assumes the mouse as an infinite

homogenous slab medium. In contrast, when the actual mouse boundary and anatomical priors were employed into the inversion code the number of artifacts was significantly reduced and there were significant improvements in the congruency between *in-vivo* data and fluorescence cryoslice images.

4.6 Towards multispectral hybrid FMT

Section 4.5 showed the general improvements that can be achieved when using hybrid schemes in the reconstruction of limited-projection-angle FMT. For this proof-of-principle, manually selected priors were used. While this is an appropriate approach for a first evaluation when the employed phantom and mouse model are well known, alternative schemes have to be developed that can be applied to any mouse model and any employed fluorescence probe.
Fluorescence distributions are usually unknown prior to imaging. On the contrary, imaging aims at finding these exact distributions. The approach of adapting automatic regularization factor computation to limited-projection-angle FMT is all the more important the more manual factor selection is likely to bias the outcome of the reconstruction. This is particularly relevant for studies employing multiple fluorochromes in the same animal. In this context, anatomical data always stays unchanged while the fluorescence distribution differs depending on the used probe at each wavelength. Therefore, applying the same regularization factors for reconstructing all wavelengths may be wrong, since the different fluorochromes may distribute differently. Manually selecting different factors per wavelength requires on the other hand exact knowledge on the different fluorochrome's distribution, which is rarely available. Making heuristic assumptions on the probe's accumulation site by setting regularization factors manually, may therefore introduce bias and falsify the results.

This section therefore investigates the previously unexplored ability and relative accuracy by which two different fluorescent agents can be resolved in the same object simultaneously, when using hybrid implementations in limited-projection hybrid FMT using priors. For this purpose, the previously described method automatically implementing spatially varying regularization [86] was adapted, which was initially developed based on 360 degree FMT data, and optimized for limited-projection-angle FMT-XCT. The particular interest herein was to evaluate whether and how automatic computation of regularization factors could be translated to limited-projection-angle FMT reconstructions.

Therefore, different regularization factor computation results are characterized based on varying regularization parameters used, and improved reconstruction metrics for data driven *a priori* regularization are offered. In contrast to manual factor selection as applied in the previous section, this approach solely relies on automatically computed regularization factors and therefore enables independent reconstruction of different fluorescent probes. By this experimental study a methodological framework for multi-molecular *in-vivo* investigations is provided.

4.6.1 Automatic regularization factor computation

This section introduces the methodological framework for data-driven regularization factor computation. The influence of different regularization parameters λ on the computation of regularization factors in the step-1 inversion (i.e. after Tikhonov regularization, see two-step inversion method described in Section 4.2.3) was examined for this purpose. The objective was to find an ideal λ for the automatic estimation of regularization factors for the step-2 inversion. This was initially tested on phantom data containing fluorescent insertions.

During the step-1 inversion, Tikhonov reconstruction using the identity matrix was performed and an initial regularization parameter was chosen by L-curve analysis at the L-curve corner [75]. The value of λ was subsequently increased until an over-regularized state was created, represented by smoothing the entire reconstruction towards a single bright lesion in the middle of the phantom. The motivation for this L-curve analysis was to find a value for λ where regularization is high enough to suppress surface artifacts, but still enable a representative overall fluorescence distribution. The best λ value identified in this process was then used in the step-1 inversion to derive segment-specific regularization factors, the latter employed in the $\mathbf{L}$-matrix of the step-2 inversion. The segment-specific regularization factors were determined by computing the mean reconstructed intensity $\mathbf{I}_0(seg,\lambda)$ per segment for all values of λ

$$\mathbf{I}_0(seg,\lambda) = \frac{\sum_{seg} X(\lambda)}{N_{voxels}(seg)} \tag{4.9}$$

to be the sum of the reconstructed fluorescence X in each segment divided by the number of voxels in this segment $N_{voxel}(seg)$. The $\mathbf{I}_0(seg)$ values for each wavelength were then normalized so that the segment with the highest mean intensity $\max(\mathbf{I}_0)$ was attributed

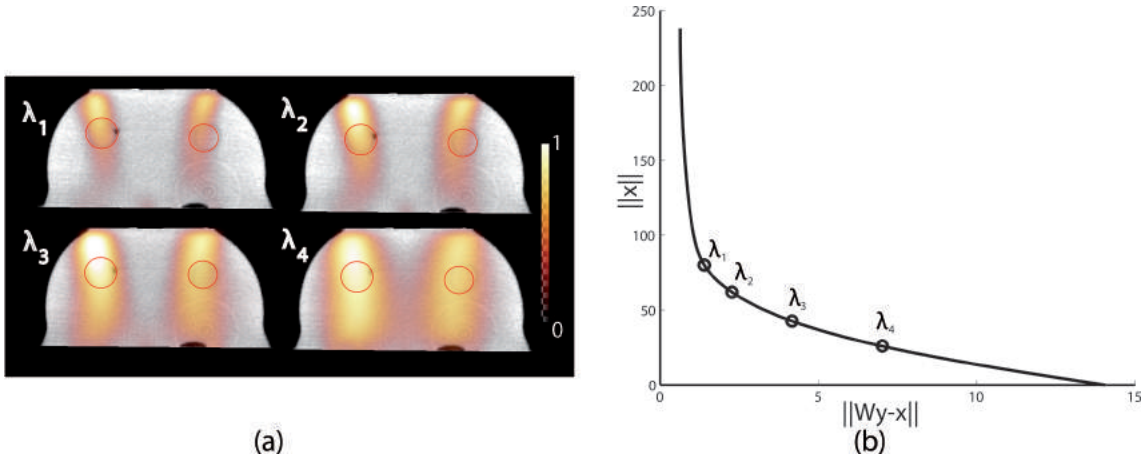

Figure 4.15: Evaluation of the influence of the regularization parameter on Tikhonov reconstructions. (a) Tikhonov reconstruction (step-1 inversion) of fluorescent inclusions (red circles) in a tissue mimicking phantom for different regularization parameters λ, marked on the corresponding L-curve in (b).

the value 1 in the $\mathbf{L}$-matrix (during the step-2 inversion), the segment with the lowest mean intensity $\min(\mathbf{I}_0)$ value was attributed the value of 3 and all other segments were regularized with a value between 1 and 3 proportionally to their $\mathbf{I}_0(seg)$ value. This can be expressed by the following equation [6] for future reference

$$f(seg) = 2 \cdot \left[\frac{\mathbf{I}_0(seg)^{-1} - \min(\mathbf{I}_0^{-1})}{\max(\mathbf{I}_0^{-1}) - \min(\mathbf{I}_0^{-1})} \right] + 1 \tag{4.10}$$

Figure 4.15 depicts four phantom reconstructions with different values of λ using standard Tikhonov regularization, and the corresponding L-curve. The shown representative values of λ_n included λ_1 at the L-curve corner and its 2^{n-1} multiples ($\lambda_2 \approx \lambda_1 \cdot 2^1$; $\lambda_3 \approx \lambda_1 \cdot 2^2$; $\lambda_4 \approx \lambda_1 \cdot 2^3$). Reconstruction for λ_1 shows an elongated appearance of the circular objects (fluorescent tubes) with the peak intensity biased toward the surface (see also Figure 4.8 for the whole volumetric reconstruction with this value of λ). As the λ values increase from λ_1 to λ_4 the reconstructed image appears more diffusive in nature but the elongation is retained, due to the limited angle projection data collected by the system. While resolution drops with increasing λ, reconstructed signals also become less surface weighted and overlap between reconstructions and actual tube location increases.

Data-driven regularization factor computation depends on the step-1 reconstruction and therefore on the used value of λ. Step-2 reconstruction in turn differs depending on

the used regularization factor. This can be summarized in the following relationship:

$$\text{step-2 inversion} \propto \text{regularization factor} \propto \text{step-1 inversion} \propto \lambda$$

meaning that both step-2 reconstruction and regularization factors can be expressed as functions of λ. In order to evaluate which λ yields best regularization factor estimation and step-2 reconstruction, the dependency of these two parameters has to be more closely analyzed.

Regularization factors can be directly computed based on Equation 4.10 for all values of λ, as described above.
For the evaluation of step-2 reconstructions two metrics have to be introduced. The first evaluates the localization accuracy of the reconstructed signals the same way as presented in Section 4.5.2. That is, an area delineated by a distance of 2 mm around the fluorescence tubes was assumed as admissible reconstruction area and the percentage of the reconstructed signal within the region was computed. The threshold set for assuming that a fluorescence signal originates from a location of true probe accumulation was set as the mean signal intensity in the entire phantom plus two standard deviations of background noise (as previously described in [5]). This yields the following formulation for the assessment of signal localization $l(tube,\lambda)$ per tube

$$l(tube,\lambda) = \frac{X(tube,\lambda) > T}{X(\lambda) > T} \tag{4.11}$$

where T is the threshold value and $X(\lambda)$ is the reconstruction obtained from Equation 4.7. $X(tube,\lambda)$ hence denotes only the voxels of $X(\lambda)$ that are localized in the respective tube.
The second metric compares the relative contrast of the fluorescence strength between different anatomical segments. For that the relative contrast $C_{T1,T2}$ between any two regions $T1$ and $T2$ is computed analogously to standard contrast-to-noise calculations as:

$$C_{T1,T2} = \frac{\mu_{T1} - \mu_{T2}}{\frac{1}{n}\sqrt{\sum_n \sigma_{Tn}}} \tag{4.12}$$

where μ_{T1} represents the mean signal intensity in one region (for instance one tube) and μ_{T2} represents the mean signal intensity in a second region (for instance the surrounding tissue), n is the number of different regions (or segments) in the phantom (and equivalently in a mouse in Section 4.6.2) and σ_{Tn} is the standard deviation of

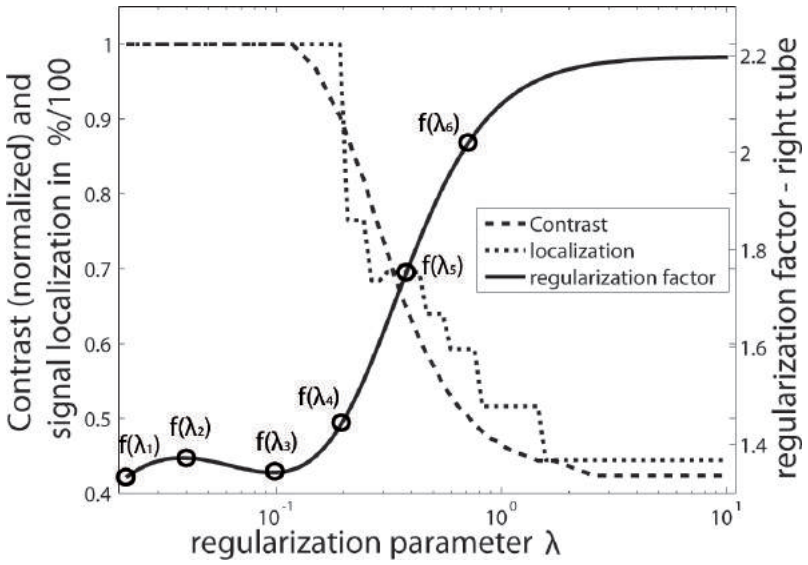

Figure 4.16: Computed regularization factor of the right tube as a function of λ (continuous line), normalized contrast between right tube and tissue (dashed line) and percentage of signal localized within 2 mm distance of the right tube (dotted line).

the signal in the n^{th} region. $C_{T1,T2}$ can become negative if the mean signal intensity in $T2$ is higher than in $T1$, i.e. $\mu_{T1} < \mu_{T2}$. For $|C_{T1,T2}| \leq 1$, the contrast is not distinguishable from the noise level in the images. For good contrast we expect $|C_{T1,T2}| \gg 1$.

Using Equations 4.10, 4.11 and 4.12, $f(seg,\lambda)$, $l(tube,\lambda)$ and $C_{T1,T2}$ were computed for all values of $\lambda > \lambda_1$. Figure 4.16 shows the computed regularization factors for the right tube as a function of all λ starting at the L-curve corner with λ_1 as a continuous line. It can be observed that regularization factors between λ_1 and λ_3 are in a similar value range, with a local minimum at λ_3, but rise quickly for higher values of λ. The dashed line shows the change of the normalized relative contrast (i.e. contrast values divided by the largest contrast value, which was 17.5) in the right tube after step-2 inversion as a function of the used regularization parameter for regularization factor estimation. The dotted line depicts the change of the percentage of the reconstructed signal lying within a distance of 2 mm from the tube. Numerical examples for some representative values of λ are listed in Table 4.1. The rows contain the values for λ_1 to λ_6 (highlighted in Figure 4.16) and the columns the corresponding regularization factors for the two tubes and the background. The left tube was assigned the lowest regularization factor of 1 for all cases while the regularization factor for the right tube changed with λ. The step-2 reconstructions resulting from using the regularization factors computed with

Regularization parameter λ		Regularization factors			Reconstruction evaluation	
		Tissue	Left tube	Right tube	$C_{Tu,Ti}$	Localization
λ_1	0,0216	3	1	1,33	1,00	100%
λ_2	0,0447	3	1	1,37	1,00	100%
λ_3	0,0926	3	1	1,34	1,00	100%
λ_4	0,1770	3	1	1,41	0,92	100%
λ_5	0,3670	3	1	1,74	0,66	70%
λ_6	0,7016	3	1	2,02	0,51	59%

Table 4.1: Regularization factors computed from the respective reconstructions using 6 different λ values and resulting contrast ratios and localization accuracy.

λ_1 to λ_6 are evaluated in the rightmost two columns. The normalized relative contrast between right tube and tissue, and the percentage of reconstructed signal lying up to 2 mm outside the tube margin are given.

The results from Figures 4.16 and Table 4.1 suggest that the relative contrast decreases for regularization factors computed with $\lambda > \lambda_3$ and the localization accuracy for $\lambda > \lambda_4$. Intuitively, because the fluorescence content in both tubes is known in this case, the rising value of the regularization factor in the right tube also already indicates worsening reconstruction results. Results presented in Figure 4.15 in turn suggest that low values of λ may yield surface weighted step-1 reconstructions which could lead to erroneous regularization factor computation in deep seated segments. This is less of an issue for such simple and homogeneous tissues like the phantom, but may be more relevant when investigating more realistic, heterogeneous tissues.
Visualization of the reconstructed images after step-2 inversion can further elucidate the resulting effects of the employed regularization parameter in step-1 inversion. Figure 4.17 shows examples for the fluorescence distribution after step-2 inversion using the regularization factors computed from step-1 inversion with λ_3, λ_5 and λ_6. The decrease in contrast and localization become obvious in the presented examples. The top two phantom slices show the same reconstruction with regularization factors computed with λ_3, but with different scaling to bring out the maximum signal in the right tube. The two reconstructions on the bottom of Figure 4.17 for λ_5 and λ_6 are also scaled to the maximum value of the signal in the right tube. Here it becomes obvious that similarly high signals are also reconstructed outside the tube area (arrows). Red circles highlight the region that was used for the localization evaluation, i.e. tube radius + 2 mm. The independent regularization parameter λ used in step-2 was chosen to be the

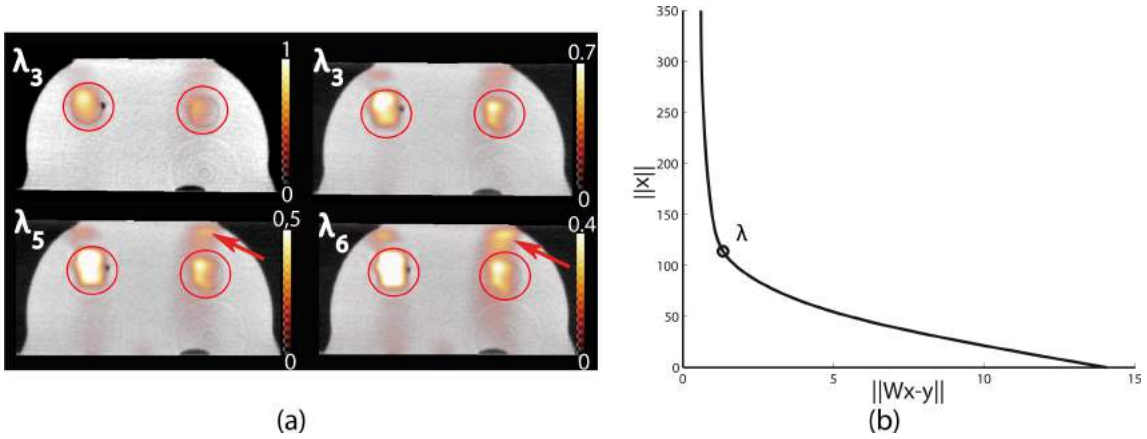

Figure 4.17: Step-2 reconstruction employing regularization factors computed from step-1 inversion using different λ. (a) Reconstructions using regularization factors calculated for λ_3, λ_5 and λ_6 (step-2 inversion). The red circles represent the area for localization evaluation defined by the tube radius + 2 mm. (b) The chosen regularization parameter for step-2 lies near the point of maximum curvature of the step-2 L-curve, at the L-curve corner.

commonly used optimal solution lying at the L-curve corner. In contrast to the phantom reconstruction using priors shown in Section 4.5.1 where the regularization factors were manually set, the result in Figure 4.17 was achieved by automatic computation based on experimentally determined regularization factors.

According to these results, regularization with $\lambda_3 \approx 4 \cdot \lambda_1$ can be considered a good choice for automatic regularization factor computation. This value proved to be a good compromise between high surface weighting and over-regularization in the case of homogeneous tissue phantom reconstructions and yielded optimal step-2 reconstruction results. Whether this holds true for the reconstruction of heterogeneous tissues and in presence of different fluorochrome distributions and imaging wavelength, will be subject of the following section.

4.6.2 Evaluation in dual-wavelengths experiments on heterogenous tissues

Two mouse models were employed to study the performance of the automatic regularization factor estimation method, one exhibiting superficial tumors and one exhibiting deeper seated tumors. Optical signals attenuate non-linearly with the source depth. Consequently,

	KRas				4T1			
Wavelength	Segment	λ_1	λ_2	λ_3	Segment	λ_1	λ_2	λ_3
680	*Tissue*	*1,60*	*2,85*	*3,00*	*Tissue*	*2,89*	*3,00*	*3,00*
	Bone	*1,00*	*1,00*	*2,10*	*Bone*	*3,00*	*2,54*	*1,78*
	Lung	*2,21*	*1,41*	*1,00*	*Tumor*	*1,00*	*1,00*	*1,00*
	Heart	*3,00*	*3,00*	*1,77*				
750	*Tissue*	*1,55*	*3,00*	*3,00*	*Tissue*	*3,00*	*3,00*	*3,00*
	Bone	*1,00*	*1,49*	*1,92*	*Bone*	*2,94*	*2,76*	*2,51*
	Lung	*3,00*	*2,67*	*1,09*	*Tumor*	*1,00*	*1,00*	*1,00*
	Heart	*2,08*	*1,00*	*1,00*				

Table 4.2: Regularization factors computed for different values of λ after Tikhonov reconstruction of Kras and 4T1 mouse models. Columns contain values for each respective λ, rows contain values for each respective segment.

the selection of different depths is important in investigations of optical imaging to examine the ability of the method to reliably perform as a function of depth.
Deep-seated tumors were investigated using the same lung tumor mouse model as in Section 4.5.2. Mice were intravenously injected 24 hours prior to imaging with two different fluorescent probes, one targeting $\alpha_v\beta_3$-integrins (IntegriSense680, Perkin Elmer Waltham MA) and a blood-pool agent (AngioSense750 Perkin Elmer Waltham MA). The excitation/emission maxima of IntegriSense680 and AngioSense750 are approximately at 680 nm/705 nm and 750 nm/770 nm, respectively. AngioSense can be used in oncology to study angiogenesis and was, therefore, chosen to provide information on vascularization and perfusion, in addition to the molecular information granted by the $\alpha_v\beta_3$-integrin over-expression. This study examined therefore a physiological parameter (vascularization/perfusion) and a molecular parameter ($\alpha_v\beta_3$-integrin overexpression).
The second mouse model was a xenograft breast cancer model. 10^6 4T1 breast cancer cells were subcutaneously injected into nude mice in the neck region and the tumor was allowed to grow for 10 days. 24 hours prior to imaging, mice were intravenously administered scVEGF/Cy (SibTech Inc., Brookfield, CT, USA), a fluorescence agent binding to VEGF receptor 2 (VEGFR-2) and emitting at around 700 nm. This agent was employed to study the ability to visualize a second molecular target in one channel, whereby the second channel again imaged IntegriSense750. In this way the relative distribution patterns of VEGFR-2 and $\alpha_v\beta_3$-integrin could be examined.

4.6.2.1 Deep seated fluorescence emission

Table 4.2 lists the computed regularization factors after step-1 inversion both for Kras and 4T1 mouse models at the two employed wavelengths and represents the mean

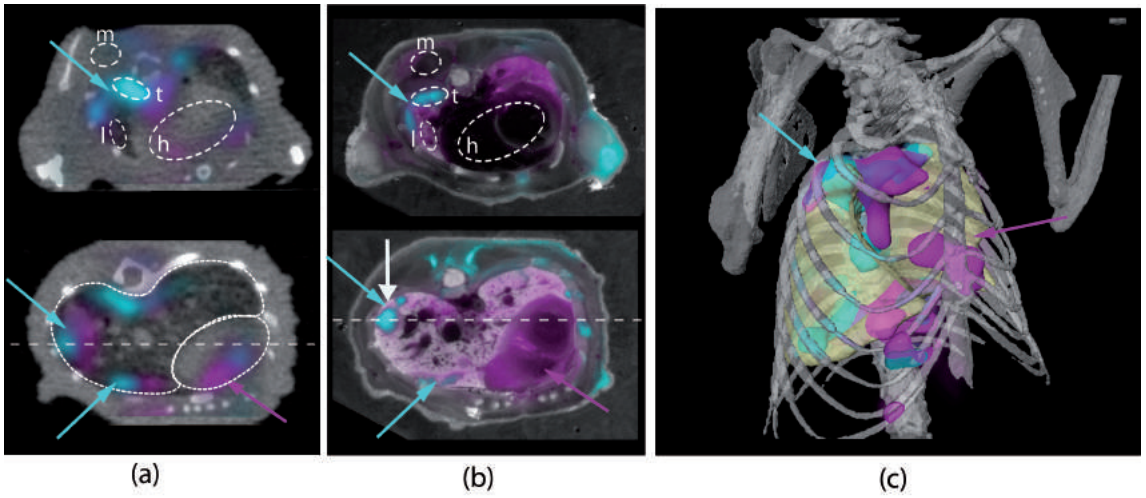

Figure 4.18: Reconstruction of Kras tumor model using two different fluorescent probes and the two-step inversion approach. (a) Overlay of two representative slices of *in-vivo* reconstructions of IntegriSense680 (cyan) and AngioSense750 (magenta) of the Kras mouse. (b) Overlay of the corresponding fluorescence cryosection images. (c) 3D representation of the reconstructions throughout the volume.

reconstructed fluorescence strength per λ (columns) and segment (rows).

For Kras mice, step-1 inversion with λ_1 suggests that the fluorescent probe uptake at both wavelengths was highest in the bones. This would result in a segment specific regularization factor of 1 in the $\mathbf{L}$-matrix of Equation 4.7, representing the step-2 inversion. The other segment specific entries into the $\mathbf{L}$-matrix, i.e. for tissue, lung and heart, at 680 nm would for instance be 1.6, 2.21 and 3, respectively. The computation of these segment-specific regularization factors changes as a function of increasing λ, as can be seen in Table 4.2 for the values computed with λ_2 and λ_3. In contrast to the results obtained with λ_1, step-1 inversion with λ_3 suggests that the highest fluorescence probe uptake at 680 nm is in the lung. In this case, the elements of the $\mathbf{L}$-matrix corresponding to the lung segment would be assigned a value of 1.

Considering the available prior knowledge on IntegriSense distribution in this particular mouse model (see Section 4.5.2), it becomes clear that only λ_3 enabled a realistic assessment of fluorescence strength in the different segments.

Figure 4.18 shows the results after step-2 inversion of the Kras mouse model using the respective regularization factors from Table 4.2 for λ_3. Figure 4.18(a) depicts two *in-vivo* reconstruction slices at different locations in the chest of the mouse and Figure 4.18(b) contains the corresponding *ex-vivo* cryosections for validation. Different regions of

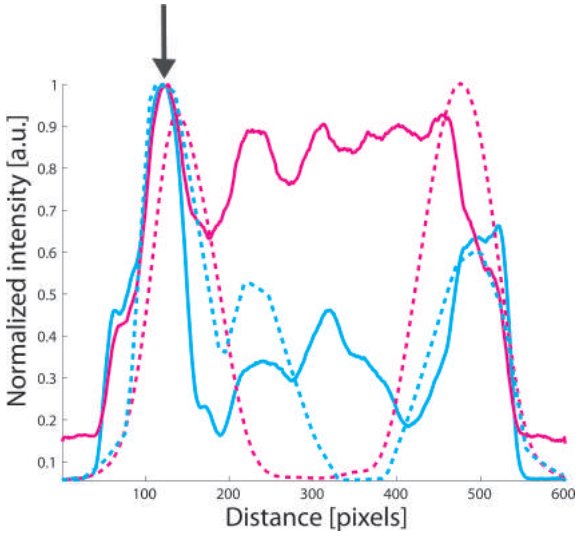

Figure 4.19: Intensity profiles through the straight white dashed lines in Figure 4.18(a) and (b) of IntegriSense680 (cyan) and AngioSense750 (magenta), for *in-vivo* (dashed lines) and *ex-vivo* (continuous lines).

interest were chosen for the determination of the relative contrast between tissues using Equation 4.12. Examples for those ROIs are given in the top *in-vivo* and *ex-vivo* slices by dashed white ellipses for tumor (t), muscle (m), lung (l) and heart (h). The bottom slice in Figure 4.18(a) additionally shows the segmentation of lung and heart in the *in-vivo* data as white dashed contour lines. Figure 4.18(c) depicts a three-dimensional (3D) rendered image of the whole reconstructed volume. Here, the lung is shown in transparent light yellow in order to allow the evaluation of the location of the reconstructed fluorescence distribution. In all panels of Figure 4.18, the cyan signal represents the distribution of IntegriSense680, and magenta the distribution of AngioSense750. Cyan arrows highlight the tumors, magenta arrows the heart. A clear difference in the biodistribution of the two probes is observable in the *ex-vivo* slices (which were acquired by the same method as presented in Section 4.5.2). This is reflected in the *in-vivo* reconstruction, where IntegriSense680 is mainly reconstructed in the tumor area and AngioSense750 is more broadly distributed in the lung and heart area.

Figure 4.19 shows normalized intensity profiles through the dashed straight white lines in the *in-vivo* and *ex-vivo* slices in Figures 4.18(a) and (b). Dashed lines in the graph represent *in-vivo* and continuous lines *ex-vivo* data. An arrow is highlighting the position of the biggest tumor in the *ex-vivo* slice (Figure 4.18(b)) and the graph (Figure 4.19) to facilitate correlation of corresponding data points. The *ex-vivo* intensity profile shows high IntegriSense680 uptake in the tumor compared to the surrounding lung as well as to heart and the other tissue. *Ex-vivo* fluorescence distribution of AngioSense750

Kras - relative contrast (whole segments)			Kras - relative contrast (ROI)				
Regions	in-vivo		Regions	in-vivo		ex-vivo	
	IS680	AS750		IS680	AS750	IS680	AS750
lung / tissue	2,47	1,24	tumor / lung	10,81	5,69	24,43	3,98
lung / bones	1,42	0,18	tumor / muscle	11,60	6,42	20,75	11,01
lung / heart	1,85	-0,37	tumor / heart	12,43	3,89	34,78	5,82

Table 4.3: Comparison of *in-vivo* and *ex-vivo* contrast ratios in Kras mouse model. Left: Computed relative contrast for whole segments for both wavelengths. Right: Relative contrast of model specific regions of interest.

in tumor, lung and heart on the contrary is of a similar intensity level. The *in-vivo* profiles qualitatively mirror the *ex-vivo* profiles when it comes to recovering the highest fluorescence peaks. For AngioSense750 though, a descent between tumor and heart area can be observed that is higher than observable in the *ex-vivo* validation slices.

A comparison of the agreement between *in-vivo* reconstructions and *ex-vivo* cryosections in terms of relative contrast between tissue segments and between selected regions of interest is given in Table 4.3. Rows contain the different contrast ratios, columns the respective fluorescent probe. The respectively compared tissues are given in the "Regions" column, where the first tissue goes as μ_{T1} and the second tissue as μ_{T2} into Equation 4.12. Highest whole segment contrast for IntegriSense680 was obtained for the lung region and accordingly for ROIs in the tumor, both *in-vivo* and *ex-vivo*. While the contrast between the whole lung and other tissues is still rather low due to the contribution of both diseased and normal lung tissue, contrast ratios rise significantly when focusing on the contribution of the tumors alone. For AngioSense750 the small absolute value of the lung/heart contrast ratio indicates little contrast between those segments. Similarly high values were also obtained when comparing localized tumor signals to both heart and lung.

4.6.2.2 Superficial fluorescence emission

Table 4.2 lists the computed regularization factors after step-1 inversion for the 4T1 mouse model at the two employed wavelengths.
The tumor in 4T1 mice already lay close to the surface, which simplifies the imaging problem and renders it more similar to the phantom case. Therefore, regularization factors were computed to be 1 in the tumor for λ_1 to λ_3. However, the regularization factors for the deeper seated tissues, i.e. bones, changed with increasing λ.

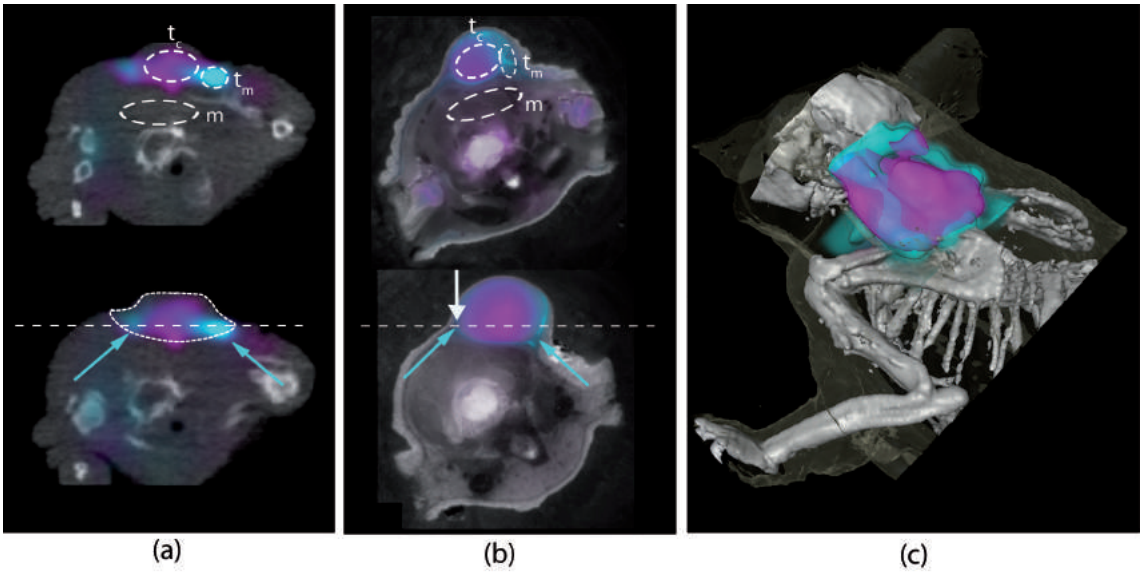

Figure 4.20: Reconstruction of 4T1 tumor model using two different fluorescent probes and the two-step inversion approach. (a) Overlay of scVEGF/Cy (cyan) and IntegriSense750 (magenta) in two representative slices from *in-vivo* reconstruction. (b) Overlay of the corresponding fluorescence cryosection images. (c) 3D representation of the reconstructions throughout the volume.

Figure 4.20 shows the results after step-2 inversion of the 4T1 mouse model using the respective regularization factors listed in Table 4.2 for λ_3. Figure 4.20(a) depicts two *in-vivo* reconstruction slices at different locations in the neck/shoulder region of the mouse and Figure 4.20(b) contains the corresponding *ex-vivo* cryosections for validation. An example for the choice of ROIs is given in the top *in-vivo* and *ex-vivo* slices by dashed white ellipses for tumor margin (t_m), tumor center (t_c) and muscle (m). The bottom slice in Figure 4.20(a) shows the contour of the tumor segment used for *in-vivo* reconstruction. In all panels of Figure 4.20, the cyan signal represents the distribution of scVEGF/Cy, and magenta the distribution of IntegriSense750. Both *in-vivo* and *ex-vivo* slices show IntegriSense750 accumulation in the center of the tumor whereas scVEGF/Cy is accumulated at the tumor margin (cyan arrows). Figure 4.20(c) depicts a 3D rendered image of the reconstructed fluorescence at both wavelengths. The reconstruction of scVEGF/Cy uptake throughout the mouse is equivalent as for the single slices shown in Figure 4.20(a), namely on the tumor boundary. This probe mainly accumulates in the margins (note the donut shape of the reconstruction) and IntegriSense750 is in its center, with some overlap of both probes in the peripheral regions of the tumor.

The same quantitative analysis as for the Kras model was performed on the 4T1

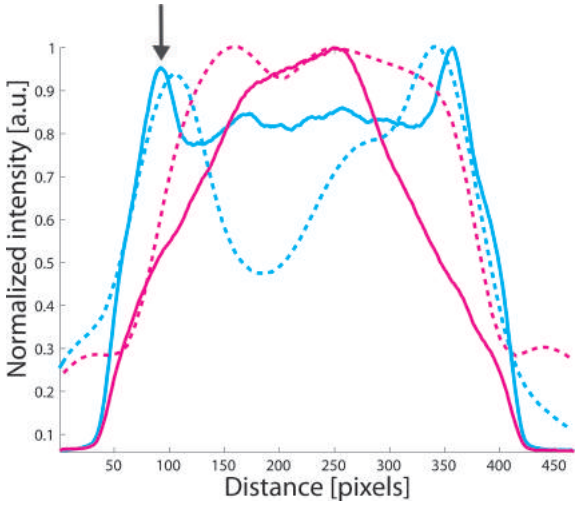

Figure 4.21: Intensity profiles through the straight white dashed lines in 4.20(a) and (b) of scVEGF/Cy (cyan) and IntegriSense750 (magenta), for *in-vivo* (dashed lines) and *ex-vivo* (continuous lines) data.

4T1 - relative contrast (whole segments)			4T1 - relative contrast (ROI)				
ratios	in-vivo		ratios	in-vivo		ex-vivo	
	scVEGF/Cy	IS750		scVEGF/Cy	IS750	scVEGF/Cy	IS750
tumor / tissue	2,98	3,71	margin / center	5,81	-1,25	5,37	-9,94
tumor / bones	1,68	3,57	margin / tissue	8,46	4,90	20,78	10,11
			center / tissue	2,65	6,15	15,41	20,06

Table 4.4: Comparison of *in-vivo* and *ex-vivo* contrast ratios in 4T1 mouse model. Left: Computed relative contrast for whole segments for both wavelengths. Right: Relative contrast of model specific regions of interest.

model. Figure 4.21 depicts intensity profiles through the dashed white straight lines in *ex-vivo* and *in-vivo* slices in Figures 4.20(a) and (b). The graph shows in cyan the normalized intensity of scVEGF/Cy emission and in magenta the normalized intensity of IntegriSense750 emission. Dashed lines represent *in-vivo* and continuous lines *ex-vivo* data. An arrow is highlighting the position of the tumor boundary in the *ex-vivo* slice (Figure 4.20(b)) and the graph (Figure 4.21) to facilitate correlation of corresponding data points. The intensity profile of scVEGF/Cy shows the highest intensities at the tumor margins while the highest peak for IntegriSense750 is in the tumor center, both for *ex-vivo* and *in-vivo* data. Contrast ratios for whole tissue segments and for selected regions of interest are listed in Table 4.4. The whole segment contrast ratios show that both probes are accumulated in the tumor segment. Contrast between ROIs in the tumor center and margin furthermore confirm the exact localization of the accumulation of each probe, i.e. in the margin for scVEGF/Cy and in the center for IntegriSense750.

In-vivo and *ex-vivo* contrast ratios were in qualitative agreement, i.e. highest contrast was achieved for margin/tissue for scVEGF/Cy and for center/tissue in both reconstructions and cryosections.

4.6.2.3 Comparison of deep seated and superficial reconstruction performance

The results from the two heterogeneous tissue experiments (Kras and 4T1 mice) confirm the finding from the phantom experiment. By applying the proposed method for regularization factor estimation to different mouse models, containing deep seated tumors and superficial tumors, individual channel specific regularization factors were found using λ_3. *In-vivo* reconstruction results using this prior knowledge correlated with the validation from *ex-vivo* cryosections, both in respect to signal localization and relative contrast.
Several limitations are however present in this study. Slight discrepancies in tumor localization still exist and were observed in this study in mice containing more than one tumor (Kras). The fluorescence emission from multiple locations, hence, still affects accurate reconstruction. Additionally, broadly distributed fluorescence, as exhibited by AngioSense in the Kras model, was less consistently recovered than the localized signal from IntegriSense, as shown in the intensity profile in Figure 4.19. The distinction of signal from background in such cases seems less reliable.

4.7 Towards multi-modality hybrid FMT

To exploit the full potential of limited-projection-angle FMT, coregistration with other imaging modalities like MRI or PET should be considered. This section demonstrates an extension of the application of hybrid FMT-XCT by using the XCT to further register hybrid FMT findings with those from another molecular imaging modality, i.e. PET. This approach leads to the integration of optical contrast with that of other imaging modalities yielding an information data set, which is of increased descriptive ability as to disease parameters. The particular example herein combined imaging of $\alpha_v\beta_3$-integrin overexpression and tumor metabolism using co-registered $[^{18}F]$-FDG-PET and FMT-XCT, providing multi-parametric data sets.

For this purpose, a third mouse model was used. 6×10^6 Lewis Lung Carcinoma (LLC) cells were injected subcutaneously in the right shoulder region and 4×10^6 cells

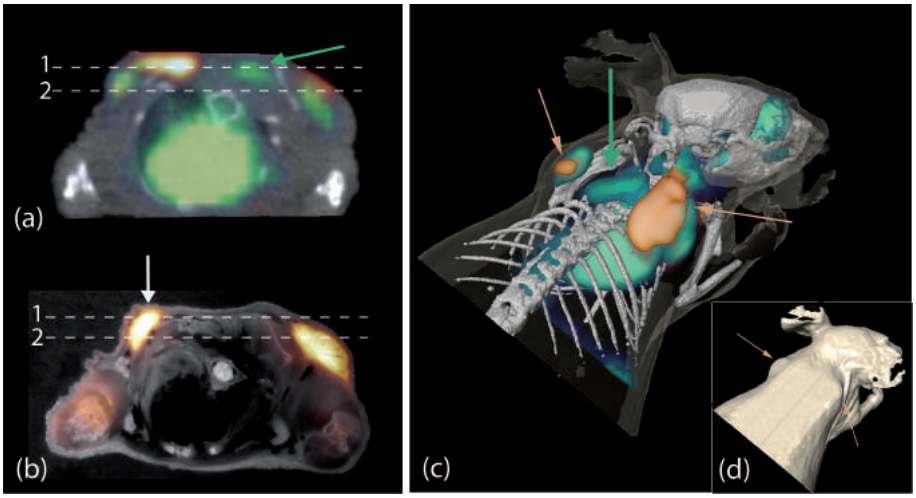

Figure 4.22: Reconstruction of LLC mouse model and coregistration of FMT-XCT-PET. (a) *In-vivo* reconstruction of IntegriSense680 (orange) and overlay of FDG-PET reconstruction (green). (b) *Ex-vivo* validation slice of IntegriSense 680 fluorescence (orange). (c) 3D representation of both FMT (orange) and PET (green) reconstructions. (d) 3D rendering of mouse skin and highlighted tumor areas (arrows).

in the left shoulder region of a nude mouse. The tumors were allowed to grow for 9 days. 24 hours before FMT-XCT imaging the mice were injected with IntegriSense680. Additionally, 45 minutes before PET imaging the mice were injected with approximately 13 MBq of $[^{18}F]$-FDG tracer. $[^{18}F]$-FDG tracer is a commonly used PET agent that is accumulated in sites of increased metabolic activity. This is usually given in tumors, but also in regions like heart and brain.

PET data was acquired using the same micro PET-XCT device as for XCT data acquisition. After XCT imaging the mouse was automatically passed on into the PET device. Reconstruction of PET data was realized by the manufacturer's software and DICOM images were exported for coregistration to FMT-XCT data. Since PET and XCT data were acquired with a hybrid device, coordinates for coregistration of both data sets were given by the device manufacturer and coregistration to FMT-XCT reconstructions was therefore straightforward.

Figure 4.22 shows the reconstruction results of the LLC mouse model including FMT, XCT and PET data. The reconstruction of IntegriSense680 was performed analogously to the phantom, Kras and 4T1 studies, i.e. using $\lambda_3 \approx 2^2 \cdot \lambda_1$, with λ_1 being the regularization parameter at the L-curve corner of the step-1 regularization of the LLC

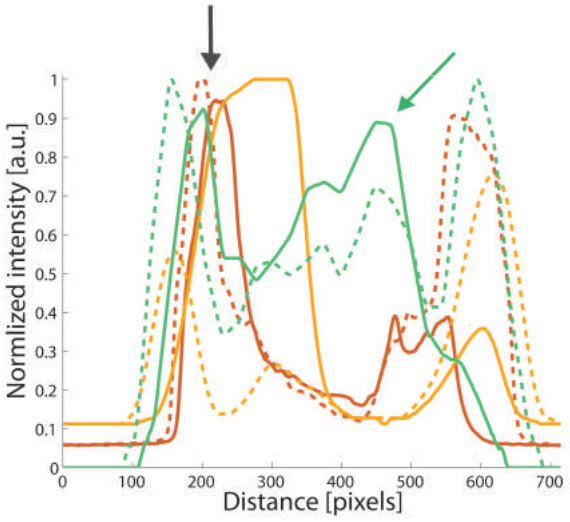

Figure 4.23: Intensity profiles through the white dashed lines in 4.22 (a) and (b) of *ex-vivo* IntegriSense680 (orange), *in-vivo* InegriSense680 (yellow) and of [18F]-FDG (green), for line 1 (continuous) and line 2 (dashed).

mouse. Figure 4.22(a) depicts the different distribution of the two tracers, the *in-vivo* reconstruction of IntegriSense680 being shown in orange and the $[^{18}F]$-FDG-PET tracer in green. Figure 4.22(b) shows the *ex-vivo* validation of the optical probe distribution where the fluorescence signal is shown as contrast enhanced orange overlay on a white light image. Figure 4.22(c) visualizes the 3D distribution of IntegriSense680 and $[^{18}F]$-FDG reconstructions and Figure 4.22(d) indicates the locations of the subcutaneous LLC tumors on the 3D rendered mouse skin by orange arrows.
Figure 4.23 depicts normalized intensity profiles through the white dashed lines in Figures 4.22(a) and (b). Continuous curves represent profiles through line 1 and dashed curves through line 2. The graph shows in orange the normalized intensity of IntegriSense680 emission in the *ex-vivo* slice (Figure 4.22(b)), in yellow the *in-vivo* IntegriSense680 reconstruction (Figure 4.22(a)) and in green the normalized intensity of $[^{18}F]$-FDG. A gray arrow is highlighting the position of the left tumor in the *ex-vivo* slice (Figure 4.22(b)) and the graph to facilitate correlation of corresponding data points.

It can be observed that IntegriSense680 is only reconstructed in the tumor area, in accordance with the *ex-vivo* slice image. The size of the left tumor, though, was overestimated and a slight dislocation between *ex-vivo* and *in-vivo* fluorescence locations could be observed. As can be expected, FDG (green) shows metabolic activity and is therefore not only distributed in the tumors but also in heart and brain. An

additional aggregation of FDG can be observed, though, between the two tumors, as highlighted by green arrows in Figures 4.22(a), (c) and 4.23. This is neither visible after IntegriSense680 reconstruction nor is a third tumor distinguishable in the *ex-vivo* slice.

It can be concluded that on the one hand PET reliably reconstructs the tumor location while FMT results exhibit a slight displacement between reconstruction and *ex-vivo* validation. On the other hand the uptake of $[^{18}F]$-FDG in non-diseased tissue can complicate the distinction of tumors from normal tissue. In this context, FMT was capable of contributing important information to this study since it reliably enabled the assessment of the number of tumors. Nevertheless, both modalities were able to reconstruct one large and one smaller tumor, in agreement with the injected cell number and cryosection results.
This approach takes advantage of particular strengths that each imaging modality may have, especially in regard to the availability of different agents that complement the ability to label desired targets. Thus, combination of PET and FMT in this case provided complementary information on the mouse model. An obvious further extension would be the integration of MRI data and the exploitation of its anatomical and functional imaging properties in combination with the molecular and anatomical data provided by limited-projection-angle FMT, PET and XCT.

4.8 Summary, conclusions and recommendations for future work

This chapter showed the development of multi-spectral and multi-modality FMT using a limited-projection-angle hybrid implementation in combination with X-ray CT (XCT). The work presented aimed particularly at enabling simultaneous investigation of multiple molecules using hybrid FMT-XCT, a capacity not documented before in the literature.
First, imaging improvements achieved by limited-projection-angle FMT systems employing anatomical priors were investigated. The use of priors requires the availability of a second tomographic modality imaging anatomy, for example an X-ray micro-CT system, an MRI system or ultrasound. The integration of XCT data into the FMT framework was achieved by coregistration of the individual data sets by means of a translatable imaging cartridge. Reconstruction problems inherent to stand-alone limited-projection-angle FMT, like lower resolution and accuracy along the median axis of projections as evident

on Figures 4.7 and 4.12(a), could be overcome by this approach. The results proved that the use of anatomical priors improves the imaging performance over stand-alone implementations, offering better image fidelity and superior quantification.
The next step consisted in implementing a spatially varying regularization inversion method, previously described for 360 degree FMT data, to the limited-projection-angle implementation. The particular challenge herein was to identify on whether regularization parameters are wavelength dependent and then on overall developing a methodology for automatic computation of regularization factors which would be optimal for limited-projection-angle FMT reconstructions. The defined 2-step inversion method proved suitable for independent assessment of different spectral signatures in the same animal and can hence be used for multi-spectral studies.
A final aim of the work was to offer the first co-registration of PET-FMT-XCT hybrid data, based on FMT reconstructions using priors. This study demonstrated how the combination of a different molecular imaging modality can be also employed to offer complementary information into different molecular processes.

Future work should tackle some of the remaining limitations, like improvement of localization in presence of multiple tumors or of broad fluorescence distributions, which were also outlined throughout the chapter in the respective results discussions. Absolute quantification, in contrast to relative quantification as shown herein, would be a further important step in advancing hybrid limited-projection-angle FMT.
Several approaches to account for these limitations are conceivable. Using contrast agents for XCT or employing MRI as anatomical imaging modality could improve the segmentation of tumor tissue and hence directly influence the FMT reconstruction in terms of localization. More importantly, localization as well as quantification and background detection issues could be resolved by adapting alternative dual-wavelength approaches, previously proposed in epi-illumination imaging [11]. One such approach aims at improving quantification of fluorescence expression by separation of probe uptake and target presence. In this example, one wavelength was used to establish an internal control by providing a background measurement by an untargeted fluorescence probe. Similarly, such a concept was recently applied to 360 degree FMT [181] and showed improved reconstruction of fluorescence localization. Applied to the work presented herein, one untargeted probe could consequently be used to normalize many other functional probes.
Needless to say, due to the wavelength independent nature of the presented hybrid method, an extension of the concept to measuring more than two probes would suggest itself.

FMT systems containing up to four imaging channels already exist and implementation of additional channels should be straight forward, from a hardware perspective. Hence, accurate and quantitative reconstructions of many fluorescence molecules could be achieved in future.

To conclude, the potential of FMT to perform tomographic imaging in planar geometry renders it a flexible and fast multi-modality compatible device. The reduced acquisition times and the coregistration potential to basically any other *in-vivo* imaging device provided by the imaging cartridge, make limited-projection-angle FMT particularly interesting for multi-parameter studies.
The automatic computation of regularization factors for *a priori* reconstruction enables simultaneous but independent investigation of multiple molecules and accurate comparison and combination of limited-projection-angle FMT with other molecular imaging devices. This is of utmost importance for the realistic assessment of any disease, since multiple molecules play a role in their progression and therapy. Such *in-vivo*, non-invasive and multi-parameter investigations can significantly improve the understanding of dynamic processes on a volumetric level, because the same animal can be imaged over longer time periods and information is gathered from the most realistic experimental setup possible - the living organism.

5 Conclusion and outlook

This thesis was dedicated to the investigation of appropriate spectral imaging methods for the detection of multiple molecules in living subjects. Visible and near-infrared light was employed to enable the study of wavelength dependent effects of light-tissue interactions of pathological significance. Thereby, two routes for systems and methodological developments were pursued. The first aimed at interrogating molecular readouts in superficial tissue processes, and the second explored molecular characterization in volumetric investigations. Both, spectral detection of intrinsic tissue chromophores, as well as extrinsically introduced contrast generating molecules (fluorescent proteins, probes or dyes) were considered.

A novel method for the quantification of tissue oxygenation based on multispectral reflectance measurements was developed. The application of transformations on the raw reflectance spectra allowed for the correction of the effects of varying optical properties. Spectral unmixing, rather than oxygenation computation based on one single wavelength, then resulted in oxygenation readouts of increased accuracy compared to previously published results. The potential of the developed method to monitor oxygenation changes in a variety of applications was shown in pilot experiments representing surgical, skin and superficial vascular oxygenation detection.
The same method was employed to quantify intravascular oxygenation in the mouse retina. A multispectral mouse fundus camera, to the author's knowledge the first of this kind, was developed. The system was capable of acquiring fundus images of high spectral and spatial resolution. Multispectral imaging did not only serve for detection of intrinsic tissue contrast, but also enabled the acquisition of multiple molecular markers *in-vivo*. PCA was shown to provided the means to adequately separate mixed fluorescence contributions. Furthermore, morphological and fluorescence expression changes could be assessed using the developed system, therefore proving its utility in monitoring pathological alterations.
Taking advantage of the spectral properties of light when investigating surface-bound

molecular processes *in-vivo*, hence, proved to be a promising approach for simultaneously detecting different molecular actors.
Biochemical processes, however, do not occur only in superficial tissues. Methods providing molecular readouts on deep seated processes were therefore adapted and newly developed to meet the needs of multi-molecular volumetric imaging. The capabilities of fluorescence molecular tomography to independently reconstruct two fluorescent probes in the same animal were studied. For this purpose, hybrid reconstruction schemes were developed to improve limited-projection-angle FMT reconstruction accuracy. Furthermore, a two-step inversion approach providing fluorochrome specific regularization was translated and adapted to limited-projection-angle FMT-XCT. Accurate volumetric reconstructions of the biodistribution of different fluorescent probes were hence achieved, as well as multi-modality molecular read outs using a PET-FMT-XCT combination.

The results presented within this thesis constitute an important starting point for the advancement of molecular imaging towards multi-molecular investigations. Simultaneous imaging of several hallmarks of disease in living subjects would improve the understanding of underlying biochemical processes and the involved molecular actors, as well as their dynamics and interrelationship. Besides, some of the presented multispectral methods show great promise for translation from pre-clinical to human medicine. Quantitative oxygenation imaging is one example. Furthermore, detection of both intrinsic and extrinsic contrast, for instance in fluorescence guided surgery or in retinal imaging in human subjects, could be facilitated by multispectral strategies as presented herein. Multispectral concepts can therefore have a crucial impact on the future development of molecular imaging and will surely soon belong to the standard methods used in molecular imaging research and diagnosis.

I would like to conclude this thesis with a personal remark on the potential significance of multispectral molecular imaging in an emerging biological field - systems biology. Multispectral imaging concepts could be used to deliver input to mathematical models, providing information that no traditional *in-vitro* biological analysis method can deliver: *in-vivo* dynamics and spatial localization. Both are properties that can considerably influence a molecule's role in a biological process. Mathematical and computational models are increasingly employed to describe and simulate biological processes involving many components on different levels, from kinetic modeling using differential equations to network properties investigations using network theory. This emerging research field, generically termed systems biology, relies on concepts developed

in computational sciences and engineering to understand systemic, i.e. large scale, correlations. Multispectral molecular imaging, and its panoply of practical implementations, is an invaluable and unique tool for complementing the data available to systems biology modeling concepts.
Advancing multispectral molecular imaging by developments directed to hardware as well as algorithms therefore remains a predominant research topic.

Appendix A

Examples for BSS employing varying numbers of wavelength bands

The following figures illustrate the results from employing different blind source separation methods to separate GFP and YFP signals in retinal images. Figure A.1 depicts the effects of unmixing with PCA, using 2 to 7 spectral bands in the range from 500 nm to 570 nm. The first three PCA components are displayed (except for the case where only 2 spectral bands were used), as well as the recovered spectra of the endmembers. Figure A.2 equivalently shows three components of ICA unmixing emplyoing the same 2 to 7 spectral bands as for PCA. Most significant ICA components were chosen manually. Figure A.3 finally shows the analogue results obtained with PCA-ICA, where the first 4 components of PCA were used for ICA computation.
Figure A.4(left) evaluates the overlap between PCA and PCA-ICA results and Figure A.4(right) gives an example of the original mixed images that were used for unmixing.

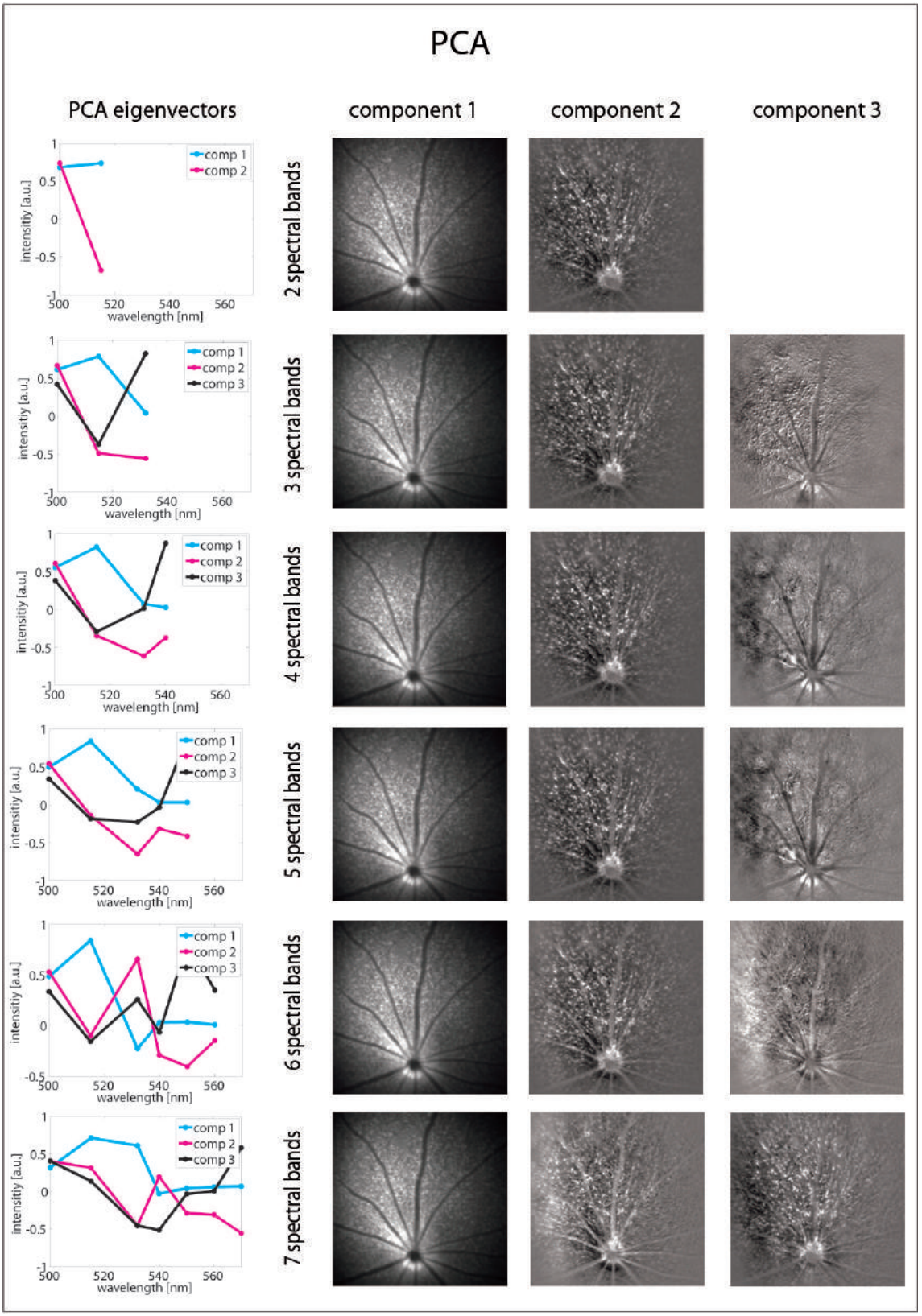

Figure A.1: First three components computed by PCA employing different numbers of wavelength bands.

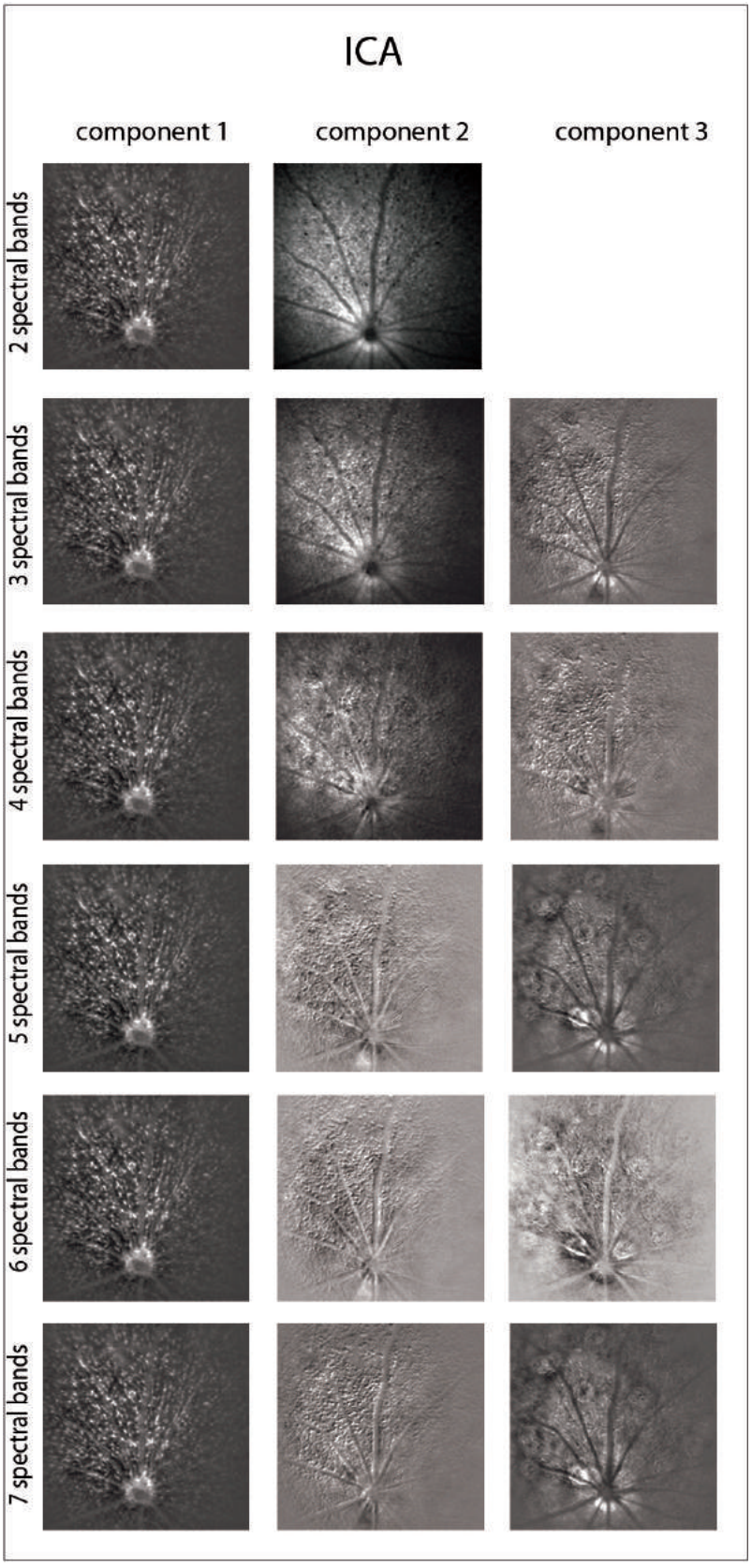

Figure A.2: Three manually selected ICA components computed employing different numbers of wavelength bands.

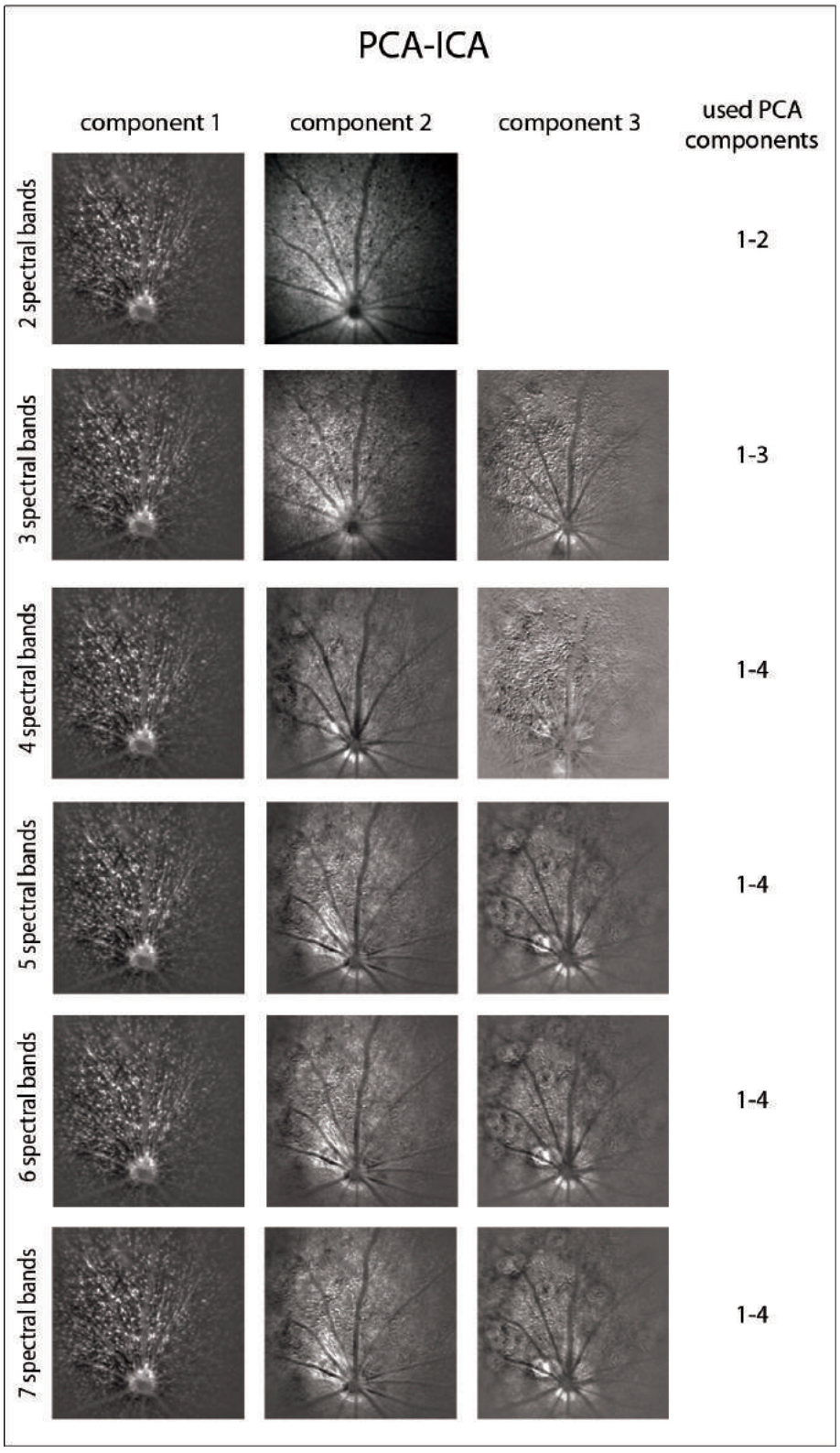

Figure A.3: Three manually selected components computed by ICA employing the first four PCA components.

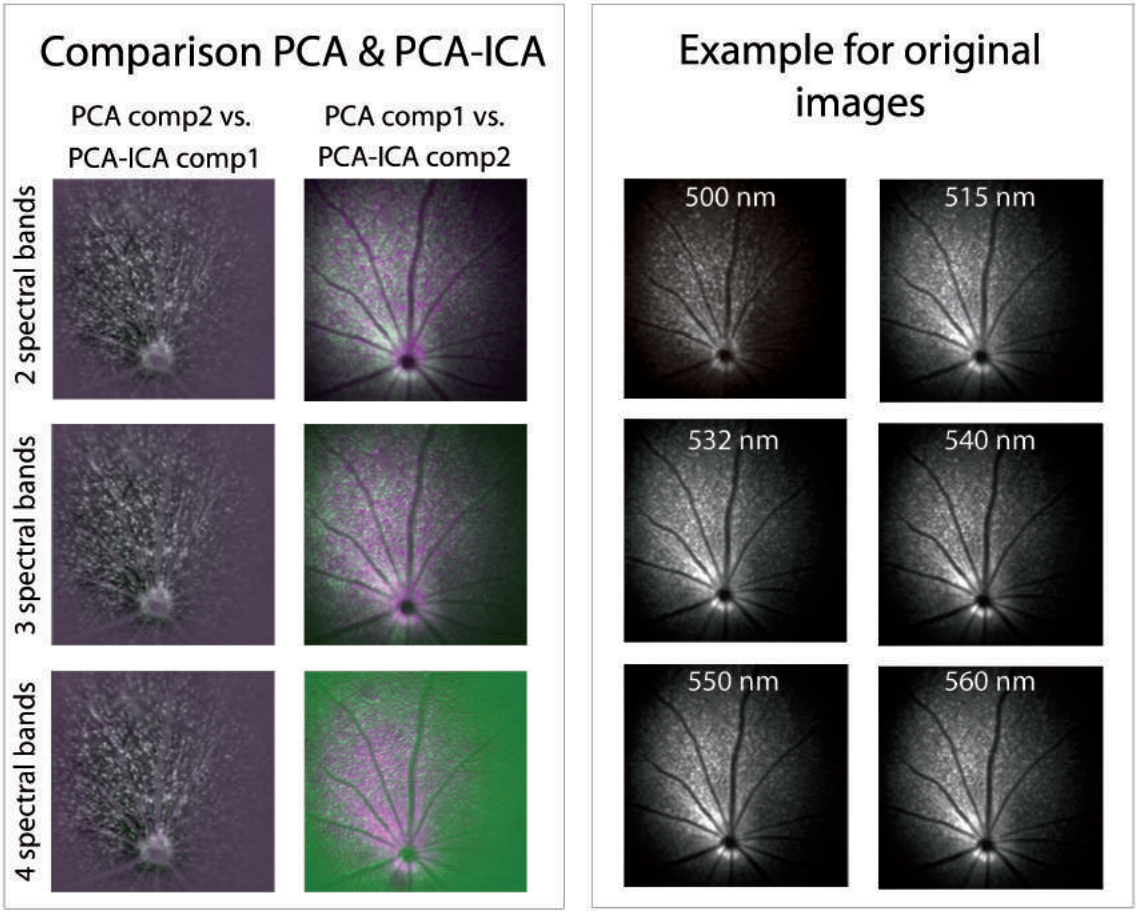

Figure A.4: Left: Comparison of PCA and ICA-PCA. Right: Example for raw images.

Bibliography

[1] M. D. Abramoff, M. K. Garvin, and M. Sonka. Retinal imaging and image analysis. IEEE Rev Biomed Eng, 3:169–208, 2010.

[2] A. Adamis. The Retina and its Disorders, chapter Pathological Retinal Angiogenesis, pages 541–550. Academic Press Inc., 2011.

[3] A. Ale, V. Ermolayev, E. Herzog, C. Cohrs, M. H. de Angelis, and V. Ntziachristos. Fmt-xct: in vivo animal studies with hybrid fluorescence molecular tomography-x-ray computed tomography. Nature methods, 9(6):615–20, 2012.

[4] A. Ale, R. B. Schulz, A. Sarantopoulos, and V. Ntziachristos. Imaging performance of a hybrid x-ray computed tomography-fluorescence molecular tomography system using priors. Med Phys, 37(5):1976–86, 2010.

[5] A. Ale, F. Siebenhaar, K. Kosanke, M. Aichler, K. Radrich, S. Heydrich, M. Schiemann, I. Bielicki, P. B. Noel, R. Braren, M. Maurer, A. K. Walch, E. J. Rummeny, V. Ntziachristos, and M. Wildgruber. Cardioprotective c-kit(+) bone marrow cells attenuate apoptosis after acute myocardial infarction in mice - in-vivo assessment with fluorescence molecular imaging. Theranostics, 3(11):903–13, 2013.

[6] A. B. Ale. Hybrid Fluorescence Molecular Tomography and X-ray CT Methods and Applications. PhD thesis, Technische Universitaet Muenchen, 2012.

[7] J. Ambati, J. P. Atkinson, and B. D. Gelfand. Immunology of age-related macular degeneration. Nat Rev Immunol, 13(6):438–51, 2013.

[8] S. R. Arridge. Optical tomography in medical imaging. Inverse Problems, 15:R41–R93, 1999.

[9] S. R. Arridge and J. C. Hebden. Optical imaging in medicine: Ii. modelling and reconstruction. Phys Med Biol, 42(5):841–53, 1997.

[10] E. G. Atkinson, S. Jones, B. A. Ellis, D. C. Dumonde, and E. Graham. Molecular size of retinal vascular leakage determined by fitc-dextran angiography in patients with posterior uveitis. Eye (Lond), 5 (Pt 4):440–6, 1991.

[11] J. Baeten, J. Haller, H. Shih, and V. Ntziachristos. In vivo investigation of breast cancer progression by use of an internal control. Neoplasia, 11(3):220–7, 2009.

[12] T. Bakir, A. Peter, R. Riley, and J. Hackett. Non-negative maximum likelihood ica for blind source separation of images and signals with application to hyperspectral image subpixel demixing. In IEEE International Conference on Image Processing. IEEE, 2006.

[13] A. Bakker, B. Smith, P. Ainslie, and K. Smith. Near-infrared spectroscopy. Applied Aspects of Ultrasonography in Humans, Prof. Philip Ainslie (Ed.), InTech, 2012.

[14] B. Ballou, G. W. Fisher, A. S. Waggoner, D. L. Farkas, J. M. Reiland, R. Jaffe, R. B. Mujumdar, S. R. Mujumdar, and T. R. Hakala. Tumor labeling in vivo using cyanine-conjugated monoclonal antibodies. Cancer Immunol Immunother, 41(4):257–63, 1995.

[15] R. Barbour, H. Graber, J. Chang, S.-L. Barbour, P. Koo, and R. Aronson. Mri-guided optical tomography: Prospects and computation for a new imaging method. IEEE Computational Science & Engineering, 2(4):63–77, 1995.

[16] P. R. Bargo, S. A. Prahl, T. T. Goodell, R. A. Sleven, G. Koval, G. Blair, and S. L. Jacques. In vivo determination of optical properties of normal and tumor tissue with white light reflectance and an empirical light transport model during endoscopy. J Biomed Opt, 10(3):034018, 2005.

[17] J. Beach, J. F. Ning, and B. Khoobehi. Oxygen saturation in optic nerve head structures by hyperspectral image analysis. Current Eye Research, 32(2):161–170, 2007.

[18] C. M. Bishop and SpringerLink. Pattern recognition and machine learning. Information science and statistics. Springer Springer Science+Business Media, New York New York, NY, 2006.

[19] D. A. Boas, D. H. Brooks, E. L. Miller, C. DiMarzio, M. Kilmer, R. J. Gaudette, and Q. Zhang. Imaging the body with diffuse optical tomography. IEEE Signal Processing Magazine, pages 57–75, Nov 2001.

[20] R. Boushel and C. A. Piantadosi. Near-infrared spectroscopy for monitoring muscle oxygenation. Acta Physiol Scand, 168(4):615–22, 2000.

[21] M. A. Branch, T. F. Coleman, and Y. Li. A subspace, interior, and conjugate gradient method for large-scale bound-constrained minimization problems. SIAM Journal on Scientific Computing, 21(1):1–23, 1999.

[22] K. Briley-Saebo and A. Bjornerud. Accurate de-oxygenation of ex vivo whole blood using sodium dithionite. Proc. Intl. Sot. Mag. Reson. Med., 8, 2000.

[23] F. J. Bruggeman and H. V. Westerhoff. The nature of systems biology. Trends Microbiol, 15(1):45–50, 2007.

[24] R. H. Byrd, M. H. Hribar, and J. Nocedal. An interior poiont algorithm for larg-scale nonlinear programming. SIAM Journal on Optimization, 40:247–263, 1988.

[25] A. Carreau, B. El Hafny-Rahbi, A. Matejuk, C. Grillon, and C. Kieda. Why is the partial oxygen pressure of human tissues a crucial parameter? small molecules and hypoxia. J Cell Mol Med, 15(6):1239–53, 2011.

[26] B. Chance, Q. Luo, S. Nioka, D. C. Alsop, and J. A. Detre. Optical investigations of physiology: a study of intrinsic and extrinsic biomedical contrast. Philos Trans R Soc Lond B Biol Sci, 352(1354):707–16, 1997.

[27] E. Chekmenev. Mri hyperpolarization and molecular imaging. MI-Gateway - The newsletter of the SNMMI, 7(3):1–3, 2013.

[28] C. Cheung, J. P. Culver, K. Takahashi, J. H. Greenberg, and A. G. Yodh. In vivo cerebrovascular measurement combining diffuse near-infrared absorption and correlation spectroscopies. Phys Med Biol, 46(8):2053–65, 2001.

[29] T. Christen, M. Nahrendorf, M. Wildgruber, F. K. Swirski, E. Aikawa, P. Waterman, K. Shimizu, R. Weissleder, and P. Libby. Molecular imaging of innate immune cell function in transplant rejection. Circulation, 119(14):1925–32, 2009.

[30] C. Collet, J. Chanussot, and K. Chehdi. Multivariate image processing. Digital signal and image processing series. Hoboken, London, 2010.

[31] M. Cope and D. T. Delpy. System for long-term measurement of cerebral blood and tissue oxygenation on newborn infants by near infra-red transillumination. Med Biol Eng Comput, 26(3):289–94, 1988.

[32] D. P. Cormode, E. Roessl, A. Thran, T. Skajaa, R. E. Gordon, J. P. Schlomka, V. Fuster, E. A. Fisher, W. J. Mulder, R. Proksa, and Z. A. Fayad. Atherosclerotic plaque composition: analysis with multicolor ct and targeted gold nanoparticles. Radiology, 256(3):774–82, 2010.

[33] N. J. Crane, P. A. Pinto, D. Hale, F. A. Gage, D. Tadaki, A. D. Kirk, I. W. Levin, and E. A. Elster. Non-invasive monitoring of tissue oxygenation during laparoscopic donor nephrectomy. BMC Surg, 8:8, 2008.

[34] D. J. Cuccia, F. Bevilacqua, A. J. Durkin, F. R. Ayers, and B. J. Tromberg. Quantitation and mapping of tissue optical properties using modulated imaging. J Biomed Opt, 14(2):024012, 2009.

[35] J. P. Culver, R. Choe, M. J. Holboke, L. Zubkov, T. Durduran, A. Slemp, V. Ntziachristos, B. Chance, and A. G. Yodh. Three-dimensional diffuse optical tomography in the parallel plane transmission geometry: evaluation of a hybrid frequency domain/continuous wave clinical system for breast imaging. Med Phys, 30(2):235–47, 2003.

[36] J. P. Culver, T. Durduran, D. Furuya, C. Cheung, J. H. Greenberg, and A. G. Yodh. Diffuse optical tomography of cerebral blood flow, oxygenation, and metabolism in rat during focal ischemia. J Cereb Blood Flow Metab, 23(8):911–24, 2003.

[37] C. Curtet, F. Maton, T. Havet, M. Slinkin, A. Mishra, J. F. Chatal, and R. N. Muller. Polylysine-gd-dtpan and polylysine-gd-dotan coupled to anti-cea f(ab')2 fragments as potential immunocontrast agents. relaxometry, biodistribution, and magnetic resonance imaging in nude mice grafted with human colorectal carcinoma. Invest Radiol, 33(10):752–61, 1998.

[38] A. Da Silva, M. Leabad, C. Driol, T. Bordy, M. Debourdeau, J. M. Dinten, P. Peltie, and P. Rizo. Optical calibration protocol for an x-ray and optical multimodality tomography system dedicated to small-animal examination. Appl Opt, 48(10):D151–62, 2009.

[39] B. L. Davidson and X. O. Breakefield. Viral vectors for gene delivery to the nervous system. Nat Rev Neurosci, 4(5):353–64, 2003.

[40] S. Davis, S. L. Gibbs-Strauss, S. B. Tuttle, S. Jiang, R. Springett, H. Dehghani, B. Pogue, and K. Paulsen. Mri-coupled spectrally-resolved fluorescence tomography for in-vivo imaging. In F. S. Azar and X. Intes, editors, Proc. of SPIE: Multimodal Biomedical Imaging III, volume 6850, 2008.

[41] S. C. Davis, H. Dehghani, J. Wang, S. Jiang, B. W. Pogue, and K. D. Paulsen. Image-guided diffuse optical fluorescence tomography implemented with laplacian-type regularization. Opt Express, 15(7):4066–82, 2007.

[42] S. C. Davis, K. S. Samkoe, K. M. Tichauer, K. J. Sexton, J. R. Gunn, S. J. Deharvengt, T. Hasan, and B. W. Pogue. Dynamic dual-tracer mri-guided fluorescence tomography to quantify receptor density in vivo. Proc Natl Acad Sci U S A, 110(22):9025–30, 2013.

[43] N. C. Deliolanis, T. Wurdinger, L. Pike, B. A. Tannous, X. O. Breakefield, R. Weissleder, and V. Ntziachristos. In vivo tomographic imaging of red-shifted fluorescent proteins. Biomed Opt Express, 2(4):887–900, 2011.

[44] F. C. Delori. Noninvasive technique for oximetry of blood in retinal vessels. Appl Opt, 27(6):1113–25, 1988.

[45] D. T. Delpy and M. Cope. Quantification in tissue near-infrared spectroscopy. Philosophical Transactions of the Royal Society B-Biological Sciences, 352(1354):649–659, 1997.

[46] L. W. Dobrucki and A. J. Sinusas. Pet and spect in cardiovascular molecular imaging. Nat Rev Cardiol, 7(1):38–47, 2010.

[47] T. Durduran, R. Choe, W. B. Baker, and A. G. Yodh. Diffuse optics for tissue monitoring and tomography. Rep Prog Phys, 73, 2010.

[48] A. T. Eggebrecht, S. L. Ferradal, A. Robichaux-Viehoever, M. S. Hassanpour, H. Dehghani, A. Z. Snyder, T. Hershey, and J. P. Culver. Mapping distributed brain function and network with diffuse optical tomography. Nat Photonics, 8:448–454, June 2014.

[49] D. B. Ellegala, H. Leong-Poi, J. E. Carpenter, A. L. Klibanov, S. Kaul, M. E. Shaffrey, J. Sklenar, and J. R. Lindner. Imaging tumor angiogenesis with contrast ultrasound and microbubbles targeted to alpha(v)beta3. Circulation, 108(3):336–41, 2003.

[50] G. Feng, R. H. Mellor, M. Bernstein, C. Keller-Peck, Q. T. Nguyen, M. Wallace, J. M. Nerbonne, J. W. Lichtman, and J. R. Sanes. Imaging neuronal subsets in transgenic mice expressing multiple spectral variants of gfp. Neuron, 28(1):41–51, 2000.

[51] M. D. Fischer, G. Huber, S. C. Beck, N. Tanimoto, R. Muehlfriedel, E. Fahl, C. Grimm, A. Wenzel, C. E. Reme, S. A. van de Pavert, J. Wijnholds, M. Pacal, R. Bremner, and M. W. Seeliger. Noninvasive, in vivo assessment of mouse retinal structure using optical coherence tomography. PLoS One, 4(10):e7507, 2009.

[52] M. Freyer, A. Ale, R. B. Schulz, M. Zientkowska, V. Ntziachristos, and K. H. Englmeier. Fast automatic segmentation of anatomical structures in x-ray computed tomography images to improve fluorescence molecular tomography reconstruction. J Biomed Opt, 15(3):036006, 2010.

[53] J. G. Fujimoto. Optical coherence tomography for ultrahigh resolution in vivo imaging. Nat Biotechnol, 21(11):1361–7, 2003.

[54] J. G. Fujimoto, D. L. Farkas, and I. ebrary. Biomedical optical imaging [electronic resource]. Oxford University Press, Oxford ; New York, 2009.

[55] F. A. Gallagher. An introduction to functional and molecular imaging with mri. Clin Radiol, 65(7):557–66, 2010.

[56] Y. Garini, I. T. Young, and G. McNamara. Spectral imaging: principles and applications. Cytometry A, 69(8):735–47, 2006.

[57] Y. Geng, A. Dubra, L. Yin, W. H. Merigan, R. Sharma, R. T. Libby, and D. R. Williams. Adaptive optics retinal imaging in the living mouse eye. Biomed Opt Express, 3(4):715–34, 2012.

[58] N. Georgiou. Development of a fast, high throughput hyper spectral hysteroscope. Master's thesis, Technical University of Crete, 2010.

[59] B. N. Giepmans, S. R. Adams, M. H. Ellisman, and R. Y. Tsien. The fluorescent toolbox for assessing protein location and function. Science, 312(5771):217–24, 2006.

[60] S. Gioux, A. Mazhar, B. T. Lee, S. J. Lin, A. M. Tobias, D. J. Cuccia, A. Stockdale, R. Oketokoun, Y. Ashitate, E. Kelly, M. Weinmann, N. J. Durr, L. A. Moffitt, A. J.

Durkin, B. J. Tromberg, and J. V. Frangioni. First-in-human pilot study of a spatial frequency domain oxygenation imaging system. J Biomed Opt, 16(8):086015, 2011.

[61] J. Glatz, N. C. Deliolanis, A. Buehler, D. Razansky, and V. Ntziachristos. Blind source unmixing in multi-spectral optoacoustic tomography. Opt Express, 19(4):3175–84, 2011.

[62] A. F. H. Goetz. Three decades of hyperspectral remote sensing of the earth: A personal view. Remote Sensing of Environment, 113:S5–S16, 2009.

[63] E. E. Graves, J. Ripoll, R. Weissleder, and V. Ntziachristos. A submillimeter resolution fluorescence molecular imaging system for small animal imaging. Med Phys, 30(5):901–11, 2003.

[64] K. P. Greenberg, S. F. Geller, D. V. Schaffer, and J. G. Flannery. Targeted transgene expression in muller glia of normal and diseased retinas using lentiviral vectors. Invest Ophthalmol Vis Sci, 48(4):1844–52, 2007.

[65] H. J. Grein. What do retinal vessels reveal about systemic disease? retinal vessels and systemic disease–basic findings. Coll Antropol, 37 Suppl 1:71–4, 2013.

[66] T. Grill. Ars machina. http://www.arsmachina.com, July 2014.

[67] G. Gulsen, O. Birgul, M. B. Unlu, R. Shafiiha, and O. Nalcioglu. Combined diffuse optical tomography (dot) and mri system for cancer imaging in small animals. Technol Cancer Res Treat, 5(4):351–63, 2006.

[68] M. Guven, B. Yazici, X. Intes, and B. Chance. Diffuse optical tomography with a priori anatomical information. Phys Med Biol, 50(12):2837–58, 2005.

[69] N. Hagen, R. T. Kester, L. Gao, and T. S. Tkaczyk. Snapshot advantage: a review of the light collection improvement for parallel high-dimensional measurement systems. Opt Eng, 51(11), 2012.

[70] G. M. Hale and M. R. Querry. Optical constants of water in the 200-nm to 200-microm wavelength region. Appl Opt, 12(3):555–63, 1973.

[71] J. Haller, D. Hyde, N. Deliolanis, R. de Kleine, M. Niedre, and V. Ntziachristos. Visualization of pulmonary inflammation using noninvasive fluorescence molecular imaging. J Appl Physiol, 104(3):795–802, 2008.

[72] M. Hammer and D. Schweitzer. Quantitative reflection spectroscopy at the human ocular fundus. Phys Med Biol, 47(2):179–91, 2002.

[73] M. Hammer, E. Thamm, and D. Schweitzer. A simple algorithm for in vivo ocular fundus oximetry compensating for non-haemoglobin absorption and scattering. Phys Med Biol, 47(17):N233–8, 2002.

[74] M. Hammer, W. Vilser, T. Riemer, A. Mandecka, D. Schweitzer, U. Kuhn, J. Dawczynski, F. Liemt, and J. Strobel. Diabetic patients with retinopathy show increased retinal venous oxygen saturation. Graefes Arch Clin Exp Ophthalmol, 247(8):1025–30, 2009.

[75] P. Hansen. Analysis of discrete ill-posed problems by means of the l-curve. SIAM Rev., 34:561–580, 1992.

[76] P. C. Hansen, I. Society for, and M. Applied. Rank-deficient and discrete ill-posed problems [electronic resource] : numerical aspects of linear inversion. SIAM monographs on mathematical modeling and computation. Society for Industrial and Applied Mathematics (SIAM, 3600 Market Street, Floor 6, Philadelphia, Philadelphia, Pa., 1998.

[77] S. H. Hardarson. Retinal oximetry. Acta Ophthalmologica, 91(5):489–490, 2013.

[78] S. H. Hardarson, A. Harris, R. A. Karlsson, G. H. Halldorsson, L. Kagemann, E. Rechtman, G. M. Zoega, T. Eysteinsson, J. A. Benediktsson, A. Thorsteinsson, P. K. Jensen, J. Beach, and E. Stefansson. Automatic retinal oximetry. Investigative Ophthalmology and Visual Science, 47(11):5011–5016, 2006.

[79] J. C. Hebden, S. R. Arridge, and D. T. Delpy. Optical imaging in medicine: I. experimental techniques. Phys Med Biol, 42(5):825–40, 1997.

[80] A. H. Hielscher, A. Y. Bluestone, G. S. Abdoulaev, A. D. Klose, J. Lasker, M. Stewart, U. Netz, and J. Beuthan. Near-infrared diffuse optical tomography. Dis Markers, 18(5-6):313–37, 2002.

[81] T. Higashide, I. Kawaguchi, S. Ohkubo, H. Takeda, and K. Sugiyama. In vivo imaging and counting of rat retinal ganglion cells using a scanning laser ophthalmoscope. Invest Ophthalmol Vis Sci, 47(7):2943–50, 2006.

[82] E. M. Hillman and A. Moore. All-optical anatomical co-registration for molecular imaging of small animals using dynamic contrast. Nat Photonics, 1(9):526–530, 2007.

[83] R. M. Hoffman. The multiple uses of fluorescent proteins to visualize cancer in vivo. Nat Rev Cancer, 5(10):796–806, 2005.

[84] V. S. Hollis. Non-Invasive Monitoring of Brain Tissue Temperature by Near-Infrared Spectroscopy. PhD thesis, University College London, 2002.

[85] D. Hyde, R. de Kleine, S. A. MacLaurin, E. Miller, D. H. Brooks, T. Krucker, and V. Ntziachristos. Hybrid fmt-ct imaging of amyloid-beta plaques in a murine alzheimer's disease model. Neuroimage, 44(4):1304–11, 2009.

[86] D. Hyde, E. L. Miller, D. H. Brooks, and V. Ntziachristos. Data specific spatially varying regularization for multimodal fluorescence molecular tomography. IEEE Trans Med Imaging, 29(2):365–74, 2010.

[87] D. Hyde, R. Schulz, D. Brooks, E. Miller, and V. Ntziachristos. Performance dependence of hybrid x-ray computed tomography/fluorescence molecular tomography on the optical forward problem. J Opt Soc Am A Opt Image Sci Vis, 26(4):919–23, 2009.

[88] A. Hyvarinen. Fast and robust fixed-point algorithms for independent component analysis. IEEE Trans Neural Netw, 10(3):626–34, 1999.

[89] A. Hyvarinen and E. Oja. Independent component analysis: algorithms and applications. Neural Netw, 13(4-5):411–30, 2000.

[90] X. Intes, C. Maloux, M. Guven, B. Yazici, and B. Chance. Diffuse optical tomography with physiological and spatial a priori constraints. Phys Med Biol, 49(12):N155–63, 2004.

[91] S. L. Jacques and B. W. Pogue. Tutorial on diffuse light transport. J Biomed Opt, 13(4):041302, 2008.

[92] M. L. James and S. S. Gambhir. A molecular imaging primer: modalities, imaging agents, and applications. Physiol Rev, 92(2):897–965, 2012.

[93] S. Jiao, M. Jiang, J. Hu, A. Fawzi, Q. Zhou, K. K. Shung, C. A. Puliafito, and H. F. Zhang. Photoacoustic ophthalmoscopy for in vivo retinal imaging. Opt Express, 18(4):3967–72, 2010.

[94] F. F. Jobsis. Noninvasive, infrared monitoring of cerebral and myocardial oxygen sufficiency and circulatory parameters. Science, 198(4323):1264–7, 1977.

[95] T. R. Johnson. Dual-energy ct: general principles. AJR Am J Roentgenol, 199(5 Suppl):S3–8, 2012.

[96] S. Jung, J. Aliberti, P. Graemmel, M. J. Sunshine, G. W. Kreutzberg, A. Sher, and D. R. Littman. Analysis of fractalkine receptor cx(3)cr1 function by targeted deletion and green fluorescent protein reporter gene insertion. Mol Cell Biol, 20(11):4106–14, 2000.

[97] J. M. Kainerstorfer, F. Amyot, S. G. Demos, M. Hassan, V. Chernomordik, C. K. Hitzenberger, A. H. Gandjbakhche, and J. D. Riley. Quantitative assessment of ischemia and reactive hyperemia of the dermal layers using multi - spectral imaging on the human arm. Proc SPIE 06/2009, 2009.

[98] J. M. Kainerstorfer, P. D. Smith, and A. H. Gandjbakhche. Noncontact wide-field multispectral imaging for tissue characterization. Ieee Journal of Selected Topics in Quantum Electronics, 18(4):1343–1354, 2012.

[99] M. Kaiser, A. Yafi, M. Cinat, B. Choi, and A. J. Durkin. Noninvasive assessment of burn wound severity using optical technology: a review of current and future modalities. Burns, 37(3):377–86, 2011.

[100] T. S. Kern. Interrelationships between the retinal neuroglia and vasculature in diabetes. Diabetes Metab J, 38(3):163–70, 2014.

[101] N. Keshava and J. F. Mustard. Spectral unmixing. Ieee Signal Processing Magazine, 19(1):44–57, 2002.

[102] L. Khaodhiar, T. Dinh, K. T. Schomacker, S. V. Panasyuk, J. E. Freeman, R. Lew, T. Vo, A. A. Panasyuk, C. Lima, J. M. Giurini, T. E. Lyons, and A. Veves. The use of medical hyperspectral technology to evaluate microcirculatory chaves in diabetic foot ulcers and to predict clinical outcomes. Diabetes Care, 30(4):903–910, 2007.

[103] D. E. Kim, D. Schellingerhout, F. A. Jaffer, R. Weissleder, and C. H. Tung. Near-infrared fluorescent imaging of cerebral thrombi and blood-brain barrier disruption in a mouse model of cerebral venous sinus thrombosis. J Cereb Blood Flow Metab, 25(2):226–33, 2005.

[104] H. Kitano. Systems biology: a brief overview. Science, 295(5560):1662–4, 2002.

[105] T. Knopfel. Genetically encoded optical indicators for the analysis of neuronal circuits. Nat Rev Neurosci, 13(10):687–700, 2012.

[106] H. Kobayashi, M. Ogawa, R. Alford, P. L. Choyke, and Y. Urano. New strategies for fluorescent probe design in medical diagnostic imaging. Chem Rev, 110(5):2620–40, 2010.

[107] C. Kostic, F. Chiodini, P. Salmon, M. Wiznerowicz, N. Deglon, D. Hornfeld, D. Trono, P. Aebischer, D. F. Schorderet, F. L. Munier, and Y. Arsenijevic. Activity analysis of housekeeping promoters using self-inactivating lentiviral vector delivery into the mouse retina. Gene Ther, 10(9):818–21, 2003.

[108] M. H. Kuehn, J. H. Fingert, and Y. H. Kwon. Retinal ganglion cell death in glaucoma: mechanisms and neuroprotective strategies. Ophthalmol Clin North Am, 18(3):383–95, vi, 2005.

[109] T. Lasser and V. Ntziachristos. Optimization of 360 degrees projection fluorescence molecular tomography. Med Image Anal, 11(4):389–99, 2007.

[110] A. Leroy-Willig, V. Ntziachristos, and B. Tavitian. Textbook of in vivo imaging in vertebrates [electronic resource]. J. Wiley, Chichester, England ; Hoboken, NJ, 2007.

[111] R. M. Levenson, D. T. Lynch, H. Kobayashi, J. M. Backer, and M. V. Backer. Multiplexing with multispectral imaging: from mice to microscopy. ILAR J, 49(1):78–88, 2008.

[112] R. M. Levenson and J. R. Mansfield. Multispectral imaging in biology and medicine: slices of life. Cytometry A, 69(8):748–58, 2006.

[113] A. Li, G. Boverman, Y. Zhang, D. Brooks, E. L. Miller, M. E. Kilmer, Q. Zhang, E. M. Hillman, and D. A. Boas. Optimal linear inverse solution with multiple priors in diffuse optical tomography. Appl Opt, 44(10):1948–56, 2005.

[114] A. Li, E. L. Miller, M. E. Kilmer, T. J. Brukilacchio, T. Chaves, J. Stott, Q. Zhang, T. Wu, M. Chorlton, R. H. Moore, D. B. Kopans, and D. A. Boas. Tomographic optical breast imaging guided by three-dimensional mammography. Appl Opt, 42(25):5181–90, 2003.

[115] M. L. Li, J. T. Oh, X. Y. Xie, G. Ku, W. Wang, C. Li, G. Lungu, G. Stoica, and L. V. Wang. Simultaneous molecular and hypoxia imaging of brain tumors in vivo using spectroscopic photoacoustic tomography. Proceedings of the Ieee, 96(3):481–489, 2008.

[116] LifeTechnologies. Fluorescence spectra viewer. http://www.lifetechnologies.com/, July 2014.

[117] Y. Lin, H. Yan, O. Nalcioglu, and G. Gulsen. Quantitative fluorescence tomography with functional and structural a priori information. Appl Opt, 48(7):1328–36, 2009.

[118] J. Livet, T. A. Weissman, H. Kang, R. W. Draft, J. Lu, R. A. Bennis, J. R. Sanes, and J. W. Lichtman. Transgenic strategies for combinatorial expression of fluorescent proteins in the nervous system. Nature, 450(7166):56–62, 2007.

[119] A. London, I. Benhar, and M. Schwartz. The retina as a window to the brain-from eye research to cns disorders. Nat Rev Neurol, 9(1):44–53, 2013.

[120] G. Lu and B. Fei. Medical hyperspectral imaging: a review. J Biomed Opt, 19(1):10901, 2014.

[121] U. Mahmood and R. Weissleder. Near-infrared optical imaging of proteases in cancer. Mol Cancer Ther, 2(5):489–96, 2003.

[122] J. R. Mansfield, K. W. Gossage, C. C. Hoyt, and R. M. Levenson. Autofluorescence removal, multiplexing, and automated analysis methods for in-vivo fluorescence imaging. J Biomed Opt, 10(4):41207, 2005.

[123] MathWorks. Support vector machines. http://www.mathworks.de/de/help/stats/support-vector-machines-svm.html, July 2014.

[124] D. T. Miller, D. R. Williams, G. M. Morris, and J. Liang. Images of cone photoreceptors in the living human eye. Vision Res, 36(8):1067–79, 1996.

[125] T. Moffitt, Y. C. Chen, and S. A. Prahl. Preparation and characterization of polyurethane optical phantoms. J Biomed Opt, 11(4):041103, 2006.

[126] P. Mohajerani, A. Hipp, M. Willner, M. Marschner, M. Trajkovic-Arsic, X. Ma, N. C. Burton, U. Klemm, K. Radrich, V. Ermolayev, S. Tzoumas, J. T. Siveke, M. Bech, F. Pfeiffer, and V. Ntziachristos. Fmt-pcct: Hybrid fluorescence molecular tomography-x-ray phase-contrast ct imaging of mouse models. IEEE Trans Med Imaging, 33(7):1434–46, 2014.

[127] M. Nahrendorf, D. E. Sosnovik, P. Waterman, F. K. Swirski, A. N. Pande, E. Aikawa, J. L. Figueiredo, M. J. Pittet, and R. Weissleder. Dual channel optical tomographic imaging of leukocyte recruitment and protease activity in the healing myocardial infarct. Circ Res, 100(8):1218–25, 2007.

[128] M. Nahrendorf, P. Waterman, G. Thurber, K. Groves, M. Rajopadhye, P. Panizzi, B. Marinelli, E. Aikawa, M. J. Pittet, F. K. Swirski, and R. Weissleder. Hybrid in vivo fmt-ct imaging of protease activity in atherosclerosis with customized nanosensors. Arterioscler Thromb Vasc Biol, 29(10):1444–51, 2009.

[129] N. Nakano, H. O. Ikeda, M. Hangai, Y. Muraoka, Y. Toda, A. Kakizuka, and N. Yoshimura. Longitudinal and simultaneous imaging of retinal ganglion cells and inner retinal layers in a mouse model of glaucoma induced by n-methyl-d-aspartate. Invest Ophthalmol Vis Sci, 52(12):8754–62, 2011.

[130] J. Neefjes and N. P. Dantuma. Fluorescent probes for proteolysis: tools for drug discovery. Nat Rev Drug Discov, 3(1):58–69, 2004.

[131] R. A. Neher, M. Mitkovski, F. Kirchhoff, E. Neher, F. J. Theis, and A. Zeug. Blind source separation techniques for the decomposition of multiply labeled fluorescence images. Biophys J, 96(9):3791–800, 2009.

[132] S. P. Nighswander-Rempel, R. Anthony Shaw, J. R. Mansfield, M. Hewko, V. V. Kupriyanov, and H. H. Mantsch. Regional variations in myocardial tissue oxygenation mapped by near-infrared spectroscopic imaging. J Mol Cell Cardiol, 34(9):1195–203, 2002.

[133] V. Ntziachristos. Fluorescence molecular imaging. Annu Rev Biomed Eng, 8:1–33, 2006.

[134] V. Ntziachristos. Going deeper than microscopy: the optical imaging frontier in biology. Nat Methods, 7(8):603–14, 2010.

[135] V. Ntziachristos and B. Chance. Probing physiology and molecular function using optical imaging: applications to breast cancer. Breast Cancer Res, 3(1):41–6, 2001.

[136] V. Ntziachristos, X. H. Ma, A. G. Yodh, and B. Chance. Multichannel photon counting instrument for spatially resolved near infrared spectroscopy. Review of Scientific Instruments, 70(1):193–201, 1999.

[137] V. Ntziachristos and D. Razansky. Molecular imaging by means of multispectral optoacoustic tomography (msot). Chem Rev, 110(5):2783–94, 2010.

[138] V. Ntziachristos, J. Ripoll, L. V. Wang, and R. Weissleder. Looking and listening to light: the evolution of whole-body photonic imaging. Nat Biotechnol, 23(3):313–20, 2005.

[139] V. Ntziachristos, C. H. Tung, C. Bremer, and R. Weissleder. Fluorescence molecular tomography resolves protease activity in vivo. Nat Med, 8(7):757–60, 2002.

[140] V. Ntziachristos, A. G. Yodh, M. Schnall, and B. Chance. Concurrent mri and diffuse optical tomography of breast after indocyanine green enhancement. Proc Natl Acad Sci U S A, 97(6):2767–72, 2000.

[141] V. Ntziachristos, A. G. Yodh, M. D. Schnall, and B. Chance. Mri-guided diffuse optical spectroscopy of malignant and benign breast lesions. Neoplasia, 4(4):347–54, 2002.

[142] N. A. of Engineering. Greates engineering achievements of the 20th century. http://www.greatachievements.org/, July 2014.

[143] D. Pankajakshan and D. K. Agrawal. Gene Therapy - Tools and Potential Applications, chapter Clinical and Translational Challanges in Gene Therapy of Cardiovascular Diseases, pages 651–683. InTech, 2013.

[144] M. Paques, J. L. Guyomard, M. Simonutti, M. J. Roux, S. Picaud, J. F. Legargasson, and J. A. Sahel. Panretinal, high-resolution color photography of the mouse fundus. Invest Ophthalmol Vis Sci, 48(6):2769–74, 2007.

[145] B. W. Pogue and K. D. Paulsen. High-resolution near-infrared tomographic imaging simulations of the rat cranium by use of a priori magnetic resonance imaging structural information. Opt Lett, 23(21):1716–8, 1998.

[146] B. W. Pogue, H. Zhu, C. Nwaigwe, T. O. McBride, U. L. Osterberg, K. D. Paulsen, and J. F. Dunn. Hemoglobin imaging with hybrid magnetic resonance and near-infrared diffuse tomography. Adv Exp Med Biol, 530:215–24, 2003.

[147] S. Prahl and S. Jacques. Optical properties spectra. http://omlc.org/spectra/, July 2014.

[148] S. Prilloff, J. Fan, P. Henrich-Noack, and B. A. Sabel. In vivo confocal neuroimaging (icon): non-invasive, functional imaging of the mammalian cns with cellular resolution. Eur J Neurosci, 31(3):521–8, 2010.

[149] X. Qiu, J. R. Johnson, B. S. Wilson, S. T. Gammon, D. Piwnica-Worms, and E. M. Barnett. Single-cell resolution imaging of retinal ganglion cell apoptosis in vivo using a cell-penetrating caspase-activatable peptide probe. PLoS One, 9(2):e88855, 2014.

[150] K. Radrich, A. Ale, V. Ermolayev, and V. Ntziachristos. Improving limited-projection-angle fluorescence molecular tomography using a co-registered x-ray computed tomography scan. J Biomed Opt, 17(12):126011, 2012.

[151] K. Radrich, P. Mohajerani, J. Bussemer, M. Schwaiger, A. J. Beer, and V. Ntziachristos. Limited-projection-angle hybrid fluorescence molecular tomography of multiple molecules. J Biomed Opt, 19(4):046016, 2014.

[152] N. Rajaram, T. H. Nguyen, and J. W. Tunnell. Lookup table-based inverse model for determining optical properties of turbid media. J Biomed Opt, 13(5):050501, 2008.

[153] J. Ripoll, D. Yessayan, G. Zacharakis, and V. Ntziachristos. Experimental determination of photon propagation in highly absorbing and scattering media. J Opt Soc Am A Opt Image Sci Vis, 22(3):546–51, 2005.

[154] P. Rolfe. In vivo near-infrared spectroscopy. Annu Rev Biomed Eng, 2:715–54, 2000.

[155] E. A. Rossi, M. Chung, A. Dubra, J. J. Hunter, W. H. Merigan, and D. R. Williams. Imaging retinal mosaics in the living eye. Eye (Lond), 25(3):301–8, 2011.

[156] B. E. A. Saleh. Introduction to subsurface imaging. Cambridge University Press, Cambridge ; New York, 2011.

[157] N. Salem, J. D. Balkman, J. Wang, D. L. Wilson, Z. Lee, C. L. King, and J. P. Basilion. In vivo imaging of schistosomes to assess disease burden using positron emission tomography (pet). PLoS Negl Trop Dis, 4(9), 2010.

[158] A. Sarantopoulos, G. Themelis, and V. Ntziachristos. Imaging the bio-distribution of fluorescent probes using multispectral epi-illumination cryoslicing imaging. Mol Imaging Biol, 2010.

[159] F. E. Schmidt, J. C. Hebden, E. M. Hillman, M. E. Fry, M. Schweiger, H. Dehghani, D. T. Delpy, and S. R. Arridge. Multiple-slice imaging of a tissue-equivalent phantom by use of time-resolved optical tomography. Appl Opt, 39(19):3380–7, 2000.

[160] R. B. Schulz, A. Ale, A. Sarantopoulos, M. Freyer, E. Soehngen, M. Zientkowska, and V. Ntziachristos. Hybrid system for simultaneous fluorescence and x-ray computed tomography. IEEE Trans Med Imaging, 29(2):465–73, 2010.

[161] R. B. Schulz, J. Ripoll, and V. Ntziachristos. Experimental fluorescence tomography of tissues with noncontact measurements. IEEE Trans Med Imaging, 23(4):492–500, 2004.

[162] M. W. Seeliger, S. C. Beck, N. Pereyra-Munoz, S. Dangel, J. Y. Tsai, U. F. Luhmann, S. A. van de Pavert, J. Wijnholds, M. Samardzija, A. Wenzel, E. Zrenner, K. Narfstrom, E. Fahl, N. Tanimoto, N. Acar, and F. Tonagel. In vivo confocal imaging of the retina in animal models using scanning laser ophthalmoscopy. Vision Res, 45(28):3512–9, 2005.

[163] W. Semmler and M. Schwaiger. Molecular imaging. Handbook of experimental pharmacology, v. 185/1-v. 185/20171-2004. Springer, Berlin, 2008. (Wolfhard) ill. (some col.) ; 24 cm. Includes bibliographical references and index.

[164] J. W. Severinghaus. History and recent developments in pulse oximetry. Scand J Clin Lab Invest Suppl, 214:105–11, 1993.

[165] K. Shah and R. Weissleder. Molecular optical imaging: applications leading to the development of present day therapeutics. NeuroRx, 2(2):215–25, 2005.

[166] D. M. Shcherbakova and V. V. Verkhusha. Near-infrared fluorescent proteins for multicolor in vivo imaging. Nat Methods, 2013.

[167] J. Shlens. A tutorial on principle component analyis. http://www.brainmapping.org/NITP/PNA/Readings/pca.pdf, 2005.

[168] X. Shu, A. Royant, M. Z. Lin, T. A. Aguilera, V. Lev-Ram, P. A. Steinbach, and R. Y. Tsien. Mammalian expression of infrared fluorescent proteins engineered from a bacterial phytochrome. Science, 324(5928):804–7, 2009.

[169] D. A. Sipkins, D. A. Cheresh, M. R. Kazemi, L. M. Nevin, M. D. Bednarski, and K. C. Li. Detection of tumor angiogenesis in vivo by alphavbeta3-targeted magnetic resonance imaging. Nat Med, 4(5):623–6, 1998.

[170] T. J. Snoeks, C. W. Lowik, and E. L. Kaijzel. 'in vivo' optical approaches to angiogenesis imaging. Angiogenesis, 13(2):135–47, 2010.

[171] M. Solonenko, R. Cheung, T. M. Busch, A. Kachur, G. M. Griffin, T. Vulcan, T. C. Zhu, H. W. Wang, S. M. Hahn, and A. G. Yodh. In vivo reflectance measurement of optical properties, blood oxygenation and motexafin lutetium uptake in canine large bowels, kidneys and prostates. Phys Med Biol, 47(6):857–73, 2002.

[172] W. Song, Q. Wei, T. Liu, D. Kuai, J. M. Burke, S. Jiao, and H. F. Zhang. Integrating photoacoustic ophthalmoscopy with scanning laser ophthalmoscopy, optical coherence tomography, and fluorescein angiography for a multimodal retinal imaging platform. J Biomed Opt, 17(6):061206, 2012.

[173] A. Soubret, J. Ripoll, and V. Ntziachristos. Accuracy of fluorescent tomography in the presence of heterogeneities: study of the normalized born ratio. IEEE Trans Med Imaging, 24(10):1377–86, 2005.

[174] S. Srinivasan, B. W. Pogue, C. Carpenter, S. Jiang, W. A. Wells, S. P. Poplack, P. A. Kaufman, and K. D. Paulsen. Developments in quantitative oxygen-saturation imaging of breast tissue in vivo using multispectral near-infrared tomography. Antioxid Redox Signal, 9(8):1143–56, 2007.

[175] R. St-Jacques. Corps humain. http://www.corpshumain.ca, July 2014.

[176] H. B. Stone, J. M. Brown, T. L. Phillips, and R. M. Sutherland. Oxygen in human tumors: correlations between methods of measurement and response to therapy. summary of a workshop held november 19-20, 1992, at the national cancer institute, bethesda, maryland. Radiat Res, 136(3):422–34, 1993.

[177] J. V. Stone. Independent component analysis: an introduction. Trends Cogn Sci, 6(2):59–64, 2002.

[178] J. V. Stone. The Encyclopedia of Statistics in Behavioral Science, chapter Independent Component Analysis. Wiley, 2005.

[179] F. Stuker, C. Baltes, K. Dikaiou, D. Vats, L. Carrara, E. Charbon, J. Ripoll, and M. Rudin. Hybrid small animal imaging system combining magnetic resonance imaging with fluorescence tomography using single photon avalanche diode detectors. IEEE Trans Med Imaging, 30(6):1265–73, 2011.

[180] B. Terelak-Borys, K. Skonieczna, and I. Grabska-Liberek. Ocular ischemic syndrome - a systematic review. Med Sci Monit, 18(8):RA138–144, 2012.

[181] K. M. Tichauer, R. W. Holt, F. El-Ghussein, S. C. Davis, K. S. Samkoe, J. R. Gunn, F. Leblond, and B. W. Pogue. Dual-tracer background subtraction approach for fluorescent molecular tomography. J Biomed Opt, 18(1):16003, 2013.

[182] A. Tikhonov and V. Arsenin. Solutions of ill-posed problems. John Wiley & Sons, 1977.

[183] D. W. Townsend. Dual-modality imaging: combining anatomy and function. J Nucl Med, 49(6):938–55, 2008.

[184] G. M. van Dam, G. Themelis, L. M. Crane, N. J. Harlaar, R. G. Pleijhuis, W. Kelder, A. Sarantopoulos, J. S. de Jong, H. J. Arts, A. G. van der Zee, J. Bart, P. S. Low, and V. Ntziachristos. Intraoperative tumor-specific fluorescence imaging in ovarian cancer by folate receptor-alpha targeting: first in-human results. Nat Med, 17(10):1315–9, 2011.

[185] H. J. van Staveren, C. J. Moes, J. van Marie, S. A. Prahl, and M. J. van Gemert. Light scattering in intralipid-10400-1100 nm. Appl Opt, 30(31):4507–14, 1991.

[186] A. Villringer, J. Planck, C. Hock, L. Schleinkofer, and U. Dirnagl. Near infrared spectroscopy (nirs): a new tool to study hemodynamic changes during activation of brain function in human adults. Neurosci Lett, 154(1-2):101–4, 1993.

[187] A. J. V. G. Visser and O. J. Rolinski. Basic photophysics. http://www.photobiology.info/Visser-Rolinski.html, July 2014.

[188] T. Vo-Dinh. Biomedical photonics handbook [electronic resource]. CRC Press, Boca Raton, Fla., 2003.

[189] R. Waehler, S. J. Russell, and D. T. Curiel. Engineering targeted viral vectors for gene therapy. Nat Rev Genet, 8(8):573–87, 2007.

[190] G. L. Walls. The vertebrate eye and its adaptive radiation. Bulletin /Cranbrook Institute of Science. printed by the Cranbrook Press], [Bloomfield Hills, 1942.

[191] L. V. Wang and H.-i. Wu. Biomedical optics principles and imaging. Wiley-Interscience, Hoboken, NJ.

[192] J. P. Weichert, J. Lee, F. T., S. G. Chosy, M. A. Longino, J. E. Kuhlman, D. M. Heisey, and G. E. Leverson. Combined hepatocyte-selective and blood-pool contrast agents for the ct detection of experimental liver tumors in rabbits. Radiology, 216(3):865–71, 2000.

[193] R. Weissleder. Scaling down imaging: molecular mapping of cancer in mice. Nat Rev Cancer, 2(1):11–8, 2002.

[194] R. Weissleder and V. Ntziachristos. Shedding light onto live molecular targets. Nat Med, 9(1):123–8, 2003.

[195] R. Weissleder and M. J. Pittet. Imaging in the era of molecular oncology. Nature, 452(7187):580–9, 2008.

[196] R. Weissleder, C. H. Tung, U. Mahmood, and J. Bogdanov, A. In vivo imaging of tumors with protease-activated near-infrared fluorescent probes. Nat Biotechnol, 17(4):375–8, 1999.

[197] J. K. Willmann, R. Paulmurugan, K. Chen, O. Gheysens, M. Rodriguez-Porcel, A. M. Lutz, I. Y. Chen, X. Chen, and S. S. Gambhir. Us imaging of tumor angiogenesis with microbubbles targeted to vascular endothelial growth factor receptor type 2 in mice. Radiology, 246(2):508–18, 2008.

[198] J. K. Willmann, N. van Bruggen, L. M. Dinkelborg, and S. S. Gambhir. Molecular imaging in drug development. Nat Rev Drug Discov, 7(7):591–607, 2008.

[199] P. K. Yalavarthy, B. W. Pogue, H. Dehghani, C. M. Carpenter, S. Jiang, and K. D. Paulsen. Structural information within regularization matrices improves near infrared diffuse optical tomography. Opt Express, 15(13):8043–58, 2007.

[200] X. Yang, H. Gong, G. Quan, Y. Deng, and Q. Luo. Combined system of fluorescence diffuse optical tomography and microcomputed tomography for small animal imaging. Rev Sci Instrum, 81(5):054304, 2010.

[201] N. Yavari. Optical spectroscopy for tissue diagnostics and treatment control. PhD thesis, University of Bergen, 2006.

[202] A. Yodh and B. Chance. Spectroscopy and imaging with diffusing light. Physics Today, 1995.

[203] D. Yudovsky and L. Pilon. Simple and accurate expressions for diffuse reflectance of semi-infinite and two-layer absorbing and scattering media. Appl Opt, 48(35):6670–83, 2009.

[204] D. Yudovsky and L. Pilon. Rapid and accurate estimation of blood saturation, melanin content, and epidermis thickness from spectral diffuse reflectance. Appl Opt, 49(10):1707–19, 2010.

[205] D. Yudovsky and L. Pilon. Retrieving skin properties from in vivo spectral reflectance measurements. J Biophotonics, 4(5):305–14, 2011.

[206] G. Zacharakis, J. Ripoll, R. Weissleder, and V. Ntziachristos. Fluorescent protein tomography scanner for small animal imaging. IEEE Trans Med Imaging, 24(7):878–85, 2005.

[207] K. Zhang, L. Zhang, and R. N. Weinreb. Ophthalmic drug discovery: novel targets and mechanisms for retinal diseases and glaucoma. Nat Rev Drug Discov, 11(7):541–59, 2012.

[208] M. Zhao, D. A. Beauregard, L. Loizou, B. Davletov, and K. M. Brindle. Non-invasive detection of apoptosis using magnetic resonance imaging and a targeted contrast agent. Nat Med, 7(11):1241–4, 2001.

[209] Q. Zhu, T. Durduran, V. Ntziachristos, M. Holboke, and A. G. Yodh. Imager that combines near-infrared diffusive light and ultrasound. Opt Lett, 24(15):1050–2, 1999.

[210] T. Zimmermann. Spectral imaging and linear unmixing in light microscopy. Adv Biochem Eng Biotechnol, 95:245–65, 2005.

[211] G. Zonios and A. Dimou. Modeling diffuse reflectance from semi-infinite turbid media: application to the study of skin optical properties. Opt Express, 14(19):8661–74, 2006.

List of publications

Published papers

[I] K. Radrich, P. Mohajerani, J. Bussemer, M. Schwaiger, A. J. Beer, and V. Ntziachristos. Limited-projection-angle hybrid fluorescence molecular tomography of multiple molecules. J Biomed Opt, 19(4), 2014.

[II] K. Radrich, A. Ale, V. Ermolayev, and V. Ntziachristos. Improving limited-projection-angle fluorescence molecular tomography using a co-registered X-ray computed tomography scan. J Biomed Opt, 17(12), 2012.

[III] P. Mohajerani, A. Hipp, M. Willner, M. Marschner, M. Trajkovic-Arsic, X. Ma, N. C. Burton, U. Klemm, K. Radrich, V. Ermolayev, S. Tzoumas, J. T. Siveke, M. Bech, F. Pfeiffer, and V. Ntziachristos. FMT-PCCT: Hybrid fluorescence molecular tomography - X-ray phase-contrast CT imaging of mouse models. IEEE Trans Med Imaging, 33(7), 2014.

[IV] N. C. Deliolanis, A. Ale, S. Morscher, N. C. Burton, K. Schaefer, K. Radrich, D. Razansky, and V. Ntziachristos. Deep-tissue reporter-gene imaging with fluorescence and optoacoustic tomography: A performance overview. Mol Imaging Biol, 2014.

[V] A. Ale, F. Siebenhaar, K. Kosanke, M. Aichler, K. Radrich, S. Heydrich, M. Schiemann, I. Bielicki, P. B. Noel, R. Braren, M. Maurer, A. K. Walch, E. J. Rummeny, V. Ntziachristos, and M. Wildgruber. Cardioprotective c-kit(+) bone marrow cells attenuate apoptosis after acute myocardial infarction in mice - in-vivo assessment with fluorescence molecular imaging. Theranostics, 3(11), 2013.

Papers submitted or in preparation

[VI] K. Radrich, and V. Ntziachristos. Quantitative multi-spectral oxygen saturation measurements independent of tissue optical properties. Submitted.

[VII] K. Radrich, A. Ly, S. Michalakis, S. Glasl, S. Hauck, M. Ueffing, and V. Ntziachristos. Visualization of multi-parametric biology by smart contrast generation and multispectral molecular imaging. In preparation.

[VIII] P. B. Garcia-Allende, K. Radrich, P. Symvoulidis, J. Glatz, M. Koch, K. M. Jentoft, J. Ripoll, and V. Ntziachristos. Scale invariance and diagnostic value of multispectral measurements of the total diffuse reflectance from biological tissues. In preparation.